The evolution of spiral galaxies in distant clusters

Bo Milvang–Jensen

Thesis submitted to the University of Nottingham
for the degree of Doctor of Philosophy

May 2003

Supervisor: Dr Alfonso Aragón-Salamanca

Examiners: Prof Roger L Davies
Prof Michael R Merrifield

Contents

List of Figures

(page left blank to get matching page numbers for single and double sided versions)

List of Tables

(page left blank to get matching page numbers for single and double sided versions)

Abstract

This thesis studies spiral galaxies in the high redshift cluster MS1054−03 at $z = 0.83$ and field spirals at similar redshifts. The aim is to shed light on the processes governing the evolution of galaxies in clusters, in particular the processes responsible for the morphological transformation of spiral galaxies into S0s. The main diagnostic used is the Tully–Fisher relation. We have obtained spatially-resolved optical emission line spectra carried out at the VLT, from which we have measured rotation velocities. The sample analysed contains 7 spirals in MS1054−03 and 18 field spirals at $z = 0.15$–0.90. Rest-frame B–band magnitudes were derived using HST images, and the B–band Tully–Fisher relation for the sample was studied. With respect to a local relation, most of the high redshift galaxies were found on the high luminosity / low velocity side. The cluster sample was compared to the field sample. A difference in the Tully–Fisher residuals was found at 1.5–2σ significance. If interpreted as a difference in absolute magnitude at a fixed rotation velocity, the mean difference is $\sim$1 mag in the sense that the cluster sample is brighter than the field sample. This could indicate a brightening due to enhanced levels of star formation. A similar analysis in the rest-frame H–band, but using unpublished magnitudes derived from images which we have not had access to, shows a cluster–field difference that is as large as in the B–band. This is at variance with our interpretation of the B–band results. If the H–band results are confirmed using published data we should consider the alternative interpretation that the Tully–Fisher residuals are driven by differences in rotation velocity rather than luminosity.

The size (stellar scale length)–velocity diagram showed no strong cluster–field difference. This indicates that the cluster and the field spirals are structurally similar. The gas scale lengths were compared to the stellar scale lengths, and the two were found to be well correlated. Their ratio was smaller for the cluster spirals than for the field spirals. This could indicate that centrally concentrated star formation is more common in cluster spirals than in field spirals, a phenomenon also found locally.

The B–band Tully–Fisher residuals were found to be correlated with the [OII] luminosity and with an estimate of the extinction-corrected star formation rate at $\sim 2\sigma$ significance. Galaxies with large negative Tully–Fisher residuals (indicative of a brightening) had large [OII] luminosities and star formation rates. This directly supports the interpretation of the B–band Tully–Fisher residuals as due to a brightening caused by star formation.

Taken as a whole, the results indicate that at least some spiral galaxies in high redshift clusters experience a period of enhanced star formation. This fits into the emerging picture in which spirals at high redshift fall into clusters from the field, experience a star burst and then fade and morphologically transform into S0s. As a continuation of this work we are studying larger samples and other evolutionary phases to underpin the yet unknown physical mechanisms responsible for the morphological transformation.

(page left blank to get matching page numbers for single and double sided versions)

Preface

Acknowledgements

Many people and organisations have contributed in various ways to this work. First and foremost I would like to thank my dear supervisor Alfonso, whose inspiration, insight, encouragement, dedication, patience and good sense of humour has been invaluable. The generous support from the sponsors of my PhD studentship, the Danish Research Training Council (*Forskeruddannelsesrådet*), is acknowledged with thanks. I am also indebted to my new boss Ralf Bender and the Max-Planck-Institute for Extraterrestrial Physics for letting me spend a large fraction of my time in the first months of 2003 on finishing the thesis. My new colleagues at the MPE are thanked for their good company. My parents are thanked for their continuous support throughout the years. It is also a true pleasure to thank the Nottingham astronomy group for being such an exciting place to work, as well as a very pleasant one. It has been a pleasure to interact with all of you guys in the office, at coffee, at lunch, at the seminars, at the ensuing staff–sponsored after–seminar beer sessions at the staff club, and in the world outside of the university at the lovely English pubs and in the Peak District countryside. I hesitate to single anyone out, but I nevertheless want to thank Laura, Simon and Ed for their warm friendship, and the rest of my old officemates from the pioneering early days, Jesús and Pan.

Luc Simard deserves special thanks for letting me use his emission line fitting software, which I think is unrivalled in terms of making the most of the precious photons collected.

My contact person (a requirement of my sponsors) Jens Hjorth at the University of Copenhagen is thanked for his encouragement, particularly in the days when I was an unemployed astronomer before I got the PhD studentship. Inger Jørgensen and Leif Hansen, as well as Jens Hjorth, are thanked for writing numerous reference letters before I got my PhD student career going. My friend Lars is thanked for hosting me the first month I was here in Munich. My florist friend Christine in Nottingham is thanked for taking care of my plants whenever I was on mission to Chile, Hawaii, Garching or other exotic destinations in the world. ESO is thanked for allocating one night of VLT time for the MS1054−03 observations[1], and for the support during the observations at Paranal. The co–Is on the proposal — George Hau, Inger Jørgensen and Jens Hjorth — are thanked for their assistance. The use of HST observations of MS1054−03, kindly made available by Pieter van Dokkum and Marijn Franx, is acknowledged[2]. Jean-Paul Kneib is thanked for providing an HST image of the intermediate redshift cluster A1835

[1] Based on observations collected at the European Southern Observatory, Chile (66.A–0376)

[2] Based on observations with the NASA/ESA Hubble Space Telescope, obtained at the Space Telescope Science Institute, which is operated by AURA, Inc., under NASA contract NAS5-26555

used to design a bad seeing backup programme, which fortunately was not needed. This work has benefitted from a number of software tools, including the *vim* editor[3], IRAF[4] and the STSDAS and TABLES packages[5]. The people at the IRAF project are also thanked for the help in tracking down the occasional bug and for advice in general. The bibliographical services of the ADS[6] have been extremely useful, and the service is made even better by the always helpful staff of the project. The astro–ph preprint service has also been valuable, as well as the HST archives at ST–ECF[7] and CADC[8]. The "*vulcan*" supercomputer in Nottingham has also been instrumental in making all the time consuming emission line fits possible.

Before this gets to sound too much like the Danish Queen's new year speech in which she sends her warm thoughts to everyone in the kingdom including the people of the sea, the people of the Faroe Islands and the people of Greenland, let me end by offering my apologies to anyone I have forgotten to thank or cite — the acknowledgements and the introduction were written at the last moment (yes, some things never change!).

Notation and Terminology

"log" is the base ten logarithm. The pronoun *we* is used instead of *I* to refer to the author of this thesis, as is customary for single author papers in the literature. Three–author papers are consistently cited as 'first author et al.'.

Technical information

The thesis has been typeset using LaTeX2e with standard fonts at 11 point size and with standard line spacing. In accordance with University rules[9] margins as wide as 4 cm on the left and 2.5 cm on the right have been used, as well as single sided printing. Some figures are in colour. For the pseudo-colour (i.e. greyscale) images there is no extra information in the colours. For the colour line drawings no "critical" information should be carried by the colour coding.

[3] `http://www.vim.org/`

[4] IRAF is distributed by the National Optical Astronomy Observatories, which are operated by the Association of Universities for Research in Astronomy, Inc., under cooperative agreement with the National Science Foundation. See also `http://iraf.noao.edu/`

[5] STSDAS is distributed by the Space Telescope Science Institute, operated by AURA, Inc., under NASA contract NAS 5-26555. See also `http://stsdas.stsci.edu/STSDAS.html`

[6] e.g. `http://adsabs.harvard.edu/abstract_service.html`

[7] `http://archive.eso.org/wdb/wdb/hst/science/form`

[8] `http://cadcwww.dao.nrc.ca/hst/science.html`

[9] `http://www.nottingham.ac.uk/physics/pgrad/submit.phtml`

Chapter 1

Introduction

Galaxies are found in a variety of environments, from the low density so-called field to rich clusters. A range of galaxy morphologies are also seen, with the vast majority of galaxies at low redshift fitting into the main classes devised by Hubble (1926, 1936): ellipticals, S0s and spirals. Moreover, the morphological mix is a strong function of the environment. Already Hubble & Humason (1931) noted that "The predominance of early types is a conspicuous feature of clusters in general [...]". This phenomenon was quantified by Dressler (1980), who in a study of $\sim$6000 galaxies in 55 local ($z \lesssim 0.06$) rich clusters found the morphological mix to vary smoothly with projected galaxy density, see Fig 1.1. This striking result is the so-called *morphology–density relation*.

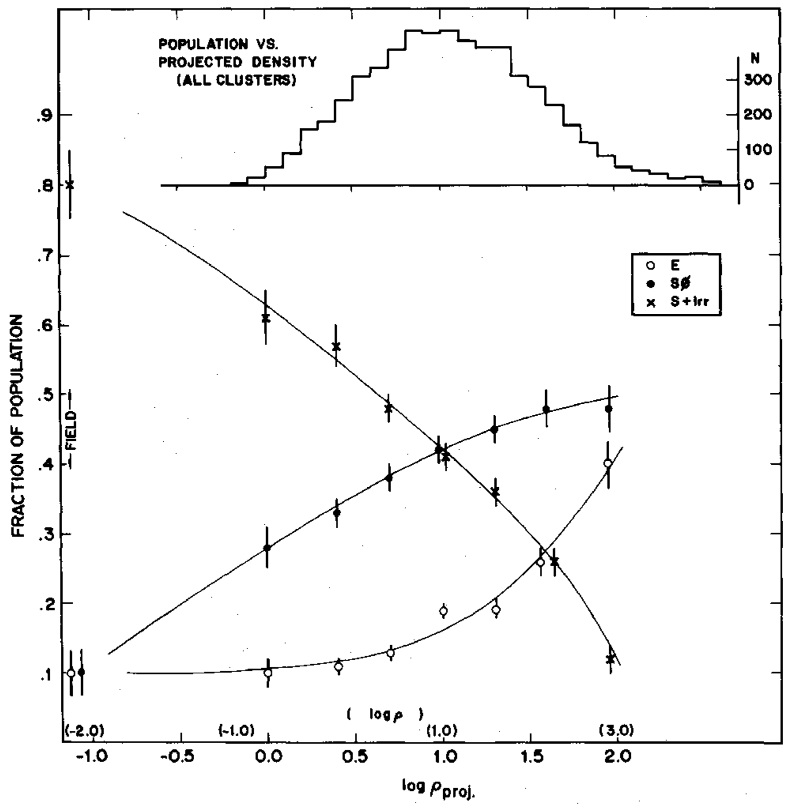

Figure 1.1: The morphology–density relation for local clusters. Figure reproduced from Dressler (1980).

The star formation rate (SFR) has long been known to increase along the Hubble sequence of morphological types, from ellipticals to spirals and irregulars. Therefore, given the morphology–density relation it is not surprising that a *SFR–density relation* exists. This relation has been studied by Hashimoto et al. (1998), Lewis et al. (2002) and Gómez et al. (2003) using very large samples (∼10 000) of local galaxies (mainly at $z < 0.1$). A strong correlation between SFR and either projected density or radius within clusters was indeed found in all three studies, in the sense that the SFR was lower (suppressed) in high density environments. Not only did the mean SFR change with density in this way, but also the skewness of the SFR distribution changed, with the tail of highly star forming galaxies being most prominent at low densities (Lewis et al.; Gómez et al.). In terms of cluster galaxies, a difference of the SFR with respect to field galaxies could be detected as far out as 3–4 virial radii (Lewis et al.; Gómez et al.). Furthermore, using the concentration index as a quantitative measure of morphology, it was found that galaxies of the same concentration index (∼morphological type) also showed a SFR–density relation, with galaxies in high density environments having lower SFRs. This indicates that the SFR–density relation is partially independent of the morphology–density relation (Hashimoto et al.; Gómez et al.).

Density also seems to influence the distribution of star formation within individual galaxies. In an Hα imaging survey of local cluster galaxies, Moss & Whittle (2000) found an increase in 'compact' (i.e. centrally concentrated) star formation with increasing projected density. The incidence of centrally concentrated star formation was also seen to be higher in more dense clusters. Centrally concentrated star formation was generally associated with a bar or with a disturbed galaxy morphology indicative of ongoing tidal interactions.

The obvious question is whether these trends of galaxy properties with density were imprinted early on or are the result of evolutionary effects that depend on the environment. Observations of galaxies at high redshift help shedding light on this, so we will turn to the high redshift observations before discussing the implications of the low redshift findings.

Before the advent of the Hubble Space Telescope (HST) morphologies of high redshift galaxies could not be studied. Likewise, before the advent of large ground based telescopes with efficient spectrographs the detailed spectral properties of high redshift galaxies could not be studied. However, the colours could. In a pioneering photometric study of high redshift ($z \lesssim 0.5$) clusters, Butcher & Oemler (1978, 1984) found that the fraction of blue galaxies increased with redshift. 'Blue galaxies' were defined as being bluer than 0.2 mag in $(B - V)$ with respect to the *colour–magnitude relation* for early type galaxies (Baum 1959; Sandage 1972; Visvanathan & Sandage 1977; Bower et al. 1992). The increase of blue galaxies in clusters with redshift has become known as the *Butcher–Oemler effect*. The tentative conclusion of Butcher & Oemler was that these high redshift blue cluster galaxies were normal spirals, and since spirals are not present in large numbers in local clusters the implication was that strong recent evolution of the galaxy population in clusters had taken place.

Subsequent spectroscopic observations of high redshift clusters (e.g. Dressler & Gunn 1983, 1992; Couch & Sharples 1987; Fabricant et al. 1991) showed that the majority of the blue galaxies were indeed cluster members. Surprisingly, many of these blue galaxies did not have spectra resembling those of local spirals with emission lines due to on-going star formation. Instead, the spectra of these blue high redshift cluster galaxies, and some of the red ones as well, showed strong Balmer absorption lines and no emission lines, a spectral type that is rare in the local Universe. The spectra could be synthesized as the spectrum of an E galaxy or a K–star with the spectrum of an A–star superposed (Dressler & Gunn 1983), and hence the names E+A or k+a were later adopted. Modelling of these galaxies (e.g. Dressler & Gunn 1983; Couch & Sharples 1987; Barger et al. 1996; Poggianti & Barbaro 1996; Couch et al. 1998; Morris et al. 1998; Poggianti et al. 1999; Shioya et al. 2001, 2002) requires a truncation of star formation, and the examples with stronger Balmer lines furthermore require a burst of star formation prior to the truncation. Therefore, these galaxies are often referred to as *post-starburst galaxies*. The last star formation event must have ended between a few Myr and ∼1.5 Gyr prior to the observation, a time scale set by the A–stars that are responsible for the strong Balmer lines (Poggianti & Barbaro 1997; Poggianti et al. 1999). The discovery of this substantial fraction of $z \sim 0.5$ cluster galaxies with E+A spectra was another sign that strong recent evolution had taken place in clusters.

With the advent of the refurbished HST, morphological investigations could be extended to high redshift. The MORPHS group studied the morphologies of galaxies in ten clusters at $z \sim 0.4$–0.5 (Smail et al. 1997; Dressler et al. 1997; see also Dressler et al. 1994; Oemler et al. 1997), and clusters at $z = 0.3$ were also studied (Couch et al. 1994, 1998). Galaxies in regular high z clusters were found to follow a morphology–density relation qualitatively similar to that found at low redshift, i.e. with early types dominating at high densities, and with late types dominating at low densities. Unlike at low redshift, however, galaxies in irregular clusters showed almost no morphology–density relation. The most striking result from the morphologies of the high z cluster galaxies was that the overall fraction of S0 galaxies was 2–3 times smaller than at $z \sim 0$, whereas the fraction of spiral galaxies was larger by approximately the same amount. This was more evidence of strong recent evolution. The blue galaxies responsible for the Butcher–Oemler effect were found morphologically to be predominately spirals and irregulars. The HST images revealed that many of these high redshift cluster spirals showed signs of disturbances, suggestive of merging and tidal interactions.

The ground–based study at $z = 0.1$–0.2 by Fasano et al. (2000) has filled the gap between the local clusters and the $z = 0.3$–0.5 clusters studied with the HST. The consistent picture emerging from these studies is that the S0 fraction in clusters increases rather smoothly from $z \sim 0.5$ to the present. It should nevertheless be noted that this result is not universally agreed on. Andreon (1998) found no evidence of a variation of the S0-to-E ratio with redshift and suggested that the deficit of S0s found by other authors was due to morphological classification errors. The derived morphological mix may indeed depend on who is doing the morphological classification. In an HST–based study by Fabricant et al. (2000) of a cluster at $z = 0.33$, the S0-to-E ratio was found to be 1.1 when classifications done by Dressler were used, whereas the ratio was found to be 1.6 when classifications done by Fabricant, Franx and van Dokkum were used.

Aside from the above it should be noted that the morphological "S0" classification depends on the inclination of the galaxy, implying that this classification is not optimal for a physical description[1].

[1] Specifically, in a study of early type galaxies in the Coma cluster, Jørgensen & Franx (1994) found that E and S0 galaxies (except for the very brightest Es) were a mixed class with a broad underlying distribution of the disk fraction. Only about 10% of the sample was found to be completely disk less. Galaxies classified as S0 were galaxies with a strong disk or galaxies with a weaker disk but seen close to edge-on. Ideally, instead of speaking of S0 galaxies one should speak of early type galaxies with a given disk fraction. We will not adopt this terminology, but the issue needs to be kept in mind.

The increasing S0 fraction and decreasing spiral fraction in clusters with time suggests that spirals are being morphologically transformed into S0s. If this is the case one would expect the stellar populations in S0s at low redshift to show (weak) signs of a relatively young population compared to the stellar population in ellipticals (Poggianti 2002a). This is indeed found in some studies (e.g. Kuntschner & Davies 1998; Kuntschner 2000; Poggianti et al. 2001) but not in other (e.g. Jørgensen 1997; Ziegler et al. 2001). At higher redshift, a similar discrepancy exists (e.g. Smail et al. 2001 versus Ellis et al. 1997 and Jones et al. 2000). In the studies that do find a difference, the difference is most marked at lower luminosities. Probably related to these matters is the finding of de Jong & Davies (1997) that the ages of elliptical galaxies correlate with the isophotal shape. Specifically, ellipticals with disky isophotes (as parametrised by the c_4 parameter, see e.g. Bender et al. 1989 or the review by Milvang-Jensen & Jørgensen 1999) had younger ages than ellipticals with perfectly elliptical isophotes or boxy isophotes. While c_4 cannot uniquely be translated into a disk fraction due to projection effects (e.g. Rix & White 1990; Jørgensen & Franx 1994), the quantities are nevertheless correlated. de Jong & Davies conclude that their findings suggest that the younger ages of ellipticals with disky isophotes are associated with the presence of a disk component.

With the HST–based morphological classifications of the high redshift cluster galaxies at hand, a connection to the spectroscopic properties could be made. Based on spectroscopy of three $z = 0.3$ clusters (Couch et al. 1998) and the ten $z \sim 0.4$–0.5 MORPHS clusters (Dressler et al. 1999; Poggianti et al. 1999; see also Wirth et al. 1994) the majority of post-starburst (k+a/a+k) galaxies were found to have disk-dominated morphologies. These normal disk morphologies imply that the process that is responsible for halting the star formation leaves the basic disk structure intact. A population of passive spirals with no current star formation was also found. It was suggested that the post-starburst galaxies and the passive spirals were in the process of being morphologically transformed into S0s. Since the majority of k+a/a+k galaxies did not (yet) have S0 morphologies, this morphological transformation must take place on a longer time scale than the time scale for the k+a/a+k phenomenon ($\sim$1.5 Gyr).

From the above-mentioned HST–based studies of high z clusters and from ground–based studies of the CNOC clusters at $z = 0.2$–0.6 (Balogh et al. 1997, 1998) it was found that also at these redshifts a SFR–density relation existed. Furthermore, also here this relation was found to be partially independent of the morphology–density relation. This is consistent with the picture in which the time scale for suppressing star formation in cluster spirals is shorter than the time scale for the morphological transformation of spirals to S0s.

Clusters contain not only the galaxies but also an intra-cluster medium (ICM). The ICM is the hot ($\sim$10 keV, i.e. $\sim 10^8$ K) low density ($\sim 10^{-3}$ atoms/cm^3) gas that fills the space between the galaxies and which can be observed in X–rays emitted via thermal bremsstrahlung (e.g. Sarazin 1988). The total mass of the ICM is comparable to the mass of the luminous matter (stars) in the cluster galaxies. An illustration of the ICM is shown in Fig. 1.2. The figure is an X–ray image of the local Fornax cluster. A galaxy with its own gas halo is seen falling into the cluster. The gas halo of the infalling galaxy feels the so-called *ram pressure* of the ICM of the cluster.

Many physical processes have been proposed to be responsible for the morphological transformation of galaxies in clusters. A galaxy in a cluster can interact with the ICM, with the gravitational potential of the cluster and with other individual galaxies. For

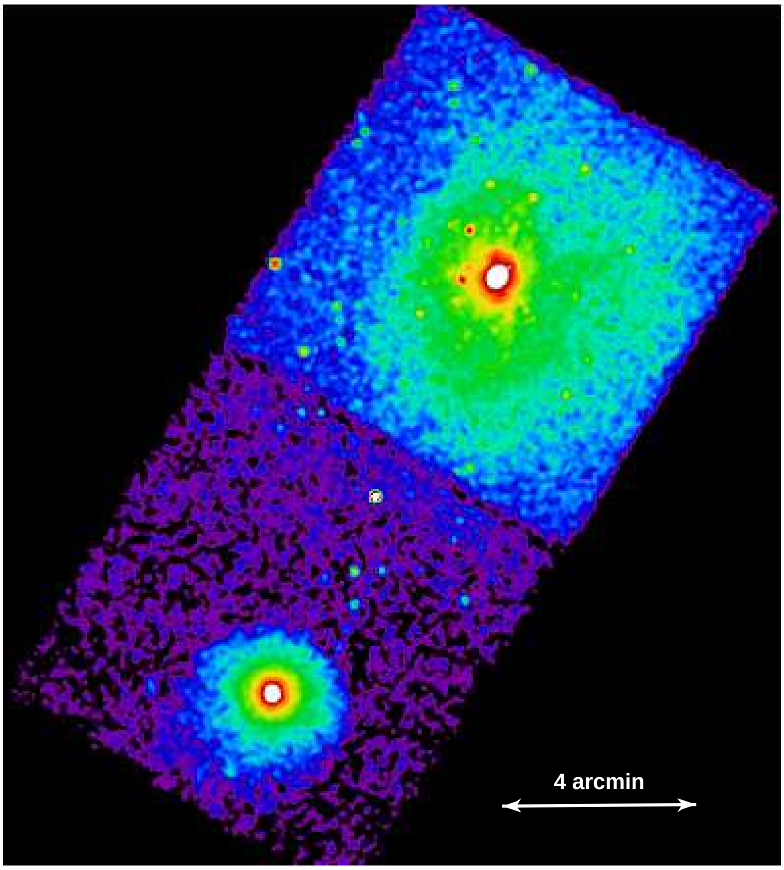

Figure 1.2: Chandra soft band X–ray image of the Fornax cluster. The cluster centre, dominated by the galaxy NGC1399, is seen at the upper right. The gas bound to the infalling bright elliptical galaxy NGC1404 is seen at the lower left. In the temperature map (not shown) this infalling gas is seen to be cooler than the Fornax ICM. From Dosaj et al. (2002); file kindly provided by Bill Forman.

a recent review of these mechanisms, see Treu et al. (2003). These processes include the following. *Ram-pressure stripping* (Gunn & Gott 1972; see also e.g. Fujita 1998; Abadi et al. 1999; Quilis et al. 2000) in which the pressure from the ICM can remove gas from the infalling galaxy. *Pressure-triggered star formation* (Dressler & Gunn 1983; see also e.g. Fujita 1998) where the ram-pressure from the ICM compresses the gas in the disk of the infalling galaxy. *Tidal compression of the gas* caused by the cluster potential (Byrd & Valtonen 1990; see also e.g. Gnedin 2003) where the tidal forces of the cluster potential can trigger star formation. *Galaxy merging* (Icke 1985; Lavery & Henry 1988, 1994; Bekki 1998) in which two galaxies can become one gravitationally bound object if the encounter occurs at a relatively low speed. *Galaxy harassment* (Moore et al. 1996, 1998, 1999) which is the gravitational perturbations due to high speed encounters with other galaxies and with the cluster potential. Finally, several processes can lead to a process known as *starvation*, *strangulation* or *suffocation* in which the gas halo (reservoir) of the galaxy is removed, leading to the galaxy slowly using up the gas in the disk without the possibility of replenishment (Larson et al. 1980; see also e.g. Bekki et al. 2001, 2002). A schematic diagram showing several scenarios for star formation truncation is shown in Fig. 1.3.

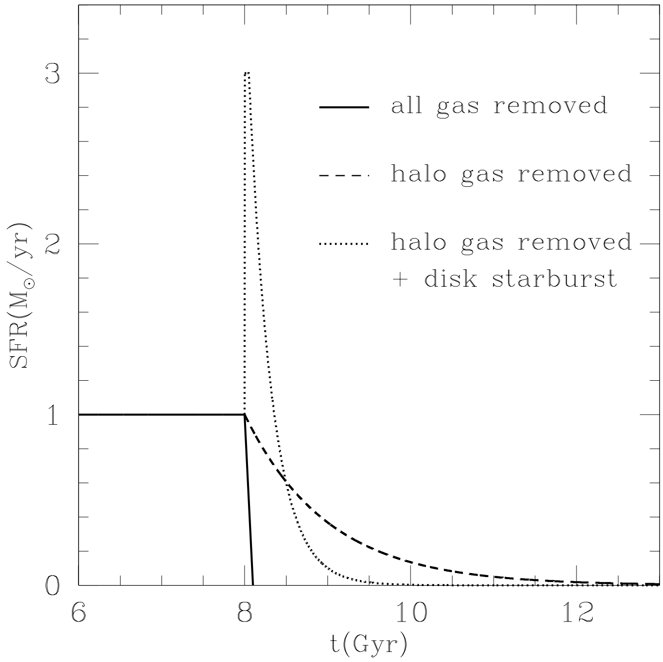

Figure 1.3: Schematic diagram of possible scenarios for SFR truncation. These are: near-immediate cessation of star formation, as may accompany the fast removal of all gas from the spiral disk; gradual decline in SFR, as would be expected following removal of the halo gas reservoir; and star burst followed by a gradual SFR decline.
This figure is from our recently submitted proposal to study the kinematics and stellar populations of k+a galaxies; cf. Sect. 6.2 on future work.

A number of studies have been made modelling the observed evolution in colour, spectra and morphologies of cluster galaxies. These studies have taken a number of complementary approaches. Unfortunately, modelling everything from first principles is computationally completely out of reach for the time being. We will describe the results from a few recent studies.

Kodama & Bower (2001) used the observed colour–magnitude diagrams for the local Coma cluster and for CNOC clusters at $z = 0.2$–0.4 as 'snapshots', i.e. assuming that these different clusters seen at different redshifts could be interpreted (statistically) as the same cluster seen at different epochs. First the galaxies were evolved forward in time in the colour–magnitude diagram, assuming that star formation had halted. It was found that the blue galaxies seen in the high redshift clusters (i.e. those giving rise to the Butcher–Oemler effect) would rapidly become redder and fade, making the predicted colour–magnitude diagram at the present epoch be compatible with what is actually observed in the Coma cluster. In other words the large fraction of blue galaxies in clusters at high redshift is not incompatible with the generally red galaxies seen in local clusters. The blue galaxies seen at high redshift could therefore possibly be the progenitors of the fainter ($> M_* + 1$) S0s in local clusters (which interestingly are those for which the evidence of a more extended star formation history is strongest).

The second part of the Kodama & Bower (2001) study used the observed colour–magnitude diagrams to infer the star formation and truncation histories from very high redshift to the epoch of the observations. The idea is that a galaxy that is bluewards of the colour–magnitude relation by a only small amount could either be a rather red field galaxy (i.e. one with a low SFR) that has been accreted recently or it could be a blue field galaxy (high SFR) that was accreted a long time ago. The assumed mix of star formation histories of the field galaxies were motivated by observations of high z field galaxies. This included the fact the star formation rate in field galaxies declines with time, cf. below. Two truncation scenarios were tried: one with a violent star burst followed by a truncation of star formation, and one with a mild burst followed by a slowly declining SFR (e-folding time 1 Gyr) due to suffocation. The latter model gave an accretion rate that fell monotonically with time and with a good match to what is expected theoretically from extended Press–Schechter theory (Bond et al. 1991; Bower 1991), indicating that this model was the most correct one. The conclusion was that the Butcher–Oemler effect was due to a combination of the declining accretion rate, the declining SFR in the accreted field galaxies and the gradual decline of star formation after the galaxies were accreted.

In a complementary study Kodama & Smail (2001) simulated the morphological mix in clusters based on a simple phenomenological model where the clusters accrete a mix of galaxies from the surrounding field, the spiral galaxies are transformed to S0s (through an unspecified process) and are added to the existing cluster population. The conclusion was that in order to reproduce the apparently rapid increase in the ratio of S0 galaxies to ellipticals in the clusters, the galaxy accretion rate had to be high and most of the accreted spirals, even the late types (Scdm), had to be transformed to S0s. To match the observed morphological mix as function of redshift the transformation had to be a relatively slow process, with the transformation being completed $\sim$1–3 Gyr after the galaxy entered the cluster environment. This time scale inferred from modelling the morphological mix agrees with time scales inferred from the stellar population properties of cluster galaxies.

In the current hierarchical clustering paradigm, structure formation is driven by the gravitational influence of the matter, mainly in the form of cold dark matter. Structure such as galaxies and clusters of galaxies is built up by a successive number of mergers, both between objects of similar mass and between objects of different mass (accretion). In the last decade, numerical simulations within this framework have been coupled to so-called semi-analytic recipes to predict various observable quantities of galaxies such as colours and SFRs (e.g. Kauffmann et al. 1993; Cole et al. 1994; Baugh et al. 1998; Cole et al. 2000). Recent hierarchical models (Balogh et al. 2000; Diaferio et al. 2001) with simple (heuristic) schemes for gas depletion, where the hot gas reservoir is removed when the galaxy halo merges with a larger halo, have shown that SFR in cluster galaxies should be lower (compared to the field) out to 2 virial radii. It is not yet clear whether these simple models is all it takes to explain the lower SFR seen all the way out to 4 virial radii (Gómez et al. 2003).

In the Universe as a whole, the SFR has been found to decline steeply from $z = 1$ to the present day (e.g. Lilly et al. 1996; Madau et al. 1996; Blain et al. 1999; Cowie et al. 1999; Wilson et al. 2002; sometimes referred to as the '*Madau plot*'). Balogh & Bower (2002) ask the interesting question whether this overall decline is due to internal processes within the galaxies, such as the gas available to feed star formation slowly being used up, or to external (i.e. environmental) processes due to the build-up of structure in the Universe. In clusters the SFR has been found to decline even more rapidly than in the field (Kodama & Bower 2001; Poggianti 2002b). Observations also show that from $z \sim 0.5$ and to the present star formation is inhibited in dense environments, i.e. the SFR–density relation. The abundance of clusters grow with time, so it is possible that the growth of structure is responsible at least in part for the decline in the global SFR. For this to work the mechanism has to operate not only in clusters but also in groups. These investigations are still on-going.

One key property remains to be mentioned about spiral galaxies, namely the fact that they follow the *Tully–Fisher relation* (Tully & Fisher 1977). This relation between rotation velocity and luminosity has been studied extensively for local spirals, using both radio observations of the neutral hydrogen gas (HI) and optical emission lines (e.g. Hα) from the ionized gas to measure the rotation velocity. If the observations are not spatially resolved, as is often the case for HI observations, the rotation velocity can be replaced by the spectral line-width. For high redshift spirals, the study of the Tully–Fisher relation has been pioneered by Vogt and collaborators (e.g. Vogt et al. 1996, 1997; Vogt 1999). The rotation velocities were determined using deep spectroscopy targeting the [OII] emission line. A sample of field spirals was studied. The zero point of the Tully–Fisher relation was found to show only a small evolution, which was interpreted as the high redshift spirals being marginally brighter than local spirals at a fixed rotation velocity ($\sim$mass). The effect was found to be $\sim$0.2 mag in the rest-frame B–band at $z \sim 0.5$ for the cosmology adopted in this thesis (see below).

The large amount of evidence for a dramatic change in the cluster spiral population since $z \sim 0.5$ and the success of Vogt and collaborators in measuring rotation velocities for high redshift spirals form the basis for the work presented in this thesis: to study the Tully–Fisher relation for high redshift clusters spirals. The thesis concentrates on the high redshift cluster MS1054−03 at $z = 0.83$.

Assumed cosmology

In this thesis cosmology-dependent quantities such as absolute magnitudes and scale lengths in linear units (kpc) are calculated assuming an open universe with matter density $\Omega_\mathrm{m} = 0.1$ (corresponding to $q_0 = 0.05$ since we assume that the cosmological constant is zero) and a Hubble constant of $H_0 = 75\,\mathrm{km\,s^{-1}\,Mpc^{-1}}$. This cosmology was adopted in order to easily compare with Vogt and collaborators. In recent years a so-called *concordance cosmology* has emerged, in which the Universe is flat (i.e. with $\Omega_\mathrm{total} = 1$), with matter density $\Omega_\mathrm{m} = 0.3$, with a non-zero cosmological constant equivalent to a density of $\Omega_\Lambda = 0.7$, and with a Hubble constant of $H_0 = 70\,\mathrm{km\,s^{-1}\,Mpc^{-1}}$ (see e.g. the recent results reported by Spergel et al. 2003 and references therein). At $z = 0.83$ the differences between the two cosmologies are as follows. A galaxy with an apparent magnitude of 22.30 would have an absolute magnitude of −21.00 in our adopted cosmology and −21.30 in the concordance cosmology. A galaxy with an angular size of $0.50''$ would have a linear size of 3.1 kpc in our adopted cosmology and 3.8 kpc in the concordance cosmology.

Layout of the thesis

The thesis is organised as follows.

- Chapter 2 describes the sample selection, the observations and the data reduction.
- Chapter 3 describes the method to derive rotation velocities and scale lengths for the gas giving rise to the emission lines.
- Chapter 4 describes the photometry, both the calculation of rest-frame B and H–band magnitudes and the bulge/disk decomposition that gives galaxy inclinations and scale lengths for the stars.
- Chapter 5 presents the analysis of the data. The B and H–band Tully–Fisher relations are studied, as well as the distribution of star formation within individual galaxies and the global star formation rates.
- Chapter 6 summarised the results and the conclusions and outlines a number of future projects that build on the work in this thesis.
- Appendix A describes the details of the cosmic ray event removal procedure.
- Appendix B presents HST images and spatially resolved emission line spectra for the galaxies studied.

(page left blank to get matching page numbers for single and double sided versions)

Chapter 2

Sample selection and data

2.1 Sample selection and mask design

We targeted the galaxy cluster MS1054−03[1] at $z = 0.83$ since it is one of the few rich clusters at high redshift with extensive HST imaging available. As an extra benefit this cluster also has literature Keck spectroscopy. We based our galaxy selection on the spectroscopic and photometric catalogues of known cluster galaxies given by van Dokkum (1999) (see also van Dokkum et al. 2000). The *spectroscopic catalogue* is based on an I–band selected sample (corresponding to the rest-frame B–band at $z = 0.83$), with $20.0 < I < 22.7$ (corresponding to $-22.3 < M_B < -19.6$ at this redshift). The catalogue gives Keck-based Hδ and [OII] equivalent widths (EWs) and spectral types (Emission, Absorption or E+A). The catalogue only contains spectroscopically confirmed cluster galaxies, totaling 80. The data for the ∼100 field galaxies also observed is not published. The completeness is stated to be 73% to $I = 22.2$ within the region imaged with the HST. The *photometric catalogue* gives HST based magnitudes, colours and morphologies for the confirmed cluster galaxies which have been imaged with the HST. This catalogue contains 81 galaxies.

Since we wanted to base the study on galaxies with HST imaging, we used the photometric catalogue for the sample selection. Out of the 81 galaxies in the catalogue, 74 had spectroscopy available. We selected spiral galaxies that were likely to give a rotation velocity as follows:

1. Galaxies having spiral morphology and Emission spectral type (EW([OII]) ≥ 5 Å). This was 7 galaxies (1403, 1639, 1733, 1763, 1888X, 1896, 2130); however, the galaxy 1888X could not be located. We added galaxy 2011, which has spiral morphology (cf. Fig. B.29, page 183), but which was classified as merger/peculiar (M/P) for unknown reasons. Of these 7 galaxies, one (1733) had to be dropped at the mask design stage due to geometrical constraints (the galaxy was outside the region where slits could be made).

2. Galaxies having spiral morphology and a less secure Emission spectral type (still EW([OII]) ≥ 5 Å, but with larger errors). This was 4 galaxies (661, 1198, 1298, 1459).

3. Galaxies having spiral morphology and no listed spectral type. This was 3 galaxies (1039, 1354, 1478), which had morphological types Sa, Sb, Sa. At the mask design

[1] Full name: MS1054.4−0321 (Gioia et al. 1990)

stage one galaxy (1354) had to be dropped due to geometrical constraints (the galaxy conflicted with the higher priority galaxy 661).

Twelve spiral galaxies in the catalogue (50% of the total number of spirals) did not have Emission spectral type and were therefore not selected. The catalogue contained two more galaxies with Emission or possible Emission spectral type. These galaxies (1340, 1801) were both morphologically classified as M/P. Galaxy 1340 (possible Emission spectral type, EW([OII] $= 5.1 \pm 3.6$ Å) looked like two galaxies slightly overlapping (possibly only in projection). Galaxy 1801 (Emission spectral type, EW([OII] $= 51.9 \pm 1.6$ Å) looked like a genuine merger. These two galaxies were added to the sample out of curiosity, since they did not conflict with any of the higher priority targets.

It could be noted that the equivalent width, which measures the flux of the line relative to the continuum, is not the best quantity to predict whether a rotation velocity can be measured. The line flux itself will be far more important in determining the signal-to-noise of the observed emission line – the strength of the continuum will only matter through the amount of photon noise the continuum contributes. Nevertheless, selecting all the galaxies from van Dokkum (1999) with Emission spectral type was still a sensible approach.

What can be measured from the spectroscopy is the rotation velocity projected onto the line-of-sight, $V_{\rm rot} \sin i$, where i is the line-of-sight inclination (with 0° being face-on). In order to be able to reliably derive $V_{\rm rot}$ from $V_{\rm rot} \sin i$, the galaxies have to have a reasonable inclination, say $i \geq 30°$ (this is the limit used by Vogt and collaborators, e.g. Vogt 1999). The inclination can be calculated from the apparent ellipticity ε, or equivalently from the apparent axis ratio b/a. Assuming the disk is intrinsically circular and infinitely thin, the relation is $\cos i = 1 - \varepsilon = b/a$. This means that $i \geq 30°$ corresponds to $\varepsilon \geq 0.13$. The ellipticities were measured in the HST images (cf. below) using the IRAF task `imexamine`. The precise value of the apparent ellipticity depended on which radius was used for the measurement, and which filter (F814W or F606W). None of the selected galaxies were more face-on than the 30° limit, so no galaxies were excluded based on their inclination. The adopted inclinations for the galaxies for which a rotation velocity was eventually measured will be discussed in Chapter 4.

At this stage (about 3 months before the observations) the request for *pre-imaging* was made. By designing the masks using such pre-images taken with the same instrument (here FORS2) that will be used for the spectroscopic observations, a high positional accuracy can be achieved. With one night allocated for the spectroscopic observations, our exposure time estimates showed that we could do two masks. We wanted to place the slits along the major axes of the galaxies. If the two masks were made at right angles to each other then all galaxy position angles (PAs) could be accommodated with slits tilted by no more than ±45° within each mask. The positions and position angles of the two MS1054−03 pre-images were decided based on the positions and position angles of the galaxies selected from the van Dokkum catalogue; see Table 2.1 and Fig. 2.1. In choosing the pre-imaging centres and PAs we benefited from having access to a deep R–band Keck image covering the MS1054−03 field kindly provided by Douglas Clowe (cf. Clowe et al. 2000).

The galaxies selected from the van Dokkum (1999) catalogue would not fill the two masks, so additional targets were needed. These were found by inspecting the available HST images. MS1054−03 has been observed with the WFPC2 instruments onboard the HST. In the programme by Marijn Franx et al. six fields in MS1054−03 were

Table 2.1: Specifications for the pre-imaging

Object-name	RA (J2000)	Dec (J2000)	PA	Exptime	Filter
MS1054−03 pos1	10 57 03.72	−03 37 50.0	10°	300 sec	R–band
MS1054−03 pos2	10 56 59.49	−03 38 50.4	100°	300 sec	R–band

observed for typically 6.5 ksec in the filters F814W and F606W (see e.g. van Dokkum 1999; van Dokkum et al. 1999, 2000). The mosaic of the six fields covers a region on the sky of about $7' \times 5'$, see Fig. 2.1. A nice pseudo colour image of the mosaic can be found in van Dokkum et al. (2000). The reduced and combined WFPC2 images were kindly made available by Marijn Franx and Pieter van Dokkum[2]. The individual WFPC2 images were registered to each of the FORS2 pre-images (but at the WFPC2 pixel size of $0.1''$) and combined to form a mosaic image. Photometric zero points to bring the magnitudes from the different images (WFPC2 F814W; WFPC2 F606W; FORS2 R–band) to the standard system used by van Dokkum (1999) were determined using aperture photometry.

Candidate extra targets for mask 1 were selected as follows. The WFPC2 F606W and F814W mosaic images were carefully inspected to find galaxies with spiral/disk morphology and suitable inclination ($i \geq 30°$) and which were not in the catalogue of van Dokkum (1999). The F814W magnitude and (F606W−F814W) colour were required to be approximately in the range spanned by the sample of cluster galaxies selected from the van Dokkum (1999) catalogue, namely F814W = 20.1–22.7 and (F606W−F814W) = 0.8–2.2. To be able to put a slit along the major axis of the galaxy and not have to tilt the slit by more that $\sim \pm 45°$, only galaxies with position angles within $\sim \pm 45°$ of the position angle of the mask were included. The found galaxies were named A, B, C, ..., Z, A1, A2, ..., A6. The same exercise was done for mask 2, naming the galaxies A7, ..., D6. The galaxy A4, which had been identified as a possible target for mask 1, was also suitable for mask 2. The combined mask 1 and 2 sample of candidate extra targets spanned the range F814W = 19.7–23.7 and (F606W−F814W) = 0.7–2.3.

The two MS1054−03 masks were designed using the FIMS (FORS Instrumental Mask Simulator) tool[3], which is a plug-in to the graphical interface Skycat[4]. The orientation for the FORS2 images is wavelength along the x-axis and spatial direction along the y-axis. Slits can be placed everywhere within a box of size $5.7' \times 6.8'$. However, since the wavelength range achieved for a given slit depends on its location in x, only a certain range in x will give the desired wavelength range. FIMS can indicate the region within which a certain wavelength range will be achieved. We required that the narrow wavelength range 6735–6905 Å ([OII] 3727 Å at $z = 0.83 \pm 0.02$) was observed for all slits. For the 600R grism which we wanted to use, this corresponded to a $3.8'$ wide region in the left hand side of the mask. The centre of the mask was moved (with respect to the centre of the pre-image) so that our targets were in this region. Slits were put on the galaxies selected from the van Dokkum (1999) catalogue. The pre-images had good seeing ($0.6''$), so identifying the galaxies seen in the HST images

[2] `http://www.strw.leidenuniv.nl/~franx/clusters/ms1054/Data/combined/`
[3] `http://www.eso.org/observing/p2pp/OSS/FIMS/FIMS-tool.html`
[4] `http://archive.eso.org/skycat/`

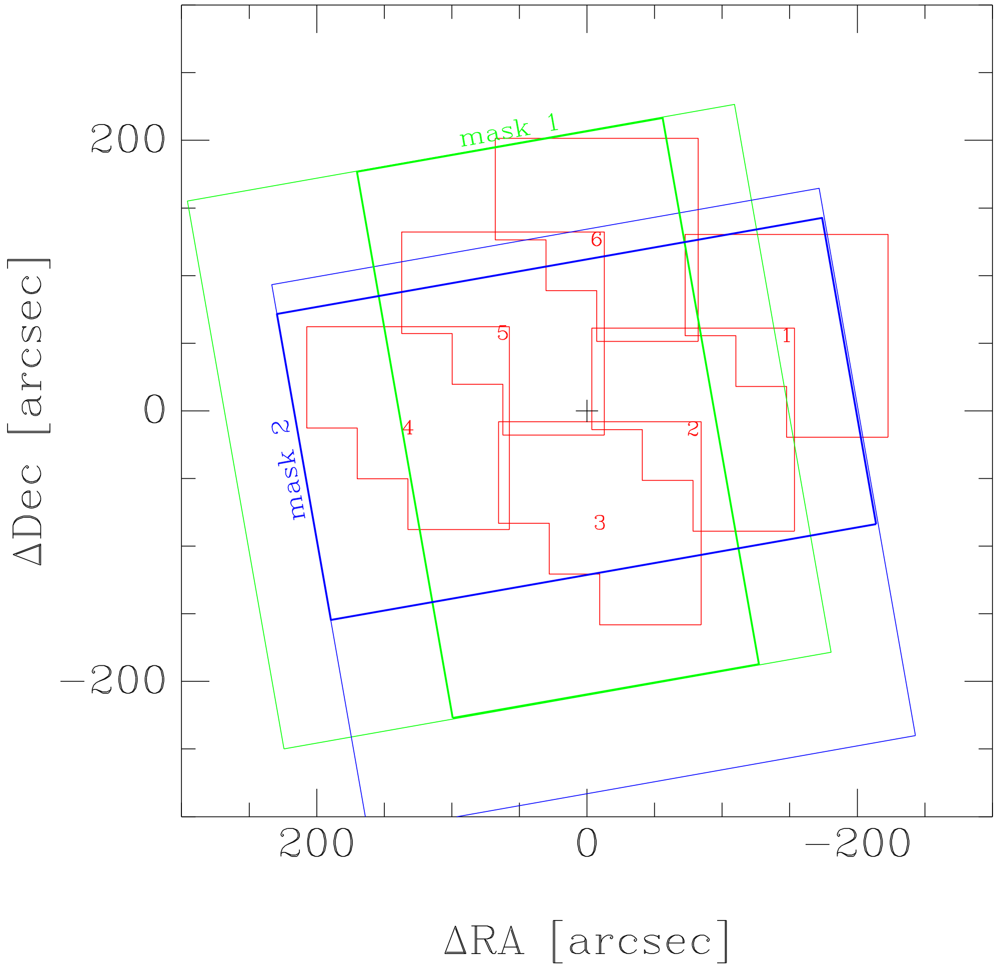

Figure 2.1: Footprints on the sky of the 6 WFPC2 fields, the pre-images and the regions of the masks containing the slits (see also Fig. 2.3 and 2.4). The coordinates have been computed relative to the coordinates of the central galaxy (marked by a cross) at $(\mathrm{RA,Dec})_{\mathrm{J2000}} = (10\ 56\ 59.9, -03\ 37\ 37.3)$ (Donahue et al. 1998). North is up and east is to the left.

was not difficult. Depending on their position angle (measured in the HST images) the galaxies were allocated to either mask 1 or 2. For each galaxy the slit was aligned with the major axis of the galaxy by tilting the slit by an angle θ_{slit}. The width of the slit *in the dispersion direction* (i.e. x-direction) was always $1.0''$ regardless of θ_{slit}. In this way, the spectral resolution was the same for all slits. See Fig. 2.2. The length of the slit was set according to the size of the galaxy in such a way that the slit would contain blank sky on both sides of the galaxy. The typical length in the y-direction was $12''$, and the typical length along the axis of the slit was $13''$. The typical value of $|\theta_{\mathrm{slit}}|$ was $20°$. As mentioned above, slits could not be put on two of the selected galaxies due to geometrical constraints.

In order to be able to align the mask on the sky before the start of the spectroscopic exposures, a number of reference stars need to be designated. It is also wise to put slits on some of them to be able to check the alignment (using the *through-slit image*, cf. the next section) and to measure the seeing in the spectral frames. We decided to put

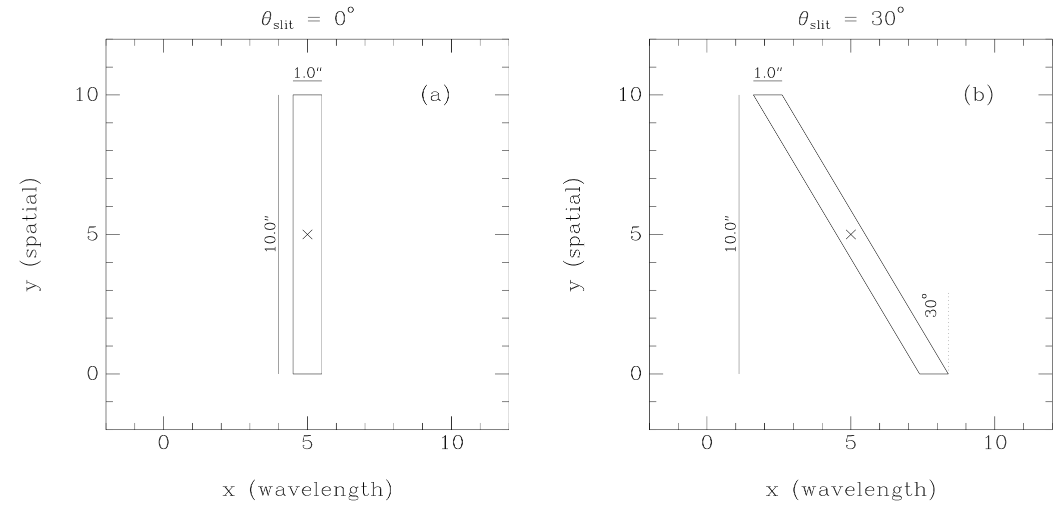

Figure 2.2: Illustration of the geometry of a non-tilted slit (panel a) and a tilted slit with slit angle $\theta_{\text{slit}} = 30°$ (panel b). Note that the width of the slit in the wavelength direction always was $1.0''$ regardless of θ_{slit}.

slits on all the reference stars. Stars well distributed over the image were chosen. The slits were short ($5''$) and untilted. The number of reference star slits was 7 for mask 1 and 5 for mask 2.

Following this, slits were put on galaxies from the list of candidate extra targets. When there was a geometrical conflict, the brightest galaxy was chosen. In order to fill the mask "substandard" slits were used in a few cases: somewhat short slits, or slits with the object close to the edge, or with a large slit angle. The majority of these still provided good data. As a test, the galaxy U, which was in mask 1 with $\theta_{\text{slit}} = 39°$ was also put in mask 2 with $\theta_{\text{slit}} = -51°$. The few remaining gaps were filled with whatever spiral/disk looking galaxies could be found, usually galaxies that were brighter than the sample of cluster galaxies selected from the van Dokkum (1999) catalogue. These additional galaxies were named XX1, ..., XX6. Finally, the very top of mask 2 was outside the WFPC2 mosaic, so targets XX7 and XX8 were identified from the pre-image. For the galaxies not from the van Dokkum (1999) catalogue, the typical slit length in the y-direction was $10''$ and the typical value of $|\theta_{\text{slit}}|$ was 30°. Prints from FIMS of the two masks with the galaxies labelled are shown in Fig. 2.3 and 2.4.

The gaps between the slits were usually made no smaller than $1''$. This turned out to be important, since the edges of the spectra were used to map the geometrical distortion, as will be discussed later (Sect. 2.3.4).

In addition to the two MS1054−03 masks, three masks for backup programmes for bad seeing were made. None of these were needed, fortunately.

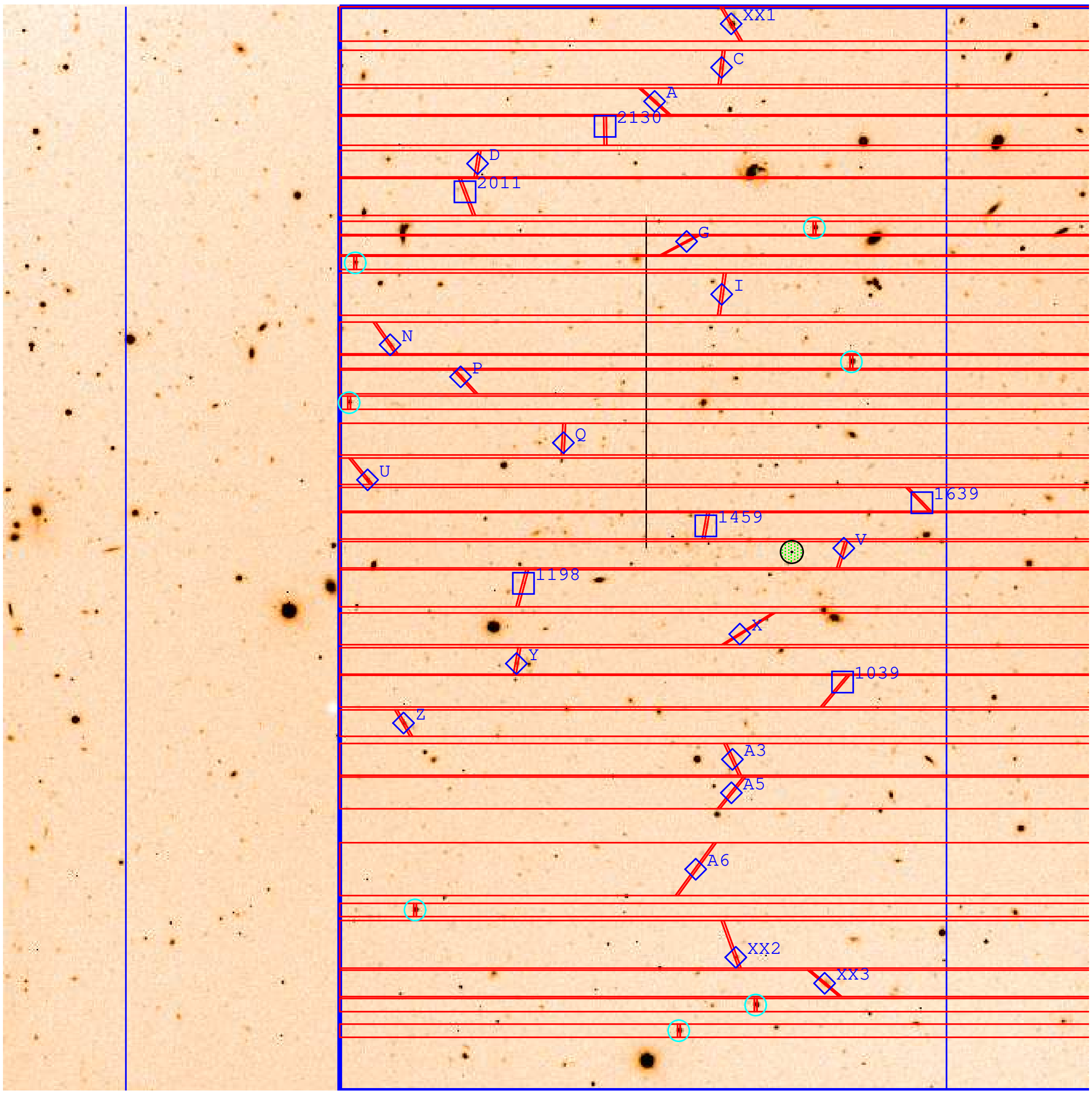

Figure 2.3: Print from FIMS showing mask 1 on top of the mask 1 pre-image. The galaxies have been labelled (squares: known cluster members; diamonds: other galaxies; circles: stars). The centre of the mask (the green filled circle) has been offset from the centre of the pre-image so that all the spectra will cover [OII] 3727 Å at $z \approx 0.83$. The height of the image is $6.8'$. North is $10°$ clockwise from straight up, cf. Fig. 2.1.

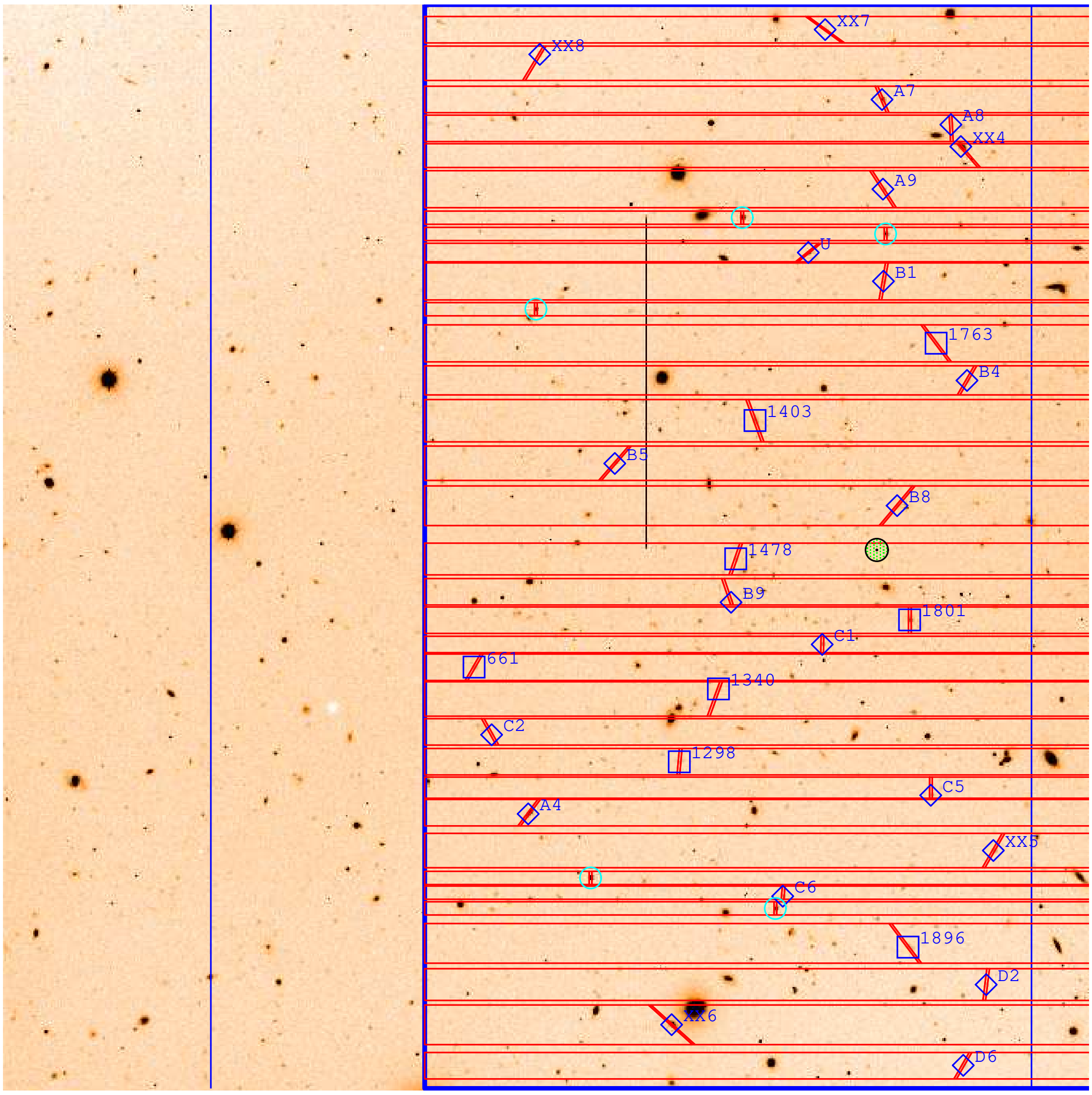

Figure 2.4: As Fig. 2.3, just for mask 2. For this mask north is 10° clockwise from straight to the right, cf. Fig. 2.1.

2.2 Spectroscopic observations

The masks were cut using the Mask Manufacturing Unit (Conti et al. 2001). The masks are called *MXU* masks after the *Mask eXchange Unit*, the jukebox-like mechanism inside the FORS2 instrument which brings the desired mask into the optical path, cf. Fig. 2.5.

Figure 2.5: An MXU mask about to be inserted into the FORS2 instrument (partially visible behind the ladder). The parrot 'supervising' the procedure is the Nottingham astronomy mascot, Pepé (`http://www.nottingham.ac.uk/astronomy/parrot/`).

Observations were carried out with the FORS2 instrument[5] at the VLT (UT2) on 2001 Feb 23. Sky flats for the two masks were taken in the bright part of the evening twilight. Following this spectrophotometric standard stars were observed with a wide slit ($5''$), and hot stars (spectral types O or early B, for the telluric absorption correction) were observed with a $1''$ longslit, same slit width as the MXU slits. The 600R grism was used.

The acquisition procedure for the first mask was started when MS1054−03 was at two airmasses. An acquisition image (R–band, 60 sec) was taken. The reference stars were automatically identified, and relatively small offsets in position and rotation were calculated and applied to match the mask with the targets on the sky. A so-called through-slit image (also R–band, 60 sec) was taken. This is an image with the mask but not the grism in the optical path. From the slits placed on the reference stars it could be seen that the stars were well centered in the slits. The first 1800 sec MXU exposure was started at an airmass of 1.93. A total of seven such exposures were taken of mask 1. The signal level in the MXU frames indicated that the objects remained in the slits throughout, and since the system indeed was reported to be very stable, no

[5] `http://www.eso.org/instruments/fors/`

re-acquisition was done, and no extra through-slit images were taken. The instrument has a so-called longitudinal atmospheric dispersion corrector (LADC, see Avila et al. 1997), which works for zenith distances of less than 45 degrees. The LADC was set at the start of each exposure. When the seventh exposure finished the cluster was culminating at an airmass of 1.07. Following this the same procedure was done for mask 2.

The exposure time for the acquisition and through-slit images was chosen to be one fifth of that of the pre-image. This was a good compromise between getting enough signal for the reference stars and not spending too much time taking these images.

During the observations only a relative short time (say 1 minute) can be spent checking if the objects (particularly the reference stars) are well centered in the slits. Afterwards, however, the through-slit images can be examined closer to get a better feeling for how well the acquisition went. Figure 2.6 shows the star slits in the through-slit images. The stars are indeed seen to be well centered in the slits, and both acquisitions must be said to have been good. There is a hint that the stars in mask 1 are slightly above the centre in the y-direction, and the stars in mask 2 are slightly below the centre. For a non-tilted slit an offset in the y-direction would simply move the object along (i.e. within) the slit. For a tilted slit, however, an offset in the y-direction would also move the object out of the slit. It is important that the slits go through the centre of the galaxies, since that is assumed in the 2D emission line modelling, and since that gives the most light.

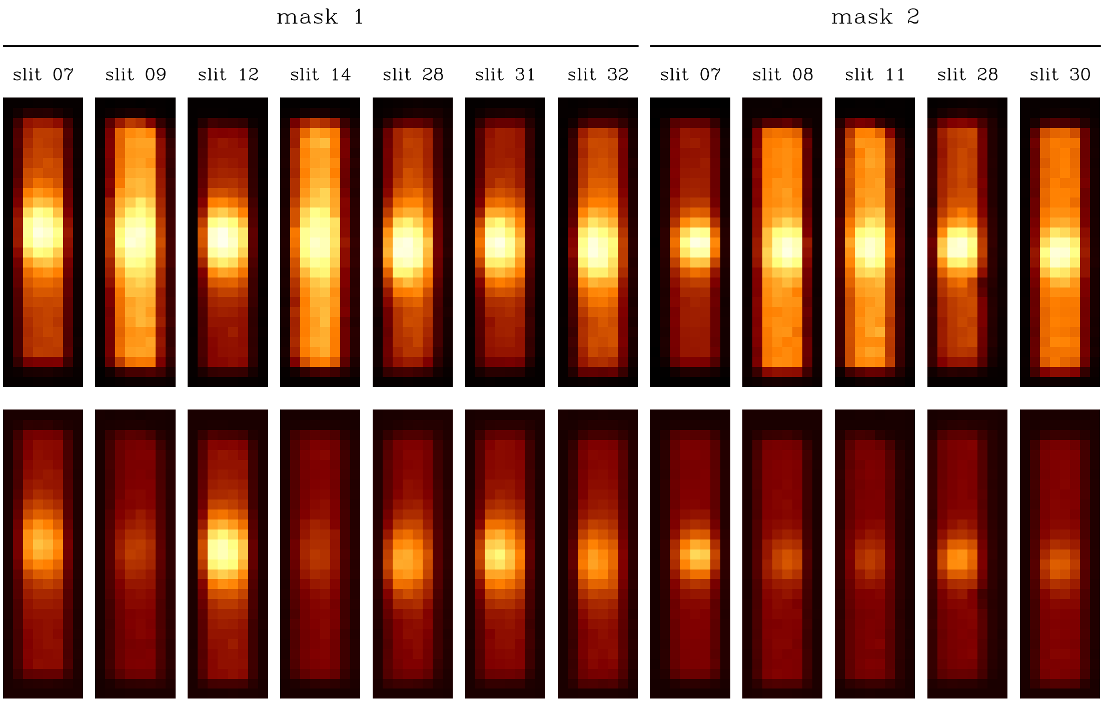

Figure 2.6: The reference stars in the through-slit images. To make this illustration image sections of size 8 px × 29 px ($1.6'' \times 5.8''$) were selected as well centered on each star as possible. The slits are of course unaware of the pixels, so it is not possible to find image sections (i.e. using integer pixel ranges) that have the slits exactly centered in them. Top row: display cuts vary from star to star. Bottom row: all images are shown with the same display cuts (0–4500 ADU).

Another interesting thing can be noted from the through-slit images of the reference star slits: The slits were designed to be $1''$ wide and $5''$ long. Using the spatial scale of $0.201''/\mathrm{px}$ taken from the manual that corresponds to $5\,\mathrm{px} \times 25\,\mathrm{px}$. A careful inspection of Fig. 2.6 will show that the sky background does not form a $5\,\mathrm{px} \times 25\,\mathrm{px}$ rectangle with a constant level and with sharp edges. Rather, the edges are a bit soft. This effect must be due to the "point spread function" of the optics. This is not a problem. It has the implication that when the spectra of the reference stars are cut out of the MXU frames using limits that are defined by the level falling to say 90%, the number of pixels in the spatial direction will be a few less than 25. This is indeed found to be the case (Sect. 2.3.6).

Some cirrus was seen at the start of the night, and some was also present during the night.

During the day following the observing night the staff carried out further calibrations: bias frames, arc frames, and screen flats. The latter are similar to dome flats taken at other observatories. They are called screen flats at the VLT because they are taken with a screen placed in front of telescope when the telescope is pointing towards zenith.

The detector used was a $2048\,\mathrm{px} \times 2048\,\mathrm{px}$ thinned and anti-reflection coated Tektronix CCD. For the spectroscopic observations single port read-out was used, with "high" ADU setting, giving a gain (aka. conversion factor) of $1.91\,\mathrm{e}-/\mathrm{ADU}$ and a read-out noise of $5.41\,\mathrm{e}- = 2.83\,\mathrm{ADU}$.

2.3 Basic spectroscopic reduction

This section describes the reduction of the MS1054−03 MXU spectra. Where nothing else is stated, the reductions were carried out using IRAF.

2.3.1 Bias and dark current

The 5 available bias images were combined. Some structure was seen: a gradient in the y-direction and a few columns had slightly higher or lower level than the bulk of the pixels. For this reason the bias image could not be well approximated by a constant or by a fitted surface, so the combined bias image itself was used in the following reduction.

The level in the overscan regions did not provide any extra information. The images were *trimmed* to remove the overscan regions, giving images of size 2046×2048.

Dark current was ignored since it was irrelevant for the determination of rotation velocities.

2.3.2 Cosmic ray event removal

The correction of pixels affected by cosmic ray events (hereafter *cosmics*) is described in Appendix A and is summarised below.

The basic idea is to identify the cosmics using the fact that multiple images (here 7) are available for each spectroscopic mask. To identify pixels affected by cosmics in the individual images one needs to know the expected standard deviation (hereafter *sigma*) in the absence of cosmics. This sigma cannot be predicted using the standard CCD noise model (i.e. photon noise + read-out noise), since the frame-to-frame variation of the intensity of the many bright sky emission lines is many times greater than predicted by this model. Therefore the sigma has to be estimated from the data. This was done by sorting the 7 data values for each pixel and then calculating the rms of the lowest 5 values ($\sigma_{\mathrm{low}\,5}$). From simulations free from cosmics it was found that $\sigma_{\mathrm{low}\,5}$ was on average lower than the rms of all 7 values ($\sigma_{\mathrm{all}\,7}$) by a certain factor, and $\sigma_{\mathrm{low}\,5}$ was multiplied by this factor. A sigma based on the data was now available, but a refinement was introduced: when the measured sigma occasionally was *below* what the CCD noise model would predict (due to small number statistics), then the CCD noise model value was used for the final sigma instead of the measured one.

Having the final sigma image and the median image of the 7 images, cosmics in each spectroscopic image could now be automatically identified as those values exceeding the median by N times sigma. This number of sigmas, N, had to be individually set for each image. Typically a value of 4–5 was used, but for the few images in which the sky lines were much brighter than in the rest of the images, a higher value had to be used in order to avoid flagging the sky lines as cosmics. *Cleaned* versions of the 2×7 individual images were then produced by linear interpolation within each image (using the task `fixpix`). By having individual cleaned images it would be possible to apply shifts in the wavelength and/or spatial direction if needed before combining the images. A straightforward average image for each mask was made as a test at this stage. As will be discussed below (Sect. 2.3.10 and 2.3.12) it turned out that those two images could be used for the analysis since the frame-to-frame shifts were small.

2.3.3 Bad columns

The science frames were inspected, and the few bad columns identified. The bad column bad pixel map was added to the bad pixel maps containing the cosmics and applied in a single call to the task `fixpix`.

2.3.4 Removal of geometrical distortion (S–distortion)

The spectra in the top of the MXU frames curve like a U, and the spectra in the bottom of the MXU frames curve like an upside-down U, see Fig. 2.7. Such a distortion in the spatial direction is also known as S–distortion. The effect is 6 pixels, which is non-negligible compared to the height of each spectrum (∼50 pixels). Experiments showed that the best approach was to deal with this curvature right from the start (the reasons will be highlighted later). The curvature was mapped from the edges of the spectra in the screen flats, as described below.

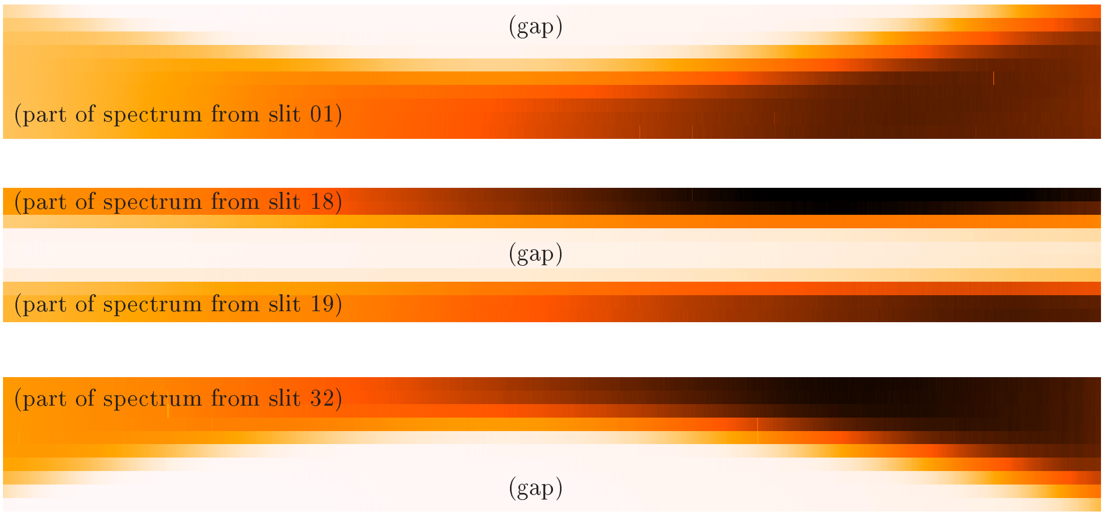

Figure 2.7: Illustration of the geometrical distortion (S–distortion). The 3 panels of this figure show 3 image sections from an MXU screen flat. Each image section is of size 2046 px × 10 px, but the images have here been stretched by a factor of 20 in the y direction to make the curvature clearly visible.
Top panel: section near the top of the frame.
Middle panel: section near the middle of the frame.
Bottom panel: section near the bottom of the frame.

The screen flats were trimmed and bias subtracted, and then combined and fixpixed for bad columns. Following a suggestion by Gianni Busarello, the spectrum edges were "made traceable" by taking the screen flat image, shifting it one pixel down, and subtracting it from the unshifted version of the image. This procedure is equivalent to a convolution with a "`-1; 1`" kernel. The lower edges will appear as positive features and the upper edges will appear as negative features in the convolved image, and it is convenient to take the absolute value. The resulting *spectrumedge* image is shown in Fig. 2.8.

The geometrical distortion was mapped and corrected for as follows: For each of the two spectroscopic mask we defined that the edge positions at the central column

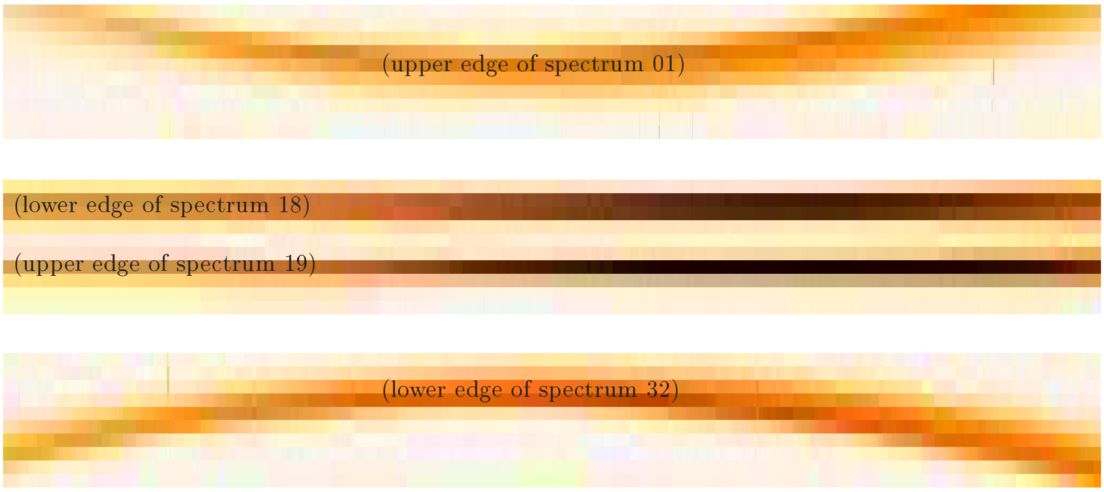

Figure 2.8: Illustration of the *spectrumedge* image. The 3 panels shown in this figure correspond to those in Fig. 2.7. Note how the edges in the screen flat (i.e. Fig. 2.7) have turned into positive features in this spectrumedge image.

($x = 1023$) were the *correct* ones. The goal is then to establish a transformation that takes an MXU frame (with curved spectra, cf. Fig. 2.7) and outputs a frame in which the edges are horizontal and are at an unchanged y-position at $x = 1023$. This can be achieved using the standard IRAF wavelength calibration and S–distortion tasks `identify`, `reidentify` and `fitcoords`. The `identify` and `reidentify` steps were done using the spectrumedge image (Fig. 2.8), where the features (the edges) are treated much like arc lines in a wavelength calibration. Most of the edges were usable, since they were sufficiently unblended thanks to the imposed minimum separation between the spectra of $1''$. In the `fitcoords` step the edge position as function of (x, y) was fitted using a 2nd order polynomial in x (describing the U / upside-down U shape) and a 3rd order polynomial in y (describing how the change from U to upside-down U shape takes place as function of y).

The remaining frames in the data set (sky flats and arcs) were trimmed and bias subtracted, and then *all* frames – science, screen flats, sky flats and arcs – were corrected for the geometrical distortion. The number of pixels in the spatial (y) direction was kept at 2048. As desired, around the central column ($x = 1023$) the transformation was virtually a one-to-one mapping. It may not be aesthetically pleasing to interpolate the flats before they are applied, but it turns out that there are a large number of advantages to this approach, as will be detailed in the following. The transformed images will be referred to as *straightened*, although *made horizontal* would be more correct.

2.3.5 Pixel-to-pixel flat field

Two types of flat field images were taken: screen flats and [twilight] sky flats, with the idea of deriving the pixel-to-pixel flat from the screen flats and the slit profile from the sky flats.

The screen flats are spectra of the flat field lamp. To get the pixel-to-pixel flat, which we want to represent only the relative pixel-to-pixel variation in sensitivity at a given wavelength, the screen flats have to be normalised in the wavelength direction. Since the screen flats (one combined image per mask) had been straightened, the wavelength axis was simply the x axis. This is the first of several advantages of correcting for the S–distortion at the early stage.

It turned out that that the wavelength normalisation could only be done *row by row*. Normalising the entire image by a single fit, as can be done for longslit data, cannot be done here simply because there are multiple spectra within each image, and each spectrum has a different wavelength at a given x. Normalising all rows belonging to a given *spectrum* with a single fit would seem viable at first (one would of course first have to determine the y-limits of each spectrum). However, with tilted slits each row within a given spectrum has a slightly different wavelength coverage, see Fig. 2.9. In the example shown in the figure, the bottom rows have a redder wavelength coverage than the top ones. Since there happens to be more signal in the red end, the average level in the bottom of this 2D spectrum is higher than at the top. Thus, if fitting and normalising by a single function within the 2D spectrum, an artificial gradient in the y-direction would be introduced.

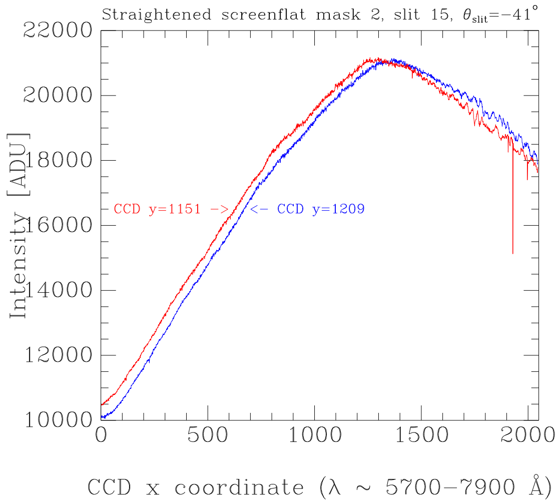

Figure 2.9: Plot of the intensities in two rows within a particular screen flat spectrum as function of x (∼ wavelength). Red line (labelled $y = 1151$): row at the bottom of the spectrum. Blue line (labelled $y = 1209$): row at the top of the spectrum. Since the slit for this spectrum is tilted ($\theta_{\rm slit} = -41°$), the wavelength range is not the same for the two rows, which is why the two curves on the figure do not coincide.

The normalising function was chosen to be a 20 piece cubic spline. The number of spline pieces was chosen as follows: For a low number (say 8), the residuals showed "bumps" on the 100–200 px scale, and these bumps were not at the same place in the two masks, indicating that the used fitting function was not adequate. For a high number (say > 30) the bumps would disappear since the function was able to fit all the structure. This would seem to indicate that this was a good fitting function, but: For a number of 15–20, the residuals would still show bumps, but these would be the same in the two masks. Since the two masks have different wavelengths at the given x, this meant that the bumps now seen were non-chromatic variations (at the 1% level) of CCD sensitivity, i.e., part of the pixel-to-pixel flat. The typical rms in the pixel-to-pixel flats was ∼0.5%, which must be said to be very good.

2.3.6 Determination of the y-limits of the spectra

We want to cut the individual spectra out of the (straightened) MXU frames. To do this the y-limits of each spectrum need to be determined. This *could* be done by eye, but this is time consuming and does not give well defined limits. Instead a script was developed. It essentially works as follows. The spatial profile of the entire sky flat MXU frame is derived (Fig. 2.10a). The profile is normalised by the global maximum, and everything above a certain threshold (e.g. 0.5) is defined to be a spectrum (Fig. 2.10b). A linear function is fitted to the profile for each spectrum to approximately take out the gradient introduced by the tilted slits (Fig. 2.10c; cf. the discussion in the last section). The final y-limits are determined from the normalised profiles as the points where the intensity has fallen to 90% (Fig. 2.10d).

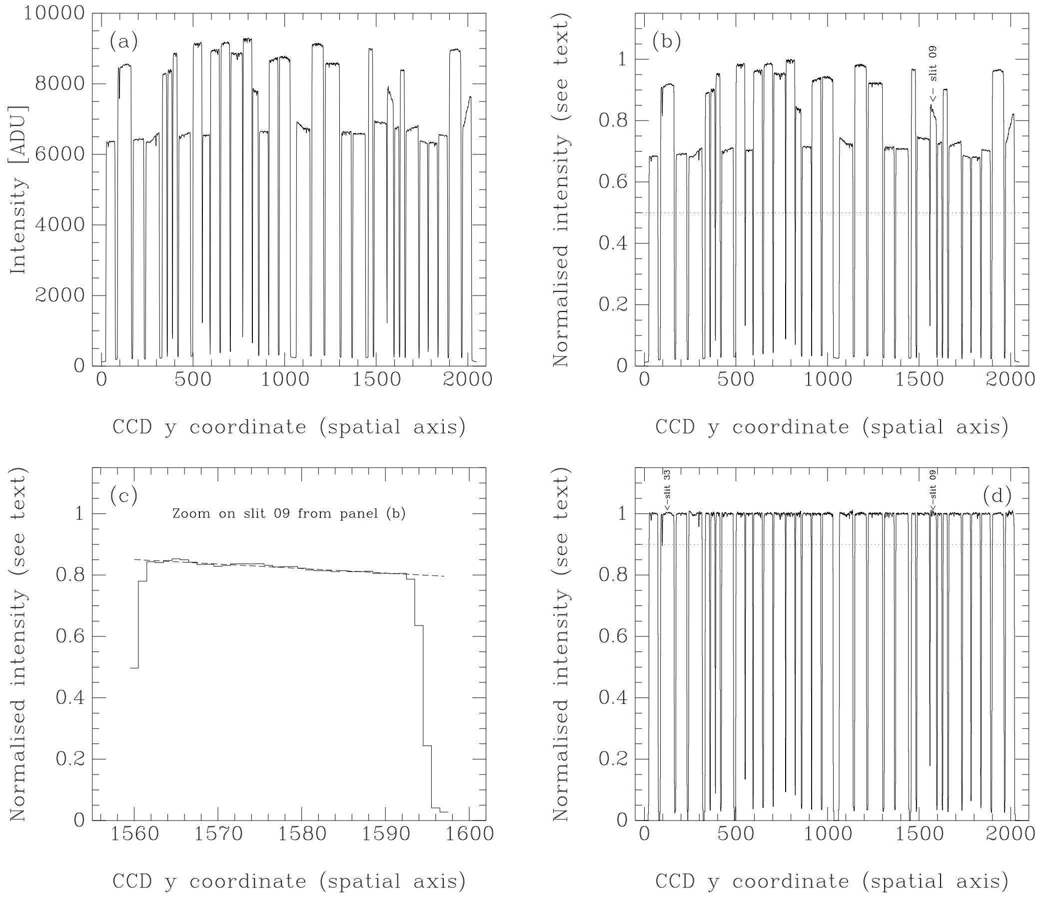

Figure 2.10: Illustration of the procedure to determine the y-limits of the spectra, here using a sky flat for mask 2, cf. the text.

Two sky flat images were taken for each mask. Between each exposure the telescope was moved, the idea being that if a very bright star had accidentally landed in a slit in one of the exposures, this would show when comparing the two set of slit profiles. No differences were found, and the final y-limits of the spectra was derived from the mean of the two images.

While getting the y-limits of the spectra exactly right is not "mission critical", it is nevertheless desirable to get them right, so that all the usable rows of the spectra are included, but not too many unusable ones, since they will have to be manually discarded when establishing the 2D wavelength calibration (cf. the next section).

The derived y-limits of the spectra were visually checked against the science frames. The result from this exercise was that for mask 2, the y-limits derived from the sky flats were appropriate for the science frames. For mask 1, however, there was a mismatch: the appropriate y-limits for the science frames of mask 1 were about 1 pixel lower than those derived from the sky flats.

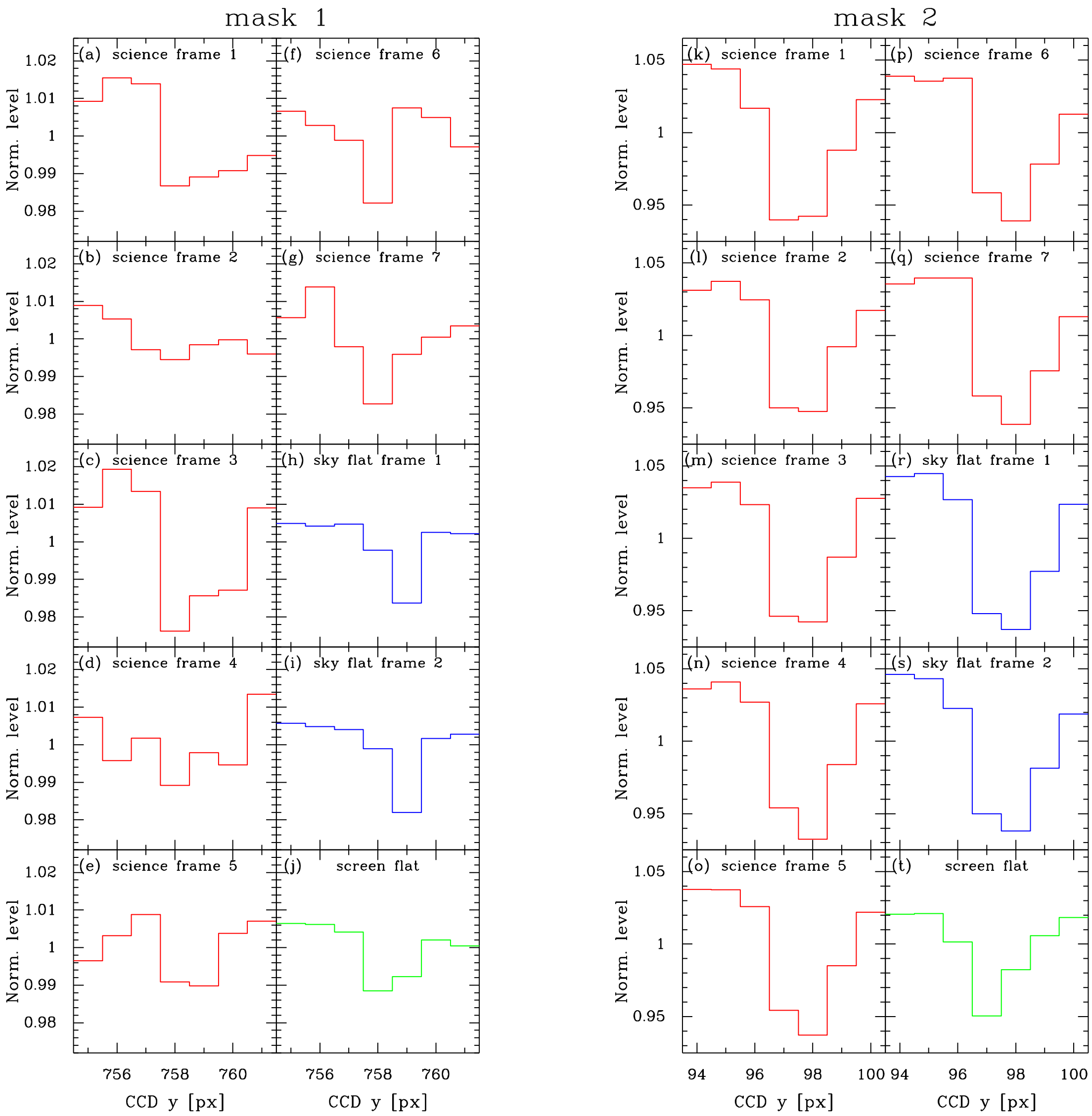

Figure 2.11: Examples of dips in the spatial profiles. Left: mask 1, right: mask 2. In each case the profiles of 10 images are shown: the 7 science frames, the 2 sky flats and the combined screen flat. For both masks the location of the dip does not vary much from science frame to science frame. For mask 1, only, a difference between the science frames and the sky flats of about 1 pixel is seen.

This mismatch for mask 1 was investigated. First it was checked whether something could have gone wrong in the read-out or in the reduction of some of the frames. By looking at discernible features in the pixel-to-pixel flat field such as low response regions, it was found that they were in the same places for all images (mask 1 and 2, and sky flats and science images). I.e., the pixel coordinates as seen from IRAF corresponded to the same physical pixels on the CCD for all images. Following this the position of dips in the slit profile was investigated to see if the slits were moving with respect to the CCD. Unfortunately, the slit profiles for mask 1 had no deep and sharp dips, and with the relatively low signal levels in the science frames this was a difficult task. For the best of these dips, the location in all seven science frames was at $y = 758$, whereas in the two sky flat frames it was at $y = 759$. Incidentally, in the screen flat the position was intermediate between the two. See Fig. 2.11. This supported that for mask 1 the y-limits derived from the sky flats should be shifted down by 1 pixel to match the science images.

The arc and the sky flat frames (size: 2046 px $\times$ 2048 px) were now cut up into individual spectra (size: 2046 px$\times \sim$50 px). For mask 2, the y-limits derived from the sky flats were used to cut up both the arc and the sky flats. For mask 1, the y-limits derived from the sky flats were only used to cut up the sky flats, whereas the y-limits shifted down by 1 px were used to cut up the arc frame (and later the science frames). In this way, the anticipated shift in the slit profile (which was going to be derived from the sky flats) of 1 px with respect to the science frames was hard-wired into the following reduction. If this had *not* been done, the arcs and sky flats would have had to be cut with *wider* y-limits so that there would still be data available if shifts were applied at a later stage.

The adopted numbering scheme for the individual slit spectra was to number them from the top of the frame down.

Finally, returning to a point made in Sect. 2.2, the number of pixels in the spatial direction of the reference star spectra was found to be either 22 or 23 ($4.42''$ or $4.62''$) and not 25 ($5''$), in agreement with the prediction.

2.3.7 Wavelength calibration

The 2D wavelength calibration for the 66 spectra (32 from mask 1 and 34 from mask 2) was established using the standard IRAF procedure and hence the tasks `identify`, `reidentify`, `fitcoords` and `transform`. One arc frame per mask was used. As mentioned in Sect. 2.2 these had been taken during daytime. The mask 1 and 2 arc frames were flat fielded using the respective pixel-to-pixel flats.

In the `identify` step, the single central row of each arc spectrum was displayed, a few arc lines were manually identified, a dispersion solution was fitted, after which more lines were automatically identified and a new fit made. Each arc line was inspected and rejected if looking bad, and deviating points (i.e. arc lines) in the fit were also rejected. The arc lamps which had been used were He+Ne+Ar. The function used for the dispersion solution is not critical, since only the positions of the lines is used by `fitcoords`, not the fitted coefficients of the function. A 3rd order polynomial was used[6]. The rms of the fits was typically 0.026 Å, but 4 spectra out of 66 had rms values in the range 0.06–0.12 Å. For these spectra (which interestingly all had reasonably large slit angles, but a wavelength range near the median of the 66 spectra) increasing the order by one did not make the rms go down, so this is “random scatter”). The number of arc lines used was typically 32.

[6]A 3rd order polynomial is known in IRAF terminology as having `order=4`, since the number of free parameters is counted. In this text we will not use the IRAF terminology.

In the `reidentify` step the positions of the lines were automatically measured for each row above and below the central row. Also this step benefited from the frames being straightened at this point.

In the `fitcoords` step the wavelength was fitted as a function of CCD x and y. The function that was first tried for each spectrum was a polynomial of 3rd order in x and 1st order in y, the latter representing the arc lines as tilted but straight lines. The residuals were plotted versus CCD x, CCD y and laboratory wavelength ("z") and inspected. Entire CCD rows (y-features) which deviated systematically were deleted. For mask 1 the bottom row of the spectra was often deleted, and for mask 2 the top row was often deleted. Entire arc lines (z-features) which deviated systematically or which had a large random scatter (due to being faint) were deleted, with the exception of faint lines in the blue part when no brighter lines were available. Single points that deviated were also deleted. In most cases the polynomial x-order was increased to 5 (or in two cases to 6) to remove structure in the residuals, and in some cases the polynomial y-order was also increased.

Since `fitcoords` does not calculate the rms of the 2D fit, this information is not available. The rms for the 2D fits would probably be just slightly larger than for the 1D fits.

The FWHM of the arc lines was found to be 4.2 Å. The typical wavelength range (for the galaxy slits) was ∼5400–7600 Å. The bluest range was ∼5000–7200 Å, and the reddest range was ∼6000–8300 Å. A lack of lines in the blue was often seen. In the worst case, no arc lines were available for the first 489 Å (the typical number being 180 Å). The He+Ne+Ar combination (which was the standard for grism 600R at that time) was not adequate for the slits with a blue wavelength range. The lack of arc lines in the blue sometimes showed up as an imperfect subtraction of the 5577 Å sky line, as will be discussed below (Sect. 2.3.11).

2.3.8 Slit profiles

The individual 2D sky flat spectra were wavelength calibrated and inspected. One would expect that within each spectrum the intensity in the y-direction should reflect the slit profile (i.e. show minor dips and maybe a small gradient), and that this profile should be the same for all values of x. However, in the spectra from the top and the bottom of the masks a fairly large gradient (up to 20%) was seen at low x only (in the worst case for $x \lesssim 475$), and in a few cases a large-ish gradient was seen at high x going in the other direction. This demonstrated that the total flat field was *not* just the pixel-to-pixel flat (caused by the varying sensitivity of the CCD pixels) times the slit profile (caused by the varying thickness of the slits), but that there also was a large-scale illumination pattern.

To avoid contamination from the large-scale illumination pattern when deriving the slit profiles from the sky flats, only the section `[501:1546,*]` was used. The profiles were derived simply by medianing over the x direction (one could also have averaged over the x direction). For this procedure to give the slit profile it is vital that the frames have been straightened.

Two sky flat images had been taken for each mask. Since the difference between the two sets of profiles were found to be small the final slit profiles were taken as the average of the two determinations. Examples of slit profiles are shown in Fig. 2.12. In most cases the slit profiles are "well-behaved", i.e. with only small dips.

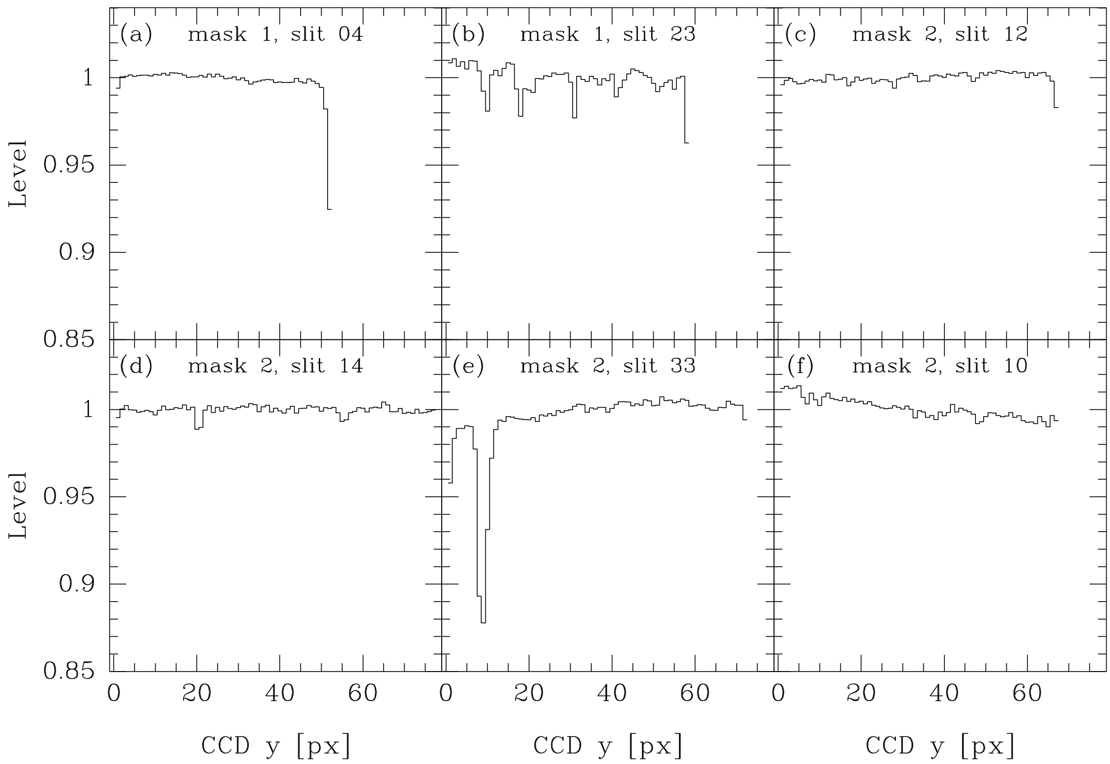

Figure 2.12: Examples of slit profiles. The 'worst' slit profiles for mask 1 and 2 are shown in panels (b) and (e), respectively.

If sky flats had not been available, the slit profiles could have been derived from the screen flats using the same procedure as used for the sky flats. It would be an interesting experiment to do this to see how the two compare and thus whether sky flats are needed at all (if not, the observer would have time to enjoy the sunset!).

2.3.9 Final flat field

The 32 or 34 individual slit profiles for each mask were put together and expanded in the x-direction to make two 2D images. These images were multiplied by the respective two pixel-to-pixel flat field images to create the two final flat field images.

The science frames were flat fielded with the final flats, and the reduced science frames (Fig. 2.13) were then cut up into the individual spectra.

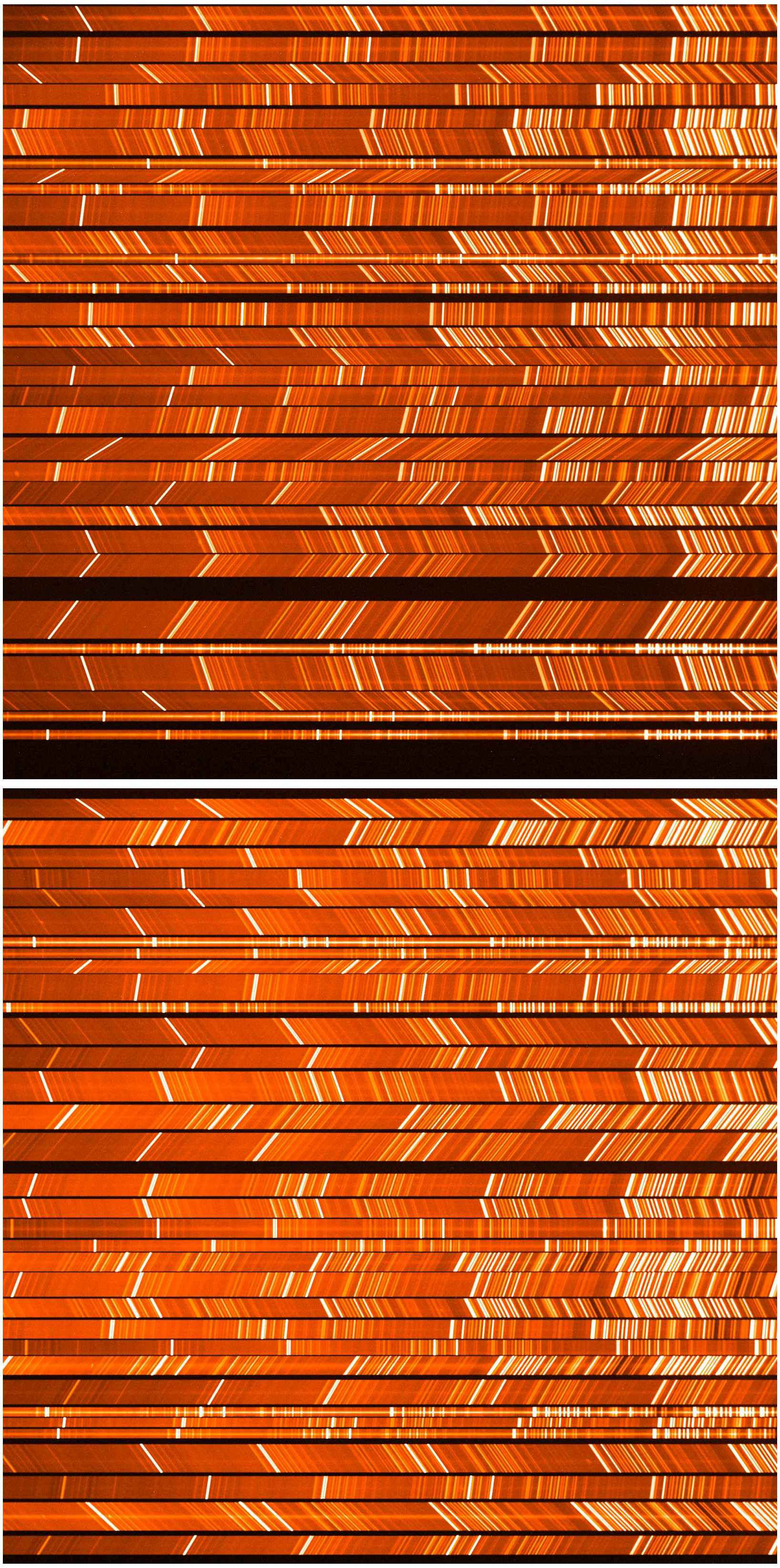

Figure 2.13: The straightened and flat fielded combined mask 1 and 2 images.

2.3.10 Stability of the science frames in the wavelength direction

The spectra from the 2×7 individual science frames as well as from the 2 straightforward average frames (cf. Sect. 2.3.2) were wavelength calibrated. Linear interpolation and flux conservation was used. The pixel scale ("dispersion") was set to 1.075 Å/px.

The wavelength calibration (cf. Sect. 2.3.7) was based on a single arc frame per mask, taken during daytime with the telescope at zenith. The question was whether there would be (apparent) wavelength shifts within the 7 frames, and whether the zero point would be correct. This was addressed by measuring the (apparent) wavelengths of 3 strong and relatively unblended sky lines in all frames. The lines were the 6300.12 Å, 6363.78 Å and 6863.84 Å sky lines, with laboratory wavelengths taken from Osterbrock et al. (1996). The line centres were measured by fitting a Gaussian profile to the given sky line at each CCD row using the task `fitprofs`. Thus, for each sky line, for each of the $2 \times (7 + 1)$ images, for each spectrum and for each row within the given spectrum the line centre was measured.

At first we ignore possible variations in wavelength as function of y (caused by the lines not being vertical) and take the median over the rows within each spectrum. This means that for each spectrum (and for each image) we have a single measured wavelength for each sky line. We compare these wavelengths to the laboratory values. In Fig. 2.14 these differences ($\lambda_{\text{frame } i} - \lambda_{\text{laboratory}}$) are plotted versus frame number i for the 3 sky lines for all spectra.

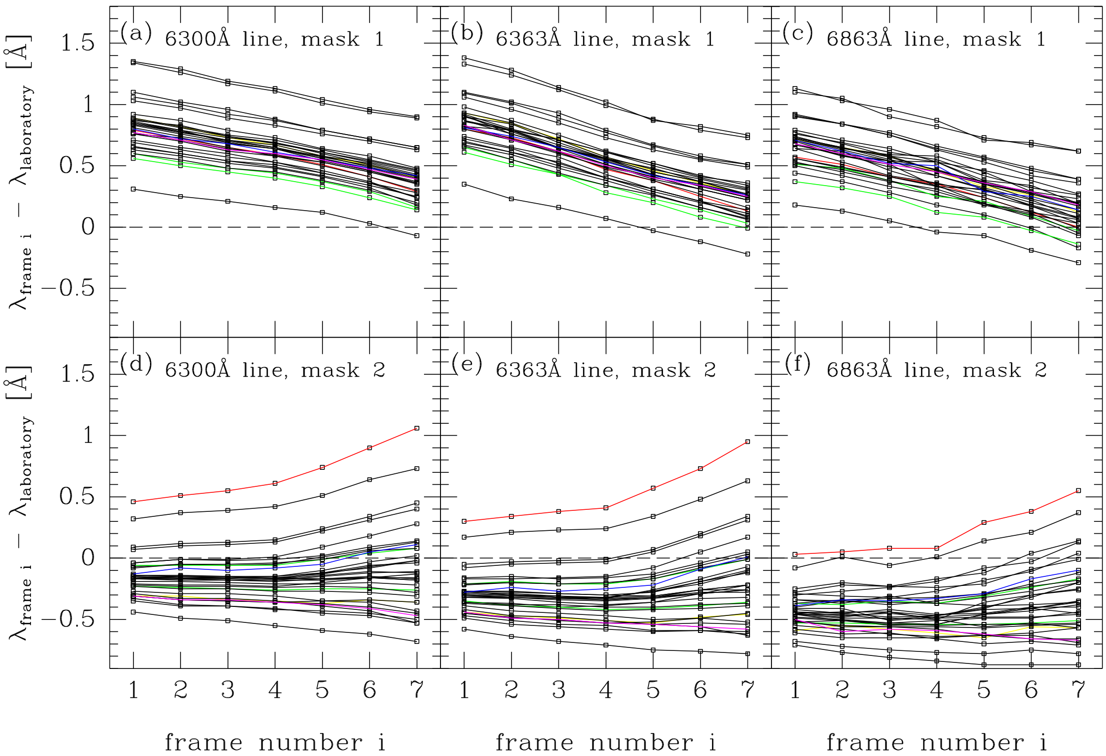

Figure 2.14: Sky line wavelengths compared to the laboratory values. Each point represents one spectrum. The points for the same spectrum in the 7 frames are connected with a line. The lines for a few of the spectra at different positions within the MXU frames have been coloured: red, yellow: the 2 top spectra; green: the 2 middle spectra; blue and magenta: the 2 bottom spectra.

The following conclusions can be drawn from Fig. 2.14.

- The 3 sky lines give similar results. The small differences nevertheless seen between them could be due to imperfections in the wavelength calibration or to problems with the measurements (such as varying line strength, since the 6300 Å and 6863 Å sky lines are actually blends of a strong line with a ∼10 times weaker line).

- The absolute differences with respect to the laboratory values are at maximum 1.4 Å, which does not pose a problem.

- For a given spectrum (i.e. a given line on Fig. 2.14), the variation over the 7 frames is at most 0.6 Å peak to peak. This is only about 0.3 times the sigma of the spectral resolution, and therefore no offsets in wavelength were necessary before combining the 7 frames.

- From spectrum to spectrum within a given mask there is quite some variation. This variation is not correlated with the position of the spectrum within the mask, as can be seen from the coloured lines in Fig. 2.14. It is not known what causes this difference.

- The pattern for mask 1 is quite different for that of mask 2. This is slightly surprising since the observations were carried out in a symmetrical way (mask 1 was observed from airmass 2 to culmination, and mask 2 was observed from culmination to airmass 2). However, the position angles for the two masks are 90 degrees different, so the direction of the gravity vector will have differed.

In summary the wavelength calibration was adequate for our science applications.

The measured sky line centres can also be used to test how well the 2D wavelength calibration has been done in terms of making the sky lines vertical. (This could also have beed tested using wavelength calibrated arc spectra.) For the 66 combined spectra, the plots for the 3 sky lines of wavelength versus CCD y were inspected. In general the plots were flat, indicating that these sky lines were vertical, as desired. In a few cases the lines were seen to be tilted. In the worst case, the tilt was about 0.24 Å over 47 pixels. This worst case is shown in Fig. 2.15 together with two typical cases. It is seen in the figure that the scatter is not the same for the 3 lines. This is due simply to varying photon noise.

What are the implications of the non vertical sky lines seen in a few cases? The sky subtraction will be imperfect of course. And the underlying incorrectness of the wavelength calibration will add a systematic error to the derived rotation velocities. Consider an emission line observed near 6300 Å. For a typical/large spatial extension of 16 pixels ($3.2''$), the worst case error of 0.24 Å over 47 pixels will amount to 0.08 Å. Since the emission line will be seen to go from $-V_{\rm rot}$ to $+V_{\rm rot}$ or vice versa, the effect on $V_{\rm rot}$ is a factor of 2 lower. In velocity, that is $c \cdot 0.5 \cdot 0.08\,\text{Å}/6300\,\text{Å} = 2\,\mathrm{km\,s^{-1}}$, i.e. a negligible amount. The way to cure the problems might have been to increase the order in the wavelength calibration fits so that the changing tilt of the lines as function of wavelength could be adequately fitted.

Note that the 3 sky lines tested are all in the region where a sufficient number of arc lines were available. In the far blue where no arc lines were available, far worse problems were seen, but no emission lines were badly affected, cf. the next section.

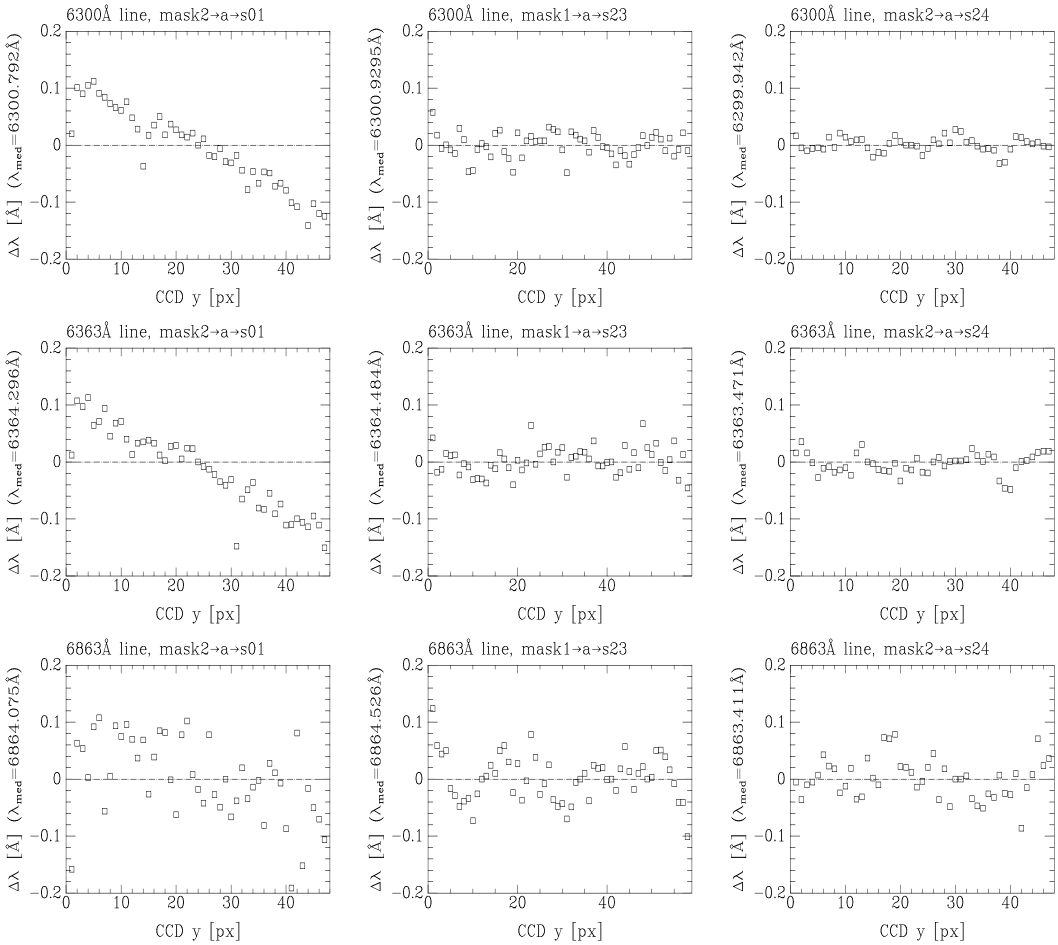

Figure 2.15: Sky line wavelength as function of CCD y. For a successful wavelength calibration the sky lines would be vertical, corresponding to the points being horizontal in these plots. From top to bottom the 3 sky lines studied are shown. From left to right 3 different spectra are shown (the worst case and two typical cases).

2.3.11 Background subtraction

To determine what part of the spectra were free from galaxy signal the spatial profile of the the 66 combined science spectra was derived. The profiles were normalised by the median. These *science profiles* were used rather than the 2D images themselves, since the outer parts of the galaxy continuum can only be seen when “averaging” (here taking the median) over a large number of pixels. The profiles were inspected and the regions free from galaxy signal (the background regions) were noted. The rows that had been deleted when establishing the 2D wavelength calibration were not included in the background regions. If there was doubt about what was galaxy and what was sky in the profiles, the HST images and in some cases the FORS2 pre-images were inspected in FIMS with the mask overlayed to check for faint extra objects in the slits. The derived background regions were also compared to a visual inspection of the 2D spectra. It was ensured that the full extend of the emission lines seen were outside the background regions. As long as the background regions excluded the emission lines it was not deemed a problem if the very outer edges of the galaxy continuum was included – there is a trade-off between getting background regions completely free of galaxy continuum and getting enough pixels (hence signal) in the background regions.

Examples of the science profiles are shown in Fig. 2.16. The figure also shows the adopted background regions. Panel (a)–(c) show the typical case with sky on both sides of the objects. Panel (d) shows a slit which has two objects on it. Panel (e) shows an unusually short slit, and a slit with the object close to the edge. Panel (f) shows a slit with an object having a faint but very extended continuum.

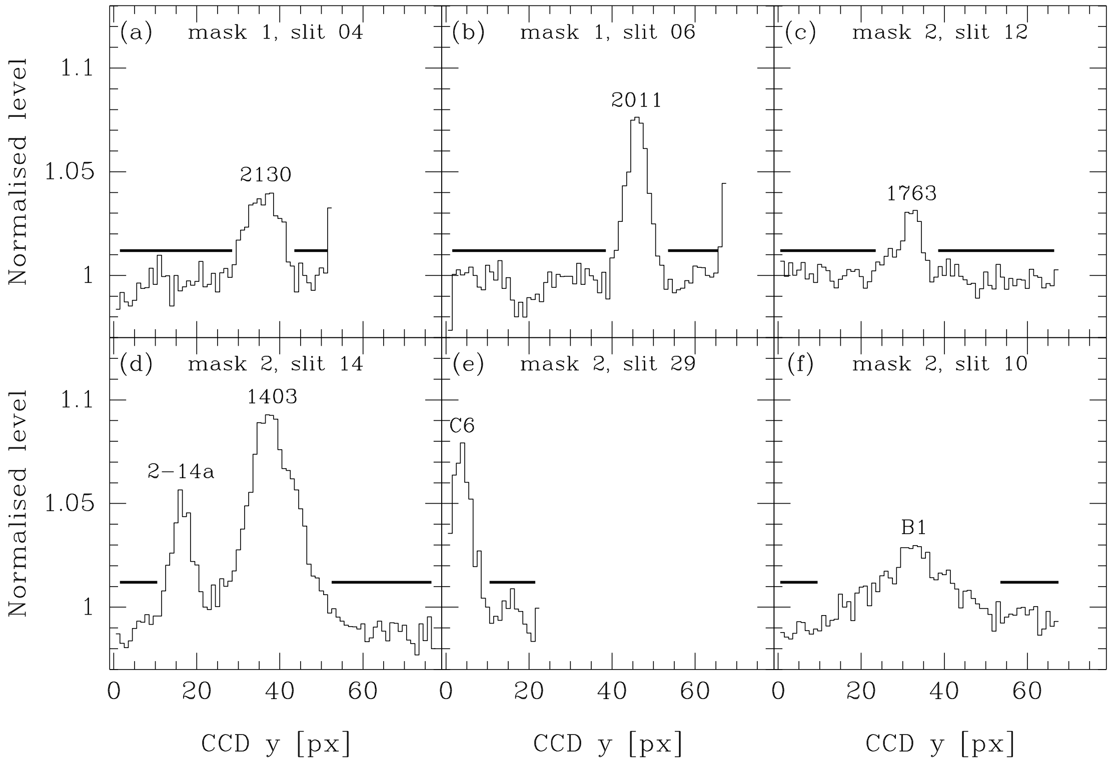

Figure 2.16: Examples of science profiles. The adopted background regions (used for the sky subtraction) are indicated by the thick lines. The names of the galaxies are given.

In many of the mask 1 profiles the first pixel ($y = 1$) was low and the last pixel was high. This is seen in panel (a) and (b) of Fig. 2.16. Thus, the applied slit profile for mask 1 is not quite right. As described above (Sect. 2.3.6) the y-limits of the spectra in mask 1 derived from the sky flats needed to be shifted by [approximately] 1 pixel to match features of the slit profile (dips) seen in the science images. The residuals now seen in the science profiles (i.e. after the final flat field has corrected for the slit profile derived using this 1 pixel shift) shows that the shift was slightly less than 1 pixel. A shift on 1 pixel was still the best choice of an integer shift. For the purpose of determining the background regions the first and last pixel of the mask 1 spectra were simply omitted.

The spectra were background subtracted (i.e. sky subtracted) using the `background` task. For the galaxy spectra, for each x (i.e. column) the constant background value was determined as the mean value in the background region(s), using a ± 3 sigma 4–iterations clipping to be robust against the odd hot pixel or the very odd surviving cosmic. For the reference stars (observed with slits only $5''$ long), the background regions contained too few pixels to use this method, so the median value in the background regions was used instead.

An inspection of the background subtracted spectra showed that in general the background subtraction had worked well. When taking into account where the galaxies had emission lines, the worst case of non vertical sky lines indicated systematic problems of only $2.4\,\mathrm{km\,s^{-1}}$ in the derived rotation velocity, i.e. still negligible.

The inspection of the background subtracted spectra also showed that in some slits there was a gradient in the spatial direction in the left hand side of the spectrum. This is the non-flat illumination that was discussed above when deriving the slit profiles (Sect. 2.3.8). When fitting an emission line that is subject to a non-flat illumination the fit will be slightly worse, but no systematic error in the derived rotation velocity should be introduced.

2.3.12 Stability of the science frames in the spatial direction

As described above (Sect. 2.3.10), the frame to frame stability in the wavelength direction was sufficiently good that there was no need to further align the seven science frames for each mask before combining them. The frame to frame stability in the *spatial direction* is a more complicated matter. As for the wavelength direction, varying flexure could cause the same location on the slit to be mapped to a varying y-location on the CCD. The positions of dips in the slit profiles indicate that this effect is small (less than 1 px), as seen on Fig. 2.11 (p. 30). The slits could also move in RA and/or Dec with respect to the objects on the sky due to e.g. incorrect auto-guiding. For a given slit such a movement would be a combination of movement along the slit and perpendicular to the slit, and since the slits have different angles this combination would vary from slit to slit.

The stability in the spatial direction was studied in two ways using the reference star spectra (of which there were 7 in mask 1 and 5 in mask 2). First the spatial profile for each spectrum was derived by taking the median over the x direction, excluding only the first and last 100 px. This is similar to the *science profiles* made earlier to determine the background regions (Sect. 2.3.11), except this time the background subtracted images were used, and the profiles were not normalised, since in that way also the frame to frame count levels could be studied. For each star the profiles for the 7 individual frames and for the combined frame were plotted, see Fig. 2.17. It is seen that the frame to frame shift in the spatial direction is $\lesssim 1$ px, which is small compared to the width of the profiles (i.e. the seeing), which is ~ 5 px FWHM, or ~ 2 px sigma. Therefore, the individual frames can be combined without any shifts.

As a second test of the spatial stability and of the “straightening” (which was supposed to make the spectra horizontal), the reference star spectra were traced in bins of 10 px in the wavelength direction, fitting a linear function to the traces. It was found that the spectra (i.e. the stellar continua) were close to being straight lines. The slopes of the lines were close to zero, with a typical absolute value of 0.2 px from end to end. The conclusion was that regardless of x position (i.e. wavelength), the maximum difference in spatial position from frame to frame was typically still $\lesssim 1$ px, again indicating that the 7 frames could be combined without any shifts.

As mentioned in Sect. 2.2 there was some cirrus during the observations. The area under the star profiles in Fig. 2.17 is proportional to the flux received in each 30 min exposure. No huge variations are seen, but the first frame of mask 2 has only ∼60% of

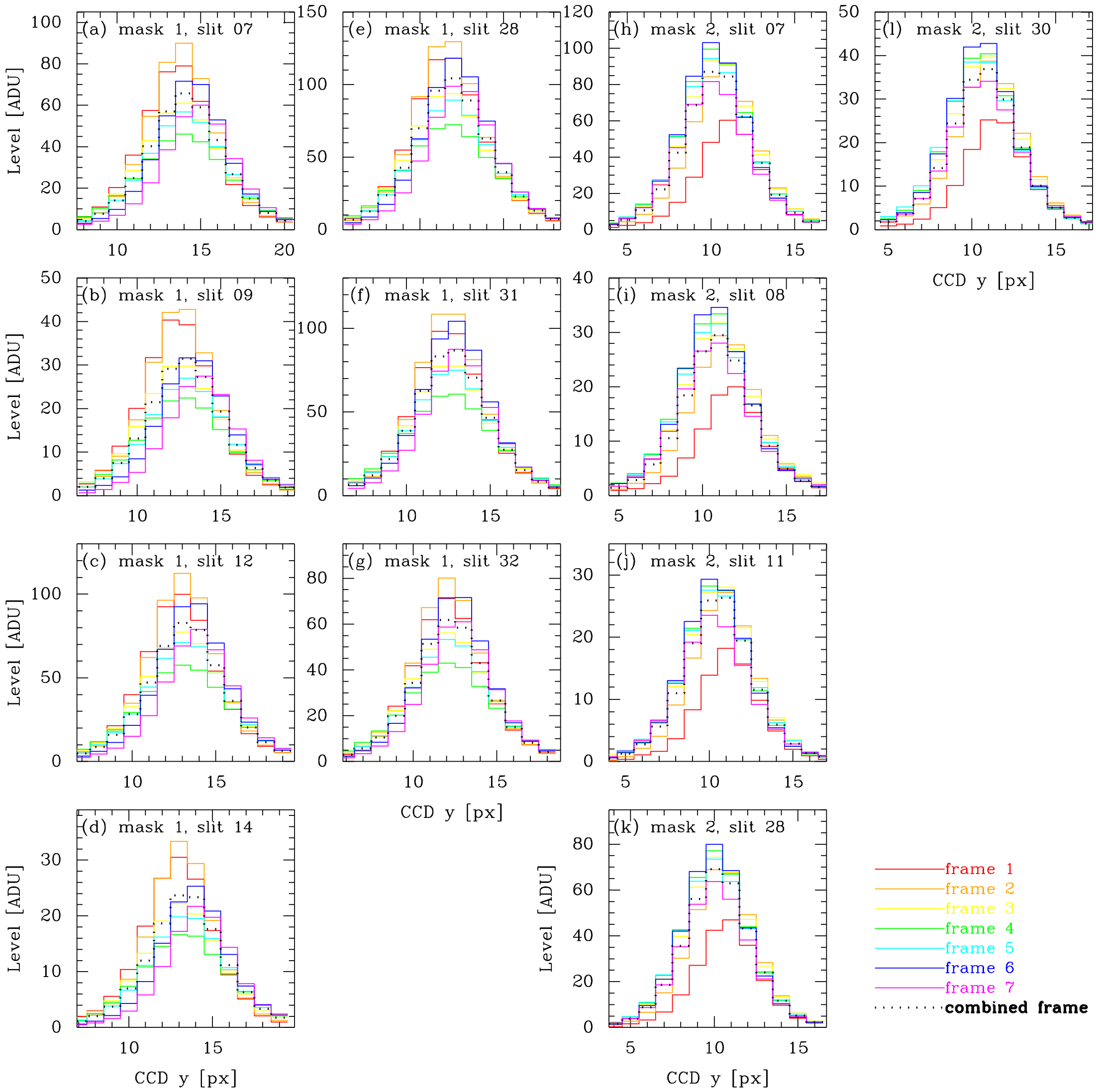

Figure 2.17: The spatial profiles of the reference star spectra in the individual frames and in the combined frame. It is seen that the centre of the stars does not vary much from frame to frame, attesting to the good mechanical stability of the FORS2 instrument. The width of the x-axis of the plots is fixed, so the FWHM of the stars can be visually compared from panel to panel.

the flux seen in the other frames. This was sufficiently small to be ignored.

The seeing was measured as the FWHM of Gaussian fits to the stellar profiles in the combined images. The following mean values were found: mask 1: $1.04''$; mask 2: $0.94''$. The variation from star to star was found to be small ($0.015''$ rms), and the variations with wavelength was also found to be small ($0.03''$ rms). It was therefore decided that a single seeing value per mask could be used in the 2D emission line fits, cf. Ch. 3.

2.3.13 Standard stars

As mentioned in Sect. 2.2, spectrophotometric standard stars (for flux calibration) and hot stars (for correction for telluric absorption) had been observed. However, these data were not needed for the science we wanted to do (primarily rotation velocities, but also emission line fluxes). None of the emission lines fell in the strong telluric absorption bands (the A and B–band), and a proper flux calibration was not needed, since the emission line fluxes could be calculated from the equivalent widths and the broad band magnitudes.

2.3.14 Identification of emission lines

The combined background subtracted 2D spectra were carefully examined to find and identify emission lines. Depending on redshift, the emission lines seen were typically [OII] 3726.1,3728.8 Å, Hγ, Hβ, [OIII] 4959 Å, [OIII] 5007 Å and Hα. The observed separation of the [OII] doublet is $(1 + z) \cdot 2.7$ Å, and with a spectral resolution of 4.2 Å FWHM, a secure line identification could often be done based on [OII] alone (recall that [OII] is only within the observed wavelength range of $\sim$5400–7600 Å for $z > 0.4$).

The result from the line identification process is given in Table 2.2 and 2.3. The galaxies have been sorted after their selection category 1–8 (cf. Sect. 2.1) as follows

Galaxies from the van Dokkum (1999) catalogue of known cluster galaxies:

1. Galaxies with spiral morphology and Emission spectral type
2. Galaxies with spiral morphology and a less secure Emission spectral type
3. Galaxies with spiral morphology and no listed spectral type
4. Galaxies with Merger/Peculiar morphology and Emission or less secure Emission spectral type

Other galaxies:

5. Galaxies with spiral morphology and the slit along the major axis
6. Galaxies without spiral morphology or with the slit not along the major axis
7. Galaxies outside the area covered by the HST+WFPC2 mosaic
8. Extra galaxies serendipitously located on the slits

In terms of spiral galaxies with a slit along the major axis and with sufficient signal to allow 2D fitting of the emission line(s) (cf. Ch. 3), the numbers are: 8 $z = 0.83$ cluster spirals, and 22 $z = 0.15$–0.90 field spirals. Note that the tables introduces alternative names from Milvang-Jensen et al. (2003) for these galaxies. The names are Fnn for the 22 field galaxies and C01 for the single new MS1054−03 cluster galaxy found.

Finding only one new MS1054−03 cluster galaxy is not completely surprising given the high completeness of the van Dokkum (1999) study. However, the field galaxies observed provided an ideal comparison sample since it was observed under the same conditions as our cluster sample. The field galaxies at lower redshift (say $z \lesssim 0.5$) further have the advantage that more than one emission line is observed, which enables important internal checks of the derived rotation velocities, cf. Ch. 3.

Cat[a]	Name	Alt.[b]	z	van Dokkum (1999) z	van Dokkum (1999) morph	van Dokkum (1999) type	van Dokkum (1999) EW([OII]) [Å]	From Ch. 4 F814W [mag]	From Ch. 4 colour[c] [mag]	From Ch. 4 M_B^i [mag]	$V_{\rm rot}$?[d]	Emission lines identified	Notes
1	1403	1403	0.8132	0.8132	Sc	emi	14.7 ± 2.2	20.04	1.49	-22.89	yes	[OII]	
1	1639	—	0.838	0.8377	Sb	emi	8.1 ± 2.3					[OII]	Emission line VERY faint and small
1	1763	1763	0.8384	0.8390	Sb	emi	20.8 ± 4.7	22.68	1.29	-19.99	yes	[OII]	
1	1896	1896	0.8224	0.8227	Sc	emi	20.6 ± 3.1	20.96	1.31	-21.62	yes	[OII]	
1	2011	2011	0.8411	0.8413	M/P[e]	emi	32.5 ± 3.4	22.09	1.16	-20.59	yes	[OII]	
1	2130	2130	0.8245	0.8250	Sd	emi	10.2 ± 4.5	21.78	1.68	-20.95	yes	[OII]	
2	1198	—	—	0.8313	Sa	emi?	5.2 ± 2.9					—	No emission lines detected
2	1298	—	—	0.8363	Sa	emi?	5.9 ± 4.3					—	No emission lines detected
2	1459	1459	0.8459	0.8461	Sc	emi?	5.9 ± 1.2	20.61	1.72	-22.70	(yes)	[OII]	Emission line very faint and small
2	661	661	0.8462	0.8470	Sc	emi?	5.4 ± 2.2	20.96	1.40	-21.72	yes	[OII]	
3	1039	—	—	—	Sa	—	—					—	
3	1478	—	—	—	Sa	—	—					—	No emission lines detected
4	1340	—	—	0.8403	M/P	emi?	5.1 ± 3.6					—	No emission lines detected
4	1801	1801	0.8328	0.8328	M/P	emi	51.9 ± 1.6	20.36	0.88	-22.33	(yes)	[OII]	
5	Z	F01	0.1538					20.48	0.86	-17.82	yes	[OIII]5007, Hα, [SII]6716, [SII]6731	
5	XX6	F02	0.1805					19.00	0.85	-19.57	no	Hβ, [OIII]4959, [OIII]5007, Hα, [NII]	Hbeta also in absorption
5	A	F03	0.2172					21.42	0.62	-17.82	yes	Hβ, [OIII]4959, [OIII]5007	
5	V	F04	0.2297					21.17	0.61	-18.75	no	Hβ, [OIII]4959, [OIII]5007	
5	G	F05	0.2495					21.05	0.81	-18.80	yes	Hβ, [OIII]4959, [OIII]5007	
5	A4	F06	0.2594					19.74	0.81	-20.17	no	Hβ, [OIII]4959, [OIII]5007	
5	C	F07	0.2640					20.68	0.94	-18.87	yes	Hβ, [OIII]5007	
5	U	F08	0.2870					20.60	0.90	-19.15	yes	Hβ, [OIII]4959, [OIII]5007	In both masks
5	P	F09	0.3232					21.46	1.03	-18.89	yes	Hβ, [OIII]5007	
5	A7	F10	0.3237					20.45	1.01	-19.62	yes	Hγ, Hβ, [OIII]5007	
5	N	F11	0.3246					20.88	0.63	-19.31	yes	Hβ, [OIII]4959, [OIII]5007	
5	XX4	F12	0.3253					19.13	1.15	-20.74	yes	Hβ	Abs. line spectrum, Hβ also in em.
5	B5	F13	0.3737					22.03	0.84	-18.93	yes	Hβ, [OIII]4959, [OIII]5007	
5	C2	F14	0.4290					23.19	0.62	-18.18	yes	[OIII]4959, [OIII]5007	
5	D	F15	0.4694					22.78	0.86	-18.56	yes	Hβ, [OIII]4959, [OIII]5007	
5	XX1	F16	0.4700					19.64	0.88	-21.30	yes	[OII], Hγ, Hβ, [OIII]5007	Hβ also in absorption
5	C6	F17	0.4936					22.22	0.87	-18.96	yes	[OII], Hβ, [OIII]4959, [OIII]5007	
5	Y	F18	0.5530					21.20	0.96	-20.32	yes	[OII], Hγ, Hβ	
5	D2	F19	0.6841					21.87	1.09	-20.65	yes	[OII]	
5	B4	F20	0.6865					22.27	1.04	-20.34	yes	[OII]	
5	D6	F21	0.7558					21.35	1.37	-20.98	yes	[OII]	
5	A8	C01	0.8280					22.25	1.11	-20.96	yes	[OII]	
5	B1	F22	0.8965					20.84	1.46	-22.57	yes	[OII]	

[a] Category, see text [b] Name used in Milvang-Jensen et al. (2003) [c] (F606W−F814W) [d] If ELFIT2D was used, was a rotation velocity derived? (cf. Ch. 3) [e] Spiral

Table 2.2: Identified emission lines (if any) for the observed galaxies, part 1

				van Dokkum (1999)			From Ch. 4					
Cat[a]	Name	Alt.[b]	z	z	morph type	EW([OII]) [Å]	F814W [mag]	colour[c] [mag]	M_B^i [mag]	V_{rot}?[d]	Emission lines identified	Notes
5	A3	—	...								([OII], [NeIII])/([OII])	Two galaxies, $z = 0.574$ and 0.832
5	XX5	—	...								([OII]?)/(Hβ, [OIII]4959, [OIII]5007)	Two galaxies, $z = 0.870$? and 0.250
5	C1	—	0.547								—	Abs. line spectrum (no em. lines found)
5	XX2	—	0.548								—	Abs. line spectrum (no em. lines found)
5	I	—	—								—	No emission lines detected
5	Q	—	—								—	No emission lines detected
5	X	—	—								—	No emission lines detected
5	A5	—	—								—	No emission lines detected (virtually no cont.)
5	A6	—	—								—	No emission lines detected (virtually no cont.)
5	B8	—	—								—	No emission lines detected
5	B9	—	—								—	No emission lines detected
6	A9	—	0.4309				22.41	0.74	−18.37	no	[OII], [NeIII], Hβ, [OIII]4959, [OIII]5007	Slit along bar; galaxy is the size of the slit
6	XX3	—	0.546??								[OII]??	Slit along bar, line morph strange (zig–zag)
6	C5	—	0.762?								[OII]?	Slit not along major axis, line morph strange
7	XX8	—	0.979??								[OII]??	
7	XX7	—	0.557?								[OII]?	
8	2–14a	—	0.596								[OII]	
8	2–17a	—	0.775								[OII]	
8	2–08a	—	0.831?								[OII]?	Galaxy on star slit
8	2–31a	—	0.948?								[OII]?	
8	2–01a	—	0.548??								[OII]??	

[a] Category, see text [b] Name used in Milvang-Jensen et al. (2003) [c] (F606W−F814W) [d] If ELFIT2D was used, was a rotation velocity derived? (cf. Ch. 3)

Table 2.3: Identified emission lines (if any) for the observed galaxies, part 2

As a curiosity it can be mentioned that Dan Maoz enquired whether we had a redshift for a particular galaxy in the MS1054−03 field. This galaxy is located near SN 1996cp and may be the host galaxy of this supernova. We were able to report a redshift for this galaxy (see Gal-Yam et al. 2002). The galaxy was 2–14a ($z = 0.596$), a galaxy serendipitously observed in our study.

It should be noted that the redshifts reported in Table 2.2 and 2.3 have not been corrected for the inaccuracies in the wavelength calibration (as seen from the sky lines, cf. Sect. 2.3.10), nor have the redshifts been transformed from the observed frame to the heliocentric frame. Both effects are sufficiently small not to be a concern. As can be seen from Table 2.2 our redshifts agree well with those from van Dokkum (1999).

2.4 [OII] equivalent widths, fluxes and luminosities

For the 16 galaxies with [OII] emission, 1D spectra were extracted. For each galaxy the size of the extraction aperture was determined visually to encompass all of the spatially extended emission line flux. The 1D spectrum was made simply by summing the rows within the the extraction aperture. Equivalent widths (EWs) were measured by fitting a Gaussian to the 1D spectra using the task `splot`. The two edges of the continuum region as well as the initial guess of the line centre were manually marked. The continuum level (linear function of λ) and the line centre and width were then fitted. Error bars were computed using the CCD noise characteristics. The error bars do no account for the uncertainty in where to fit the continuum. Experiments showed that by choosing various "reasonable" continuum regions, rms variations in the EW of $\sim$10% could be achieved, which usually is larger than the formal error bar. The measured EWs (and their calculated uncertainties) were divided by $(1+z)$ to get the rest frame values, which will be quoted throughout. For 15 of the 16 galaxies, the EW was in the range 2.4–53.8 Å, whereas for galaxy A8 it was 120 Å.

For the 7 cluster galaxies in common with van Dokkum (1999) the [OII] EWs are compared in Fig. 2.18. The agreement is good in general. The one deviating galaxy is 2011, where we find a much larger EW than van Dokkum does. This is the galaxy which van Dokkum classified as M/P (probably due to a 'companion' which is quite far away), so if van Dokkum had a slit that encompassed both objects, this could explain the difference.

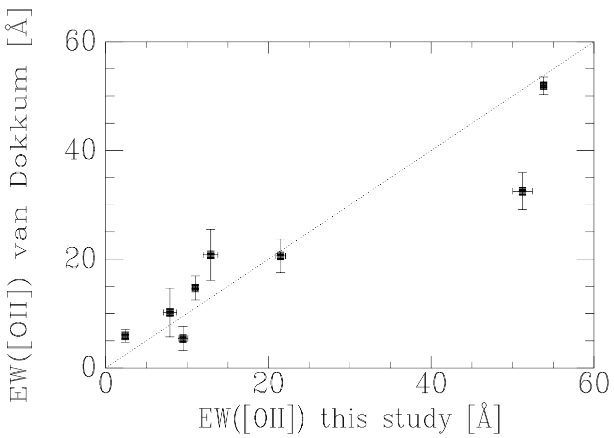

Figure 2.18: Comparison of rest frame [OII] equivalent widths between van Dokkum (1999) and this study. The deviating galaxy (for which we find EW = 51 Å) is 2011.

The [OII] emission line luminosities, which are needed to estimate the star-formation rates, were derived as follows. From the definition of the equivalent width (see e.g. Fig. 3.3 in Binney & Merrifield 1998) it follows that

$$F_{\rm line} = W_{\rm line} \cdot F_{\lambda,\rm cont} \quad , \tag{2.1}$$

where

$$\begin{array}{lcll} F_{\rm line} & = & \text{rest-frame line flux} & \text{(e.g. in erg s}^{-1}\text{ cm}^{-2}) \\ W_{\rm line} & = & \text{rest-frame line EW} & \text{(e.g. in Å)} \\ F_{\lambda,\rm cont} & = & \text{continuum flux at the line} & \text{(e.g. in erg s}^{-1}\text{ cm}^{-2}\text{ Å}^{-1}) \end{array} \quad .$$

Equation (2.1) can be applied to any part of the galaxy, specifically to the entire galaxy or to the light that fell within the slit. We are interested in obtaining the line flux for the entire galaxy. We can estimate the continuum flux for the entire galaxy by using the broad band total magnitudes (see below). We can estimate the EW for the entire galaxy simply by assuming that it is identical to the EW that we have measured for the light that fell within the slit.

As will be shown later (Sect. 4.2, p. 79), the observed-frame F606W and F814W total magnitudes for each galaxy were transformed into a rest-frame B–band total magnitude using local galaxy SEDs of different types. This magnitude, B, can be turned into a continuum flux at the effective wavelength of the B–band (∼4450 Å) as

$$F_{\lambda,\mathrm{cont},B} = 6.19 \cdot 10^{-9}\,\mathrm{erg\,s^{-1}\,cm^{-2}\,\text{Å}^{-1}} \cdot 10^{-0.4B} \quad , \tag{2.2}$$

where the zero point has been taken from Fukugita et al. (1995). The continuum flux at the location of the [OII] line, $F_{\lambda,\mathrm{cont,[OII]}}$, is usually lower than $F_{\lambda,\mathrm{cont},B}$ since [OII] is bluewards of the 4000 Å break, whereas the B–band is redwards of the 4000 Å break. The ratio $F_{\lambda,\mathrm{cont,[OII]}}/F_{\lambda,\mathrm{cont},B}$ depends on the SED. For the used SEDs (Coleman et al. 1980) the ratio is found to be: Sab: 0.53, Sbc: 0.67, Scd: 0.74, Sdm: 0.83. For comparison, Gallego et al. 2002 found: disklike objects: 0.70, HII–like objects: 0.87, blue compact dwarfs: 1.06. Each of the 16 galaxies with observed [OII] was assigned a fractional best-matching SED based on the observed colour (i.e., Fig. 4.1, p. 79) and the corresponding interpolated $F_{\lambda,\mathrm{cont,[OII]}}/F_{\lambda,\mathrm{cont},B}$ value was calculated. The [OII] line flux, $F_{\mathrm{[OII]}}$, was then obtained using Eq. (2.1).

The line flux can be converted to a line luminosity simply by

$$L_{\mathrm{[OII]}} = 4\pi d_L^2 F_{\mathrm{[OII]}} \quad , \tag{2.3}$$

where d_L is the luminosity distance for the given redshift and the assumed cosmology, here $H_0 = 75\ \mathrm{km\,s^{-1}\,Mpc^{-1}}$ and $q_0 = 0.05$. The [OII] luminosity can with certain caveats be turned into a star formation rate; this will be done in Sect. 5.5 (p. 112).

The [OII] equivalent widths, fluxes and luminosities are given in Table 2.4.

Table 2.4: [OII] equivalent widths, fluxes and luminosities

z	name	altname[a]	EW [OII] [Å]	σ(EW) [Å]	$F_{[\mathrm{OII}]}$ [$10^{-18}\,\mathrm{erg\,s^{-1}\,cm^{-2}}$]	$L_{[\mathrm{OII}]}$ [$10^{42}\,\mathrm{erg\,s^{-1}}$]
0.4700	XX1	F16	29.2	0.6	623	0.391
0.4936	C6	F17	41.3	1.4	87	0.061
0.5530	Y	F18	39.1	1.3	204	0.188
0.6841	D2	F19	41.9	1.5	120	0.185
0.6865	B4	F20	46.4	1.9	94	0.147
0.7558	D6	F21	30.0	1.6	127	0.251
0.8132	1403	1403	11.0	0.3	159	0.378
0.8224	1896	1896	21.5	0.6	143	0.350
0.8245	2130	2130	7.9	0.8	21	0.051
0.8280	A8	C01	119.7	6.9	260	0.648
0.8328	1801	1801	53.8	0.4	706	1.784
0.8384	1763	1763	12.9	0.9	18	0.046
0.8411	2011	2011	51.2	1.2	128	0.332
0.8459	1459	1459	2.4	0.3	18	0.048
0.8462	661	661	9.5	0.6	63	0.165
0.8965	B1	F22	32.9	1.1	252	0.768

[a] Name used in Milvang-Jensen et al. (2003)

(page left blank to get matching page numbers for single and double sided versions)

Chapter 3

2D fitting of the emission lines

3.1 The synthetic rotation curve method

Rotation velocities were derived from the 2D emission line spectra, of which examples are shown in Fig. 3.1.

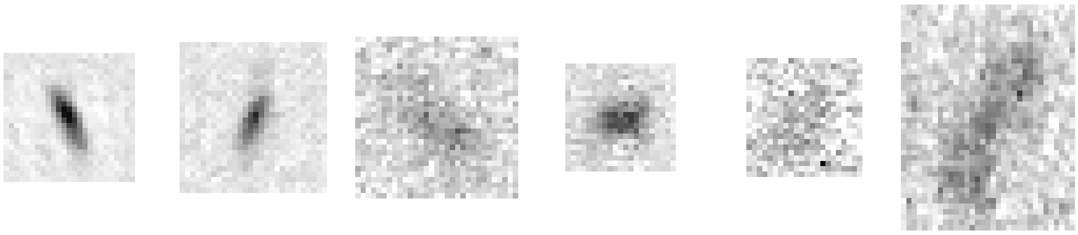

Figure 3.1: Examples of 2D emission line spectra. Wavelength is along the x-axis. The continuum has been subtracted. The first two lines are singlets (Hβ and [OIII], resp.), and the last 4 are the [OII] doublet. (For more information see Fig. 3.7, page 62.)

The *synthetic rotation curve method* of Simard & Pritchet (1998, 1999) was used. The method is implemented in the IRAF task ELFIT2D, kindly made available by Luc Simard. The method consists of two conceptually separate parts:

- The procedure which creates a model (or synthetic) 2D emission line spectrum given a set of model parameters
- The algorithm which finds the 'best fit' model parameters and their associated confidence intervals

These two parts are described in the followings two sections.

3.1.1 Synthetic 2D emission line spectra

The gas that emits the emission line flux is modelled as a circular disk of negligible thickness (i.e. a 'thin disk'). The surface brightness of the emission line flux is assumed to be exponential with galactocentric distance r, i.e.

$$\Sigma(r) = \Sigma_0 \, \mathrm{e}^{-r/r_{\mathrm{d,spec}}} \quad , \quad r \geq 0 \ , \tag{3.1}$$

where Σ_0 is the central surface brightness of the disk and $r_{\rm d,spec}$ is the scale length. The "spec" subscript denotes that this scale length is for the emission line gas, which we measure spectroscopically. An alternative name for $r_{\rm d,spec}$ could have been $r_{\rm d,gas}$. At a given galactocentric distance the motion is assumed to be circular with rotation speed given by a function $V(r)$, which we will call the *intrinsic rotation curve*. Two choices of the intrinsic rotation curve are implemented in ELFIT2D: a flat rotation curve

$$V(r) = \begin{cases} 0 & \text{for } r = 0 \\ V_{\rm rot} & \text{for } r > 0 \end{cases} \tag{3.2}$$

where $V_{\rm rot}$ is a parameter, and the 'Universal' rotation curve (hereafter URC)

$$V(r) = \begin{cases} 0 & \text{for } r = 0 \\ V_{\rm rot}\left\{1 + \left[0.12 - 0.24\log\left(\frac{L_B}{L_{B*}}\right)\right]\left(\frac{r}{2.2\,r_{\rm d,spec}} - 1\right)\right\} & \text{for } 0 < r \leq 3\,r_{\rm d,spec} \\ V_{\rm rot} & \text{for } r > 3\,r_{\rm d,spec} \end{cases}, \tag{3.3}$$

where L_B is the B–band luminosity of the galaxy and $L_{B*} = 6 \times 10^{10} h_{50}^{-2} L_{B\odot}$ is a parametrization constant (corresponding to $M_{B*} = -21.5 + 5\log h_{50}$), with h_{50} given by $H_0 = 50\,h_{50}\,{\rm km\,s^{-1}\,Mpc^{-1}}$. Note that the constant M_{B*} is not the constant from the Schechter galaxy luminosity function, although the latter has a similar value, $M^*_{B,\rm Schechter} = -21.2 \pm 0.1 + 5\log h_{50}$ (Efstathiou et al. 1988). As can be seen, the rotation speed at 2.2 scale lengths is equal to the parameter $V_{\rm rot}$.

The URC in ELFIT2D is heavily inspired by Persic & Salucci (1991). Based on the rotation curves for a sample of 58 spiral galaxies (with $-17.5 \geq M_B - 5\log h_{50} \geq -23.2$), these authors found the shape of the rotation curve to be tightly correlated with the luminosity of the galaxy (cf. earlier findings by Rubin et al. 1985). Specifically, the part of the rotation curve going from ~ 1 to ~ 3 optical scale lengths was found to be approximately linear, with a slope depending on the luminosity. Since the velocity amplitude is also correlated with the luminosity (cf. the Tully–Fisher relation [Tully & Fisher 1977]), the rotation curves of spiral galaxies were found to be a universal function of the luminosity:

$$V(r) \simeq 200\,{\rm km\,s^{-1}}\left(\frac{L_B}{L_{B*}}\right)^{1/4}\left\{1 + \left[0.12 - 0.24\log\left(\frac{L_B}{L_{B*}}\right)\right]\left(\frac{r}{2.2\,r_{\rm d}} - 1\right)\right\}\ , \tag{3.4}$$

valid for $1\,r_{\rm d} \lesssim r \lesssim 3\,r_{\rm d}$, where $r_{\rm d}$ is the optical scale length. As can be seen, this rotation curve is only flat if the factor $[0.12 - 0.24\log(L_B/L_{B*})]$ is zero, which corresponds to a quite bright luminosity of $3.2L_{B*}$. For galaxies fainter than $3.2L_{B*}$ the velocity rises with r, and for the few galaxies brighter than $3.2L_{B*}$ the velocity falls with r. Indeed, when considering the luminosity function of spiral galaxies Persic & Salucci (1991) comment that flat rotation curves are very rare!

The URC in ELFIT2D is that from Persic & Salucci (1991) with the following modifications: The "velocity amplitude" $V_{\rm rot}$ is naturally a free parameter; the spectroscopic scale length is used in place of the optical scale length (since the latter is not used as input to ELFIT2D); the Persic & Salucci function is assumed to work also between 0 and 1 scale lengths; and from 3 scale lengths $V(r)$ is assumed to be flat at the value $V_{\rm rot}$. The galaxies in the present study span the range 0.04–4.23 in L_B/L_{B*}, and the ELFIT2D version of the URC is shown for representative values in Fig. 3.2. The discontinuity at 3 scale lengths is a bit surprising, although it follows directly from the way the function was extended beyond 3 scale lengths (cf. Eq. 3.3; not discussed in Simard & Pritchet 1999, but as seen in the actual ELFIT2D code). The intensity of an exponential profile at 3 scale lengths is a factor of 20 smaller than at the centre, so in practice the behaviour at > 3 scale lengths is of little importance.

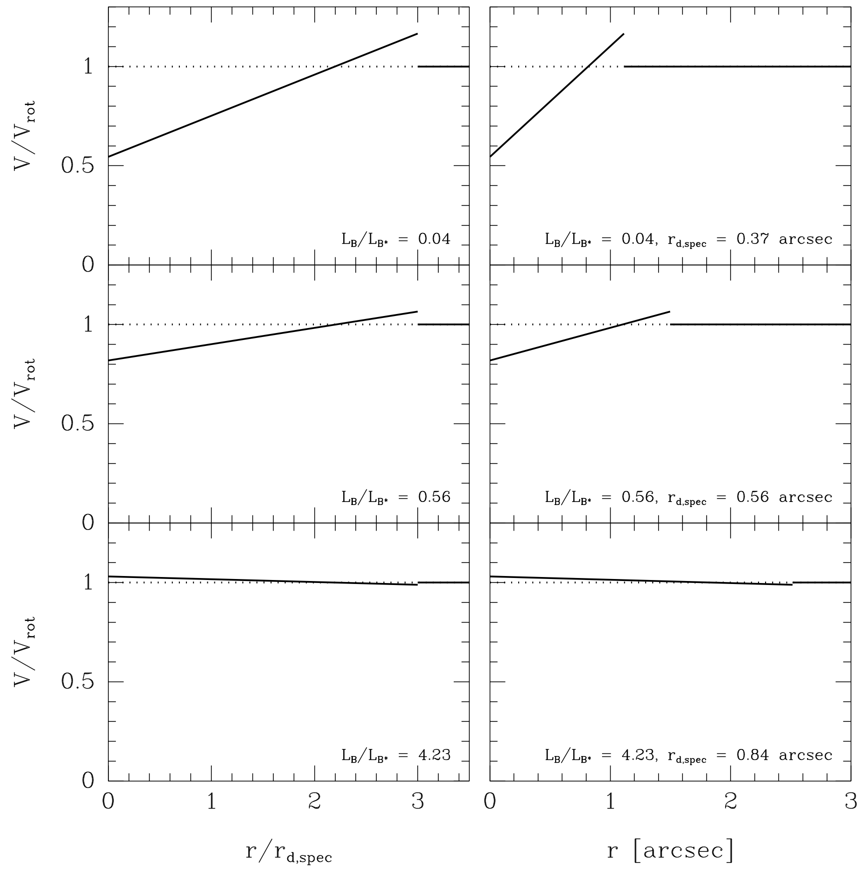

Figure 3.2: Illustration of the flat rotation curve (Eq. 3.2; dotted line) and the URC (Eq. 3.3; solid line). The URC depends on L_B/L_{B*}, and 3 representative values are shown. The radius is shown both in units of the scale length and in units of arcsec. The 3 sets of parameters (L_B/L_{B*}, $r_{\rm d,spec}$) shown correspond to 3 of the galaxies in the sample: Z (least luminous field galaxy, $z = 0.15$), A8 (least luminous cluster galaxy, $z = 0.83$) and 1403 (most luminous cluster galaxy, $z = 0.81$).

When the intrinsic rotation curve $V(r)$ is specified, the 2D line-of-sight velocity field on the plane of the sky can be calculated. This can for example be done by using

$$V_{\rm los} \equiv \hat{\vec{R}} \cdot \vec{V} \tag{3.5}$$

(Binney & Merrifield 1998, Eq. 8.54), where $\hat{\vec{R}}$ is a unit vector from the observer towards the disk, and $\vec{V}$ is the (3D) velocity field of the disk, with $|\vec{V}| = V(r)$. Let (x, y) be the coordinates of the plane of the sky, and let the disk be inclined by an angle i in such a way that the apparent major axis of the disk is along the y-axis. It then follows that

$$V_{\rm los}(x,y) = V(r) \sin i \, \frac{y}{r} \quad , \quad r = \sqrt{\left(\frac{x}{\cos i}\right)^2 + y^2} \quad , \quad 0 \leq i < 90^\circ \quad . \tag{3.6}$$

When this line-of-sight velocity field of a rotating disk is shown as a contour plot it is often referred to as a "spider diagram".

A corollary of Eq. (3.6) is that the line-of-sight velocity of a rotating disk along the apparent major-axis (coordinate y in our notation) is $V(|y|)\sin i$ on one side of the centre ($y > 0$), and $-V(|y|)\sin i$ on the other side ($y < 0$).

In analogy with Eq. (3.6), the intensity distribution of an inclined disk with apparent major-axis along the y-axis is

$$\Sigma(x,y) = \Sigma_0\, \mathrm{e}^{-r/r_{\mathrm{d,spec}}} \quad , \quad r = \sqrt{\left(\frac{x}{\cos i}\right)^2 + y^2} \quad , \quad 0 \le i < 90^\circ \ . \tag{3.7}$$

It is worth pointing out that $r_{\mathrm{d,spec}}$ is the *semimajor* exponential scale length, not the equivalent radius ($\equiv \sqrt{ab}$) exponential scale length.

Synthetic 2D spectra can now be calculated as follows. Assume that the 2D spectrum is oriented like the FORS2 spectra, i.e. with x being wavelength and y being the spatial axis[1]. The 2D spectrum will have a number of columns, N_{spectral}. Each column will have a given width in Å (e.g. 1.075 Å), which in velocity units might be $40\,\mathrm{km\,s^{-1}}$. Each column will thus correspond to a velocity interval, e.g.

$$\begin{array}{ll} \ldots,\ [-80,-40],\ [-40,0],\ [0,+40],\ [+40,+80],\ \ldots & [\mathrm{km\,s^{-1}}]\ \text{for } N_{\mathrm{spectral}}\ \text{even} \\ \ldots,\ [-60,-20],\ [-20,+20],\ [+20,+60],\ \ldots & [\mathrm{km\,s^{-1}}]\ \text{for } N_{\mathrm{spectral}}\ \text{odd} \end{array}$$

Each velocity interval corresponds to a narrowband image of the rotating disk. This image is simply given by the exponential intensity distribution (Eq. 3.7) in the region of the sky where the line-of-sight velocity is within the given velocity interval, and zero elsewhere. Each narrowband image is convolved with the point spread function (PSF). In ELFIT2D the PSF can be given by a user specified image, or by a Gaussian with a user specified width. A virtual slit of user specified length and width is placed on each convolved narrowband image. The flux within the slit is summed perpendicular to the slit, and the resulting column is put in the corresponding column in the output 2D spectrum. This spectrum is not the final one, but an intermediate one. Ideally, this spectrum would have "infinite" spectral resolution (but see below). To match the spectral resolution of the spectrograph, each row of the intermediate 2D spectrum is convolved with the instrumental profile. In ELFIT2D the instrumental profile can be a user specified 1D "image" or a Gaussian with a user specified width.

There are a few more parameters involved. In total, the 2D model spectrum in ELFIT2D is specified by the following *fixed parameters*

- Type of intrinsic rotation curve (flat or URC), and M_B if using the URC
- Seeing (empirical, or Gaussian with specified FWHM)
- Instrumental profile (empirical, or Gaussian with specified FWHM)
- Slit width and length
- Line-of-sight galaxy inclination i
- Rest-frame wavelength of the emission line (e.g. 3726.1 Å and 3728.8 Å for the [OII] doublet, or 4861 Å for Hβ) and the redshift of the galaxy
- Image scales in Å/px and ″/px.

[1] ELFIT2D actually uses the opposite orientation, but this is handled by a simple image transpose

and the following *free parameters*

- $V_{\rm rot}\sin i$: Projected (rest frame) rotation velocity [km/s]
- $r_{\rm d,spec}$: Exponential scale length [kpc] (could just as well have been in arcsec)
- I : Total line intensity [ADU]
- b : Constant residual background level [ADU]
- $R_{\rm [OII]}$: [OII] doublet ratio (only relevant if fitting the [OII] doublet)

As an illustration of what the 2D model spectra look like, we will set most of the parameters to some realistic values: Slit width = $0.82''$ [i.e. $1.0''\cos\theta_{\rm slit}$ cf. Fig. 2.2, p. 19], postage stamp image slit length = $6.87''$, $i = 44.6°$, $\lambda_{\rm rest} = 5007\,$Å (singlet line), $z = 0.3246$, spectral image scale = $1.075\,$Å/px, spatial image scale = $0.25''$/px, $L_B/L_{B*} = 0.21$. We will fix some of the free parameters: $r_{\rm d,spec} = 0.67''$, $I = 1165\,$ADU and $b = 0\,$ADU. ($R_{\rm [OII]}$ is irrelevant.)

At first we will use unrealisticly good seeing and spectral resolution, namely $0.50''$ and $2.0\,$Å, respectively (both Gaussian FWHM). Figure 3.3(a) shows 12 model spectra for $V_{\rm rot}\sin i = 0, 10, 20, \ldots, 110\,{\rm km\,s^{-1}}$. The flat intrinsic rotation curve has been used. For this setup the pixel size in the spectral direction is

$$c\,\frac{1.075\,\text{Å}}{(1+0.3246)5007\,\text{Å}} = 49\,{\rm km\,s^{-1}} \quad \text{(rest-frame velocity)}\ .$$

The spectral images in Fig. 3.3(a) have been created with an even number of columns. Hence, the two central columns correspond to (rest-frame) velocity intervals $[-49, 0]$ and $[0, +49]$ ${\rm km\,s^{-1}}$, respectively. What can be seen from Fig. 3.3(a) is:

- For $V_{\rm rot}\sin i$ = 10, 20, 30 and $40\,{\rm km\,s^{-1}}$ the upper flat part is exactly centered on the column corresponding to the velocity interval $[0, +49]$ ${\rm km\,s^{-1}}$. The lower flat part is similarly exactly centered on the column corresponding to the velocity interval $[-49, 0]$ ${\rm km\,s^{-1}}$. Little difference is seen between the images.

- For $V_{\rm rot}\sin i$ = (50), 60, 70, 80 and $90\,{\rm km\,s^{-1}}$ the same pattern is seen: the flat parts are exactly centered on the columns corresponding to the velocity intervals $[-98, -49]$ and $[+49, +98]$ ${\rm km\,s^{-1}}$.

In other words, the centroid of the flat part does not vary linearly and smoothly with the $V_{\rm rot}\sin i$ parameter, but is quantised in units of one pixel. This is a direct consequence of the way the intermediate spectrum (cf. above) was created. Consider a column corresponding to a given velocity interval, say $[+49, +98]$ ${\rm km\,s^{-1}}$. Whether the flat part has velocity 50, 70 or $97\,{\rm km\,s^{-1}}$, the signal will end up in this column. In other words, the intermediate spectrum does not have infinite spectral resolution, but one corresponding to a box of width 1 pixel.

A similar quantisation is seen for a spectrum with an odd number of columns, see Fig. 3.4. In this case the single central column corresponds to $[-24, +24]\,{\rm km\,s^{-1}}$, the next column to $[+24, +73]\,{\rm km\,s^{-1}}$, and so forth. As expected, the upper flat part is centered on the central column for $V_{\rm rot}\sin i = 0, 10, 20\,{\rm km\,s^{-1}}$; on the next column for $V_{\rm rot}\sin i = 30, 40, 50, 70, 70\,{\rm km\,s^{-1}}$; and on the next column again for $V_{\rm rot}\sin i = 80, 90, 100, 110\,{\rm km\,s^{-1}}$; and similarly for the lower flat part.

(a) Flat intrinsic rotation curve, no spectral oversampling

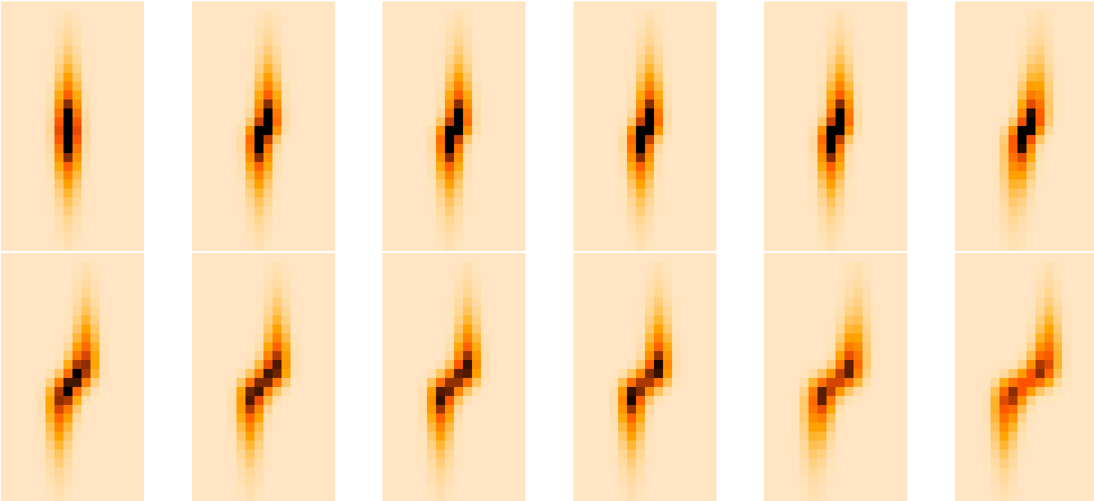

(b) Flat intrinsic rotation curve, 4–times spectral oversampling

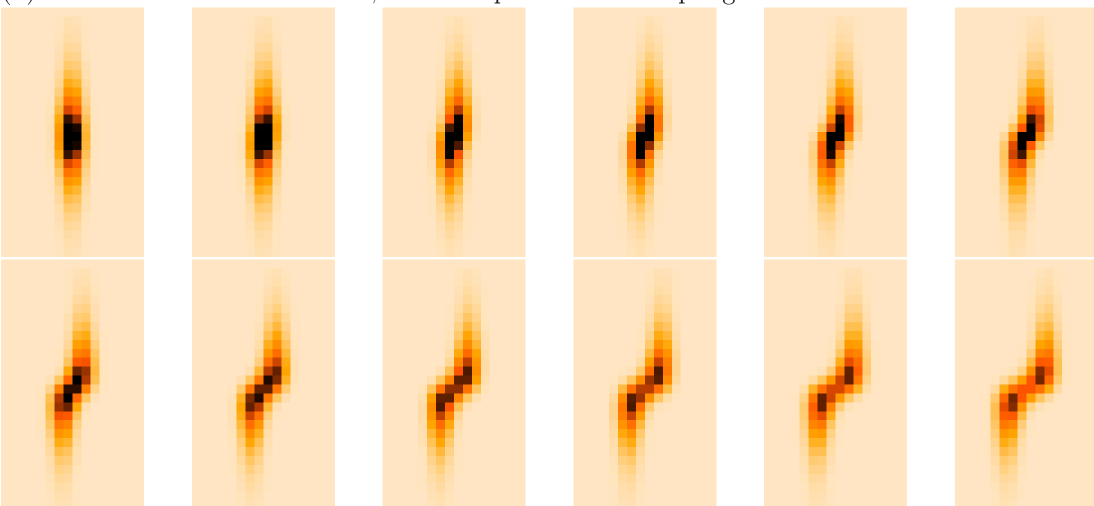

(c) Universal intrinsic rotation curve, 4–times spectral oversampling

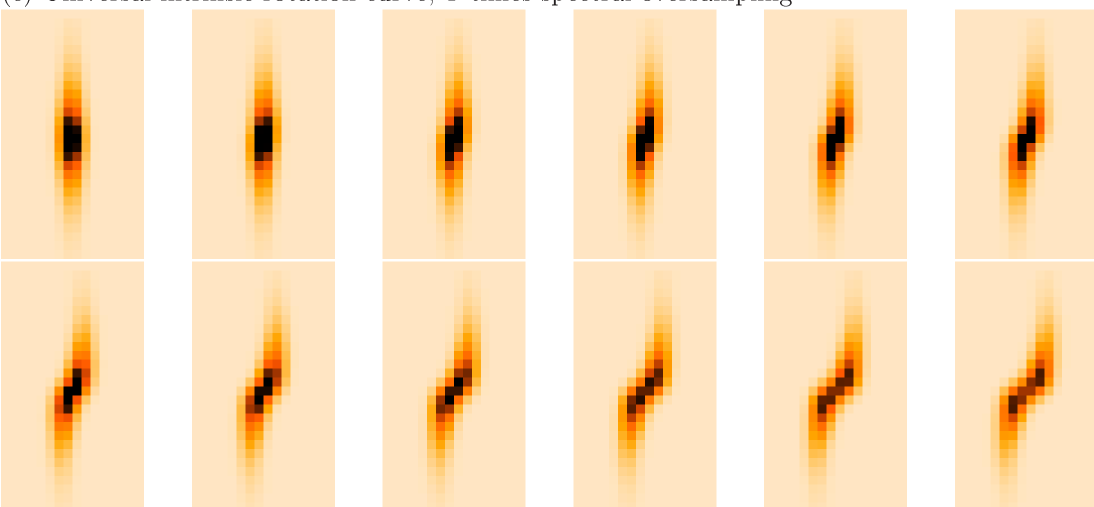

Figure 3.3: ELFIT2D model spectra (seeing = $0.50''$, spectral res. = 2.0 Å). For each of the 3 panels [(a)–(c)] the 12 images correspond to $V_{\rm rot} \sin i = 0, 10, 20, \ldots, 110\,{\rm km\,s^{-1}}$.

Flat intrinsic rotation curve, no spectral oversampling

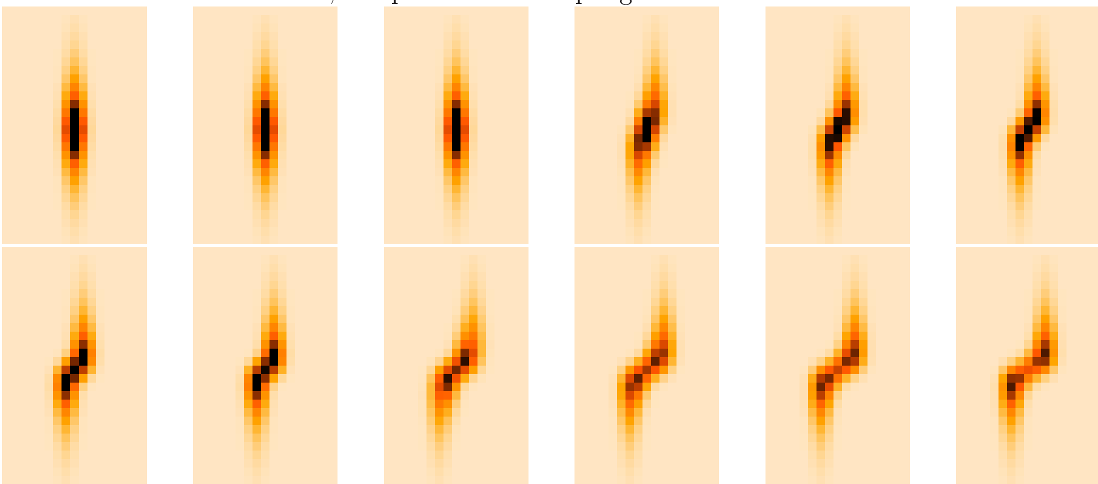

Figure 3.4: ELFIT2D model spectra (seeing = $0.50''$, spectral res. = 2.0 Å). The 12 images correspond to $V_{\rm rot} \sin i = 0, 10, 20, \ldots, 110\,{\rm km\,s^{-1}}$. These model spectra have an odd number of columns; otherwise they correspond to the spectra in Fig. 3.3(a).

The quantisation cannot be removed, but the size of the quanta can be made smaller by creating an *oversampled* intermediate spectrum, convolve it with the spectral instrumental profile, and then resample the spectrum. This is illustrated in Fig. 3.3(b), where 4–times spectral oversampling has been used. It can be seen that the centroid of the flat part now varies more smoothly with the $V_{\rm rot} \sin i$ parameter.

For the various emission lines observed, the pixel size in (rest-frame) velocity units is in the range 43–59 $\rm km\,s^{-1}$. For 4–times spectral oversampling the numbers are 4 times lower, i.e. 11–15 $\rm km\,s^{-1}$.

Spectral oversampling is not built-in to ELFIT2D, simply because oversampling was too expensive in CPU time to consider back in 1994–1995 when the code was written (Simard, private communication). It is still possible to create an oversampled spectrum by asking the model part of ELFIT2D to make a spectrum with say 4 times more columns and with a 4 times smaller pixel scale (i.e. 1.075/4 Å), and then outside ELFIT2D subsequently resample the spectrum by a factor of 4 in the spectral direction. It should be noted that ELFIT2D *has* the possibility to use spectral oversampling in the convolution with the spectral instrumental profile. However, oversampling at that stage will not help the before-mentioned quantisation, and it was not used.

To illustrate what model spectra based on the URC look like, models for this intrinsic rotation curve have also been made, see Fig. 3.3(c). Four–times spectral oversampling has been used. Not much difference is seen between the flat model spectra (panel b) and the URC model spectra (panel c). The discontinuity of the ELFIT2D URC at 3 scale lengths cannot be seen in this figure. For this setup ($L_B/L_{B*} = 0.21$) the velocity drops by 10% at 3 scale lengths, and even for the largest velocity shown (110 $\rm km\,s^{-1}$), 10% is below the pixel size even for 4 times spectral oversampling.

Model spectra for realistic values of the seeing and the spectral resolution, namely $1.04''$ and 4.2 Å, respectively (both Gaussian FWHM), are shown in Fig. 3.5. The quantisation problem is the same as for the better resolution images (Fig. 3.3).

(a) Flat intrinsic rotation curve, no spectral oversampling

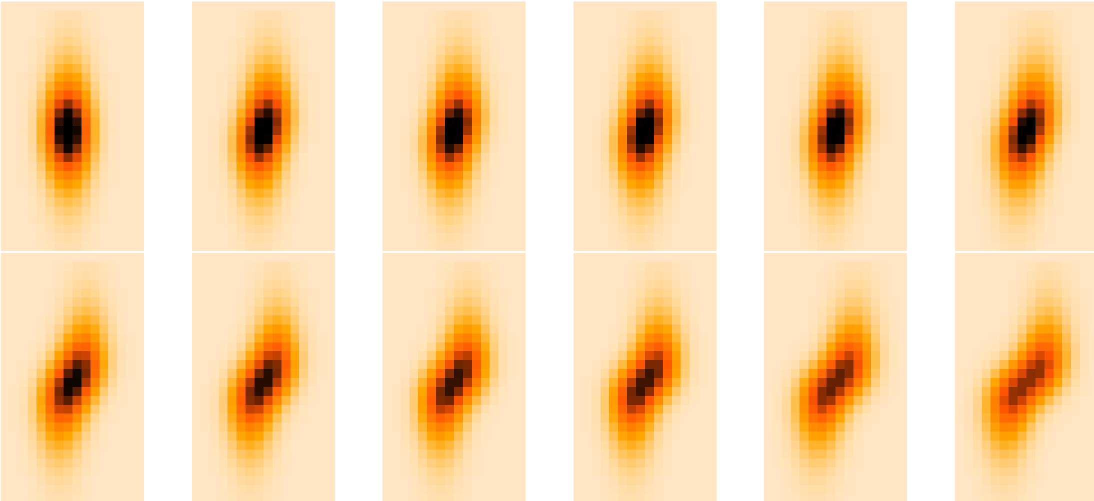

(b) Flat intrinsic rotation curve, 4–times spectral oversampling

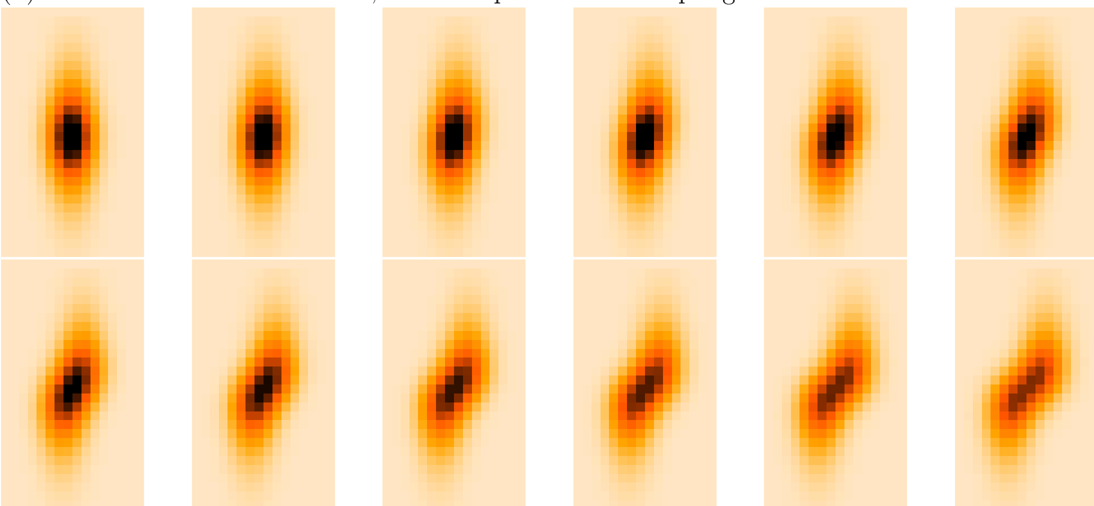

(c) Universal intrinsic rotation curve, 4–times spectral oversampling

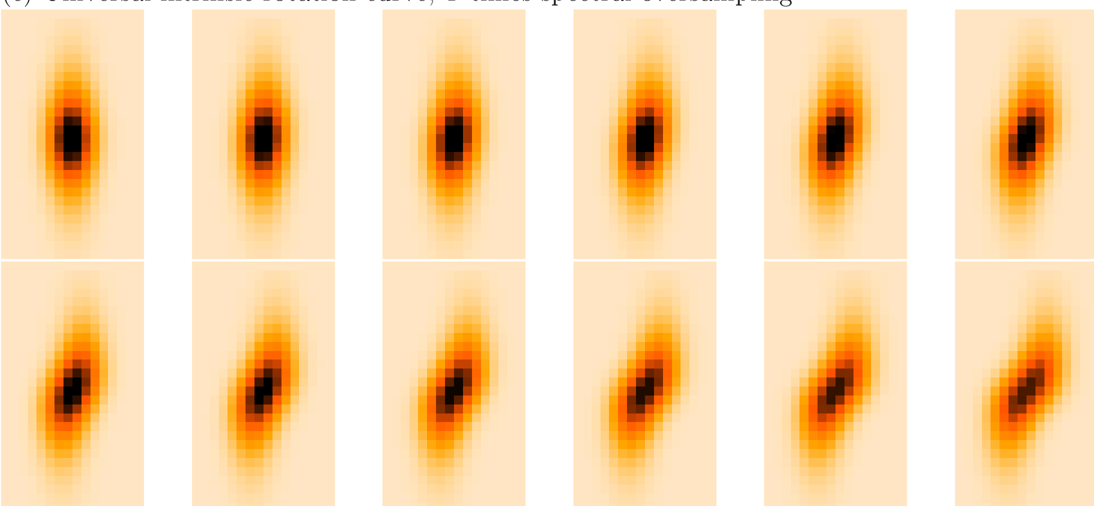

Figure 3.5: ELFIT2D model spectra (seeing = $1.04''$, spectral res. = 4.2 Å). For each of the 3 panels [(a)–(c)] the 12 images correspond to $V_{\rm rot} \sin i = 0, 10, 20, \ldots, 110\,{\rm km\,s^{-1}}$.

3.1.2 The Metropolis search

The other part of ELFIT2D is the algorithm used to find the values of the 5 free parameters that give the best match between the input spectrum and the model spectrum, and to find the confidence intervals for those best fit parameter values. For this task, the Metropolis algorithm (Metropolis et al. 1953) is used. This algorithm was designed to solve a problem in statistical mechanics, but it can also be applied in the general area of Bayesian parameter fitting (Saha & Williams 1994). Specifically, let M be a model, ω the parameters of the model, and D the data. Then Bayes' theorem states

$$\underbrace{P(\omega|D,M)}_{\text{posterior prob. distr.}} = \frac{\overbrace{P(D|\omega,M)}^{\text{likelihood}}\ \overbrace{P(\omega|M)}^{\text{prior}}}{\underbrace{P(D|M)}_{\text{global likelihood}}} \ , \tag{3.8}$$

where the different factors have been labelled with their usual names (Saha & Williams 1994). The global likelihood is just a normalising factor. The prior is assumed flat in ELFIT2D (which means that the posterior probability distribution is equal to the likelihood), but any prior could have been used. By assuming that the noise is Gaussian (and that the data points are independent), the likelihood is given by

$$P(D|\omega,M) \propto \exp\left(-\frac{1}{2}\chi^2\right) \quad , \quad \chi^2 \equiv \sum_{i=1}^{N}\left(\frac{X_i - X_i^M}{\sigma_i}\right)^2 \quad , \tag{3.9}$$

where X_i are the data values for the N pixels, and X_i^M are the corresponding model values. In ELFIT2D the individual errors σ_i are assumed identical and equal to the input parameter $\sigma_{\rm bkg}$. The constant of proportionality in Eq. (3.9) is not interesting, since only *ratios* of probabilities need to be calculated in the Metropolis algorithm.

The Metropolis algorithm (in the formulation of Saha & Williams 1994) works as follows:

1. Choose an initial guess of the parameters ω (i.e. the free parameters of the model described in the last section)
2. Calculate a random trial change $\delta\omega$ in the parameters
3.
   - If $P(\omega+\delta\omega|D,M) > P(\omega|D,M)$ then accept the move from ω to $\omega+\delta\omega$ and count $\omega+\delta\omega$ as an *accepted point*
   - If $P(\omega+\delta\omega|D,M) < P(\omega|D,M)$ then a fraction $P(\omega+\delta\omega|D,M)/P(\omega|D,M)$ of the times accept the move from ω to $\omega+\delta\omega$ and count $\omega+\delta\omega$ as an *accepted point*
4. Go to step (2) until the desired number of *accepted points* have been reached

The powerful result from Metropolis et al. (1953) (in the formulation of Saha & Williams 1994) is: Provided that all possible parameter values ω are eventually accessible, the distribution of accepted values of ω converges to $P(\omega|D,M)$.

The scheme to calculate a random trial change on a given parameter p (say $V_{\rm rot}\sin i$) is

$$\delta p = T_p U \ , \tag{3.10}$$

where T_p is the "temperature" of the parameter p, and U is a uniform random deviate in the interval $[-0.5, 0.5]$. In principle these parameter temperatures could be held fixed (as they indeed were in the Metropolis et al. 1953 implementation). However, that is not computationally efficient for the following reasons: If the temperature is large (implying that large jumps in parameter space are taken), then in most cases the probability of the trial point will be much smaller than that of the current point, and the trial point is most likely not accepted. Hence, it takes a long time to achieve the desired number of accepted points. If the temperature is small, then in most cases the probability of the trial point will be comparable to that of the current point, and the trial point is most likely accepted. This is a problem in two ways: If the current point happens to be near a local (but not global) maximum of the probability, the low temperature will mean that it will take many steps to get out, making the convergence slow. If the current point *is* near the global maximum, the slow walk around the parameter space will make it take longer to get a "fair sample", which also makes the convergence slow. For further details, see the monographs on Markov chain Monte Carlo methods by Hammersley & Handscomb (1964) and Gilks et al. (1996).

For these reasons, the temperatures are regulated as follows. Initially the temperatures are large. The first accepted point is found after a number of steps. This point is likely near the global maximum, and the temperatures are lowered somewhat. After that the temperatures are regulated up or down every 10 steps in such a way that half of the trial parameter changes are accepted.

The initial parameter temperatures are specified by the user. If a temperature is set to zero then that parameter will not be fitted but will be frozen at the initial guess value (also specified by the user). This feature is useful for tests. The user also specifies a minimum and maximum value for each parameter, e.g. 0 and $400\,\mathrm{km\,s^{-1}}$ for $V_{\mathrm{rot}} \sin i$. These bounds are only there to stop the search from going completely haywire, and they are rarely critical.

During the Metropolis search ELFIT2D outputs each accepted value of ω, i.e. the values for the 5 parameters ($V_{\mathrm{rot}} \sin i$, $r_{\mathrm{d,spec}}$, I, b and $R_{[\mathrm{OII}]}$). The parameter temperatures and the χ^2 are also output. After the desired number of accepted points has been achieved, say 1500, ELFIT2D calculates the median values for each parameter, and these values are taken as the "best fit" values. The median rather than the mean is chosen for robustness, following Saha & Williams (1994). A model image corresponding to these best fit values is also output. For each parameter the 16% and 84% percentile points are found, and these are the lower and upper bounds of the 68% confidence interval.

Simard & Pritchet (1999) have done some interesting tests of the reliability of the output from the Metropolis search in ELFIT2D. A model spectrum corresponding to some particular *true* parameters was created using the model part of ELFIT2D. Fifty copies were made of this spectrum, and to each spectrum a different realisation of noise was added. These 50 spectra were then fitted using ELFIT2D. For the 5 parameters and for the the 50 noise realisations, the *true* parameters were included in the computed 68% confidence intervals in 56–72% of the time. These deviations from 68% were compatible with the expected Poisson noise from having a finite number of realisations. In other words, the 68% confidence intervals from ELFIT2D were found to correctly represent the *random uncertainty* caused by noise (photon noise and read-out noise) in the data. It was also found the that "best fit" parameter values scattered in an unbiased way around the true parameters.

3.2 Practical implementation

ELFIT2D is written in SPP (Subset Pre-Processor, the internal language of IRAF), and we were given the source code. The following minor modifications were made:

- The inclination of the galaxy was made a user specified parameter. The original code did not take the inclination as user input. Instead, in each step in the Metropolis search a random inclination was used to compute the 2D model spectrum. This approach was adopted because Simard & Pritchet (1998, 1999) only had poor seeing images of their galaxies, and hence could not estimate the inclinations (Simard, private communication).

- The rest-frame wavelengths of the two lines in the doublet were made user specified parameters rather than being hardwired to the values for the [OII] doublet. To fit a singlet line (e.g. Hβ) these two wavelengths are simply set to the same value.

- An option was added to simply output a model spectrum created using specified parameters rather than fitting an input spectrum.

ELFIT2D does not model the continuum, only the emission line, so the continuum needs to be subtracted. For each spectrum and emission line the continuum was fitted and subtracted row by row using a linear function fitted to the levels in a background region on each side of the line. For the galaxies C2 and B1 the continuum was not visible and was not subtracted.

ELFIT2D does not fit the centre of the emission line, but expects the emission line to be "centered" in the input postage stamp image of the emission line following certain rules. These rules were determined empirically: model spectra were created with the number of columns and lines being either even or odd. For the wavelength direction it was found that the model emission line was centered at the centre of the image. For example, for an image with 4 columns the centre would be between column 2 and 3, and for an image with 5 columns the centre would be on column 3. For the spatial direction, however, the model emission line was not exactly centered in the image. For an image with 4 rows the centre would be on row 2, and for an image with 5 rows the centre would also be on row 2.

Each emission line was carefully inspected to find the best half-integer pixel centre in the wavelength direction and the best integer pixel centre in the spatial direction. The latter was compared to the spatial centre of the continuum (as seen in the science profiles, cf. Fig. 2.16, page 38), and it was made sure that the two centres agreed within reason (usually 1 pixel). When the centres had been decided postage stamp images were created. The sizes of these images were set according to the sizes of the emission lines. In cases of doubt about the wavelength and/or spatial centre postage stamp images corresponding to several centres were created and fitted.

The background noise $\sigma_{\rm bkg}$, which is used to calculate the likelihood (Eq. 3.9), was measured as the rms in a 30 pixel wide window on each side of the emission line. Values outside ± 10 ADU were excluded, and the windows were inspected to make sure they did not contain the residuals of very strong skylines (or other emission lines). The relative difference between the rms measured in each window was typically 10% and at worst 26%, indicating that the estimated $\sigma_{\rm bkg}$ values were "reasonable". The biggest noise source is photon noise from the subtracted sky lines, and this noise obviously varies with wavelength. The model of a single $\sigma_{\rm bkg}$ is therefore not completely realistic. It is conceptually trivial to use a sigma *image* (i.e. individual σ_i values in Eq. 3.9). In fact, from the cosmic ray identification exercise we *do* have such a sigma image (it would of course need to be straightened, wavelength calibrated and cut up). However, this was not done.

Fitting of the various emission lines was first done using the flat intrinsic rotation curve, and without using any spectral oversampling. ELFIT2D was run on almost all the emission lines that had been found (Table 2.2, page 42). The exceptions were:

- Emission lines with extremely low signal-to-noise. After having fitted a number of lines of varying S/N, it was possible to visually exclude (i.e. not fit) remaining lines with extremely poor S/N. The view could be taken that one should fit *all* lines and then use the derived error bars accordingly. However, for extremely poor S/N the correctness of the noise model becomes crucial, and the used noise model is not perfect. Also, for extremely poor S/N the centre of the emission line is hard to determine, requirering many values to be tried, i.e. a lot of work for little gain.

- Emission lines that were damaged by residuals from very strong sky lines.

HST images for the fitted galaxies (30 spiral galaxies with slits along the major axis, and the M/P galaxy 1801) are shown in Fig. 3.6 and in the figures of the atlas (Appendix B).

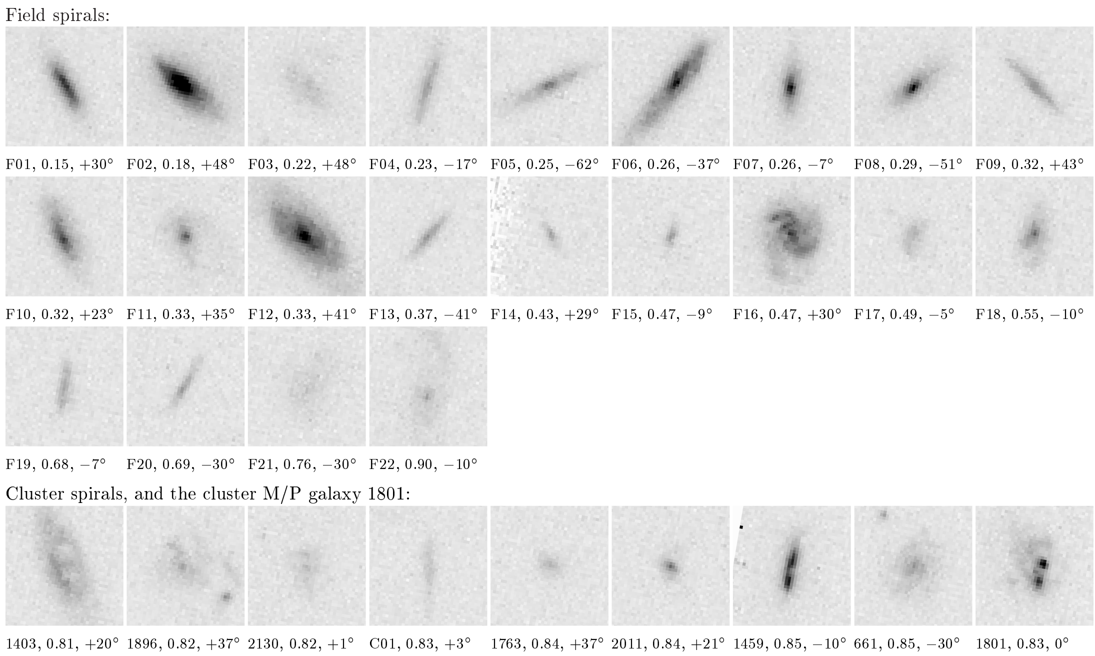

Figure 3.6: HST+WFPC2 F814W images of the galaxies fitted with ELFIT2D. Below each image is given galaxy ID, redshift and slit angle ($\theta_{\rm slit}$). The IDs are those used in Milvang-Jensen et al. (2003); for correspondence to the other names, see e.g. Table 2.2, page 42. The VLT slits were aligned with the major axes of the galaxies. The images shown have been rotated to the mask position angle and are $4''$ on the side. (In the atlas, Appendix B, the images have been further rotated to have the slit vertical.) The intensity scaling is linear, and the intensity cuts are the same for all the galaxies.

The seeing was set to a Gaussian with a FWHM of $1.04''$ for mask 1 and $0.94''$ for mask 2 (cf. Sect. 2.3.12). The spectral instrumental profile was set to a Gaussian with a FWHM of 4.2 Å. For a few emission lines there was evidence for a slightly non-Gaussian profile. The inclination was set to the value determined from the F814W HST images, cf. Ch. 4. The required number of accepted Metropolis points was set to 1500. The *direction* of the rotation is in ELFIT2D signified by the sign of the $V_{\rm rot} \sin i$ parameter: $V_{\rm rot} \sin i$ is positive if the observed wavelength of the emission line increases (rather than decreases) with increasing spatial coordinate (like the models in Fig. 3.3, 3.4 and 3.5). The direction was decided a priori by setting the allowed range for the $V_{\rm rot} \sin i$ parameter to be either 0 to $400\,{\rm km\,s^{-1}}$ or -400 to $0\,{\rm km\,s^{-1}}$ (as done by Simard & Pritchet 1998, 1999). Alternatively, the limits could have been set to -400 to $400\,{\rm km\,s^{-1}}$ and let ELFIT2D decide the direction.

After this series of fits had been completed, the problem of velocity quantisation was realised. Therefore, a series of fits using 4–times spectral oversampling was carried out as follows. The emission line spectrum was oversampled ("block replicated") by a factor of 4 in the wavelength direction. The image scale in the spectral direction was set to a fourth of the original value (i.e. 1.075/4 Å). The initial guess, temperature and maximum for the intensity parameter I was set to 4 times the normal values, since the total intensity in the oversampled image is 4 times larger than in the original one. Otherwise the parameters of ELFIT2D were left unchanged. In particular, $\sigma_{\rm bkg}$ was left unchanged, the rationale being that the rms of the oversampled image is the same as that of the original image (but see Sect. 3.3.1 below).

Following this series of fits, a series of fits using the URC were run, still with 4–times spectral oversampling. The rest-frame B–band absolute magnitudes (not corrected for internal extinction) as measured in the HST images (cf. Ch. 4) were used.

Finally, the relevance of the inclination was realised. As mentioned above, the original version of ELFIT2D did not take the inclination as input but set it to a random number. We did not understand this feature, and it was switched off in a way corresponding to having $i = 0°$. When this was fixed and the HST-based inclinations used as input, the three series of fits were run again: flat, 4–times oversampled flat, and 4–times oversampled URC. These new fits using the actual inclination gave *slightly* lower reduced chi–square values on average than the fits corresponding to $i = 0°$, indicating that the fits were slightly better. This also indicates that the width of the slit is not completely negligible compared to the size of the galaxy for these data. The reduced chi–square ($\chi^2_{\rm r}$) is defined as the chi–square divided by the number of degrees of freedom, which in turn is given by the number of pixels minus the number of parameters being fitted. Histograms of the reduced chi–square values for the fits used in the analysis is given in Sect. 3.3.2 below.

Most fits were done on a cluster of Sun workstations with 16 fast CPUs of the type UltraSPARC3. In total 124 CPU *days* were spent on the fits! For 1500 accepted Metropolis points (which corresponds to ∼4000 trial points, i.e. ∼4000 model spectra generated), the typical run-time is 2.5 CPU hours for a non-oversampled fit, and 7 CPU hours for a 4–times oversampled fit.

An illustration of the 2D emission line fitting is given in Fig. 3.7.

For each fit the residual image was calculated. The best fit model image and the residual image was inspected and compared to the observed image. The "time series" of accepted Metropolis values of the fitted parameters was also plotted and inspected. The reduced chi–square was also calculated and plotted.

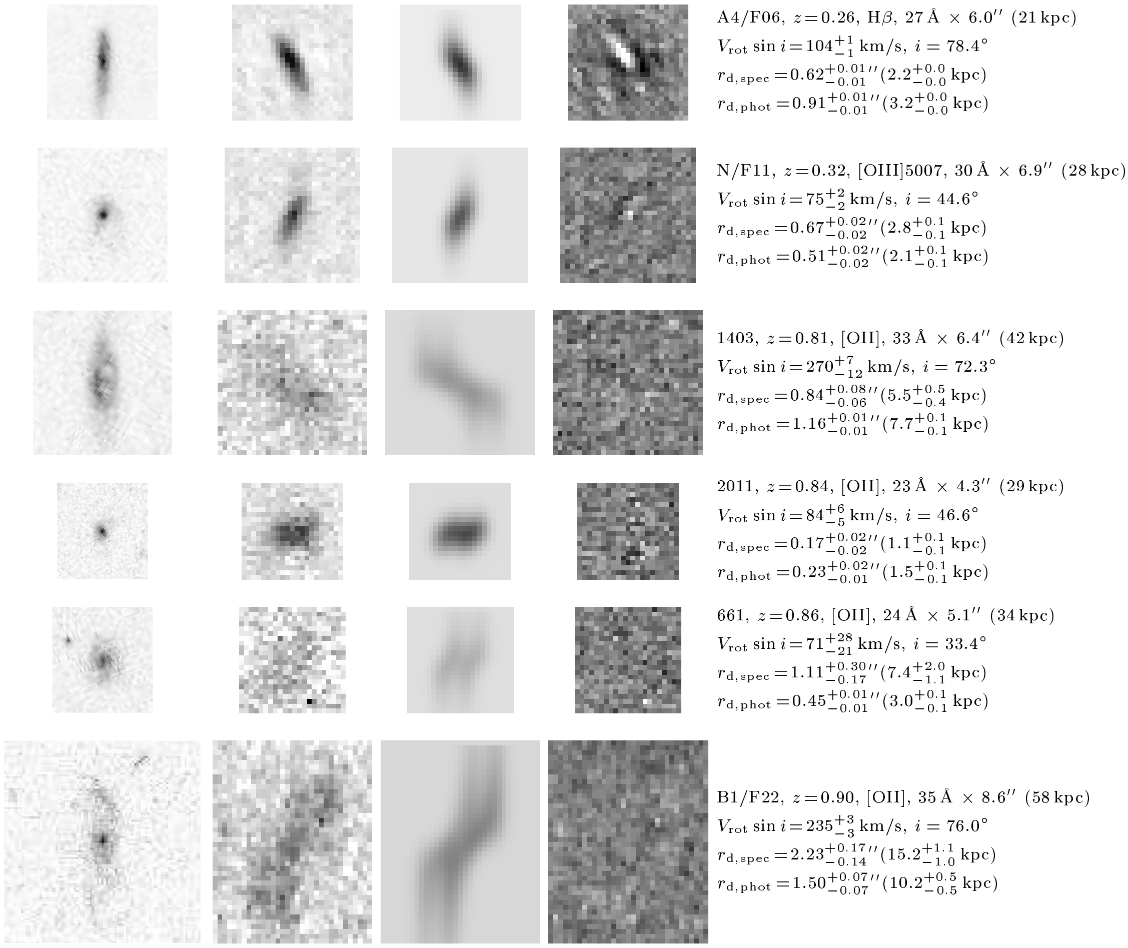

Figure 3.7: Illustration of the 2D emission line fitting. The first column shows HST+WFPC2 F814W images of the 6 example galaxies, rotated to have the slit along the y-axis. The following columns show 2D spectral images: observed, best-fit model and residual, with wavelength along the x–axis. The URC (Universal rotation curve) was used. The intensity cuts have been adjusted from galaxy to galaxy, except for the residual images. The galaxy ID, redshift, line ID and spectral image size are given on the figure, as well as the fitted values of the projected rotation velocity ($V_{\rm rot} \sin i$) and the emission line exponential scale length ($r_{\rm d,spec}$). The inclination (i) and the F814W photometric scale length ($r_{\rm d,phot}$) are also given. For each galaxy the height in arcsec of all 4 images is the same. The fit of galaxy A4/F06 was rejected, cf. Sect. 3.3.2.

An example of an ELFIT2D time series is shown in Fig. 3.8 (p. 64). This is for the flat non-oversampled fit of 1403–[OII]. For 4 of the parameters ($V_{\rm rot} \sin i$, $r_{\rm d}$, I, b) the time series appear *flat* right from the first accepted point. For $R_{\rm [OII]}$ the time series becomes flat after $\sim$100 accepted points. This flatness means that the search has found a maximum (likely to be the global one) of the quantity being maximised, which is the posterior probability distribution, here equal to the likelihood. In the thermodynamical analogy (cf. Saha & Williams 1994) this flatness indicates that *equilibrium* has been reached. The 68% confidence limits are indicated on the panels, and it is seen that the $\sim$100 points accepted before equilibrium for $R_{\rm [OII]}$ do not affect the derived 68%

confidence limits much. This is generally the case if the number of non-equilibrium accepted points is $\lesssim 200$, and such time series were deemed acceptable.

If the number of non-equilibrium accepted points was too large, several other seeds for the random number generator (controlled by the input parameter `metseed`) were tried. Usually, most of the new fits would reach equilibrium earlier than for the unacceptable metseed. An example of two fits differing only in their metseeds is shown in Fig. 3.9 (p. 65). As can be seen, "fit 1" reached equilibrium from the first accepted point, whereas "fit 2" did not reach equilibrium until after $\sim$450 accepted points, which clearly affects the derived 68% confidence intervals. It is seen that the two fits converge to the same values of the parameters, a behaviour that was always seen in these cases. It was always possible to get a reasonably flat time series when trying 3–5 different metseeds.

As stated, the adopted procedure was to (a) require a large number of accepted points (1500), (b) deem a time series acceptable if equilibrium was reached no later than $\sim$200, and (c) refit using several different metseeds if equilibrium was not reached early enough. An improvement to ELFIT2D would be to have some sort of internal equilibrium criterion. This is advocated by Saha & Williams (1994) and is also used in GIM2D, which will be discussed in Ch. 4.

Where the centre of the emission line (in the wavelength and/or spatial direction) was in question, fits were done using several centres, and the one that seemed to match the input best was used.

A note should be made about $R_{\rm [OII]}$: in ELFIT2D this parameter is defined as

$$R_{\rm [OII],\ ELFIT2D} \equiv \frac{I_{3726.1\,\text{Å}}}{I_{3728.8\,\text{Å}}} \tag{3.11}$$

However, in the literature (e.g. Osterbrock 1989) it is usually defined as

$$R_{\rm [OII],\ lit.} \equiv \frac{I_{3728.8\,\text{Å}}}{I_{3726.1\,\text{Å}}} \tag{3.12}$$

Unless otherwise stated, the $R_{\rm [OII]}$ values quoted and plotted in this work are based on the ELFIT2D definition.

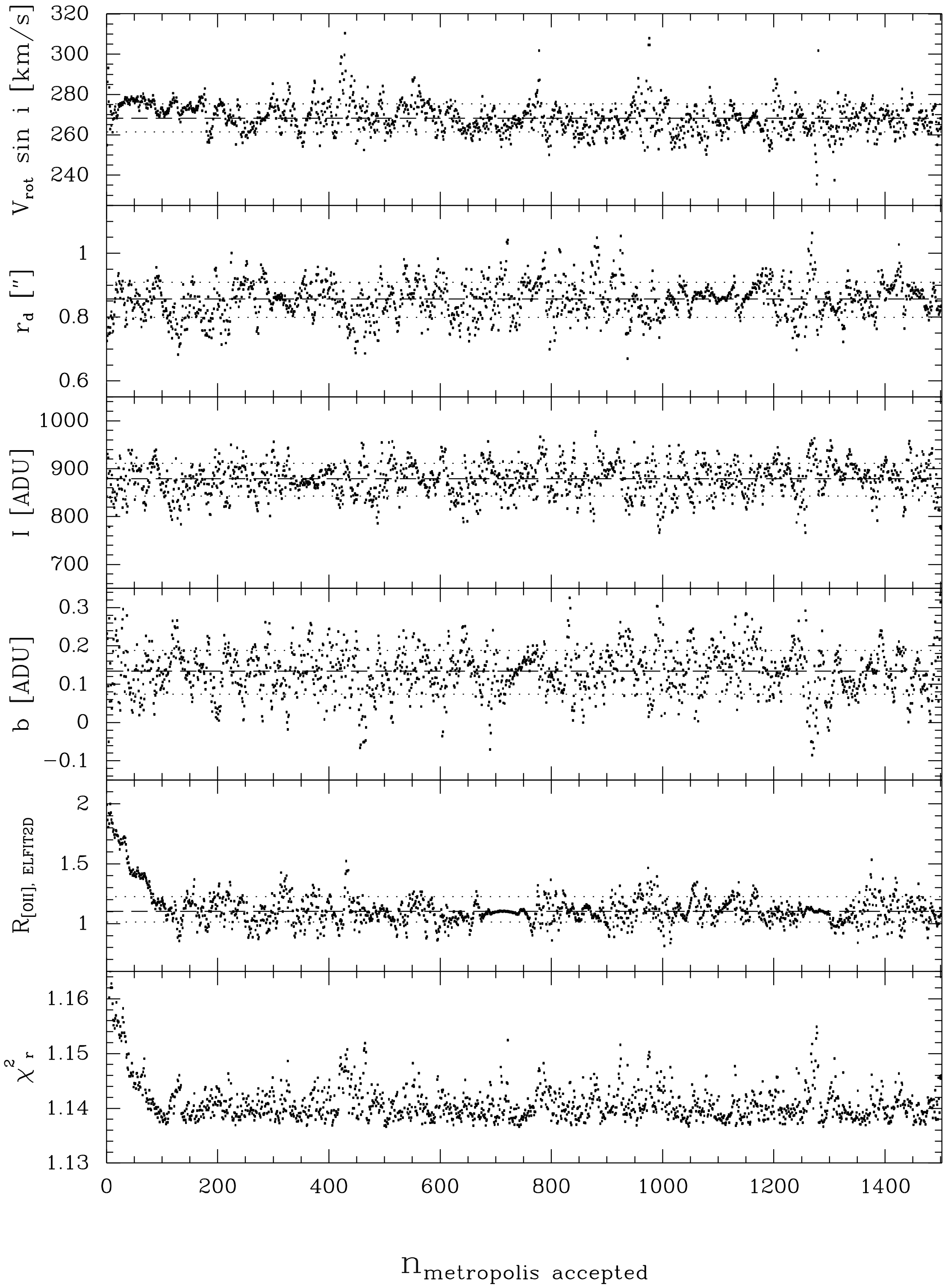

Figure 3.8: Example of a time series of accepted Metropolis points. This fit is for the [OII] doublet of galaxy 1403. The flat rotation curve and no oversampling was used. The dashed lines mark the median values, which are taken as the "best fit" values. The dotted lines mark the 68% confidence intervals.

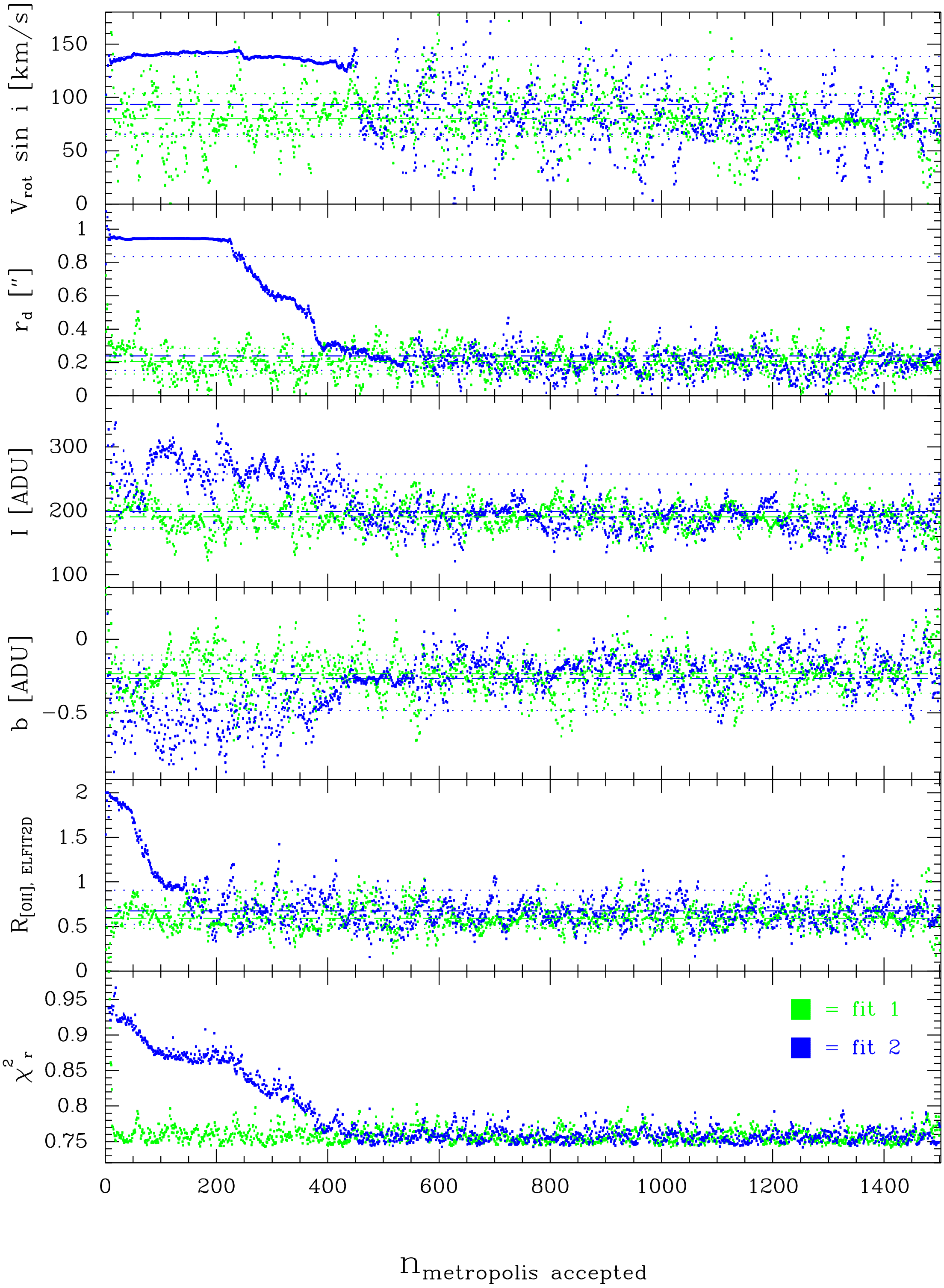

Figure 3.9: Time series for two fits which are identical except for the seed used for the random number generator. The fits are for the [OII] doublet of galaxy 1763 (this particular line is faint.) The flat rotation curve and no oversampling was used. The dashed and dotted lines have the same meaning as in Fig. 3.8.

3.3 Results

3.3.1 A small problem with oversampling scheme

The calculated uncertainties (corresponding to the 68% confidence intervals) for the 4–times oversampled fits (flat RC and URC) turned out to be substantially smaller than for the flat RC non-oversampled fits. This did not seem right. In particular, the uncertainties for the 4–times oversampled flat RC fits were a factor 2.0 smaller in the median than those from the non-oversampled flat RC fits. This turns out to be due to the way the oversampling was implemented. Recall that the oversampling was done completely externally to ELFIT2D, and that the input $\sigma_{\rm bkg}$ was unchanged with respect to the non-oversampled fits. In this setup the oversampled model spectrum is compared to the oversampled observed spectrum, which makes the χ^2 a factor of 4 too large since there are 4 times more pixels (cf. Eq. 3.9, p. 57)[2]. The corresponding likelihood is incorrect, since the equation (Eq. 3.9) assumes the data points to be independent. To do things correctly, the oversampled model spectrum should have been resampled *within ELFIT2D* and then compared to the non-oversampled observed spectrum, which would have given a correct χ^2 and hence a correct likelihood and correct uncertainties.

The above-mentioned factor of 2 can be derived as follows. Let p be a fitted parameter, and let σ_p be the calculated uncertainty on this parameter. Consider the case of N independent pixels with identical uncertainties $\sigma_{\rm bkg}$. It is clear that p is a function of the N independent pixel values $x_1, \ldots, x_N$. The propagation of errors formula gives

$$\sigma_p^2 \approx \left(\frac{\partial p}{\partial x_1}\right)^2 \sigma_{\rm bkg}^2 + \ldots + \left(\frac{\partial p}{\partial x_N}\right)^2 \sigma_{\rm bkg}^2 \ , \tag{3.13}$$

which means that σ_p is (approximately) proportional to $\sigma_{\rm bkg}$, i.e.

$$\sigma_p \approx k_p \, \sigma_{\rm bkg} \ . \tag{3.14}$$

From the definition of χ^2 it can be seen that a 4 times too large χ^2 corresponds to a 2 times too small $\sigma_{\rm bkg}$, which by virtue of Eq. (3.14) in turn corresponds to a 2 times too small σ_p, which is what we wanted to show. Accordingly, the derived uncertainties from the 4–times oversampled fits (both for the flat RC and for the URC) were multiplied by a factor of 2, and only corrected error bars are presented here.

3.3.2 Rejection of emission lines

Emission lines belonging to 30 spiral galaxies [and one M/P galaxy] were attempted fitted with ELFIT2D. See the atlas (Appendix B, p. 155), which shows all the 2D fits for the 4–times oversampled URC. For 3 of the spiral galaxies, the subjective impression was that the model did not match the observed spectra. For each of these galaxies, all the observed emission lines showed the same problem. Specifically:

- Galaxy V/F04 (see p. 159): strange line morphology, the line showed a tilt only on the lower side of the nucleus, whereas on the other side the line was flat.

[2]Actually, the calculated χ^2 is slightly *more* than a factor of 4 too large, since the intensity in the oversampled model spectrum will vary smoothly from pixel to pixel, whereas the intensity in the oversampled observed spectrum is constant within each block of 4 pixels.

- Galaxies XX6/F02 (p. 157) and A4/F06 (p. 161): the intensity profile seemed to be more extended than the exponential profile used in the model, and also asymmetric. This has the effect that the flat part of the model spectrum would occur at a lower velocity than what the eye would have chosen as the the terminal velocity, resulting in the derived velocity being too low. If the derived velocities for these 2 galaxies were nevertheless used, the galaxies would indeed be on the low velocity side of the Tully–Fisher relation defined by the other field galaxies.

These 3 galaxies were excluded from the analysis (Ch. 5).

This subjective method of identifying cases of severe mismatch between the data and the model is not completely satisfying. Ideally, a statistical approach using the reduced chi–square values should have been used. However, this can only be done reliably if the used noise model and its parameter(s) [here $\sigma_{\rm bkg}$] is correct to high accuracy, and this turns out not to be the case. In Fig. 3.10 the histograms of the reduced chi–square values for the accepted fits are shown. There is a peak around 1, which is good. However, the peak is quite broad and goes all the way down to 0.6, which most likely indicates that the uncertainty on $\sigma_{\rm bkg}$ is substantial. For the fits of the emission lines of the 3 excluded galaxies, the reduced chi–square values were: V/F04: 0.9–1.1; XX6/F02: 0.8–2.5; A4/F06: 1.6–2.6. The large variation for each galaxy is primarily due to the fits of the different lines giving quite different results (due to varying correctness of the used $\sigma_{\rm bkg}$ presumably). The different fitting methods employed (flat, URC, etc.) make little difference.

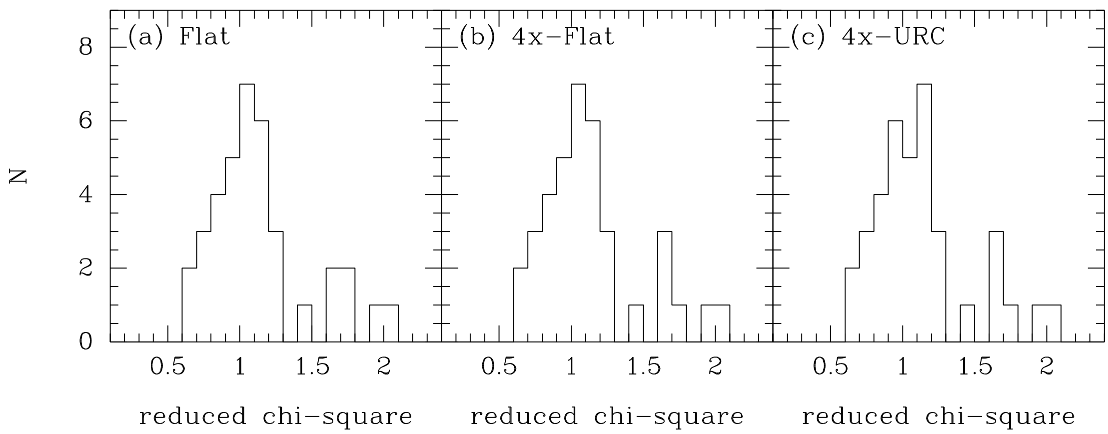

Figure 3.10: Histograms of reduced chi–square values for the 37 accepted fits of emission lines belonging to 27 spiral galaxies. The values for the 3 fitting methods are shown: flat rotation curve, flat rotation curve with 4–times oversampling, and URC with 4–times oversampling. For the oversampled fits, the reduced chi–square values were calculated from the resampled images.

A few emission lines were excluded because they were damaged by imperfect subtraction of bright sky lines. The galaxies in question still had at least one emission line left that could be fitted.

In addition to the emission lines from the 30 spiral galaxies, the very strong [OII] line from the M/P galaxy 1801 was fitted, see p. 181. The observed line was surprisingly well matched to the model. However, the emission was nevertheless asymmetric, being strongest in the two bright knots. The reduced chi–square was in the range 2.9–3.2 for the 3 fits done. Only spiral galaxies will be used in the analysis (Ch. 5), but this M/P galaxy will be shown on some of the plots using a special plot symbol.

3.3.3 The flat rotation curve versus the Universal rotation curve

First we note that no big differences were seen between the non-oversampled and the 4–times oversampled flat fits.

Then we turn out attention to the URC fits. Figure 3.11 compares the results from the flat fits with the results from the URC fits, both 4–times oversampled. The four panels show the difference in $V_{\rm rot} \sin i$, $\log V_{\rm rot} \sin i$, $r_{\rm d,spec}$ and reduced chi–square versus absolute blue magnitude. Simard & Pritchet (1999) found no differences between the results from the flat rotation curve and the URC at the 1 sigma level, and that is also seen here for $V_{\rm rot} \sin i$ and $r_{\rm d,spec}$. However, for $V_{\rm rot} \sin i$ there is nevertheless a systematic difference between the results from the two methods. As expected, this difference is the largest for low luminosities where the flat rotation curve and the URC differ the most. The URC gives higher velocities for low luminosity galaxies.

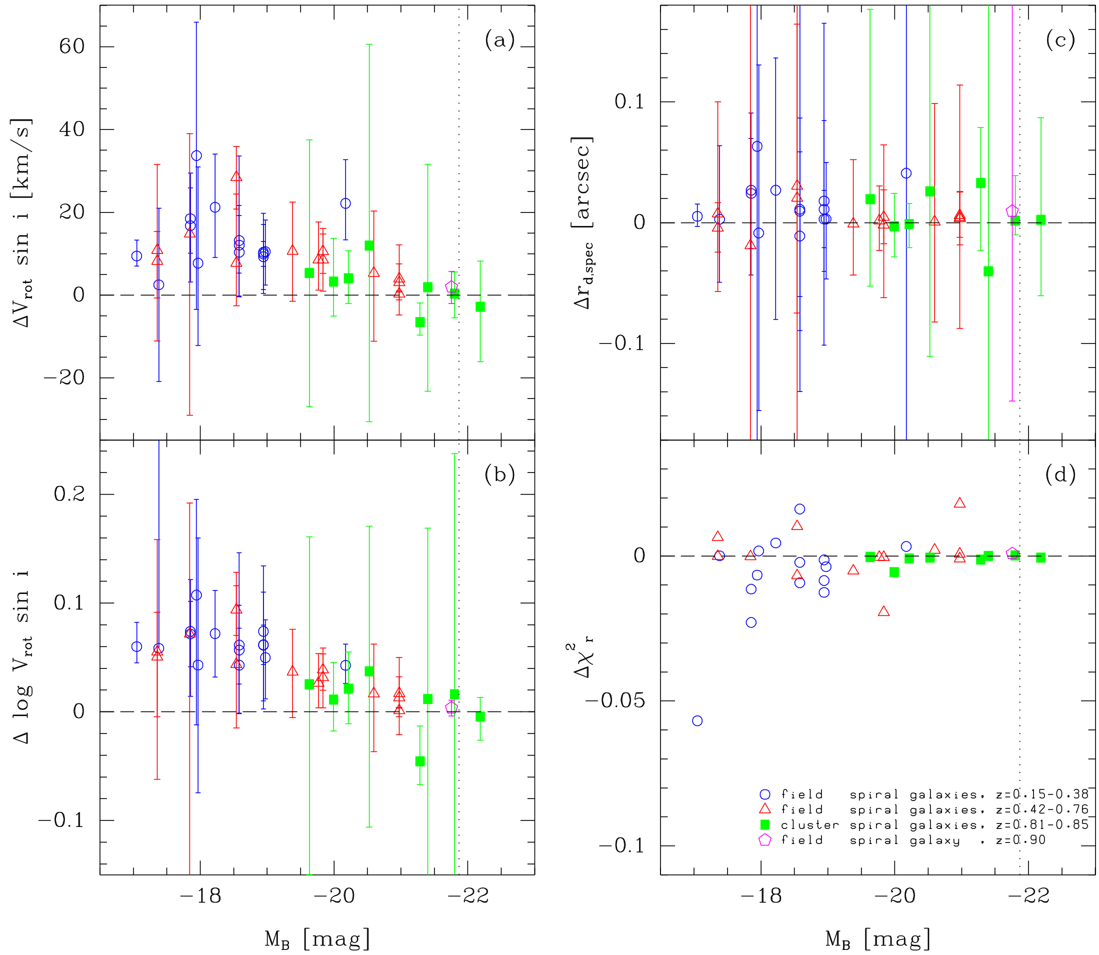

Figure 3.11: The flat rotation curve versus the URC, for fits using 4–times oversampling. All differences have been calculated as "URC"−"flat". The dotted line marks $L_B = 3.2 L_{B*}$ where the URC is identical to the flat rotation curve. The absolute magnitudes are for the default cosmology and derived from the HST images, cf. Ch. 4.

In the analysis we will use the results from the URC since that rotation curve has some physical basis, and since it gives marginally lower reduced chi–square values (see panel d of Fig. 3.11). Note that different symbols have been used in Fig. 3.11 for the cluster galaxies and the field galaxies in 3 redshift bins. It is seen that for the cluster galaxies and for the high luminosity (and typically high redshift) field galaxies there is little difference between the flat and the URC results.

3.3.4 Internal comparisons

Galaxies observed in both masks

One galaxy was observed in both masks, namely galaxy U/F08, see the two figures in the atlas on p. 163. In mask 1 it was only the [OIII] 5007 Å line that gave an acceptable fit (the Hβ line was faint and too damaged by a sky line to be fitted). In mask 2 the [OIII] 5007 Å line as well as the Hβ line gave acceptable fits. Thus, the fits of the [OIII] 5007 Å line in mask 1 and mask 2 can be compared, see Fig. 3.12 below and the figures in the atlas on p. 163. The values of $V_{\rm rot} \sin i$ and $r_{\rm d}$ agree within the errors, which is reassuring. For unknown reasons, the width in the spectral direction of the [OIII] 5007 Å line in the spectra from the two masks does not look identical.

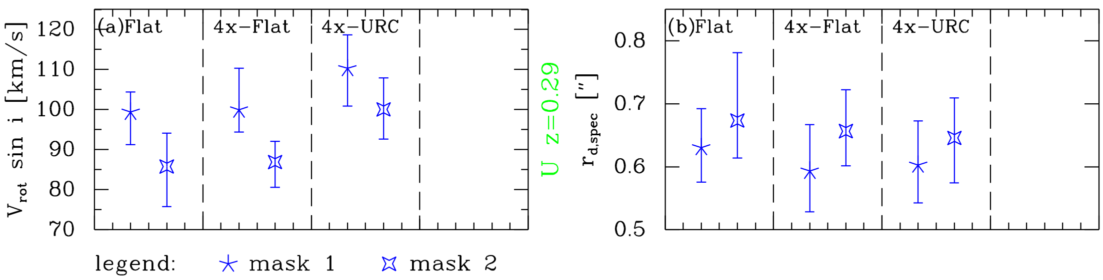

Figure 3.12: Comparison of ELFIT2D results for the single galaxy observed in both masks (galaxy U). Results using the flat rotation curve, the flat rotation curve with 4–times oversampling, and the URC with 4–times oversampling are shown.

Galaxies with several emission lines observed

A number of the field galaxies at lower redshift had several emission lines within the observed wavelength range. For 12 galaxies ELFIT2D was run on more than one line. The results for the parameters $V_{\rm rot} \sin i$ and $r_{\rm d,spec}$ are shown in Fig. 3.13 and 3.14 on the following two pages (the 12 galaxies had to be split into two figures to fit). Note that the accepted and the rejected fits are marked with different symbol colours.

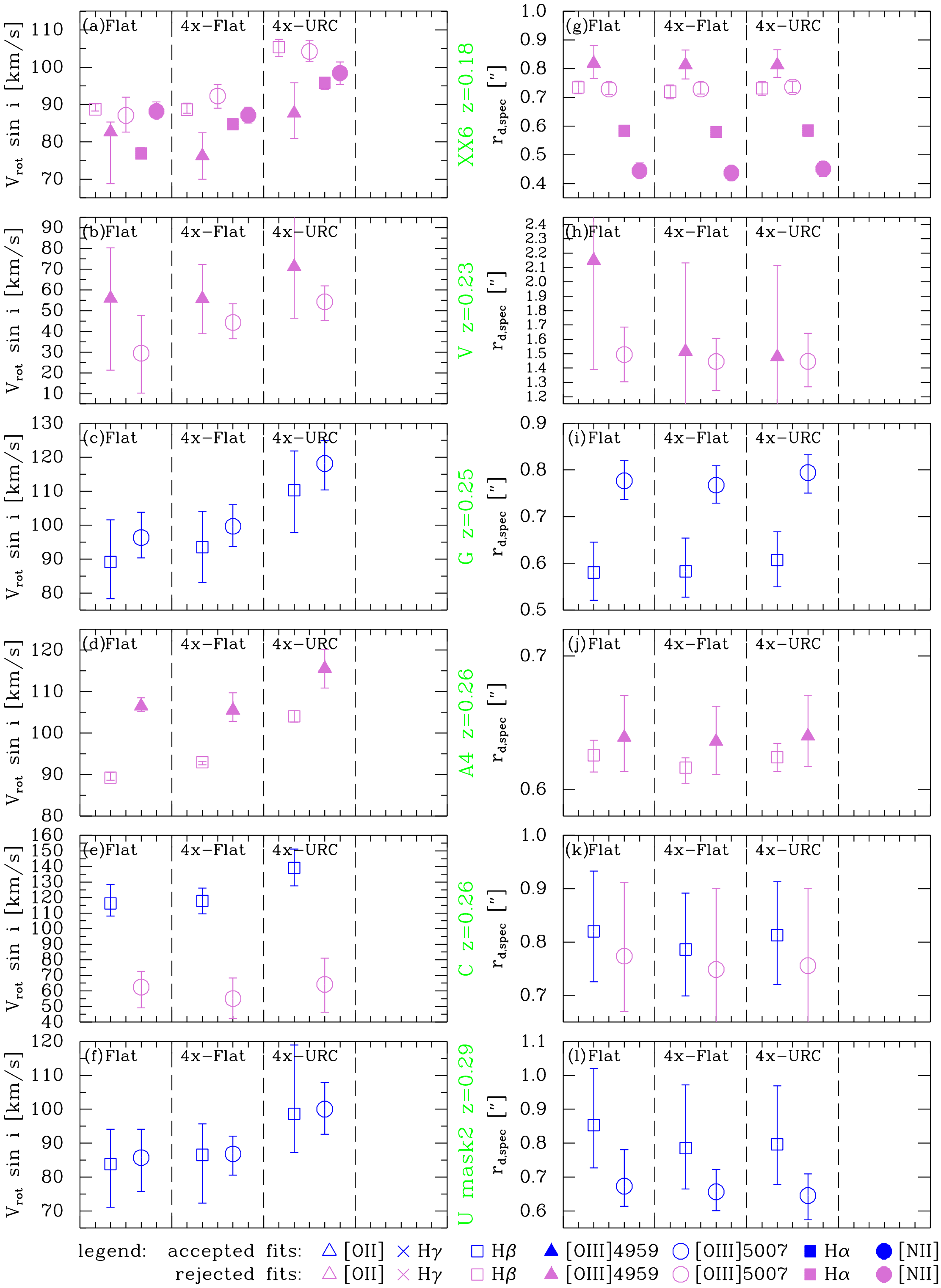

Figure 3.13: Comparison of ELFIT2D results for galaxies with multiple lines fitted, part 1 of 2. Results using the flat rotation curve, the flat rotation curve with 4–times oversampling and the URC with 4–times oversampling are shown. Occasionally (see Fig. 3.14), fits were also done using the URC but without oversampling.

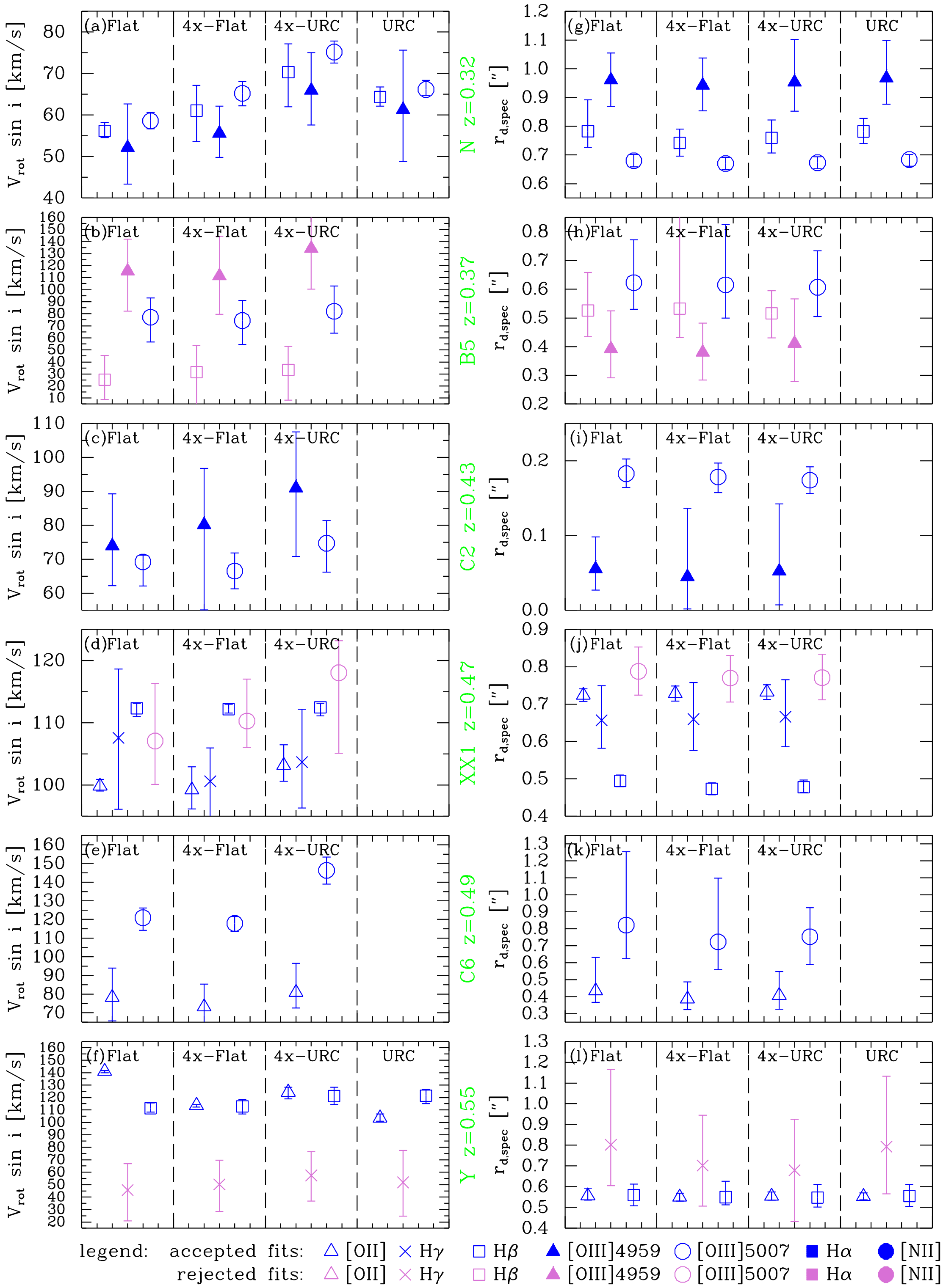

Figure 3.14: Comparison of ELFIT2D results for galaxies with multiple lines fitted, part 2 of 2. (Part 1 is Fig. 3.13.)

The 12 galaxies include the 3 galaxies that were excluded from the analysis because the model did not match the observed spectra (galaxies XX6, V, A4). The 12 galaxies also include 2 galaxies for which all but one line was rejected due to the other line(s) being damaged by imperfect sky subtraction (galaxies C and B5). This leaves 7 galaxies which have at least two lines with accepted fits. These 7 galaxies are the ones that can best be used to test the internal agreement of the derived rotation values and scale lengths. These are galaxies G and U (Fig. 3.13) and N, C2, XX1, C6 and Y (Fig. 3.14). In the atlas, they are shown on pp. 160, 163, 166, 169, 171, 172 and 173, but the line-to-line comparison is most easily done on Fig. 3.13 and Fig. 3.14. The impression from the figures for these 7 galaxies is that the results from the different lines agree within the errors, and that the errors are reasonable. There are 2 exceptions:

- XX1 (Fig. 3.14 and Fig. B.17, p. 171): For the fits of [OII] and Hβ, the results for both $V_{\rm rot}\sin i$ and $r_{\rm d,spec}$ do not agree within the errors. For the 4–times oversampled URC fits, the differences are as follows. The difference in $V_{\rm rot}\sin i$ is $-9.3 \pm 3.6\,{\rm km\,s^{-1}}$, i.e. 2.6σ and only 9%, i.e. not too bad. This difference is probably due to centering problems: the perfect centre seemed to be at spatial coordinate $y = 33.5$. Only $y = 33$ or $y = 34$ were possible (cf. earlier), and the difference between fits using the two was typically $\sim$10 km s^{-1}. The difference in $r_{\rm d,spec}$ is $0.26 \pm 0.03''$, i.e. 9σ and $\sim$40%. Looking at the spectra is *does* seem that the Hβ emission is less extended than the [OII] emission, for unknown reasons.

- C6 (Fig. 3.14 and Fig. B.18, p. 172): For the fits of [OII] and [OIII], the results for $V_{\rm rot}\sin i$ do not agree within the errors. For the 4–times oversampled URC fits, the difference is $-65 \pm 17\,{\rm km\,s^{-1}}$, i.e. 3.8σ and $\sim$60%. This galaxy is close to the edge of the slit – the spatial pixels $y = 1$–8 were used for the postage stamp image of the emission lines. This could be the reason for the discrepancy.

In summary, the internal agreement is satisfactory, in the sense that the scatter of the derived values of $V_{\rm rot}\sin i$ and $r_{\rm d}$ by and large is compatible with the estimated error bars. Nevertheless, there might still be small systematic trends present. Of particular interest is whether there is a trend with the integrated line intensity I (in ADU), since that is closely related to the S/N of the line. One might worry that the rotation velocity and the scale length would be underestimated for fainter lines. In Fig. 3.15 the derived $V_{\rm rot}\sin i$ and $r_{\rm d}$ values are plotted versus I for the galaxies (less C6) with more than one accepted fit. No trend is seen. The lines used cover the range $I = 200$–1900 ADU. The high redshift spirals with only the [OII] line observed have similar intensities, namely 200–1400 ADU (median 800 ADU) when galaxy 1459 with $I = 140$ ADU is discounted. This suggests that the faintness of the observed lines should not be a cause for concern.

3.3.5 Mean values

For the galaxies with accepted fits of more than one line, weighted averages of $V_{\rm rot}\sin i$ and $r_{\rm d}$ were calculated, see Table 3.1. The weights were set to one over the variance. The individual positive and negative error bars, corresponding to the 68% confidence intervals, were combined to give positive and negative error bars on the weighted averages. This was done simply by applying the propagation of errors formula to the positive and negative error bars separately. A more sophisticated treatment could have been done using the individual sets of accepted Metropolis points.

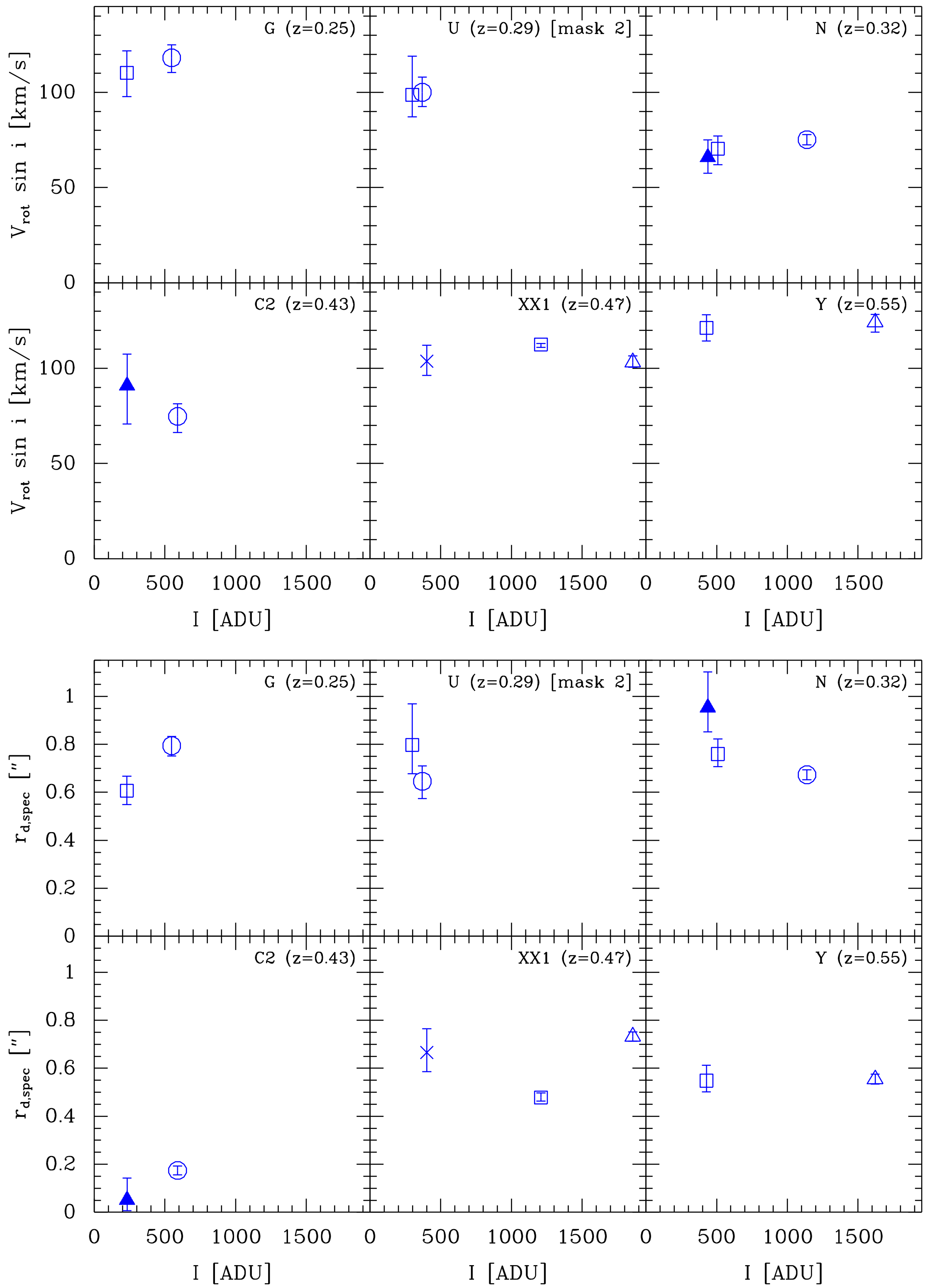

Figure 3.15: ELFIT2D results for galaxies with multiple lines fitted: plots versus the line intensity I (for the the 4–times oversampled URC fits). Error bars on I are not plotted since they are smaller than the plot symbols. No trend versus I ($\sim S/N$) is seen. (Legend: see Fig. 3.14, p. 71.) This figure sums up the internal agreement.

			Flat rotation curve			Flat rot. curve, 4–times oversampled			URC, 4–times oversampled		
Name	Alt[a]	z	$V_{\rm rot}\sin i$ [km/s]	$r_{\rm d,spec}$ [″]	$r_{\rm d,spec}$ [kpc]	$V_{\rm rot}\sin i$ [km/s]	$r_{\rm d,spec}$ [″]	$r_{\rm d,spec}$ [kpc]	$V_{\rm rot}\sin i$ [km/s]	$r_{\rm d,spec}$ [″]	$r_{\rm d,spec}$ [kpc]
Z	F01	0.1538	$58.8^{+1.0}_{-2.1}$	$0.37^{+0.01}_{-0.01}$	$0.89^{+0.02}_{-0.02}$	$63.8^{+0.9}_{-2.1}$	$0.37^{+0.01}_{-0.01}$	$0.88^{+0.02}_{-0.02}$	$73.3^{+3.7}_{-2.4}$	$0.37^{+0.01}_{-0.01}$	$0.89^{+0.02}_{-0.02}$
XX6[b]	F02[b]	0.1805	$84.6^{+1.0}_{-0.4}$	$0.60^{+0.01}_{-0.01}$	$1.65^{+0.02}_{-0.02}$	$84.8^{+0.2}_{-0.2}$	$0.60^{+0.01}_{-0.01}$	$1.64^{+0.02}_{-0.02}$	$99.1^{+0.9}_{-1.2}$	$0.64^{+0.01}_{-0.01}$	$1.74^{+0.03}_{-0.03}$
A	F03	0.2172	$26.9^{+17.5}_{-13.8}$	$0.37^{+0.06}_{-0.03}$	$1.17^{+0.17}_{-0.09}$	$17.3^{+14.8}_{-15.7}$	$0.37^{+0.05}_{-0.04}$	$1.17^{+0.15}_{-0.12}$	$19.7^{+16.8}_{-18.8}$	$0.38^{+0.06}_{-0.05}$	$1.18^{+0.18}_{-0.15}$
V[b]	F04[b]	0.2297	$37.1^{+14.8}_{-16.9}$	$1.52^{+0.19}_{-0.18}$	$4.95^{+0.62}_{-0.60}$	$46.6^{+7.9}_{-7.1}$	$1.45^{+0.16}_{-0.19}$	$4.74^{+0.51}_{-0.61}$	$56.0^{+7.3}_{-8.4}$	$1.45^{+0.19}_{-0.17}$	$4.73^{+0.61}_{-0.54}$
G	F05	0.2495	$94.5^{+6.4}_{-5.2}$	$0.72^{+0.04}_{-0.03}$	$2.48^{+0.12}_{-0.12}$	$98.1^{+5.5}_{-5.2}$	$0.71^{+0.04}_{-0.03}$	$2.47^{+0.12}_{-0.11}$	$116.0^{+5.9}_{-6.6}$	$0.73^{+0.03}_{-0.03}$	$2.54^{+0.11}_{-0.12}$
A4[b]	F06[b]	0.2594	$93.6^{+1.1}_{-0.6}$	$0.63^{+0.01}_{-0.01}$	$2.23^{+0.04}_{-0.04}$	$93.1^{+0.3}_{-0.5}$	$0.62^{+0.01}_{-0.01}$	$2.20^{+0.03}_{-0.04}$	$104.9^{+1.3}_{-1.3}$	$0.63^{+0.01}_{-0.01}$	$2.23^{+0.04}_{-0.03}$
C	F07	0.2640	$116.2^{+12.1}_{-8.1}$	$0.82^{+0.11}_{-0.09}$	$2.95^{+0.41}_{-0.34}$	$117.8^{+8.4}_{-8.1}$	$0.79^{+0.11}_{-0.09}$	$2.83^{+0.38}_{-0.31}$	$139.0^{+12.2}_{-11.4}$	$0.81^{+0.10}_{-0.09}$	$2.93^{+0.36}_{-0.33}$
U	F08	0.2870	$92.8^{+4.0}_{-5.7}$	$0.67^{+0.05}_{-0.04}$	$2.53^{+0.20}_{-0.15}$	$90.6^{+4.4}_{-4.4}$	$0.64^{+0.05}_{-0.04}$	$2.45^{+0.18}_{-0.15}$	$103.7^{+5.6}_{-5.3}$	$0.64^{+0.05}_{-0.04}$	$2.44^{+0.18}_{-0.17}$
P	F09	0.3232	$132.3^{+19.9}_{-22.9}$	$0.81^{+0.39}_{-0.21}$	$3.33^{+1.60}_{-0.85}$	$120.2^{+38.0}_{-21.1}$	$0.68^{+0.31}_{-0.17}$	$2.80^{+1.28}_{-0.68}$	$153.9^{+30.4}_{-31.9}$	$0.74^{+0.25}_{-0.20}$	$3.06^{+1.03}_{-0.82}$
A7	F10	0.3237	$85.8^{+8.8}_{-9.2}$	$0.62^{+0.10}_{-0.05}$	$2.56^{+0.43}_{-0.21}$	$86.4^{+5.1}_{-7.6}$	$0.61^{+0.04}_{-0.04}$	$2.53^{+0.17}_{-0.15}$	$96.9^{+6.6}_{-7.7}$	$0.62^{+0.04}_{-0.05}$	$2.54^{+0.18}_{-0.19}$
N	F11	0.3246	$57.2^{+1.4}_{-1.2}$	$0.70^{+0.02}_{-0.02}$	$2.89^{+0.09}_{-0.08}$	$63.2^{+2.4}_{-2.5}$	$0.69^{+0.02}_{-0.02}$	$2.86^{+0.08}_{-0.08}$	$74.0^{+2.4}_{-2.4}$	$0.69^{+0.02}_{-0.02}$	$2.85^{+0.08}_{-0.08}$
XX4	F12	0.3253	$215.9^{+7.9}_{-9.4}$	$0.95^{+0.26}_{-0.17}$	$3.94^{+1.06}_{-0.71}$	$214.4^{+8.8}_{-8.5}$	$0.91^{+0.24}_{-0.20}$	$3.77^{+1.00}_{-0.83}$	$236.6^{+9.7}_{-7.6}$	$0.95^{+0.24}_{-0.20}$	$3.94^{+1.00}_{-0.83}$
B5	F13	0.3737	$77.1^{+16.0}_{-20.5}$	$0.62^{+0.15}_{-0.09}$	$2.81^{+0.67}_{-0.42}$	$74.3^{+16.8}_{-19.8}$	$0.62^{+0.21}_{-0.12}$	$2.77^{+0.95}_{-0.52}$	$82.0^{+21.0}_{-18.0}$	$0.61^{+0.13}_{-0.10}$	$2.73^{+0.57}_{-0.46}$
C2	F14	0.4290	$69.7^{+2.3}_{-6.5}$	$0.15^{+0.02}_{-0.02}$	$0.75^{+0.09}_{-0.08}$	$67.3^{+5.1}_{-5.1}$	$0.17^{+0.02}_{-0.02}$	$0.82^{+0.09}_{-0.10}$	$77.1^{+6.2}_{-7.8}$	$0.17^{+0.02}_{-0.02}$	$0.81^{+0.09}_{-0.08}$
D	F15	0.4694	$77.2^{+21.3}_{-37.8}$	$0.06^{+0.07}_{-0.04}$	$0.33^{+0.33}_{-0.20}$	$82.6^{+17.7}_{-32.6}$	$0.07^{+0.39}_{-0.06}$	$0.34^{+2.01}_{-0.32}$	$97.4^{+17.9}_{-42.9}$	$0.05^{+0.25}_{-0.05}$	$0.25^{+1.27}_{-0.24}$
XX1	F16	0.4700	$105.2^{+0.7}_{-0.7}$	$0.60^{+0.01}_{-0.01}$	$3.09^{+0.06}_{-0.06}$	$111.5^{+0.8}_{-0.6}$	$0.57^{+0.01}_{-0.01}$	$2.93^{+0.06}_{-0.06}$	$111.4^{+0.7}_{-1.3}$	$0.59^{+0.01}_{-0.01}$	$3.02^{+0.07}_{-0.06}$
C6	F17	0.4936	$114.5^{+5.0}_{-6.0}$	$0.49^{+0.18}_{-0.06}$	$2.59^{+0.95}_{-0.34}$	$113.3^{+3.6}_{-4.0}$	$0.41^{+0.10}_{-0.06}$	$2.19^{+0.51}_{-0.31}$	$128.7^{+6.7}_{-5.9}$	$0.51^{+0.11}_{-0.08}$	$2.70^{+0.58}_{-0.40}$
Y	F18	0.5530	$139.5^{+0.7}_{-1.1}$	$0.56^{+0.03}_{-0.02}$	$3.11^{+0.18}_{-0.11}$	$113.6^{+0.7}_{-1.4}$	$0.55^{+0.02}_{-0.02}$	$3.07^{+0.11}_{-0.10}$	$123.3^{+3.6}_{-4.2}$	$0.55^{+0.02}_{-0.02}$	$3.09^{+0.11}_{-0.10}$
D2	F19	0.6841	$135.2^{+7.4}_{-7.4}$	$0.53^{+0.02}_{-0.02}$	$3.23^{+0.15}_{-0.14}$	$135.9^{+7.6}_{-5.8}$	$0.52^{+0.03}_{-0.03}$	$3.21^{+0.17}_{-0.16}$	$144.4^{+8.7}_{-6.2}$	$0.52^{+0.03}_{-0.02}$	$3.22^{+0.16}_{-0.13}$
B4	F20	0.6865	$117.2^{+8.0}_{-8.4}$	$0.47^{+0.04}_{-0.03}$	$2.87^{+0.23}_{-0.19}$	$120.5^{+9.6}_{-11.0}$	$0.48^{+0.03}_{-0.04}$	$2.93^{+0.19}_{-0.26}$	$131.1^{+10.4}_{-11.1}$	$0.47^{+0.05}_{-0.04}$	$2.92^{+0.30}_{-0.24}$
D6	F21	0.7558	$141.2^{+10.8}_{-16.3}$	$0.73^{+0.08}_{-0.06}$	$4.67^{+0.51}_{-0.39}$	$135.3^{+12.1}_{-14.3}$	$0.73^{+0.08}_{-0.07}$	$4.66^{+0.49}_{-0.47}$	$140.6^{+13.2}_{-15.3}$	$0.73^{+0.09}_{-0.07}$	$4.66^{+0.58}_{-0.47}$
1403	1403	0.8132	$268.3^{+7.1}_{-6.9}$	$0.86^{+0.05}_{-0.06}$	$5.63^{+0.35}_{-0.38}$	$273.6^{+7.8}_{-15.2}$	$0.84^{+0.06}_{-0.06}$	$5.50^{+0.40}_{-0.38}$	$270.8^{+8.0}_{-12.7}$	$0.84^{+0.08}_{-0.06}$	$5.51^{+0.52}_{-0.36}$
1896	1896	0.8224	$59.4^{+1.5}_{-1.1}$	$0.87^{+0.04}_{-0.04}$	$5.76^{+0.25}_{-0.26}$	$65.5^{+5.1}_{-6.9}$	$0.84^{+0.06}_{-0.05}$	$5.57^{+0.39}_{-0.31}$	$59.0^{+3.1}_{-1.9}$	$0.88^{+0.04}_{-0.05}$	$5.79^{+0.26}_{-0.31}$
2130	2130	0.8245	$147.9^{+32.9}_{-39.3}$	$0.35^{+0.17}_{-0.08}$	$2.32^{+1.14}_{-0.56}$	$133.8^{+38.6}_{-37.0}$	$0.31^{+0.15}_{-0.10}$	$2.08^{+0.97}_{-0.67}$	$145.8^{+44.9}_{-37.9}$	$0.34^{+0.20}_{-0.12}$	$2.25^{+1.33}_{-0.76}$
A8	C01	0.8280	$125.4^{+2.0}_{-2.7}$	$0.50^{+0.02}_{-0.02}$	$3.30^{+0.14}_{-0.14}$	$125.3^{+3.2}_{-2.9}$	$0.50^{+0.03}_{-0.02}$	$3.32^{+0.18}_{-0.16}$	$128.6^{+10.4}_{-8.1}$	$0.50^{+0.02}_{-0.02}$	$3.30^{+0.16}_{-0.14}$
1801	1801	0.8328	$154.2^{+0.3}_{-0.2}$	$0.37^{+0.00}_{-0.00}$	$2.45^{+0.02}_{-0.02}$	$146.9^{+0.2}_{-0.2}$	$0.37^{+0.00}_{-0.00}$	$2.45^{+0.02}_{-0.02}$	$147.0^{+0.3}_{-0.2}$	$0.37^{+0.00}_{-0.00}$	$2.46^{+0.02}_{-0.02}$
1763	1763	0.8384	$80.1^{+23.6}_{-16.8}$	$0.20^{+0.08}_{-0.07}$	$1.36^{+0.54}_{-0.48}$	$89.1^{+22.9}_{-25.1}$	$0.18^{+0.07}_{-0.07}$	$1.19^{+0.43}_{-0.48}$	$94.4^{+29.7}_{-30.1}$	$0.20^{+0.15}_{-0.06}$	$1.32^{+1.02}_{-0.43}$
2011	2011	0.8411	$75.9^{+7.5}_{-7.0}$	$0.17^{+0.02}_{-0.01}$	$1.14^{+0.11}_{-0.09}$	$80.8^{+5.1}_{-5.8}$	$0.17^{+0.01}_{-0.01}$	$1.13^{+0.08}_{-0.09}$	$84.8^{+6.0}_{-5.5}$	$0.17^{+0.02}_{-0.02}$	$1.12^{+0.11}_{-0.12}$
1459	1459	0.8459	$30.9^{+8.0}_{-6.5}$	$0.02^{+0.05}_{-0.02}$	$0.16^{+0.31}_{-0.12}$	$9.3^{+5.0}_{-5.3}$	$0.00^{+0.02}_{-0.00}$	$0.03^{+0.12}_{-0.03}$	$9.6^{+4.5}_{-5.3}$	$0.01^{+0.04}_{-0.01}$	$0.04^{+0.25}_{-0.04}$
661	661	0.8462	$69.4^{+10.6}_{-12.5}$	$1.21^{+0.33}_{-0.24}$	$8.07^{+2.20}_{-1.58}$	$69.4^{+25.5}_{-18.1}$	$1.15^{+0.22}_{-0.20}$	$7.68^{+1.44}_{-1.36}$	$71.3^{+28.3}_{-21.6}$	$1.11^{+0.30}_{-0.17}$	$7.41^{+2.03}_{-1.12}$
B1	F22	0.8965	$222.5^{+1.7}_{-1.9}$	$2.22^{+0.14}_{-0.11}$	$15.12^{+0.92}_{-0.76}$	$233.9^{+0.6}_{-0.7}$	$2.22^{+0.14}_{-0.13}$	$15.12^{+0.94}_{-0.88}$	$235.9^{+3.7}_{-4.0}$	$2.23^{+0.17}_{-0.14}$	$15.19^{+1.15}_{-0.96}$

Table 3.1: Mean values of $V_{\rm rot}\sin i$ and $r_{\rm d,spec}$. [a] Name used in Milvang-Jensen et al. (2003) [b] All fits of this galaxy rejected rejected

3.3.6 Tests for correlated errors

The set of accepted Metropolis points does not only give information about the uncertainties on each of the 4–5 fitted parameters, but also whether the uncertainties are correlated. Such possible correlations between the errors need only be taken into account if more than one of the fitted parameters are used together (in a given plot or equation). An example of such a situation is when comparing the residuals from the Tully–Fisher relation, which depends on $V_{\mathrm{rot}} \sin i$, with $r_{\mathrm{d,spec}}$.

Possible correlations between the errors between $V_{\mathrm{rot}} \sin i$ and $r_{\mathrm{d,spec}}$ were tested and quantified as follows, following Press et al. (1992). For each fit, a Spearman rank order test was done on the $V_{\mathrm{rot}} \sin i$ time series versus the $r_{\mathrm{d,spec}}$ time series. The first 300 points were omitted to limit problems with points accepted before reaching equilibrium. If the test found the two variables to be correlated at the 99.73% significance level ("3 sigma"), a note was made. Regardless of this, the linear correlation coefficient r was calculated. Where a significant correlation is found, the linear correlation coefficient r quantifies the strength (and direction) of the correlation.

z	Galaxy	Line	Flat		4–times flat		4–times URC	
			Corr.?	r	Corr.?	r	Corr.?	r
0.1538	Z	6563		−0.08		−0.03		0.09
0.2172	A	5007		0.03	yes	−0.11	yes	−0.11
0.2495	G	4861	yes	−0.12		−0.05	yes	−0.28
0.2495	G	5007		−0.08		−0.05	yes	−0.15
0.2640	C	4861		−0.14		−0.02	yes	0.16
0.2870	U (mask 2)	4861		−0.03	yes	−0.11	yes	−0.11
0.2870	U (mask 1)	5007	yes	0.21	yes	0.28	yes	0.11
0.2870	U (mask 2)	5007		−0.02		0.06	yes	−0.12
0.3232	P	5007	yes	−0.38	yes	−0.25	yes	−0.43
0.3237	A7	4861	yes	0.11		−0.06	yes	−0.09
0.3246	N	4861	yes	0.08	yes	−0.11		0.05
0.3246	N	4959		−0.09		−0.02		0.07
0.3246	N	5007		−0.09		−0.03		0.08
0.3253	XX4	4861		−0.07		−0.04	yes	−0.24
0.3737	B5	5007		−0.08		−0.06		−0.02
0.4290	C2	4959	yes	0.15		0.10		−0.04
0.4290	C2	5007	yes	0.23	yes	0.20	yes	0.25
0.4694	D	4861	yes	−0.22	yes	−0.26	yes	0.15
0.4700	XX1	3727	yes	−0.11		0.07		0.08
0.4700	XX1	4340	yes	0.11		0.01		0.06
0.4700	XX1	4861	yes	0.22		0.01	yes	0.13
0.4936	C6	3727		−0.02		−0.09		0.02
0.4936	C6	5007		0.05		0.09	yes	0.51
0.5530	Y	3727	yes	−0.07		0.06		−0.01
0.5530	Y	4861		−0.01		0.09		0.01
0.6841	D2	3727		−0.02		0.05		0.05
0.6865	B4	3727		0.01	yes	−0.08		−0.06
0.7558	D6	3727	yes	−0.18		−0.02		0.05
0.8132	1403	3727	yes	0.11		0.04		−0.05
0.8224	1896	3727		−0.06	yes	0.23	yes	0.14
0.8245	2130	3727	yes	0.17	yes	0.16	yes	0.28
0.8280	A8	3727		0.08	yes	0.12	yes	0.24
0.8384	1763	3727		−0.08		−0.02		0.00
0.8411	2011	3727		−0.02		−0.04	yes	−0.14
0.8459	1459	3727		0.03		0.00	yes	−0.04
0.8462	661	3727		−0.07		−0.07		−0.08
0.8965	B1	3727		−0.04		0.04		−0.02

Table 3.2: Test of correlations between the errors of $V_{\mathrm{rot}} \sin i$ and $r_{\mathrm{d,spec}}$. The columns "Corr.?" indicate whether a Spearman test found a correlation at the 99.73% significance level. The columns "r" give the linear correlation coefficient.

The results are given in Table 3.2, with the fits sorted by redshift. As can be seen, in about 50% of the cases no correlation is detected. In about 25% of the cases a positive correlation is found, and in about 25% of the cases a negative correlation is found. The correlations are seldom strong, i.e., $|r|$ is usually small. Furthermore, since the directions of the correlations where present are about equally positive and negative, no large net effect should be expected. Therefore, in the analysis we will treat the errors as being uncorrelated.

3.3.7 Comparison with other studies

Recently, Barden et al. (2003) published rotation velocities for 22 high redshift cluster and field spiral galaxies, based on 2D fitting to resolved NIR spectra of the Hα emission line. We have one galaxy in common, namely galaxy 1403 in MS1054−03 at $z = 0.81$, for which we have derived the rotation velocity from a 2D spectrum of the [OII] line (see the figure in the atlas on p. 177). Table 3.3 shows the comparison. The $V_{\rm rot} \sin i$ values agree within the errors, which is encouraging. (Our inclinations i are also fairly similar, and therefore the $V_{\rm rot}$ values also agree within the errors.) However, the errors are fairly large and only one galaxy is available for the comparison.

Table 3.3: Comparison with Barden et al. (2003) for galaxy 1403

	$V_{\rm rot} \sin i$ [km s^{-1}]	i [°]	$V_{\rm rot}$ [km s^{-1}]
Their values:	225 ± 49	76	232 ± 50
Our values:	271^{+8}_{-13}	72.3 ± 0.3	284^{+8}_{-13}

Chapter 4

Photometry and bulge/disk decomposition

4.1 Photometry

4.1.1 Optical (F606W and F814W) HST–based total magnitudes

Photometry was carried out on the F814W and F606W HST+WFPC2 images (e.g. van Dokkum et al. 1999), which kindly had been provided in cosmic-cleaned and combined form by Pieter van Dokkum and Marijn Franx. As shown on Fig. 2.1 (p. 18), MS1054−03 was covered by six WFPC2 fields (POS1–POS6). We used non-drizzled images (i.e. images with the original pixel size) since that was preferred for the bulge/disk decomposition software (cf. Sect. 4.3 below). Investigations showed that the combined images that we used were created as the average of three 1100 sec images. The exception was the F814W–POS1 image which seemed to originate from three images of exposure time 1100, 1100 and 857.5 sec, respectively. The effective exposure time for this image had to be determined empirically. This was done by retrieving the MS1054−03 images from the ST–ECF HST archive. By means of aperture photometry on selected objects an effective exposure time of 988 ± 8 sec was derived. Similar measurements on objects in a few images for other fields/filters showed that the effective exposure times for these were compatible with being 1100 sec.

Total magnitudes were measured using SExtractor (Bertin & Arnouts 1996). The object detection and definition (aka. segmentation) was done in the F814W images. The segmentation parameters were tuned until a "correct" segmentation was achieved. Specifically, the following was achieved: Galaxies 1403 and B1/F22 were *not* split into several pieces; while the 2 objects seen near galaxy 1896 (cf. p. 178) *were* split out as separate objects (the 'knot' was spectroscopically found to be in the background, and the 'disk' is bluer than 1896 indicating that it is in the foreground). Note that the same set of segmentation parameters were used for all the images. The segmentation from the F814W images was used for the measurement of the magnitudes in the F606W images. The `MAG_BEST` estimator of the total magnitude was used. For all the galaxies under study this estimator was equal to the `MAG_AUTO` estimator, which means that SExtractor considered these galaxies not to be severely affected by crowding.

The measured magnitudes were brought onto the standard system using photometric zero points from the May 1997 WFPC2 SYNPHOT update (as also used by Simard et al. 2002).

4.1.2 Near-infrared (J, H, K) VLT–based total magnitudes

MS1054−03 has been observed in the NIR using VLT+ISAAC as part of the FIRES survey (Franx et al. 2000). A mosaic of 4 pointings was observed, covering an area of $\sim 5 \times 5'$. The MS1054−03 data are being reduced by Natascha M. Förster Schreiber, who in September 2001 kindly provided preliminary data for a subset of our galaxies. This subset consists of the spiral galaxies with observed [OII] emission (i.e., the high redshift ∼half of the sample; this was the subsample we were analysing at the time), but it excludes galaxy A8/C01 which was outside the ISAAC mosaic. It also excludes the merger/peculiar galaxy 1801. As for our optical magnitudes, the magnitudes were measured using SExtractor as “best” total magnitudes, but the object segmentation (deblending) could differ somewhat from the segmentation we used for our HST magnitudes. The accuracy of these preliminary magnitudes was estimated to be “a few tenths of magnitude, but depending on the location within the mosaic”.

Due to various problems with the data, and to the desire of the FIRES group to make the most of these superb seeing ($\sim 0.5''$) NIR images, the reduction is still ongoing, and no new reduced data products are available. Therefore, we will use the preliminary data. This also means that no NIR data are available for the low redshift part of the sample.

We do not have any details of how the magnitudes at hand were calibrated to a standard system. We will assume, that these magnitudes, which were observed using J_s, H and K_s filters, are on the standard J, H and K system.

Despite our lack of control over the NIR data and its quality, we feel that it is worth exploring what results we can get from its analysis. Obviously, conclusions based on the JHK data need to be taken with the necessary caution. When the data is published, this analysis will be revised.

4.2 Transformations of the magnitudes

Rest-frame B–band magnitudes were derived from the observed F814W and F606W photometry. F814W matches almost exactly the rest-frame B–band at $z = 0.83$, and thus the B–band magnitudes can be derived very accurately for galaxies close to this z. F606W matches the B–band at $z \approx 0.37$. Thus, B–band magnitudes for all the galaxies in our sample can be interpolated with reasonably small uncertainties. The interpolation (and in a few cases, small extrapolation) was carried out using spectral energy distributions (SEDs) of local galaxies with different spectral/morphological types (Coleman et al. 1980). Figure 4.1 shows the (F606W−F814W) colours versus redshift for these local SEDs and for our galaxies at $z = 0.15$–0.90. As can be seen our spiral galaxies occupy the region spanned by the local Sab–Sdm SEDs, which is reassuring.

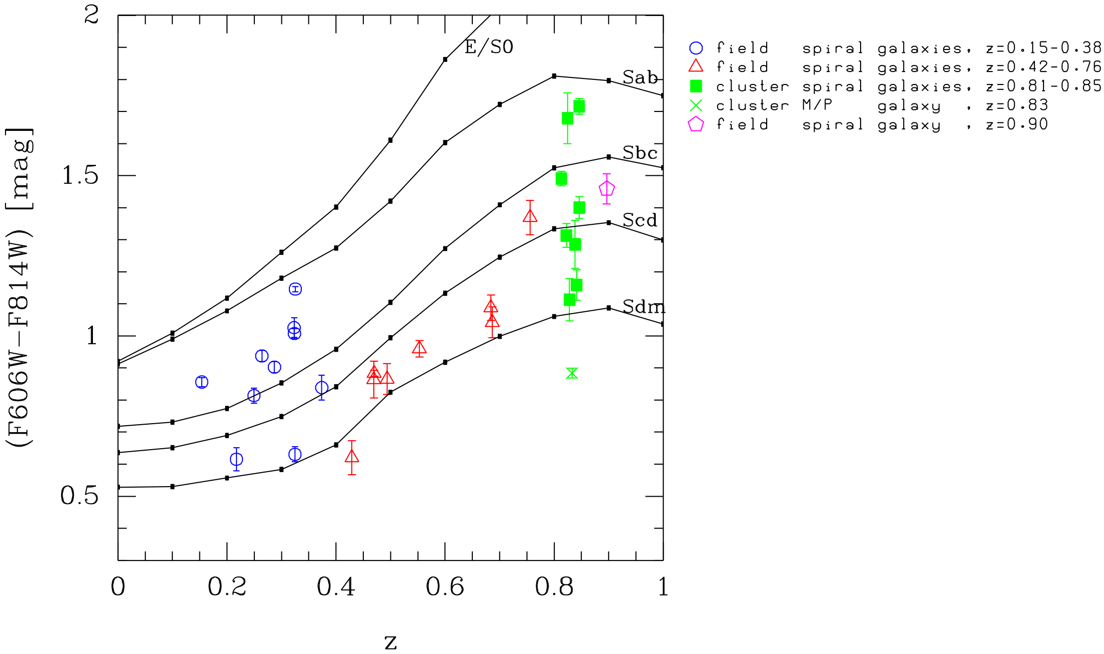

Figure 4.1: Colour versus redshift. Local galaxy SEDs are from Coleman et al. (1980).

For the given galaxy (with a given redshift), the transformation from observed F814W and F606W magnitudes to rest-frame B magnitude was done as follows. Each of the 4 spiral SEDs predicts a transformation from observed F814W to rest-frame B of the type $B_{\rm rest} = {\rm F814W_{obs}} + \xi$. Each of the SEDs also predicts an observed (F606W−F814W) colour, and thus it is possible to do a fit $\xi = a\,({\rm F606W} - {\rm F814W}) + b$ to the 4 points (one point per spiral SED at the given redshift). These fits had a very low scatter, typically <0.01 mag, and no more than 0.025 mag. The fits were used to calculate ξ for the observed (F606W−F814W) colour for the given galaxy. The very small formal uncertainty in this transformation of ∼0.01 mag assumes perfect knowledge of the filter response in each band. Tests with different filters indicate that systematic uncertainties of ∼0.1 mag could be present, but these are negligible in our analysis.

Galactic extinction at the centre coordinates of MS1054−03 is predicted to be 0.07 mag in F814W and 0.10 mag in F606W according to Schlegel et al. (1998), and 0.03 mag in F814W and 0.04 mag in F606W according to Burstein & Heiles (1982). Galactic extinction was ignored.

To calculate rest-frame colours redwards of B without extrapolation, the observed-frame preliminary NIR magnitudes are needed. Various NIR and NIR–optical colours (data and local SEDs) are plotted versus redshift in Fig. 4.2. For 'aesthetic reasons' we have transformed F814W to Cousins I using the relation I = F814W − 0.05, which is correct to within a few hundredths of a magnitude for $z = 0$–1 (Fukugita et al. 1995).

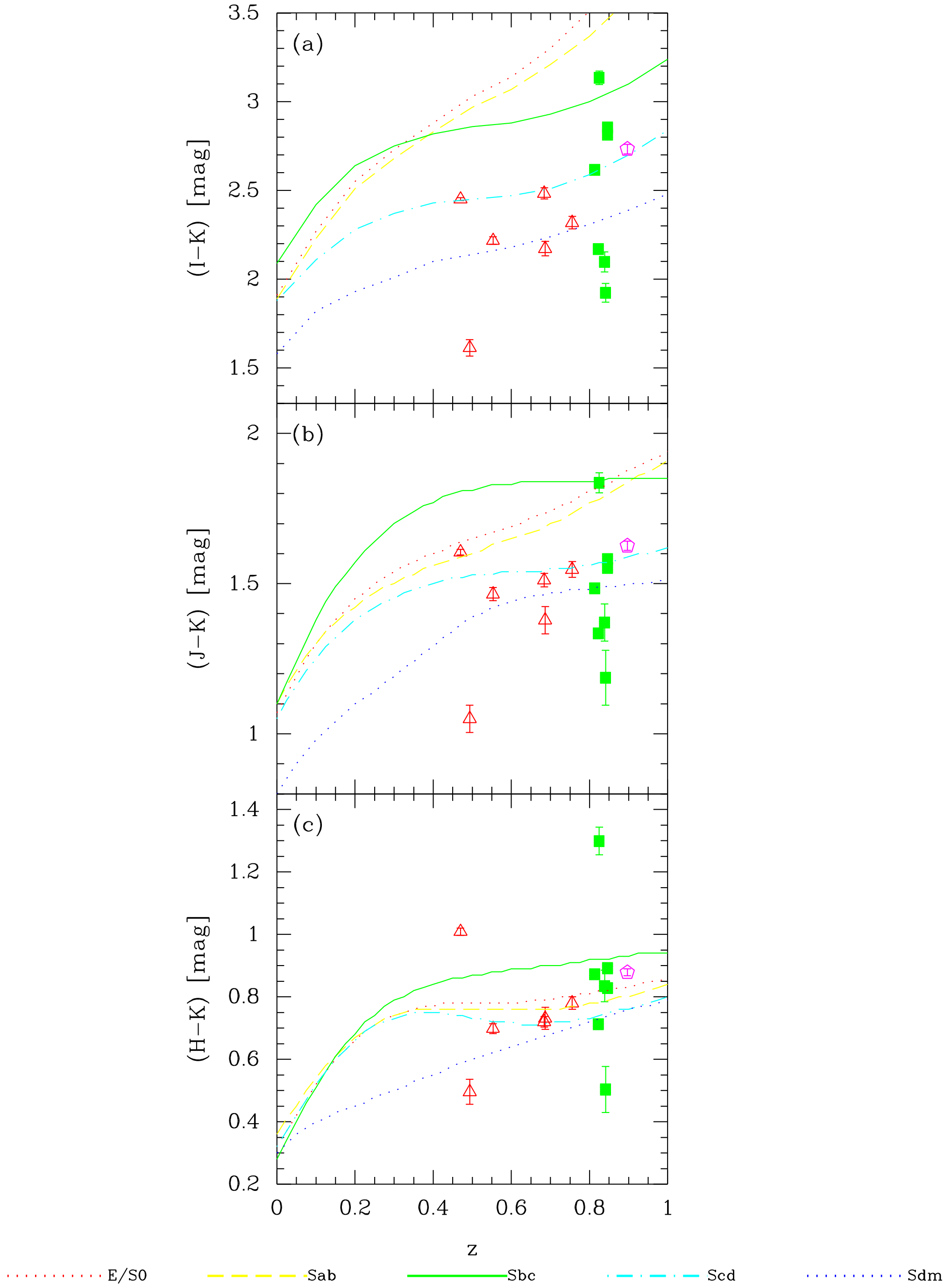

Figure 4.2: NIR and NIR–optical colours versus redshift. The NIR data is from a preliminary reduction of the FIRES data. Local galaxy SEDs are from Coleman et al. (1980), extended into the NIR by Aragón-Salamanca (1991); Aragón-Salamanca et al. (1993). Legend: SEDs, see the figure; galaxies, see Fig. 4.1, p. 79.

The agreement between the NIR colours for the galaxies and the local SEDs (Fig. 4.2) is not as good as for the optical colour (Fig. 4.1). The mild disagreement could be due to calibration problems in these preliminary data, or due to limitations in the way the optical SEDs (spectra) were extended into the NIR by means of broad-band imaging in $J/H/K$ (Aragón-Salamanca 1991; Aragón-Salamanca et al. 1993).

With the NIR data at hand it is possible to transform to several rest frame bands. An obvious choice would be the rest-frame J–band, since this is as red as one can go for our redshifts without having to extrapolate (the observed K–band approximately matches rest-frame J–band at $z \approx 0.8$). However, almost no local Tully–Fisher studies have been done in the J–band. Conversely, a number of local Tully–Fisher studies have been made in the H–band, so we will therefore transform our data to rest-frame H–band, even though that requires some extrapolation. There are certainly many local Tully–Fisher studies in the I–band, but it is interesting to go as red as possible.

The transformation to rest-frame H–band can again be written as $H_{\rm rest} = K_{\rm obs} + \xi'$, where ξ' depends on the SED and on the redshift. In Fig. 4.3(a) ξ' is plotted versus redshift for the 5 local galaxy SEDs. The curves for the 5 SEDs are not in the 'natural' early-to-late order (E/S0 to Sdm) that they were for the corresponding plot for the B–band transformation (this plot is not shown). In panel (b) and (c) ξ' is shown versus the reddest colour available, namely observed-frame $(H - K)$. It is seen that is it not possible to fit a straight line with low scatter to the 4 spiral SEDs (the filled symbols), particularly at $z = 0.85$ (panel c). This is in contrast to the B–band transformation. where such fits could be made at all redshifts with a very low scatter, typically 0.01 mag (these plots are not shown).

Since the available colours were not able to accurately decide the 'fractional' SED to be used, it was decided to use a fixed SED for all the galaxies. The Scd and Sab SEDs are in the middle of the extremes in Fig. 4.3(a). In the redshift range for which we have NIR data, $z = 0.43$–0.90, the ξ' parameter for the Scd SED is in the range 0.86–0.93, i.e. the variation is small. Therefore, to further simplify things the approximation $\xi' = 0.89$ was used for the transformation. The uncertainty on the transformation is probably about 0.2–0.3 mag, as inferred from the SED-to-SED variation in Fig. 4.3(a) and on the level of agreement between the data and the SEDs in the colours (Fig. 4.2).

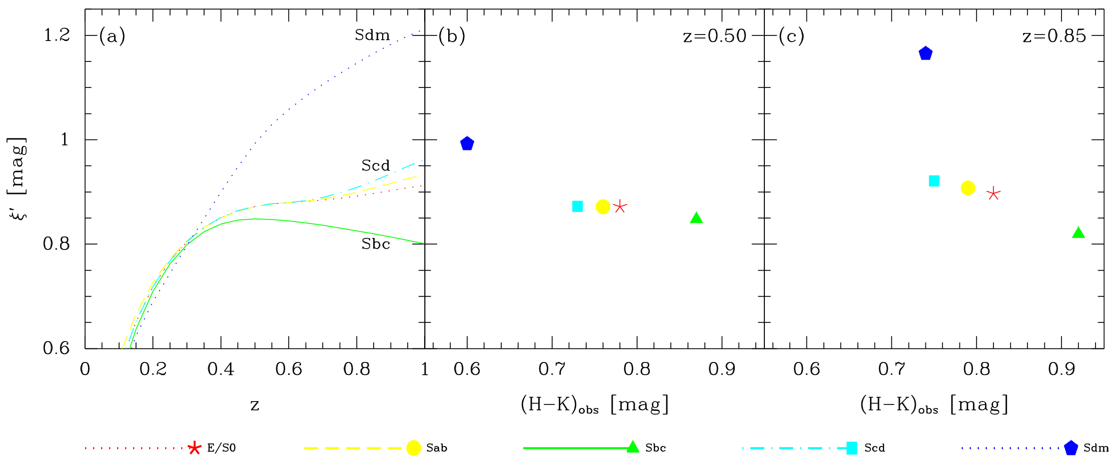

Figure 4.3: The transformation quantity ξ', defined as $H_{\rm rest} = K_{\rm obs} + \xi'$. There is a ξ' for each of the 5 local galaxy SEDs. (a): ξ' versus redshift. (b) and (c): ξ' versus observed $(H - K)$ colour at two particular redshifts. [No data are plotted in this figure.]

4.3 Bulge/disk decomposition

Bulge/disk decomposition was done on the HST images using GIM2D (Simard et al. 2002). The galaxy is modelled as a bulge with a Sérsic (1968) profile and a disk with an exponential profile. The model has a maximum of 12 free parameters: total galaxy intensity, bulge fraction, bulge semimajor effective radius, bulge ellipticity, bulge position angle, disk semimajor exponential scale length, disk inclination, disk position angle, x and y centre of galaxy, background level, and Sérsic index. Following Simard et al. (2002) we kept the Sérsic index frozen at 4, giving the bulge an $r^{1/4}$ profile (cf. de Vaucouleurs 1948). The PSF, modelled using Tiny Tim (Krist 1993), is taken into account, and oversampling is used to deal with the undersampled WFPC2 images. The segmentation images from SExtractor are used to define which pixels belong to which objects. The Metropolis algorithm (Metropolis et al. 1953) is used to find 'best fit' values and 99% confidence intervals. We scaled the corresponding errors down by a factor of 3 to get errors corresponding approximately to the 68% confidence intervals. We ran GIM2D independently on the F814W and F606W images, meaning that e.g. a disk scale length and inclination is available for each filter.

GIM2D also has a few fixed parameters. One of these is the disk internal absorption coefficient $C_{\rm abs}$. Following Simard et al. (2002) we used $C_{\rm abs} = 0$, corresponding to an optically thin disk. The $C_{\rm abs}$ parameter presumably only influences how much flux is assigned to the disk (i.e. it influences the bulge fraction), not the disk scale length and inclination, which is what we are interested in here.

GIM2D has the possibility to "symmetrize" the input images around some pivotal point (i.e. the centre of the galaxy defined in some suitable way) before the image is fitted. This procedure has been used by e.g. Schade et al. (1995), Lilly et al. (1998) and Schade et al. (1999). It was not used in the analysis in Simard et al. (2002), and it was not used here.

It is worth noting that the GIM2D disk semimajor exponential scale length, which we will denote $r_{\rm d,phot}$, is calculated in the same way as $r_{\rm d,spec}$, namely with respect to the semimajor axis.

GIM2D is much easier to use than ELFIT2D, for the following 5 reasons: (1) GIM2D computes sensible initial values and min–max values for some of the parameters using image moments. (2) GIM2D has a so-called "initial conditions filter" which coarsely samples a very large volume of the parameter space (using $N_{\rm ICF}$ points) to get a good starting point for the Metropolis search. (We used $N_{\rm ICF} = 300$.) (3) GIM2D has a criterion for when the "time series" of accepted Metropolis points has reached equilibrium. Points accepted before reaching equilibrium are discarded, and only the $N_{\rm sample}$ points accepted after reaching equilibrium are used to compute the best fit values and their confidence intervals. (4) GIM2D fits the centre of the galaxy, so the user does not have to do that manually and be limited by integer or half-integer pixels. (5) GIM2D measures the background noise in what it determines to be the background regions of the image, so the user does not have to do that manually.

Furthermore, since the HST images have a more well behaved (and probably also lower) noise than the spectral images, using GIM2D was almost *plug and play*: after just one fit per galaxy per filter, a good result was achieved. "Good result" means good-looking model and residual images, and reasonable reduced chi–square values. Given the robustness of the implementation of the Metropolis algorithm (points 1–3 above), the time series were not extracted from the log files and plotted, and different metseeds were not tried. The default value of $N_{\text{sample}} = 300$ was kept.

An atlas of the observed images, model images and residual images is given in Appendix B (pp. 155–186). For the 27 spiral galaxies with rotation velocities, the reduced chi–square values were as follows. In F814W, 25 fits gave $\chi^2_{\text{r}} = 0.99$–1.14, indicating that the fits are good and that there is a small amount of extra structure in the images, typically spiral arms. Galaxy XX1/F16 (Fig. B.17, p. 171) had $\chi^2_{\text{r}} = 1.37$ due to strong spiral arms, and galaxy 1459 (Fig. B.30, p. 184) had $\chi^2_{\text{r}} = 1.42$ due to its strange nature (more on that later). In F606W, 26 fits gave $\chi^2_{\text{r}} = 0.99$–1.32 (i.e. a somewhat broader peak just above 1, but still good). Galaxy XX1/F16 had $\chi^2_{\text{r}} = 1.90$. For the M/P galaxy 1801 the fit was bad, with $\chi^2_{\text{r}} = 1.76$ in F814W, and 2.74 in F606W. As can be seen from Fig. B.27 (p. 181) this galaxy is *not* well matched to the bulge/disk model. GIM2D has fitted a disk (and no bulge) to the two knots.

For the 27 spiral galaxies with rotation velocities, the bulge fractions were in the range 0–0.36 in F814W, and 0–0.38 in F606W. In most of the galaxies no bulge was detected. The disk scale lengths in the two filters were similar. Specifically, $\log(r_{\text{d},814}/r_{\text{d},606})$ was in the narrow range of -0.09 to $+0.01$, except for galaxy 2011 at -0.14 and galaxy 1403 at $+0.04$. The median value was -0.02, and the value was negative for $\sim$80% of the galaxies, meaning that the disks typically get bluer with increasing radius.

The GIM2D disk inclination i (with 90° being edge-on) is calculated from the apparent ellipticity of the disk component, $\varepsilon_{\text{disk}}$, as

$$\cos i = 1 - \varepsilon_{\text{disk}} \quad . \tag{4.1}$$

(This is the equation used in the code; there is a typo in Simard et al. 2002.) This equation assumes that the disk is infinitely thin. In local Tully–Fisher work (e.g. Courteau 1997; Tully & Pierce 2000) people often taken into account the intrinsic flattening ratio q_0 of the disk as

$$(\cos i)^2 = \frac{(1 - \varepsilon_{\text{disk}})^2 - q_0^2}{1 - q_0^2} \tag{4.2}$$

(Holmberg 1958), with q_0 often set to 0.13 or 0.20. As can be seen Eq. (4.2) reduces to Eq. (4.1) for $q_0 = 0$. Using the GIM2D formula, the F814W-based inclinations are in the range 33–82° (median: 70°) for the 27 spiral galaxies with rotation velocities. This corresponds to $\varepsilon_{\text{disk}} = 0.17$–$0.87$. Using $q_0 = 0.13$ gives i = 34–89°. In terms of $\sin i$ the difference is only about 1%, hence negligible. A value of $q_0 = 0.20$ is not meaningful, since that predicts that the apparent ellipticity never exceeds 0.80, which it does for 5 of the galaxies.

SExtractor calculates an ellipticity for the entire galaxy (as opposed to an ellipticity for the disk component). This SExtractor ellipticity (from the F814W images) was converted into an inclination using the GIM2D formula (Eq. 4.1). The SExtractor inclinations are plotted against the GIM2D inclinations in Fig. 4.4(a). The agreement is reasonable, although there are some outliers. We prefer the GIM2D values since they are for the disk only, and since they have error bars. In Fig. 4.4(b) the GIM2D inclinations in the two filters are compared. The F606W-based inclinations are larger (i.e. closer to edge-on) than the F814W-based ones. This is presumably because irregular features such as spiral arms are more prominent in the F606W–band. For the analysis we will use the F814W-based GIM2D inclinations.

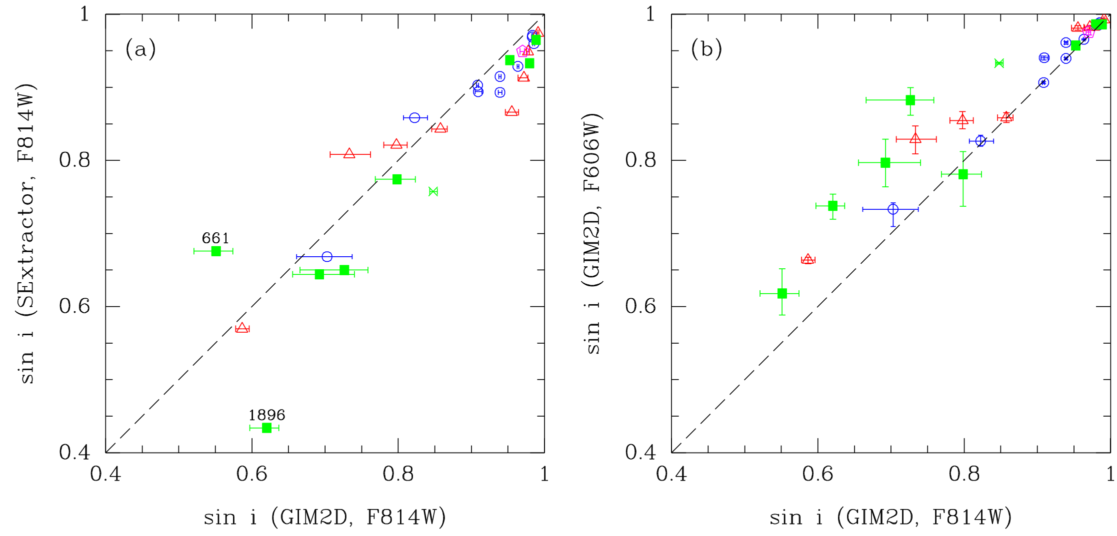

Figure 4.4: Comparison of inclinations. (Legend: see Fig. 4.1, p. 79.)

4.3.1 Correction for internal extinction, B–band

Absolute B magnitudes, M_B, were calculated for the default cosmology ($H_0 = 75$ km s^{-1} Mpc^{-1} and $q_0 = 0.05$). Absolute B magnitudes corrected for internal extinction, M_B^i, were calculated as $M_B^i = M_B - A_B^i$, with the extinction A_B^i given by the formula from Tully & Fouqué (1985),

$$A_B^i = \begin{cases} -2.5 \log \left[f(1 + \mathrm{e}^{-\tau \sec i}) + (1-2f) \left(\frac{1-\mathrm{e}^{-\tau \sec i}}{\tau \sec i} \right) \right] & \text{for } i \leq 80^\circ \\ 0.96\,\mathrm{mag} & \text{for } i \geq 80^\circ \end{cases} , \tag{4.3}$$

with $\tau = 0.55$ and $f = 0.25$. Going from $i = 0^\circ$ (face-on) to $i = 80^\circ$, the extinction increases from 0.27 mag to 0.96 mag, after which is stays constant until $i = 90^\circ$ (edge-on). For our sample A_B^i was in the range 0.32–0.96 mag, with a median value of 0.61 mag.

Tully & Fouqué (1985) write in their summary that the total correction (i.e. Eq. 4.3) is poorly determined, but the correction "to face-on orientation" (i.e. $A_B^i - A_B^{0^\circ}$) is relatively well defined. This has lead to the semantic problem that the "Tully & Fouqué (1985) scheme" can be understood in two ways. The first way is that the internal extinction correction to apply is simply given by Eq. (4.3). This is the correction we will use. The second way is that the internal extinction correction to apply is given by Eq. (4.3) *minus the face-on extinction*, i.e.

$$\begin{aligned} \widetilde{A_B^i} &\equiv A_B^i - A_B^{0^\circ} \\ &= A_B^i - 0.27\,\mathrm{mag} \ , \end{aligned} \tag{4.4}$$

where the tilde is our notation. I.e., in this way the face-on extinction is *not* corrected for. This is the method used by Pierce & Tully (1992).

Regardless of the issue of the face-on extinction, we chose to use the Tully & Fouqué (1985) formula simply because that was what Vogt and collaborators used, who in turn chose it because they use the local Tully–Fisher relation from Pierce & Tully (1992). It should be noted, however, that the later study of Tully et al. (1998) has found that the internal extinction is a function of the luminosity of the galaxy, in such a way that the extinction in high luminosity galaxies is substantially higher than that in low luminosity ones. This correlation obviously changes the derived slope of the Tully–Fisher relation. For our study it is not critical that the "true" internal extinction correction is used, but that the same scheme is used for the local Tully–Fisher relation and for our high redshift galaxies.

4.3.2 Correction for internal extinction, H–band

In the H–band we will also use the local Tully–Fisher relation from Pierce & Tully (1992), and consequently we will also use the Tully & Fouqué (1985) formula to correct for internal extinction in this band. The internal extinction in the H–band is simply given by

$$A^i_H = 0.10 A^i_B \tag{4.5}$$

(Pierce & Tully 1992, footnote to Table 1), where A^i_B is given by Eq. (4.3). From this it follows that the face-on extinction is the H–band is a mere 0.027 mag, which like for the B–band can be corrected for or not.

4.3.3 Deprojection of the rotation velocities

Deprojected rotation velocities were calculated as

$$V_{\rm rot} = \frac{\overbrace{V_{\rm rot}\sin i}^{\text{from VLT spectra}}}{\underbrace{\sin i}_{\text{from HST images}}} \quad . \tag{4.6}$$

The uncertainties on i were included in the uncertainties on $V_{\rm rot}$. Specifically, the positive error bar on $V_{\rm rot}$ was calculated using the positive error bar on $V_{\rm rot}\sin i$ and the negative error bar on $\sin i$, and vice versa.

4.3.4 Summary tables

Key photometric quantities are given in Table 4.1 and 4.2. The deprojected rotation velocities for the 4–times oversampled URC fits are also given.

Table 4.1: Photometric data

z	name2	alt.[a]	F606W [mag]	σ [mag]	F814W [mag]	σ [mag]	Js [mag]	σ [mag]	H [mag]	σ [mag]	Ks [mag]	σ [mag]	$B_{\rm rest}$ [mag]	A^i_B [mag]	$M^i_{B,\rm rest}$ [mag]	$H_{\rm rest}$ [mag]	$M^i_{H,\rm rest}$ [mag]
0.1538	Z	F01	21.34	0.01	20.48	0.01	–	–	–	–	–	–	22.06	0.77	−17.80	–	–
0.1805	XX6	F02	19.85	0.00	19.00	0.01	–	–	–	–	–	–	20.53	0.60	−19.55	–	–
0.2172	A	F03	22.03	0.02	21.42	0.03	–	–	–	–	–	–	22.59	0.44	−17.76	–	–
0.2297	V	F04	21.78	0.02	21.17	0.02	–	–	–	–	–	–	22.33	0.96	−18.67	–	–
0.2495	G	F05	21.86	0.01	21.05	0.02	–	–	–	–	–	–	22.44	0.95	−18.74	–	–
0.2594	A4	F06	20.55	0.01	19.74	0.01	–	–	–	–	–	–	21.12	0.90	−20.11	–	–
0.2640	C	F07	21.62	0.01	20.68	0.01	–	–	–	–	–	–	22.20	0.65	−18.82	–	–
0.2870	U	F08	21.50	0.01	20.60	0.01	–	–	–	–	–	–	22.05	0.57	−19.09	–	–
0.3232	P	F09	22.48	0.02	21.46	0.02	–	–	–	–	–	–	22.98	0.94	−18.83	–	–
0.3237	A7	F10	21.46	0.01	20.45	0.01	–	–	–	–	–	–	21.95	0.65	−19.56	–	–
0.3246	N	F11	21.51	0.01	20.88	0.02	–	–	–	–	–	–	22.02	0.37	−19.22	–	–
0.3253	XX4	F12	20.27	0.01	19.13	0.01	–	–	–	–	–	–	20.76	0.56	−20.68	–	–
0.3737	B5	F13	22.87	0.03	22.03	0.03	–	–	–	–	–	–	23.32	0.96	−18.86	–	–
0.4290	C2	F14	23.81	0.03	23.19	0.04	–	–	–	–	–	–	24.27	0.82	−18.12	–	–
0.4694	D	F15	23.64	0.04	22.78	0.04	–	–	–	–	–	–	24.00	0.72	−18.51	–	–
0.4700	XX1	F16	20.53	0.01	19.64	0.01	18.75	0.01	18.15	0.01	17.14	0.00	20.87	0.33	−21.25	18.03	−23.80
0.4936	C6	F17	23.09	0.03	22.22	0.04	21.61	0.03	21.05	0.03	20.56	0.03	23.43	0.42	−18.92	21.45	−20.52
0.5530	Y	F18	22.16	0.02	21.20	0.02	20.40	0.02	19.63	0.01	18.93	0.01	22.42	0.48	−20.27	19.82	−22.44
0.6841	D2	F19	22.95	0.03	21.87	0.03	20.84	0.02	20.05	0.01	19.33	0.01	23.08	0.88	−20.58	20.22	−22.64
0.6865	B4	F20	23.31	0.03	22.27	0.03	21.43	0.04	20.78	0.03	20.05	0.02	23.48	0.96	−20.27	20.94	−21.95
0.7558	D6	F21	22.72	0.04	21.35	0.03	20.53	0.02	19.77	0.02	18.99	0.01	22.54	0.38	−20.88	19.88	−23.21
0.8132	1403	1403	21.53	0.02	20.04	0.01	18.86	0.01	18.24	0.00	17.37	0.00	21.17	0.71	−22.78	18.26	−25.05
0.8224	1896	1896	22.27	0.03	20.96	0.02	20.07	0.01	19.45	0.01	18.74	0.01	22.10	0.34	−21.51	19.63	−23.68
0.8245	2130	2130	23.46	0.07	21.78	0.04	20.43	0.03	19.89	0.04	18.59	0.01	22.88	0.42	−20.83	19.48	−23.84
0.8280	A8	C01	23.36	0.05	22.25	0.04	–	–	–	–	–	–	23.41	0.96	−20.85	–	–
0.8328	1801	1801	21.25	0.01	20.36	0.01	–	–	–	–	–	–	21.55	0.47	−22.23	–	–
0.8384	1763	1763	23.96	0.06	22.68	0.05	21.90	0.05	21.36	0.04	20.53	0.03	23.81	0.36	−19.88	21.42	−21.95
0.8411	2011	2011	23.24	0.04	22.09	0.03	21.30	0.08	20.62	0.06	20.11	0.04	23.23	0.38	−20.48	21.00	−22.37
0.8459	1459	1459	22.33	0.02	20.61	0.01	19.26	0.01	18.60	0.01	17.71	0.00	21.67	0.90	−22.58	18.60	−24.84
0.8462	661	661	22.36	0.03	20.96	0.02	19.68	0.01	18.93	0.01	18.10	0.01	22.07	0.32	−21.60	18.99	−24.40
0.8965	B1	F22	22.30	0.04	20.84	0.03	19.68	0.01	18.94	0.01	18.06	0.01	21.89	0.81	−22.44	18.95	−24.65

"σ" denotes a symmetric error bar. As error bar for $B_{\rm rest}$ and $M^i_{B,\rm rest}$ use that of F814W. As error bar for $H_{\rm rest}$ and $M^i_{H,\rm rest}$ use that of $K_{\rm s}$.

[a] Name used in Milvang-Jensen et al. (2003)

Table 4.2: Photometric data and deprojected rotation velocities

z	name	alt.[a]	RA (J2000)	Dec (J2000)	(B/T)	σ_-	σ_+	$r_{\rm d,phot}$ [$''$]	σ_- [$''$]	σ_+ [$''$]	$r_{\rm d,phot}$ [kpc]	σ_- [kpc]	σ_+ [kpc]	i [°]	σ_- [°]	σ_+ [°]	$V_{\rm rot}$ km/s	σ_- km/s	σ_+ km/s
0.1538	Z	F01	10:57:06.2	−3:39:02	0.00	0.00	0.00	0.50	0.00	0.01	1.20	0.01	0.01	74.5	0.2	0.3	76.1	2.5	3.8
0.1805	XX6	F02	10:56:48.3	−3:37:33	0.21	0.04	0.05	0.55	0.01	0.00	1.51	0.02	0.01	67.6	0.7	0.7	107.1	1.4	1.1
0.2172	A	F03	10:57:02.7	−3:34:54	0.00	0.00	0.01	0.55	0.02	0.02	1.74	0.05	0.05	55.3	1.5	1.8	24.0	22.8	20.4
0.2297	V	F04	10:56:56.0	−3:37:28	0.00	0.00	0.01	0.73	0.02	0.01	2.39	0.05	0.05	80.1	0.4	0.3	56.8	8.6	7.4
0.2495	G	F05	10:57:01.3	−3:35:44	0.07	0.01	0.01	0.73	0.01	0.02	2.52	0.04	0.06	79.6	0.3	0.2	118.0	6.7	6.0
0.2594	A4	F06	10:56:53.0	−3:38:41	0.00	0.00	0.00	0.91	0.01	0.01	3.24	0.02	0.02	78.4	0.1	0.1	107.1	1.3	1.4
0.2640	C	F07	10:57:01.2	−3:34:37	0.23	0.01	0.02	0.46	0.01	0.01	1.65	0.03	0.03	69.9	0.4	0.4	148.0	12.1	13.0
0.2870	U	F08	10:57:08.2	−3:37:34	0.25	0.01	0.01	0.52	0.01	0.01	1.98	0.04	0.05	65.4	0.6	0.7	114.0	5.9	6.2
0.3232	P	F09	10:57:06.3	−3:36:49	0.00	0.00	0.00	0.54	0.01	0.01	2.23	0.04	0.03	79.5	0.3	0.3	156.5	32.5	31.0
0.3237	A7	F10	10:57:12.3	−3:37:17	0.00	0.00	0.00	0.54	0.00	0.01	2.24	0.02	0.03	69.9	0.3	0.3	103.2	8.2	7.1
0.3246	N	F11	10:57:08.2	−3:36:42	0.36	0.03	0.03	0.51	0.02	0.02	2.11	0.07	0.09	44.6	3.3	2.8	105.3	6.2	7.1
0.3253	XX4	F12	10:57:11.5	−3:36:44	0.03	0.00	0.00	0.83	0.00	0.01	3.44	0.02	0.02	65.3	0.2	0.2	260.4	8.4	10.7
0.3737	B5	F13	10:57:02.1	−3:38:32	0.00	0.00	0.01	0.42	0.01	0.01	1.89	0.04	0.05	80.3	0.6	0.4	83.2	18.3	21.3
0.4290	C2	F14	10:56:54.7	−3:39:00	0.11	0.04	0.04	0.25	0.02	0.03	1.20	0.10	0.15	76.3	1.8	1.5	79.3	8.1	6.4
0.4694	D	F15	10:57:06.9	−3:35:29	0.03	0.01	0.05	0.20	0.01	0.01	1.04	0.06	0.08	72.8	1.6	1.9	102.0	44.9	18.7
0.4700	XX1	F16	10:57:01.2	−3:34:20	0.00	0.00	0.00	0.55	0.00	0.00	2.85	0.01	0.01	35.9	0.6	0.7	189.8	3.8	3.1
0.4936	C6	F17	10:56:52.0	−3:37:01	0.00	0.00	0.00	0.31	0.01	0.01	1.64	0.05	0.06	52.9	1.6	1.4	161.4	7.9	9.1
0.5530	Y	F18	10:57:03.7	−3:38:33	0.06	0.01	0.01	0.40	0.01	0.01	2.21	0.05	0.05	59.1	1.3	1.1	143.8	5.2	4.7
0.6841	D2	F19	10:56:50.7	−3:35:39	0.00	0.00	0.00	0.45	0.01	0.01	2.79	0.07	0.07	77.8	0.6	0.5	147.8	6.4	8.9
0.6865	B4	F20	10:57:05.7	−3:36:26	0.00	0.00	0.02	0.42	0.01	0.01	2.58	0.07	0.08	82.4	0.5	0.4	132.2	11.2	10.5
0.7558	D6	F21	10:56:48.6	−3:35:42	0.00	0.00	0.01	0.60	0.02	0.02	3.81	0.10	0.12	47.2	2.2	2.5	191.7	22.2	19.2
0.8132	1403	1403	10:57:03.8	−3:37:43	0.00	0.00	0.00	1.16	0.01	0.01	7.65	0.09	0.09	72.3	0.3	0.3	284.3	13.3	8.4
0.8224	1896	1896	10:56:51.3	−3:36:11	0.01	0.00	0.00	0.55	0.01	0.01	3.60	0.08	0.09	38.4	1.7	1.2	95.1	3.9	6.2
0.8245	2130	2130	10:57:03.9	−3:35:07	0.00	0.00	0.02	0.43	0.02	0.02	2.84	0.10	0.13	53.0	2.7	2.5	182.6	47.9	56.7
0.8280	A8	C01	10:57:12.0	−3:36:50	0.00	0.00	0.02	0.59	0.02	0.03	3.93	0.16	0.19	81.3	0.6	0.6	130.1	8.2	10.5
0.8328	1801	1801	10:56:59.5	−3:36:32	0.00	0.00	0.00	0.45	0.00	0.00	2.98	0.03	0.03	58.0	0.5	0.6	173.4	1.2	1.0
0.8384	1763	1763	10:57:06.5	−3:36:40	0.04	0.01	0.05	0.23	0.01	0.02	1.51	0.07	0.12	43.8	2.9	3.9	136.4	44.5	43.5
0.8411	2011	2011	10:57:07.1	−3:35:40	0.22	0.03	0.03	0.23	0.01	0.02	1.51	0.07	0.13	46.6	4.8	2.7	116.8	9.2	12.8
0.8459	1459	1459	10:56:59.6	−3:37:29	0.00	0.00	0.00	0.47	0.00	0.01	3.11	0.03	0.04	78.4	0.2	0.2	9.8	5.4	4.6
0.8462	661	661	10:56:56.4	−3:39:11	0.00	0.00	0.02	0.45	0.01	0.01	3.00	0.06	0.05	33.4	2.1	1.6	129.3	39.6	51.8
0.8965	B1	F22	10:57:07.8	−3:37:04	0.11	0.01	0.01	1.50	0.07	0.07	10.19	0.49	0.46	76.0	0.8	0.6	243.1	4.1	3.9

The coordinates given have systematic uncertainties at the level of a few arcsec (they have been derived from the WCS in the WFPC2 headers). The bulge-to-total fractions and the photometric disk scale lengths (in arcsec and kpc) are from the F814W images (data for F606W not given). "σ" denotes a symmetric error bar, and "σ_-" and "σ_+" denote asymmetric error bars. [a] Name used in Milvang-Jensen et al. (2003)

(page left blank to get matching page numbers for single and double sided versions)

Chapter 5

Analysis

5.1 The B–band Tully–Fisher relation

The main aim of this section is to compare high redshift cluster spirals with high redshift field spirals in the Tully–Fisher plot of rotation velocity versus luminosity. Since we only have a small number of galaxies, it is not possible to accurately determine the slope of the Tully–Fisher relation (TFR, Tully & Fisher 1977) from the high redshift galaxies themselves, so we will use the slope from a local relation. The zero point of the local relation has little importance for the intercomparison at high redshift.

Many studies of the local B–band TFR have been made. Vogt and collaborators (e.g. Vogt et al. 1996, 1997; Vogt 1999, 2001) used the local TFR from Pierce & Tully (1992) as the local reference, and we will do the same. Pierce & Tully (1992) found the local B–band TFR for field spirals to be

$$\widetilde{M_B^{b,i}} = -7.48(\log W_R^i - 2.50) - 19.55 \quad . \tag{5.1}$$

$\widetilde{M_B^{b,i}}$ is the absolute B–band magnitude corrected for Galactic extinction, and corrected for internal extinction using the Tully & Fouqué (1985) formula, but without correcting for the face-on extinction. Since we *do* correct our galaxy magnitudes for the face-on extinction of 0.27 mag, the Pierce & Tully (1992) TFR becomes

$$M_B^i + 0.27 = -7.48(\log W_R^i - 2.50) - 19.55 \quad , \tag{5.2}$$

where we have dropped the superscript "b" since we are ignoring Galactic extinction, cf. the discussion on p. 79. W_R^i is the HI line-width corrected for inclination and turbulence following Tully & Fouqué (1985). This quantity is "statistically equal to twice the maximum rotation velocity" (Tully & Fouqué 1985), and hence we transform W_R^i to V_{rot} (i.e. the rotation velocity derived from optical emission lines) using

$$W_R^i = 2V_{\mathrm{rot}} \quad , \tag{5.3}$$

which has also been used by Vogt and collaborators (Vogt, private communication). Equation (5.3) is an approximation (cf. Simard & Pritchet 1998); however, Vogt et al. (1996) state that the error is small ($\lesssim 15\,\mathrm{km\,s^{-1}}$). A good agreement between HI line-widths and rotation velocities derived from spatially resolved optical emission lines was also found by Raychaudhury et al. (1997) and Kobulnicky & Gebhardt (2000). By combining Eq. (5.2) and Eq. (5.3) we get the local (field spiral) B–band Tully–Fisher relation we will use as reference,

$$M_B^i = -7.48 \log V_{\rm rot} - 3.37 \ . \tag{5.4}$$

It should be mentioned that in our *Letter* (Milvang-Jensen et al. 2003) we missed the point that Pierce & Tully (1992) did not correct for the face-on internal extinction (which is 0.27 mag in the Tully & Fouqué 1985 model), but only for the differential internal extinction between a galaxy seen at some inclination i and a galaxy seen face-on. Therefore, the local B–band TFR used in the *Letter* had a zero point of -3.10 rather than -3.37.[1] The consequences will be pointed out below.

As outlined above, the approach here in the thesis is to correct for the entire internal extinction predicted by the Tully & Fouqué (1985) model, i.e. both for the differential extinction with respect to a galaxy seen face-on *and* for the face-on extinction. This scheme is used both for the observed magnitudes and for the local TFR. In the *Letter* the observed magnitudes were also corrected for the face-on extinction. Therefore, in principle the M_B^i values in the *Letter* should be identical to those in the thesis. However, after the *Letter* was published a minor problem (due to a bug in the `trebin` task) was found in the transformation to rest-frame B–band. The correct transformation has been used for the magnitudes presented here; they are 0.02–0.13 mag fainter than those in the *Letter* (the effect is the largest at high redshift).

Our Tully–Fisher plot is shown in Fig. 5.1(a). The rotation velocities are those derived using the Universal intrinsic rotation curve (Persic & Salucci 1991) and 4–times spectral oversampling. The local TFR (Eq. 5.4) is shown as the solid line. Different plot symbols have been used for the field spirals in 3 redshift bins, the cluster spirals, and the cluster Merger/Peculiar galaxy 1801. Two galaxies deviate strongly from the rest. The cluster galaxy 1459 is completely off the scale of the plot. The determined rotation velocity is only $9.8^{+4.6}_{-5.4}\,{\rm km\,s^{-1}}$, compatible with zero. The galaxy, classified as Sc by van Dokkum (1999), has a peculiar morphology (see p. 184), probably due to dust at the centre. The galaxy was detected at 5 GHz by Best et al. (2002). When comparing the radio flux with the [OII] flux, Best et al. concluded that galaxy 1459 was a clear AGN[2]. This explains the problem: the detected (faint) [OII] emission comes from the (obscured) AGN, not from the disk. The derived gas scale length is $r_{\rm d,spec} = 0.04^{+0.25}_{-0.04}\,{\rm kpc}$, which is compatible with zero, also indicating a nuclear source (cf. Simard & Pritchet 1998). Galaxy 1459 will be excluded from the analysis. Galaxy A/F03 ($z = 0.22$) deviates somewhat from the rest of the galaxies. This galaxy has the lowest surface brightness in the sample, although not by a large margin. We will exclude this galaxy from the analysis. The M/P cluster galaxy 1801 ($z = 0.83$), on the other hand, does not deviate from the cluster spiral galaxies. However, it is not clear whether the measured $V_{\rm rot} \sin i$ originates from a rotating disk or the motion of the two knots. Furthermore, as previously mentioned the GIM2D fit for this galaxy was

[1] Apparently, this point was also missed by Vogt et al. (1996): these authors must have used the Tully & Fouqué (1985) scheme in the way that *does* correct for the face-on extinction, since their listed B–band extinction values go all the way up to 0.96 mag. On the other hand, the Pierce & Tully (1992) local TFR used by Vogt et al. had a zero point of -3.10, corresponding to *not* correcting for the face-on extinction. What Vogt (1999) did for her larger sample of $\sim$100 galaxies is not clear. It can be seen from her plot that the local TFR has a zero point of -3.10, but it is of course possible that the galaxy magnitudes had been corrected accordingly.

[2] The only other cluster galaxy from our sample which was detected by Best et al. (2002) is galaxy 1403, which was found to be a clear star-forming galaxy.

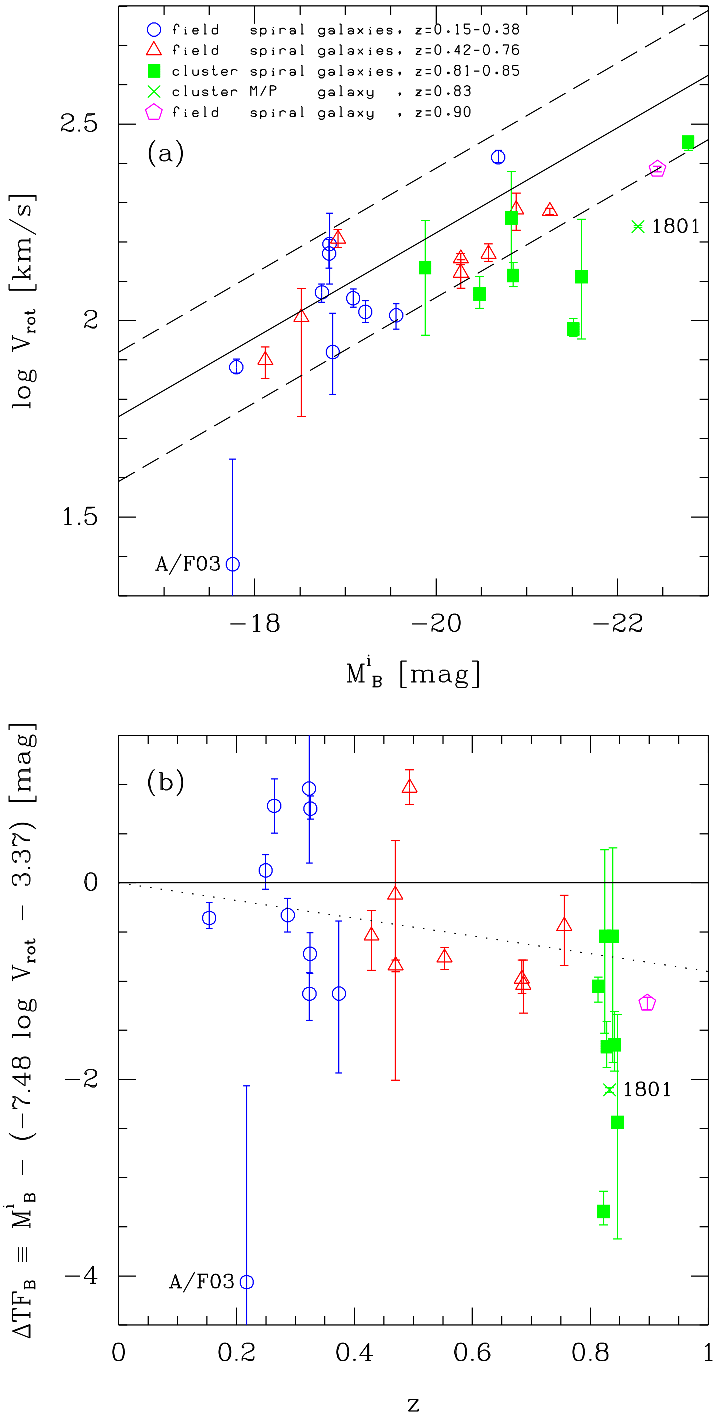

Figure 5.1: (a) High redshift cluster and field B–band Tully–Fisher relation. The solid line is the local Tully–Fisher relation from Pierce & Tully (1992), see Eq. (5.4), and the dashed lines mark the 3σ limits (with σ being the reported dispersion of 0.41 mag). Internal extinction has been consistently corrected for (following Tully & Fouqué 1985, with the correction for the face-on extinction included). Error bars on M_B^i are not shown since they are smaller than the plot symbols. Galaxy 1459 (the AGN) is off the scale of the plot at $(M_B^i, \log V_{\rm rot}) = (-22.6, 0.99)$.
(b) Residuals from the local Tully–Fisher relation versus redshift. The dotted line is a fit to the field galaxies (except galaxy A/F03), see Eq. (5.5).

bad, with the disk component being fitted to the two knots (see p. 181), making the inclination correction less meaningful. We will exclude this galaxy from the analysis.

Most of the high redshift galaxies are seen to fall on the high luminosity/low velocity side of the used local TFR in the TF plot (Fig. 5.1a). The residuals from the local B–band TFR in the absolute magnitude direction, which we will denote $\Delta\mathrm{TF}_B$, are plotted against redshift in Fig. 5.1(b). The residuals could also have been calculated in the $\log V_{\mathrm{rot}}$ direction, but our working hypothesis is that possible differences between cluster and field galaxies are due to a change in luminosity. Further down in this section we will discuss if differences instead could be caused by errors in the derived rotation velocities.

As can be seen from Fig. 5.1(b) there is a hint that the Tully–Fisher residuals for the field galaxies become more negative with increasing z. A Kendall's tau rank order correlation test (e.g. Press et al. 1992) detects such a correlation at 93% significance. Out of curiosity, we will fit the simple model $\Delta\mathrm{TF}_B = az$ to the field galaxy points. We will assume that the errors in $\Delta\mathrm{TF}_B$ are the individual measurement errors plus 0.6 mag added in quadrature. This latter number represents the intrinsic scatter in the B–band TFR for this redshift range. It has been reverse engineered to give a reduced chi–square of 1 for the fit. The chi-square fit is

$$\Delta\mathrm{TF}_B = (-0.9 \pm 0.3)z \quad , \tag{5.5}$$

which is shown as the dotted line in Fig. 5.1(b). If the intercept is also fitted, the result is $\Delta\mathrm{TF}_B = (-1.6 \pm 0.8)z + (0.4 \pm 0.4)$. This is in agreement with the result from the rank order test that the correlation is significant at the $\sim$2 sigma level. If Eq. (5.5) is taken at face value and interpreted as luminosity evolution, the effect is ~ 0.5 mag at $z = 0.5$, somewhat larger than the ~ 0.2 mag Vogt (1999) found at similar redshifts, but compatible with what Barden et al. (2003) find, cf. below. (Note: In the *Letter* we incorrectly derived an effect of ~ 0.8 mag.) This interpretation assumes a non-evolving TFR slope, which is important since our field sample has a built-in positive correlation between luminosity and redshift. Our sample does not allow us to constrain the TFR slope, but Ziegler et al. (2002) found some evidence for a slope change at $z \sim 0.5$ for a sample of 60 field spirals. The interpretation also assumes that we have used the correct cosmology to calculate the absolute magnitudes of the high redshift galaxies, since the local TFR is an absolute calibration, and therefore independent of H_0. A correct absolute calibration of the local TFR (based on a six galaxies with independent distance determinations in this case) is also assumed. The interpretation also assumes that selection effects do not introduce correlations with redshift. Since a certain emission line flux is needed in order to measure the rotation velocity, one concern is that the high z galaxies could have higher star formation rates, which could offset them from the TFR, cf. Kannappan et al. (2002b). If this effect is taken into account for the Vogt sample, one finds that the high z spirals are slightly *fainter* than the $z = 0$ ones, see Kannappan et al. (2002a). Thus, the derived luminosity evolution of the field spirals must be regarded with extreme caution.

It should also be noted that if we use the rotation velocities derived using the flat rather than the Universal intrinsic rotation curve (both using 4–times oversampling), the correlation between the B–band Tully–Fisher residuals and redshift has a lower significance, namely 69%. This is because the rotation velocities for the low luminosity galaxies are lower when using the flat rotation curve (see Fig. 3.11, p. 68), and because the low luminosity galaxies in the sample are mainly at low redshift. A linear fit of slope and intercept gives $\Delta\mathrm{TF}_B = (-1.0 \pm 0.8)z - (0.3 \pm 0.4)$, restating that no significant trend with redshift is found. Since the Universal rotation curve has observational support from the rotation curves of local spirals (Persic & Salucci 1991), we will use this in the analysis. In any case, in the analysis we will focus on an *internal* comparison between our cluster spirals and our field spirals, meaning that the same assumed intrinsic rotation curve will be used for the two samples.

In order to compare the cluster and field spirals, we will use a constant TFR slope equal to the local value from Pierce & Tully (1992). We will make this comparison under two alternative (and extreme) hypotheses. First, we will assume that the zero point of the field TFR does not evolve with z and compare the residuals from the local TFR ($\Delta\mathrm{TF}_B$) for the field and cluster spirals. Second, we will assume that the zero point of the field TFR evolves with z as given by Eq. (5.5), and compare the residuals from the local TFR corrected for this evolution, $\Delta\mathrm{TF}_{B,\mathrm{corr}} \equiv \Delta\mathrm{TF}_B - (-0.9z)$. In both cases we compare the cluster sample ($N_{\mathrm{clus}} = 7$) with the full field sample ($N_{\mathrm{field}} = 18$) and a field subsample spanning the luminosity range of the cluster galaxies ($M_B^i < -19.8$; $N_{\mathrm{field}} = 7$). Two statistical tests are carried out, a simple difference of the mean values (assuming rms/$\sqrt{N}$ uncertainties) and a Kolmogorov–Smirnov (K–S) test. For comparison purposes, the K–S probability that the field and cluster samples are drawn from two different populations has been translated into a number of sigmas for a normal distribution. The results of these comparisons are given in Table 5.1. What is seen is that on average the cluster spirals are found to be brighter than the field galaxies. The difference is slightly larger and more significant when using the first assumption, but it is clear that the data suggest the cluster spirals are ∼1 mag brighter in B than the field ones at a fixed rotation velocity. (The numbers in Table 5.1 are similar to those in our *Letter*.) It should be emphasized that the reference field sample was observed simultaneously with the cluster sample, using the same instrumental setup, and the subsequent data reduction was also identical for the two samples. Therefore, possible systematic errors in e.g. the derived rotation velocities will affect the cluster and the field galaxies in the same way.

Table 5.1: Tully–Fisher differences: cluster versus field

Assumption	Variable	Field sample	$\langle$cluster$\rangle - \langle$field$\rangle$ [mag]	$P^{\mathrm{K–S}}_{\mathrm{diff.\ distr.}}$
TF z.p. does not evolve	$\Delta\mathrm{TF}_B$	All	-1.27 ± 0.43 (3.0σ)	96% (2.0σ)
TF z.p. does not evolve	$\Delta\mathrm{TF}_B$	High L	-0.96 ± 0.46 (2.1σ)	87% (1.5σ)
TF z.p. evolves as Eq. (5.5)	$\Delta\mathrm{TF}_{B,\mathrm{corr}}$	All	-0.93 ± 0.42 (2.2σ)	96% (2.0σ)
TF z.p. evolves as Eq. (5.5)	$\Delta\mathrm{TF}_{B,\mathrm{corr}}$	High L	-0.77 ± 0.44 (1.8σ)	87% (1.5σ)

Only two other studies have been published (both as conference proceedings) on the Tully–Fisher relation for high redshift cluster spirals. Metevier et al. (2002) found a larger TFR scatter for 7 cluster spirals at $z = 0.39$, but no evidence for a zero point or slope change. Ziegler et al. (2003) found no difference between cluster and field spirals in terms of TF zero point and scatter, based on 7 cluster spirals at $z = 0.30$ and 5 cluster spirals at $z = 0.51$. The larger look-back-time of our study could explain the fact that we do find some luminosity evolution. Interestingly, Ziegler et al. (2003) found that almost half of their observed spirals showed peculiar kinematics, and hence could not be used for the Tully–Fisher analysis. In our study, only 1 spiral galaxy out of 30 was excluded due to peculiar kinematics, and 2 were excluded due to non-exponential intensity profiles (cf. Sect. 3.3.2, p. 66).

The difference we find (at the 1.5–2σ level) between the cluster and the field spirals in the Tully–Fisher plot could alternatively be explained as due to a difference in rotation velocity. This difference could in turn be a physical difference or be caused by errors. One worry could be that the gas disks in the cluster spirals were truncated, e.g. due to the interaction with the intra-cluster medium (ICM). If one was deriving the rotation velocity by measuring the velocity of the outmost detected emission, such a truncation could clearly bias the derived rotation velocity downwards. In our scheme where the rotation velocity is derived from a maximum likelihood fit of a model 2D spectrum to the observed 2D spectrum, it is less clear what the effect of such a truncation would be, since it would mean that the assumed model (i.e. an untruncated exponential gas disk) was incorrect. However, we can still address the question as follows. The fit to the observed spectrum gives the exponential scale length for the *gas* that gives rise to the emission line, $r_{\rm d,spec}$. It is conceivable that if the gas disk is truncated, the derived value of $r_{\rm d,spec}$ will be smaller than if the disk had not been truncated. We can compare the derived value of $r_{\rm d,spec}$ with the exponential scale length for the disk component in the broad band images, $r_{\rm d,phot}$, which mainly measures the scale length for the *stars*. Note that $r_{\rm d,phot}$ is *not* used as an input to the spectral fit in the method we use. An interaction with the ICM that might cause a truncation of the gas disk would probably leave the stellar disk largely unaffected. In this picture, such a truncation of the gas disk should show up as low values of $r_{\rm d,spec}/r_{\rm d,phot}$. Followingly, if the negative Tully–Fisher residuals reflected rotation velocities that were biased low by this process, we would expect the Tully–Fisher residuals to be positively correlated with $r_{\rm d,spec}/r_{\rm d,phot}$. In Fig. 5.2 we plot the Tully–Fisher residuals versus $r_{\rm d,spec}/r_{\rm d,phot}$, and the before-mentioned trend is not seen. If anything, there is a hint of a correlation in the opposite direction, but this is not significant, cf. the correlation probabilities given on the figure. How $r_{\rm d,spec}$ compares to $r_{\rm d,phot}$ will be further discussed in Sect. 5.4.

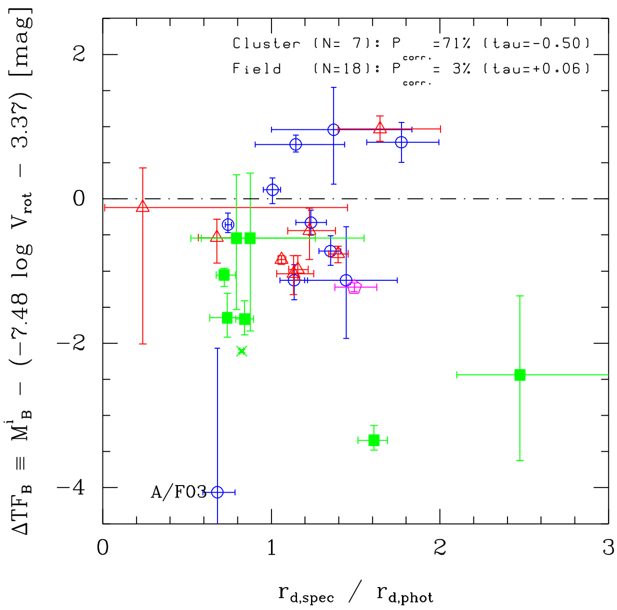

Figure 5.2: Tully–Fisher residuals versus the scale length for the gas (from the spectra) over the scale length for the stars (from the F814W images). Results from Kendall's tau tests are given on the panel. No significant correlations are found. (Legend: see Fig. 5.1, p. 91.)

Another test is to plot the Tully–Fisher residuals versus the used inclination (which is derived from the apparent ellipticity of the disk component in the F814W images, assuming that the disk intrinsically is circular and of negligible thickness). This is done in Fig. 5.3. No significant trends are found, although it is noteworthy that the two cluster spirals with the most negative Tully–Fisher residuals have low inclinations, i.e. are relatively close to face-on.

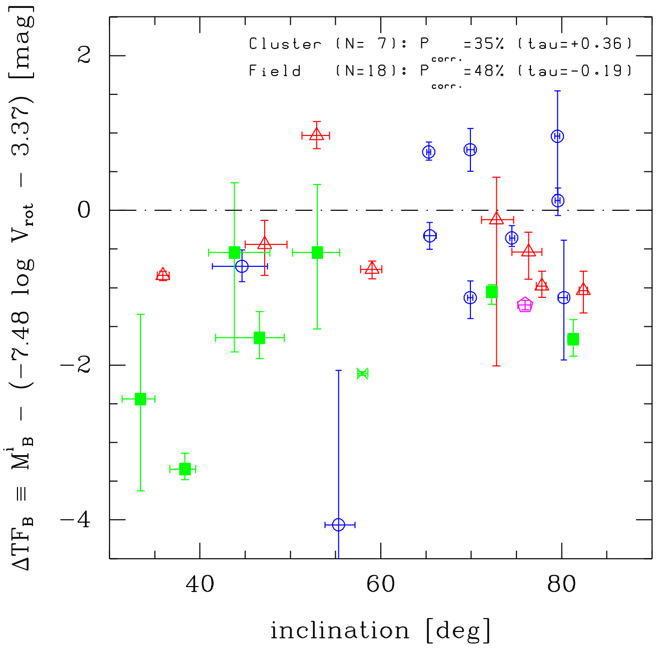

Figure 5.3: Tully–Fisher residuals versus inclination. Results from Kendall's tests are given on the panel. No significant correlations are found. (Legend: see Fig. 5.1, p. 91.)

Selection effects are also a possible concern. As described in Sect. 2.1, the cluster and the field sample were not selected in exactly the same way. The vast majority of the cluster sample used in the analysis (namely 6 galaxies out of 7) were selected from the catalogue of van Dokkum (1999). That essentially means that these galaxies were selected from a fairly complete magnitude limited sample with the selection criteria of spiral morphology (according to van Dokkum et al.) and [OII] EW $\geq$ 5 Å. The entire field sample was selected as galaxies with spiral morphology as determined by us. The sample was not magnitude limited, both because the galaxies were selected first by eye and then their magnitudes were measured and because only having two masks meant that a number of galaxies were excluded due to geometrical constraints. A sparse sampling of the field galaxies should not be a problem *per se*. The possibility of different morphological criteria could be a slight concern, but our feeling is that this could not introduce the cluster–field difference seen in the Tully–Fisher residuals. Visually, the morphologies of the cluster and field spirals do not appear significantly different except for the peculiar ones excluded from the analysis.

In summary, a difference between the cluster spirals and the field spirals has been detected at the 1.5–2σ level. This could be interpreted as an increment in luminosity, which could be the result of enhanced star formation in spiral galaxies falling onto the cluster. Star formation rates will be derived in Sect. 5.5, and the results will be discussed using stellar population models in Sect. 5.6.

5.1.1 Comparison with high redshift B–band Tully–Fisher studies from the literature

While only few rotation velocities exist for high redshift *cluster* spirals, more data are available on high redshift *field* spirals. We will compare our data with the data from two recent studies.

Ziegler et al. (2002) derived rotation velocities for 60 spiral galaxies at $z = 0.0$–1.0 ($z_{\rm median} = 0.44$) based on optical spectroscopy of spatially resolved emission lines. The galaxies, taken from the FORS Deep Field, are all field galaxies. The galaxies were selected based on multi-colour ground based imaging. In Fig. 5.4 we compare our data with the data from Ziegler et al.[3]. Identical cosmologies and internal extinction corrections have been used. Panel (a) shows the Tully–Fisher plot, while panel (b) shows the residuals (in absolute magnitude as always), computed using the Pierce & Tully (1992) local TFR as adopted by us (Eq. 5.4). We use this TFR irrespective of the fact that Ziegler et al. 2002 find some evidence of a TFR slope change with redshift. The immediate impression from the figure is that the agreement between the two field samples is reasonable. Statistical tests will be carried out below. It is also interesting to note that Ziegler et al. have galaxies near our excluded "outlier", galaxy A/F03.

Barden et al. (2003) derived rotation velocities for 22 spiral galaxies at $z = 0.60$–1.56 ($z_{\rm median} = 0.88$) based on NIR spectroscopy of spatially resolved Hα emission. The galaxies were selected from various redshift surveys, and the majority have HST imaging available. The galaxies are field galaxies, except for two cluster galaxies in MS1054−03. One of these galaxies (1403) is also in our sample, while the other (1733) is not due to geometrical constraints in the mask construction. In Fig. 5.5 and 5.6 we compare our data with the data from Barden et al. (the second figure is with error bars). We have transformed their data to our cosmology and internal extinction correction scheme. The immediate impression from the figures is also in this case that the agreement between the two field samples is reasonable. Their extra MS1054−03 cluster galaxy, 1733, falls in the middle of our 7 MS1054−03 cluster galaxies.

We will test if there are significant differences between our field sample and the field samples of Ziegler et al. (2002) and Barden et al. (2003). We will use the same statistical tests as we did above for the cluster and the field galaxies in our own sample, namely a difference of the mean values for the two samples and a Kolmogorov–Smirnov test. Also as before, we will do the tests both for all galaxies and galaxies brighter than $M_B^i = -19.8$ (the luminosity limit for our cluster sample). As before, we will also do the tests both using the plain TF residuals and the TF residuals corrected for the apparent redshift evolution present in *our* field sample. We are still excluding galaxy A/F03 from our sample, although based on the Ziegler et al. data it could be argued that this galaxy does not deviate strongly from the rest. For the Barden et al. (2003) sample we exclude the 3 galaxies which in the caption of Fig. 2 of that paper seem to be rejected due to insufficient size. We will also exclude the two remaining very high redshift ($z \sim 1.5$) galaxies in that sample, since the fit to TF zero point evolution for our field galaxies is a poor fit to these two galaxies. The results are given in Table 5.2 (Ziegler et al.) and Table 5.3 (Barden et al.). In all cases the field galaxies from Ziegler et al. or Barden et al. are brighter than our field galaxies at a fixed fixed rotation

[3]Data kindly provided by Asmus Böhm and Bodo Ziegler. In line with our analysis, the absolute magnitudes used here have not been corrected for morphological and incompleteness bias (cf. Ziegler et al. 2002).

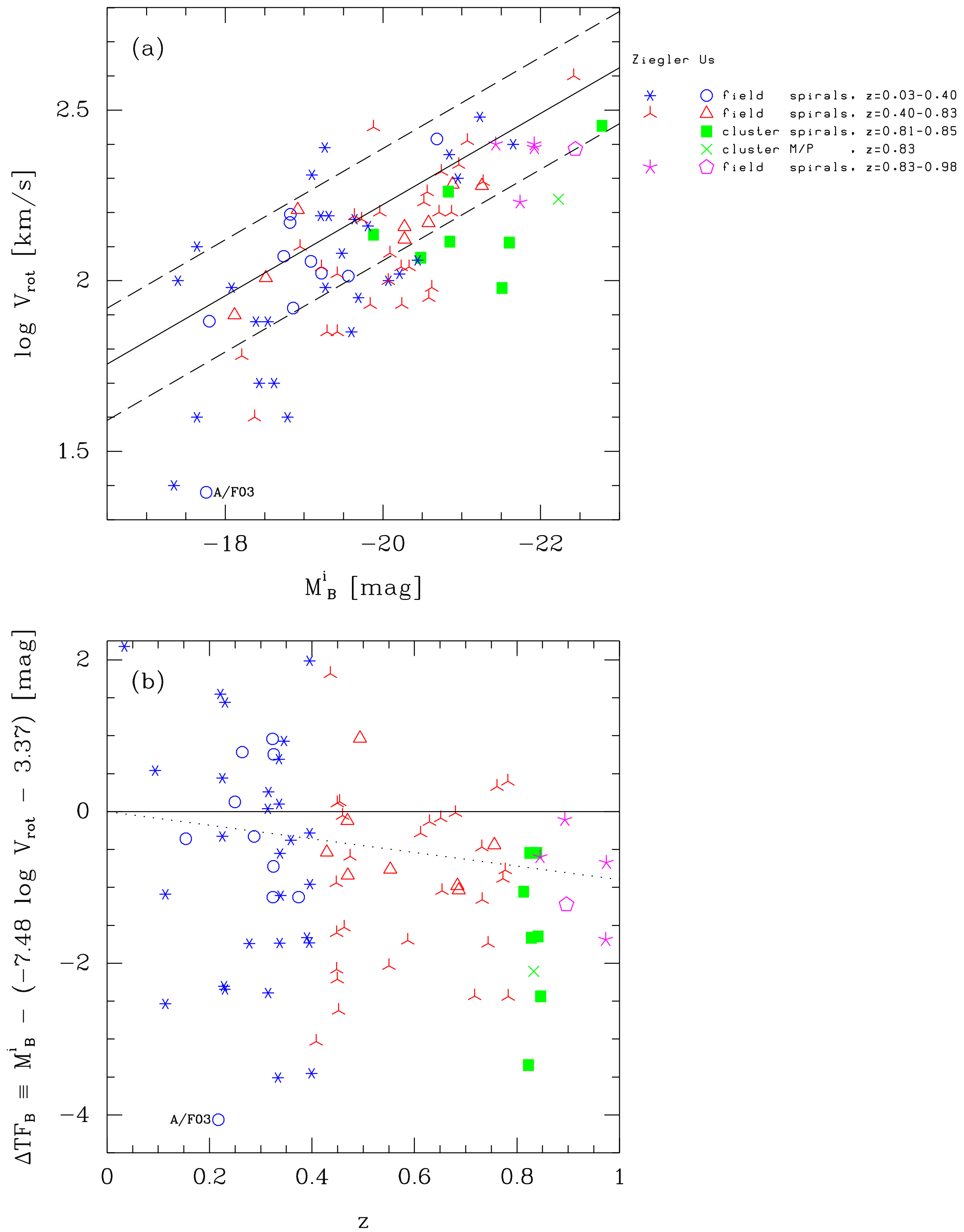

Figure 5.4: (a) High redshift B–band Tully–Fisher plot for our data and data from Ziegler et al. (2002). Solid line: local TFR (Eq. 5.4, see text). A single galaxy from Ziegler et al. at $(M_B^i, \log V_{\rm rot} = -15.78, 1.95)$ is off the scale of the plot.
(b) Residuals from the local TFR. Dotted line: fit to our field galaxies (Eq. 5.5, see text).
Error bars for the Ziegler et al. data were not available. Error bars for our data were omitted for clarity; they can been seen in Fig. 5.1, p. 91.

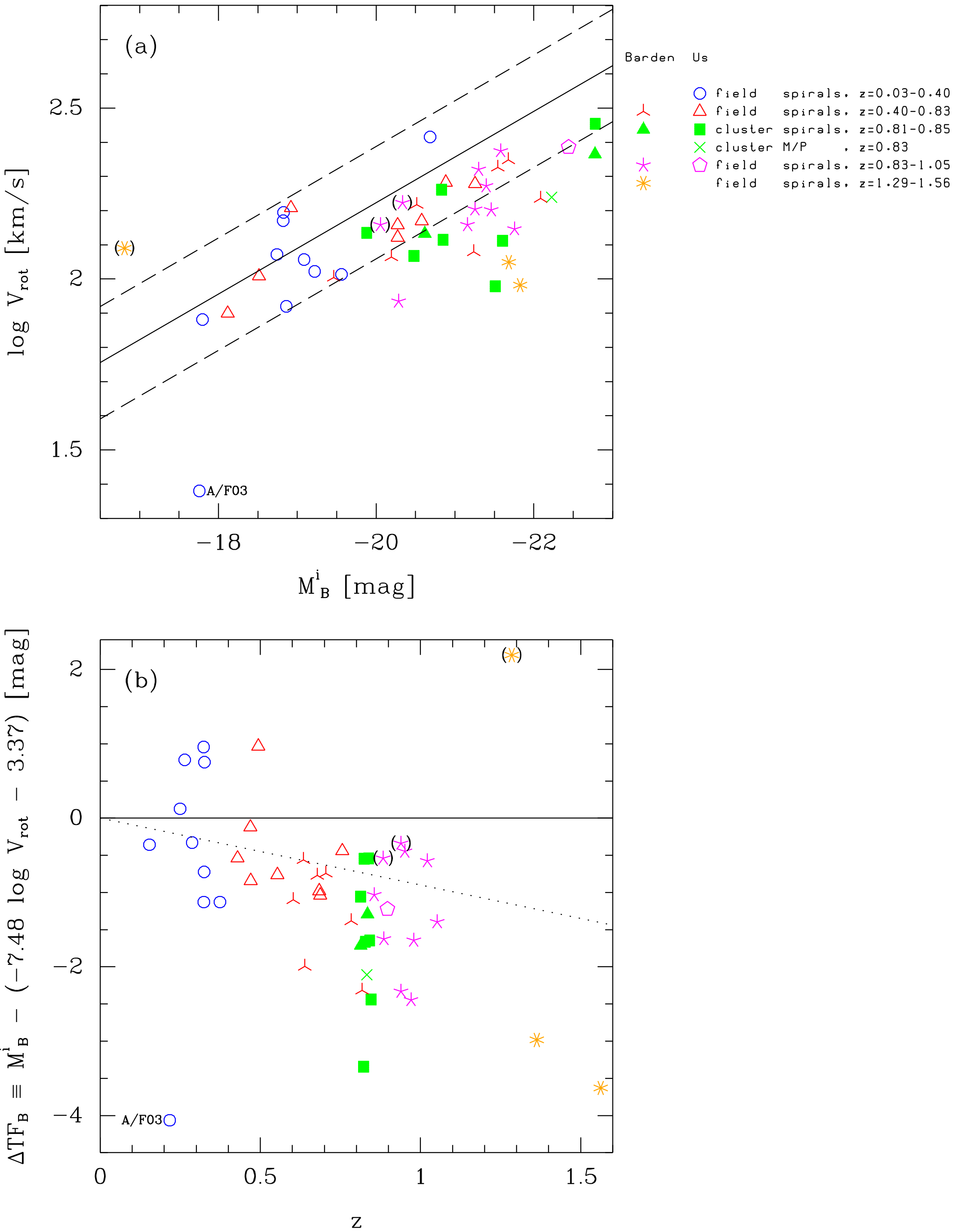

Figure 5.5: (a) High redshift B–band Tully–Fisher plot for our data and data from Barden et al. (2003). Solid line: local TFR (Eq. 5.4, see text). Galaxies in parenthesis have $R_{25} < 12.5\,\mathrm{kpc}$ (for the cosmology adopted by Barden et al.) and seem to be considered "bad" by these authors. *Note:* The brightest galaxy in both data sets is the same galaxy, 1403. As already mentioned, the two data sets agree on this galaxy within the errors. (b) Residuals from the local TFR. Dotted line: fit to our field galaxies (Eq. 5.5, see text).
A version of this figure *with* error bars can be found in Fig. 5.6

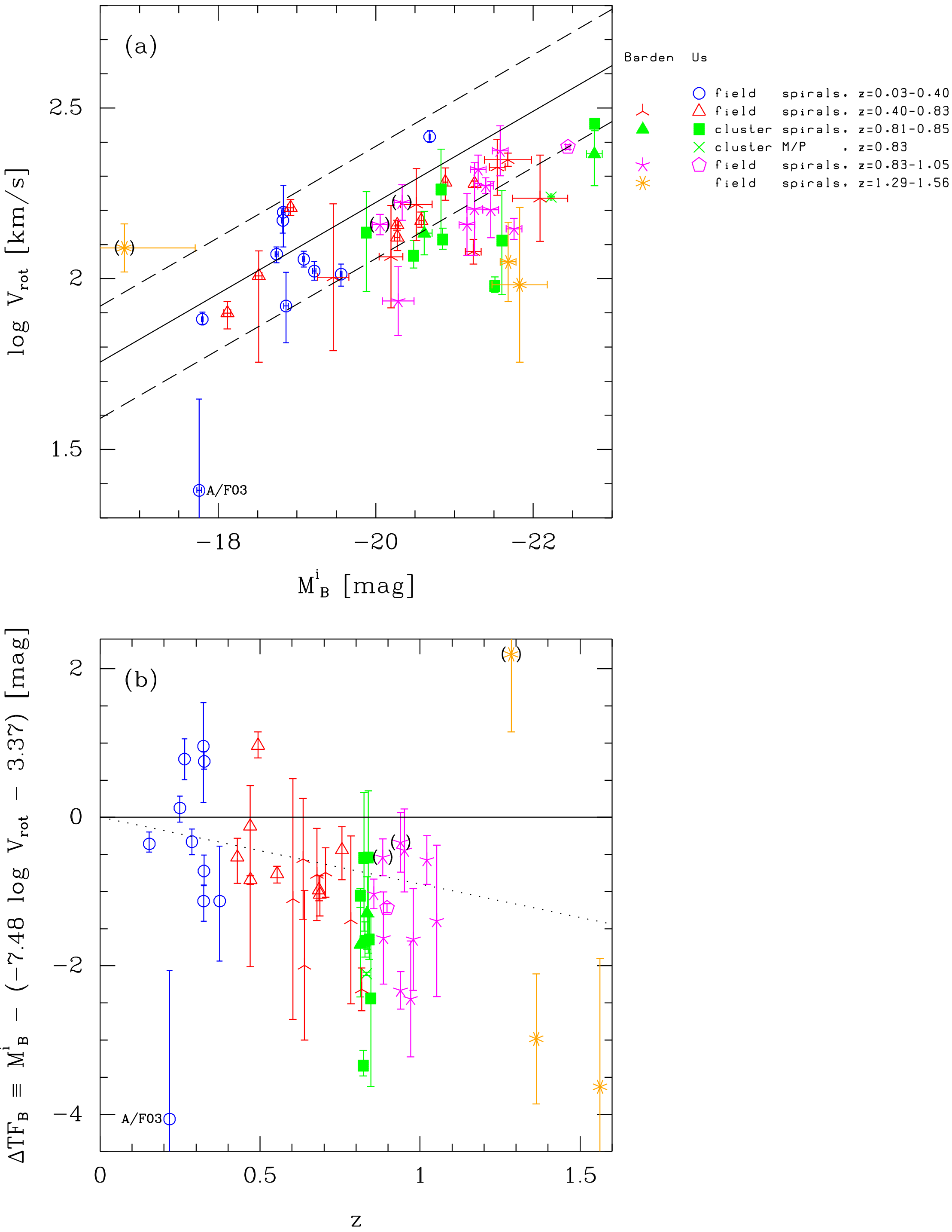

Figure 5.6: As Fig. 5.5, but with error bars.

velocity, or equivalently have a lower rotation velocity at a fixed luminosity. For the Ziegler et al. data the difference is only significant (at the 2σ level) when using the entire sample. If we had not excluded our galaxy A/F03, the disagreement for the full samples would be slightly smaller. If we had used the flat intrinsic rotation curve rather that the URC, our rotation velocities for the fainter galaxies would have been smaller by $\sim$0.05 in $\log V_{\rm rot} \sin i$ (cf. Fig. 3.11, p. 68), which is $\sim$0.06 in $\log V_{\rm rot}$, and which would have made $\Delta {\rm TF}_B$ $\sim$0.4 mag larger for these galaxies, bringing them in closer agreement with the fainter Ziegler et al. galaxies. The intrinsic rotation curve used by Ziegler et al. is rising until one optical scale length, and is then flat. This is intermediate between the URC and the flat intrinsic rotation curves in the ELFIT2D scheme (cf. Fig. 3.2, p. 51).

Table 5.2: Our field galaxies vs. field galaxies from Ziegler et al. (2002)

Variable	Selection	$N_{\rm our\ field}$	$N_{\rm their\ field}$	$\langle$our field$\rangle$ − $\langle$their field$\rangle$	$P^{\rm K-S}_{\rm diff.\ distr.}$
$\Delta {\rm TF}_B$	All	18	60	$+0.46 \pm 0.25$ mag (1.9σ)	96% (2.1σ)
$\Delta {\rm TF}_B$	High lum.	7	31	$+0.16 \pm 0.31$ mag (0.5σ)	62% (0.9σ)
$\Delta {\rm TF}_{B,{\rm corr}}$	All	18	60	$+0.45 \pm 0.24$ mag (1.9σ)	96% (2.1σ)
$\Delta {\rm TF}_{B,{\rm corr}}$	High lum.	7	31	$+0.18 \pm 0.28$ mag (0.6σ)	80% (1.3σ)

For the Barden et al. data, which practically all are high luminosity galaxies, the differences are significant at the 2σ level. The differences could be due to systematic differences in the determination of the rotation velocities, or perhaps to physical differences in the samples used. For the single galaxy in common between us and Barden et al., their rotation velocity is indeed lower than our, although the values agree within the errors, see Sect. 3.3.7, p. 76, and we *are* talking about a single galaxy only.

Stop press: at the last moment we have discovered that Barden et al. seem to correct their *rest-frame* B–band magnitudes for Galactic extinction, which is incorrect, it is the *observed frame* (say I–band) that needs to be corrected for Galactic extinction. The median B–band Galactic extinction listed in the table in Barden et al. is 0.29 mag. Using the conversion from B–band Galactic extinction to reddening $E(B-V)$ from Schlegel et al. (1998), this corresponds to a median reddening of 0.066. Since a typical redshift for the Barden et al. sample is $z \sim 0.8$, the observed I–band will be the band that correspond to the rest-frame B–band. Using the conversion factor for this band, the median reddening corresponds to a median Galactic extinction of 0.13 mag. This means that the absolute rest-frame B–band magnitudes given by Barden et al. typically are 0.16 mag too bright. This makes the disagreement between our sample and the sample of Barden et al. somewhat smaller and less significant. To be completely fair, the Galactic extinction of 0.03–0.10 mag (depending on the band and recipe, see p. 79) that we have *not* corrected our data for will also make the disagreement marginally smaller.

Table 5.3: Our field galaxies vs. field galaxies from Barden et al. (2003)

Variable	Selection	$N_{\rm our\ field}$	$N_{\rm their\ field}$	$\langle$our field$\rangle$ − $\langle$their field$\rangle$	$P^{\rm K-S}_{\rm diff.\ distr.}$
$\Delta {\rm TF}_B$	"All"	18	15	$+1.02 \pm 0.25$ mag (4.1σ)	99% (2.5σ)
$\Delta {\rm TF}_B$	High lum.	7	14	$+0.73 \pm 0.31$ mag (2.3σ)	94% (1.9σ)
$\Delta {\rm TF}_{B,{\rm corr}}$	"All"	18	15	$+0.68 \pm 0.24$ mag (2.8σ)	97% (2.2σ)
$\Delta {\rm TF}_{B,{\rm corr}}$	High lum.	7	14	$+0.52 \pm 0.27$ mag (1.9σ)	94% (1.9σ)

Since systematic differences may be present, it seems prudent not to compare our *cluster* spirals to the large sample of literature *field* spirals. This would otherwise have been interesting, since the cluster–field comparison within our data set is limited to some extend by the number of field galaxies in our sample. As already stated, the cluster–field comparison presented above in Table 5.1 is internal to our data set and thus unlikely to be affected by systematic errors in the data.

Finally we briefly return to the evolution of the B–band Tully–Fisher zero point with redshift. Barden et al. (2003) find their high redshifts sample ($z_{\rm median} = 0.9$) to be brighter than their local comparison sample by 1.1 mag in B for their adopted cosmology (the *concordance cosmology*, $h{=}0.70$, $\Omega_{\rm m}{=}0.3$, $\Omega_\Lambda{=}0.7$)[4]. For our adopted cosmology ($h{=}0.75$, $\Omega_{\rm m}{=}0.1$, $\Omega_\Lambda{=}0.0$), this brightening is 0.8 mag. If we evaluate the fit to our field sample [$\Delta{\rm TF}_B = (-0.9\pm0.3)z$, Eq. 5.5] at $z = 0.9$, we find a brightening of 0.8 mag, in striking agreement with the brightening derived by Barden et al. This agreement is somewhat surprising, since from Fig. 5.5(b) it is clear that the Barden et al. data are significantly brighter than our field spirals with respect to the adopted local TFR, as also shown by the tests in Table 5.3. Since Barden et al. (2003) cite a paper in preparation for the details of their analysis, this point cannot be investigated at the moment.

The exact amount of brightening shown by high redshift field spirals continues to be a debated issue. We will not make a strong statement regarding this. Our internal cluster–field comparison is to a large extend unaffected by this controversy.

5.1.2 B–band Tully–Fisher residuals versus clustercentric distance

We now return to our own data set. We will search for correlations between the Tully–Fisher residuals and other variables in the hope of understanding the observed difference between the cluster and the field spirals. As already reported, the difference is significant at the ∼1.5–2σ level [cf. Table 5.1, p. 93], so there is a chance that the result is spurious. We will do these tests as the various variables are introduced; for example, star formation rates will be introduced in Sect. 5.5.

We will start by searching for a dependence on position within the cluster. Only the positions projected onto the plane of the sky are available, not the 3-dimensional space positions. Figure 5.7(b) shows the position of the galaxies on the plane of the sky. The dotted line shows the region covered by the X–ray image shown in panel (a) [from Jeltema et al. 2001]. The X–ray contours reveal substantial substructure. A broad peak is centered on the cD galaxy, but a stronger and narrower peak is seen about $1.2'$ west of the cD galaxy. The distribution of red galaxies on the sky seen in the HST mosaic also shows an elongation in the east–west direction, see Fig. 4 in van Dokkum et al. (2000). The cD galaxy seems to be a reasonable origin for a projected clustercentric distance, but the non-spherical nature of the cluster should be kept in mind. In Fig. 5.7(c) the corrected B–band Tully–Fisher residuals are plotted versus the projected distance from the cD galaxy. As expected, no trend is found for the field galaxies. No trend is found for the cluster galaxies either. However, even if there was a correlation with the physical distance from the cluster centre, such a correlation will be diluted by the projection onto the plane of the sky. Statistically, an underlying correlation with the 3D radius will translate into a (weaker) correlation with the projected radius. However, even if the underlying correlation has a low dispersion, a secure detection is almost impossible with only 7 galaxies with non-zero error bars. With the much larger sample of high redshift cluster galaxies that will soon be available (cf. Sect. 6.2 on the future work), a correlation with clustercentric distance may well be found. Such a detection would be very important, since it would give clues to the nature of the mechanism that is responsible for the brightening.

[4] $h \equiv H_0/(100\,{\rm km\,s^{-1}\,Mpc^{-1}})$

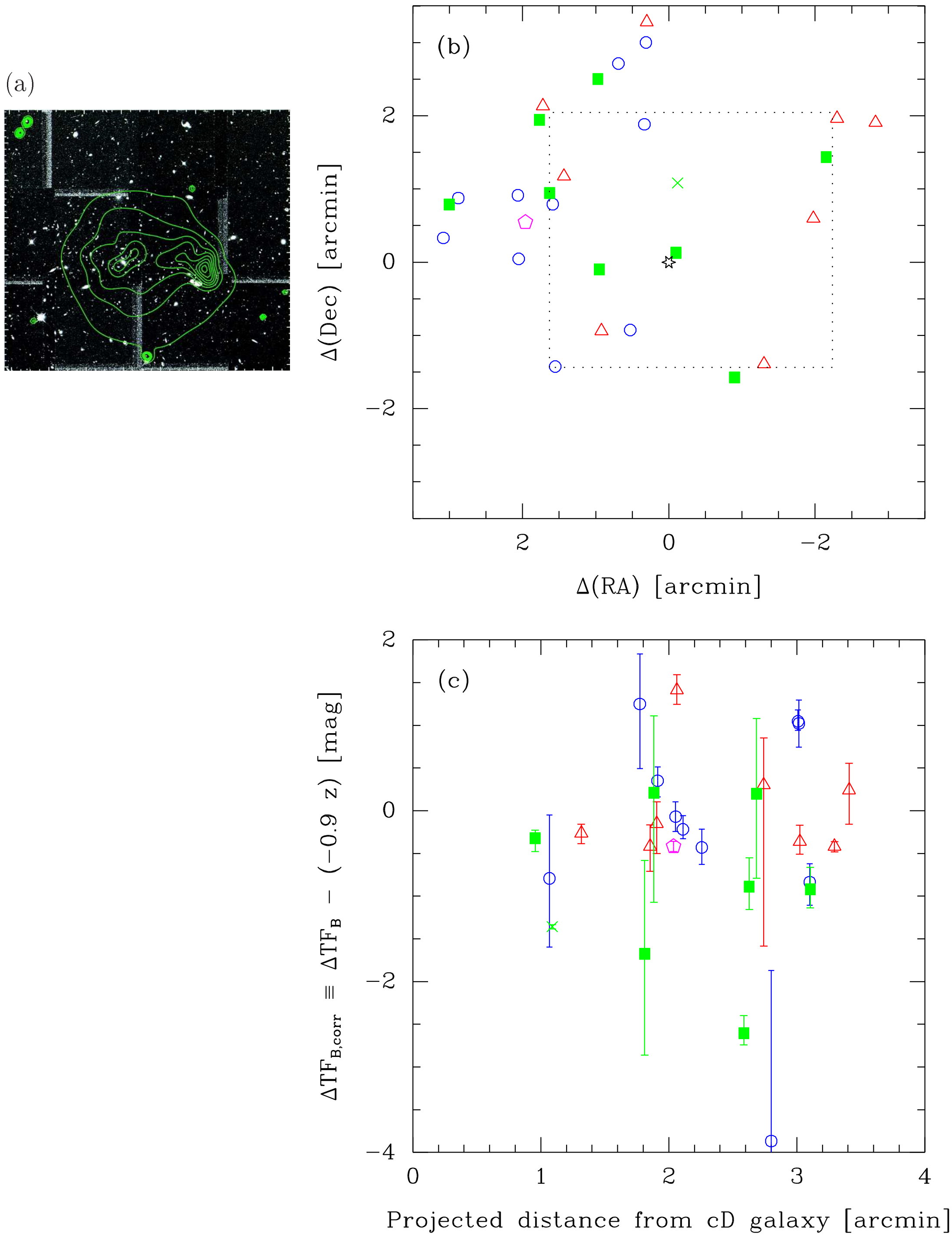

Figure 5.7: (a) Smoothed Chandra X–ray image of MS1054−03 (green contours), overlayed on an HST image. Figure reproduced from Jeltema et al. (2001). (b) The location of the galaxies on the plane of the sky with respect to the cD galaxy (marked with a black star; RA = 10:56:59.96, Dec = −03:37:36.8). The dotted rectangle shows the area covered by panel (a). North is up and east is to the left. (c) Corrected B–band Tully–Fisher residuals versus projected clustercentric distance. (Legend: see Fig. 5.1, p. 91.)

5.2 The H–band Tully–Fisher relation

The study from which we adopted the local B–band TFR, i.e. Pierce & Tully (1992), also gives a local H–band TFR, namely

$$\widetilde{M^{b,i}_{H-0.5}} = -9.50(\log W^i_R - 2.50) - 21.67 \ . \tag{5.6}$$

As before, the tilde on the absolute H–band magnitude is our notation that the (small) face-on H–band extinction of 0.027 mag in the Tully & Fouqué (1985) scheme has *not* been corrected for. Our total magnitudes *are* corrected for this face-on extinction, and in terms of those magnitudes the TFR is

$$0.027 + M^{b,i}_{H-0.5} = -9.50(\log W^i_R - 2.50) - 21.67 \ . \tag{5.7}$$

The subscript -0.5 denotes that these H–band magnitudes are not total magnitudes, but refer to a (circular) aperture of diameter $A = 10^{-0.5}D_{25}$, where D_{25} is the diameter at the $\mu_B = 25\,\mathrm{mag\,arcsec^{-2}}$ isophote. This $H_{-0.5}$ system was introduced by Aaronson et al. (1979). The Pierce & Tully (1992) H–band TFR is based on $H_{-0.5}$ magnitudes from Aaronson et al. (1982). The isophotal diameters used by these authors are essentially the diameters from the RC2 (de Vaucouleurs et al. 1976).

At a later point, the $H_{-0.5}$ system was recalibrated by Tormen & Burstein (1995) using isophotal diameters from the RC3 (de Vaucouleurs et al. 1991). These diameters are on average larger than those from the RC2, leading to the RC3–based $H_{-0.5}$ magnitudes being brighter,

$$H_{-0.5}(\mathrm{RC3}) - H_{-0.5}(\mathrm{RC2}) = -0.21\,\mathrm{mag} \ . \tag{5.8}$$

This is relevant since Watanabe et al. (2001), based on new data and on literature data (Peletier & Willner 1993; Bernstein et al. 1994), give a transformation from the RC3–based $H_{-0.5}$ magnitudes from Tormen & Burstein (1995) to *total magnitudes*. This offset was found to depend on Hubble-type, being 0.62 mag for $T \leq 4$ (i.e. until Sbc) and 0.77 mag for $T \geq 5$ (i.e. from Sc). The distributions for the early and late-type spirals is seen (their Fig. 4) to have substantial overlap, and the difference between the two populations is hard to pick up by eye. It seems reasonable to use the approximation

$$H_{-0.5} - H_{\mathrm{total}} = 0.7\,\mathrm{mag} \tag{5.9}$$

for all spiral types.

The above ingredients (Eq. 5.7, 5.8 and 5.9) and Eq. (5.3) from before give the local H–band TFR we will use as reference,

$$M^i_H = -9.50 \log V_{\mathrm{rot}} - 1.72 \ , \tag{5.10}$$

This relation is shown in Fig. 5.8(a) along with our data. It is seen that the field galaxies are only slightly offset with respect to the local H–band TFR (except for galaxy C6 which deviates strongly). No evolution of the zero point with redshift is detected. The cluster galaxies are on average substantially brighter than the field galaxies. In Fig. 5.9 the H–band residuals are compared with those in the B–band. Panel (a) plots the residuals versus each other. In panel (b) the residuals are "corrected" so that the field galaxies in the median have a value of zero. The field galaxies are thus used as the reference point. In this plot, the cluster galaxies are seen to have a *larger* (or at best comparable) brightening in the H–band than in the B–band. This is surprising since if the brightening is caused by a young stellar population, the brightening should be larger in the B–band than in the H–band by a factor of $\sim$2 in magnitudes (see Sect. 5.6). The NIR data are preliminary, but since we are doing the comparison relative to the field galaxies, zero point errors in the photometry should cancel out.

If the Tully–Fisher residuals instead are interpreted as a change in rotation velocity rather than a change in luminosity, the lower residuals of the cluster galaxies wrt. the field galaxies would indicate that the cluster galaxies had lower rotation velocities than the field galaxies. These lower rotation velocities could be real or could be due to systematic errors in the data affecting the cluster galaxies more than the field galaxies. It is interesting to note that since the $\log V_{\rm rot}$ coefficient in the H–band TFR is larger than that in the B–band TFR, the residuals in this scenario would indeed be larger in the H–band than in the B–band.

We will later see that the B–band Tully–Fisher residuals are anti–correlated with the star formation rate. This speaks strongly in favour of interpreting the negative B–band TF residuals as due to a brightening caused by a young stellar population. This offers no explanation for the H–band results.

The results from the H–band data need to be taken with perhaps more caution than the ones for the B–band because the H–band magnitudes are preliminary (and we do not have access to the final ones yet, nor the images) and the transformation from the near–IR magnitudes to H is somewhat more uncertain than from F814W to B. It will be extremely important to repeat the test when the NIR data is finally published. If the result holds, we may need to re-think the interpretation.

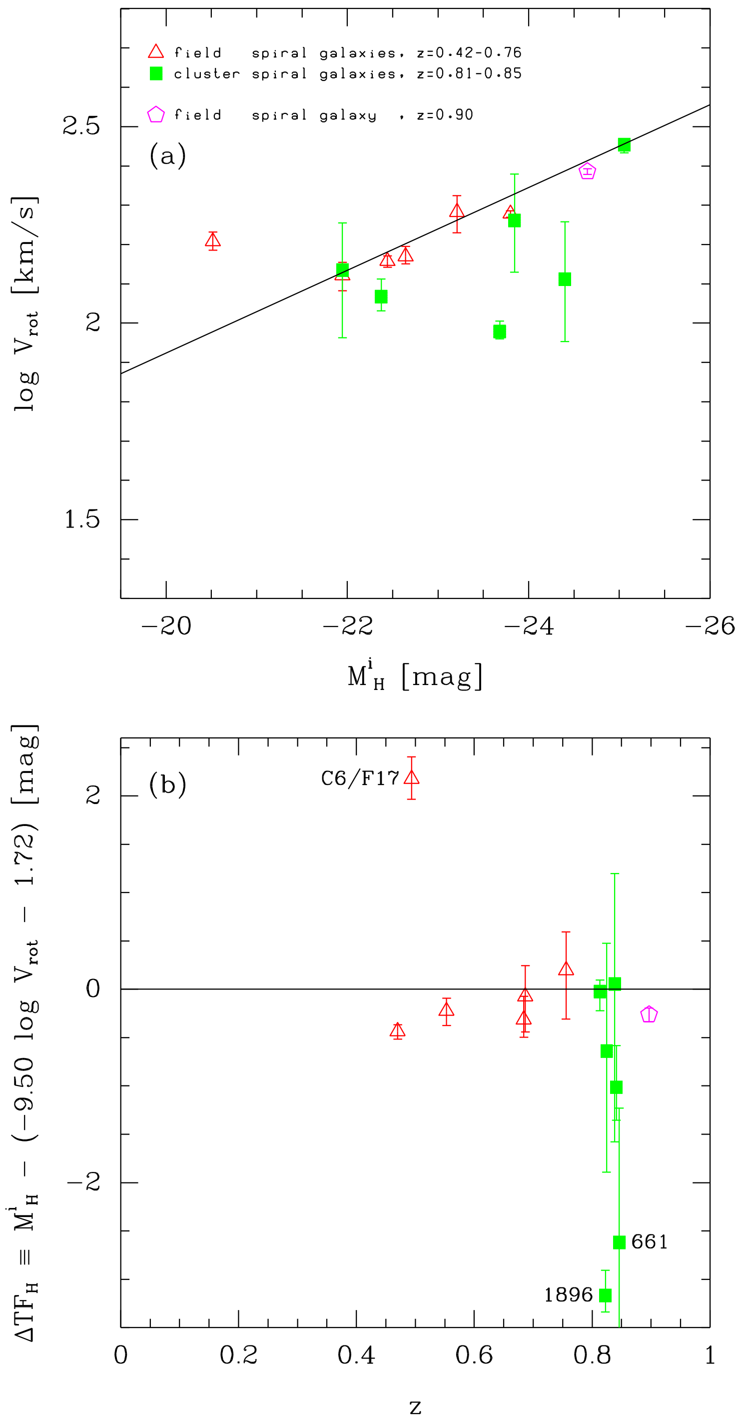

Figure 5.8: (a) High redshift cluster and field H–band Tully–Fisher relation. The reason this plot contains fewer galaxies than the B–band TFR plot (Fig. 5.1, p. 91) is that not all the galaxies have H–band data. The solid line is the local H–band Tully–Fisher relation from Pierce & Tully (1992), see Eq. (5.10).
(b) Residuals from the local H–band TFR versus redshift.

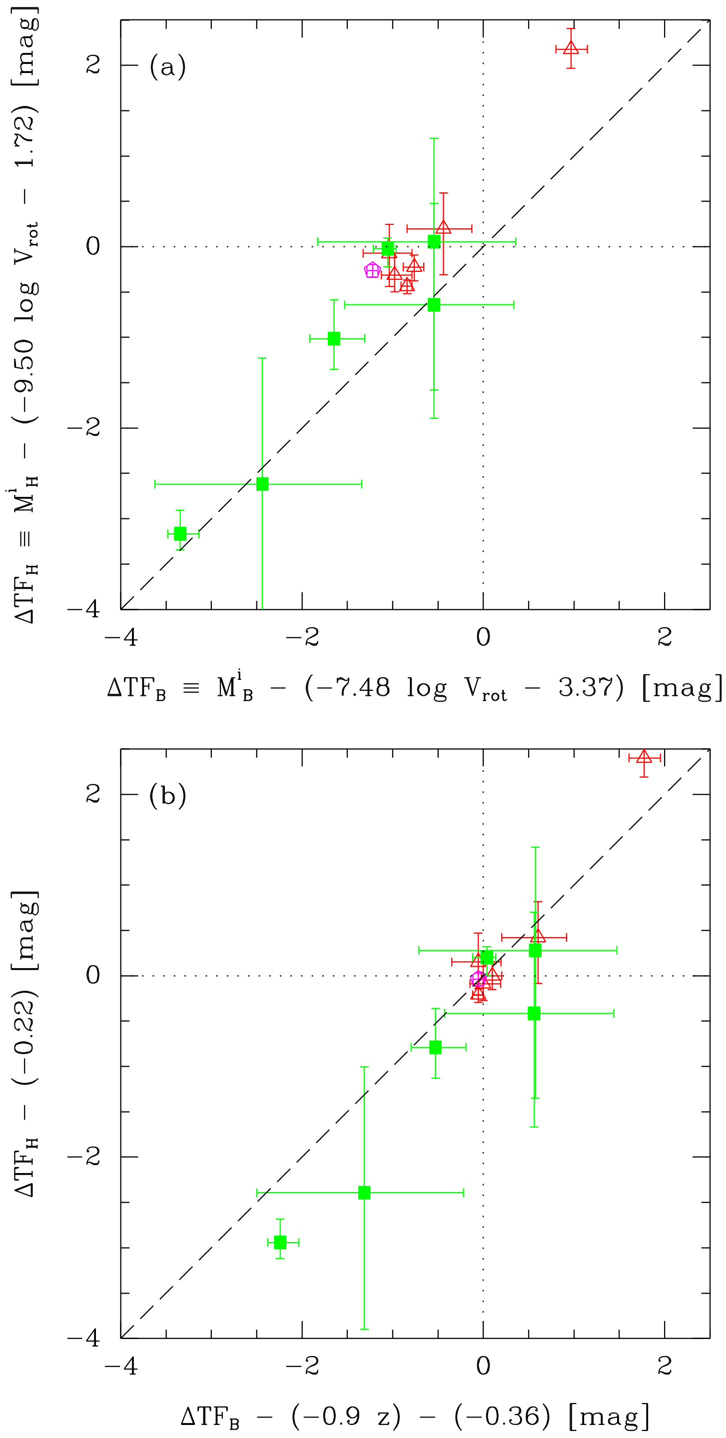

Figure 5.9: (a) Tully–Fisher residuals: *H*–band versus *B*–band. (b) Residuals corrected so that the field galaxies have a value of zero in the median. For the *B*–band data, the apparent redshift evolution has also been taken out. (Legend: see Fig. 5.1, p. 91.)

5.3 The velocity–size diagram

In Sect. 5.1 we found evidence of a cluster–field difference in the B–band Tully–Fisher residuals, which could be interpreted as a difference in luminosity (at a fixed rotation velocity). It is therefore interesting to see if there also is a cluster–field difference in a diagnostic diagram which does not involve the luminosity. Such a diagram is the velocity–size diagram, which is shown in Fig. 5.10(a). 'Size' refers to the stellar disk, as measured by the exponential scale length for the broad band (F814W) light, $r_{\rm d,phot}$. The solid line is a local relation. Panel (b) shows the residuals from this relation versus redshift. We choose to calculate the residuals, denoted Δ(Vel–Size), in the $\log r_{\rm d,phot}$ direction.

First we note that there is a small difference between our high redshift data as a whole and the adopted local relation. This offset could well be due to systematic differences in how the measurements are made. It should also be noted that the assumed cosmology affects the high redshift data through the calculation of $r_{\rm d,phot}$ in kpc. In terms of models of hierarchical structure formation, the disk scale length is expected to be smaller in the past due to the Hubble constant being larger (e.g. Dalcanton et al. 1997; Mo et al. 1998). The size of the effect depends on the cosmology (see Fig. 1 of Mo et al. 1998). For our field galaxies, we do not find any significant trend with redshift, a Kendall's tau test gives $P_{\rm corr.} = 69\%$.

We then turn to the question of whether there is a significant cluster–field difference within our sample. For this comparison within our data set systematic problems should be much less of a worry. We test for differences in the Δ(Vel–Size) distributions for the cluster and the field samples in the same way as was done for the B–band Tully–Fisher residuals. The results from the tests are given in Table 5.4. In one of the four tests, namely the K–S test for the whole field sample versus the cluster sample, there is marginal detection of a difference, namely at the 91% level ('1.7σ'). In the difference of means test, the difference is only 1σ. When only using field galaxies in the luminosity range of the cluster galaxies, no cluster–field differences are found.

Table 5.4: Velocity–size differences: cluster versus field

Variable	Field sample	$\langle$cluster$\rangle - \langle$field$\rangle$ [log kpc]	$P^{\rm K-S}_{\rm diff.\ distr.}$
Δ(Vel–Size)	All	0.087 ± 0.083 (1.0σ)	91% (1.7σ)
Δ(Vel–Size)	High L	0.028 ± 0.098 (0.3σ)	58% (0.8σ)

The velocity–size diagram needs to be watched in future studies. At the moment, the tentative conclusion is that there are no major differences between cluster and field galaxies in terms of the *structure* of the galaxies, i.e. the size of the stellar disk at a given rotation velocity. If the cluster–field difference found in the B–band Tully–Fisher plot is interpreted as a luminosity effect, the conclusion is that cluster and field spirals are structurally similar, but that the cluster galaxies on average have lower mass-to-light ratios, possibly indicative of a higher recent star formation. Furthermore, the physical mechanism responsible for the brightening must mainly affect the gas disk and not the stellar disk. Interactions with the intra-cluster medium is one such mechanism that is expected only to affect the gas disk, while gravitational interaction (galaxy–galaxy or galaxy–cluster) could affect both the gas disk and the stellar disk.

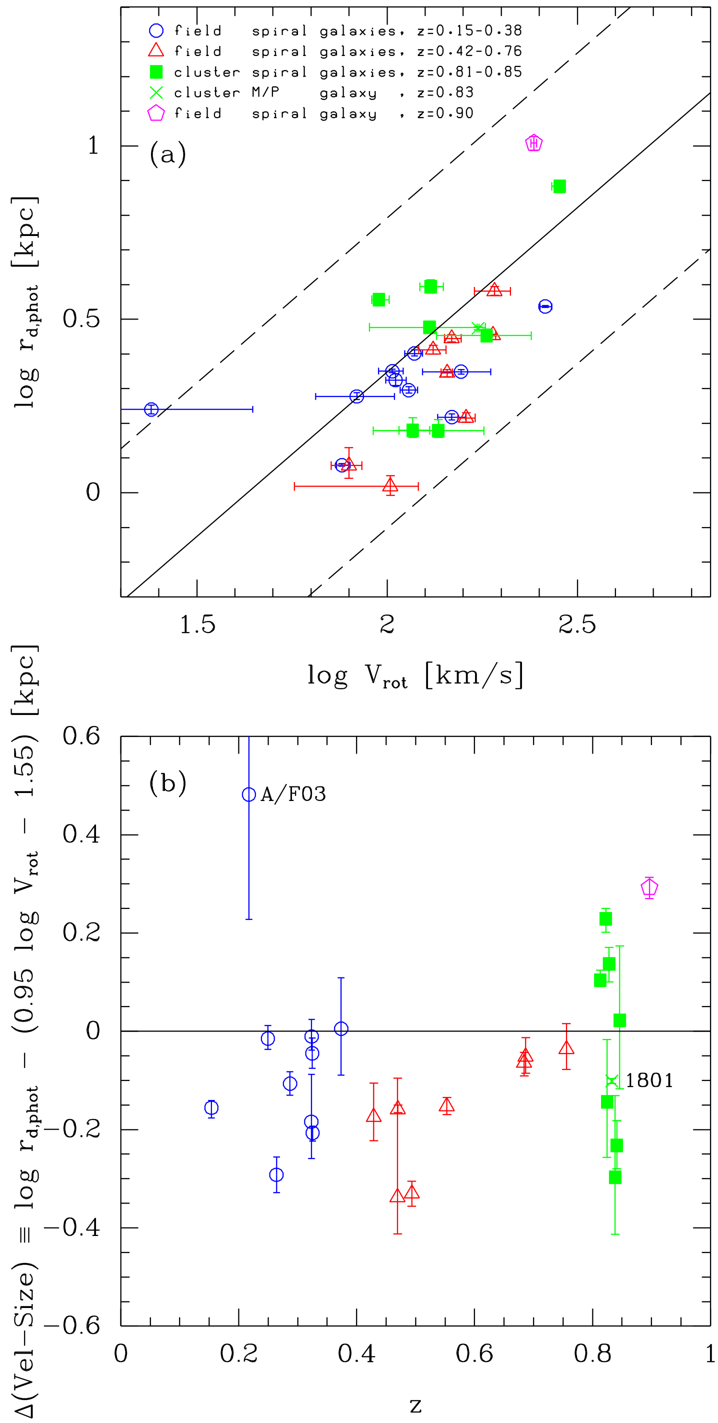

Figure 5.10: (a) High redshift velocity–size diagram. $r_{\mathrm{d,phot}}$ is the exponential disk scale length, here in the F814W band. This plot only depends on the sizes and the masses of the galaxies, not on their mass-to-light ratios (hence star formation rates). Solid line: local relation (Vogt 1995; Burstein et al. 1997; as read from Fig. 5 in Vogt 1999), $\log r_{\mathrm{d,phot}} = 0.95 \log V_{\mathrm{rot}} - 1.55$. Dashed lines: ± 3 sigma limits.
(b) Residuals from the local relation.
Galaxy 1549 is off the scale of the plots.

5.4 Spectroscopic versus photometric scale length

Following the investigation of the scale lengths for the stars, $r_{\rm d,phot}$, we now turn to the scale lengths for the gas, $r_{\rm d,spec}$. As described in Ch. 3 this quantity is output from the 2D emission line fit (Simard & Pritchet 1998, 1999). No prior knowledge of the scale length for the stars is used. This is in contrast to most other studies at high redshift: Vogt (1999) use $r_{\rm d,spec} \equiv 1.5 r_{\rm d,phot}$ (citing Ryder & Dopita 1994). Ziegler et al. (2002) do something similar (also citing Ryder & Dopita 1994), while Barden et al. (2003) use $r_{\rm d,spec} \equiv 1.0 r_{\rm d,phot}$. Thus, in this study we are in the rather unique position to discuss the spatial extend of the gas that gives rise to the observed emission lines.

In Fig. 5.11(a) we plot the gas scale length ($r_{\rm d,spec}$) versus the stellar scale length ($r_{\rm d,phot}$). Both scale lengths are shown in kpc (rather than arcsec), enabling a physical comparison across the redshift range. A clear correlation between the two scale lengths is seen, with a significance of 99.99% for the field galaxies alone, and $>$ 99.99% for the combined sample. This strongly suggests that the derived scale lengths from the spectroscopy are meaningful. The result is impressive considering that the typical $r_{\rm d,spec}$ value in angular units is $0.57''$, which is comparable to the "seeing scale length" of FWHM/2 $\approx 0.5''$. The range for $r_{\rm d,spec}$ is 0.01–2.23$''$, and almost all the $r_{\rm d,spec}$ values are significantly larger than zero when using the derived errors, see Fig. 5.11(a). These errors assume that the specified seeing has zero uncertainty, whereas the seeing actually has a small uncertainty of $\sim 0.02''$, cf. Sect. 2.3.12, p. 39. The clear exception is galaxy 1459, where no spatial extend of the emission is found. This is an AGN, cf. the discussion in Sect. 5.1. This galaxy is excluded throughout the analysis.

In Fig. 5.11(a) the one-to-one correspondence between $r_{\rm d,spec}$ and $r_{\rm d,phot}$ is shown as a dotted line. This is just to guide the eye. The exact relationship between the two scale lengths is more clearly shown in panel (b) where the ratio of the two are plotted. A range in $r_{\rm d,spec}/r_{\rm d,phot}$ ratios is found. This range encompasses the typical value seen in the Ryder & Dopita (1994) data of 1.5, although the median for our sample is lower than this, namely 1.1.

Figure 5.11(b) indicates that the mean value of $r_{\rm d,spec}/r_{\rm d,phot}$ is lower for the cluster galaxies than for the field galaxies. This tendency is even more clear if only considering field galaxies in the luminosity range of the cluster galaxies, which is shown in Fig. 5.12. This is very interesting in the light of the result from Moss & Whittle (2000). In a study of low redshift cluster and field spirals these authors found that star formation in the cluster spirals was more centrally concentrated than in the field spirals. The fact that we find $\langle r_{\rm d,spec}/r_{\rm d,phot} \rangle$ to be lower for the cluster spirals than for the field spirals could indicate that the same phenomenon is occurring at high redshift. The implication is that the cluster environment is probably affecting the star-formation regime in cluster galaxies over a large cosmic epoch (i.e. over a large redshift range). More star-formation occurs near the centre in cluster galaxies. The interaction of the galaxy gas with the intra-cluster medium or with other galaxies or with the cluster potential could drive the gas towards the centre through dynamical instabilities and thus produce more concentrated star formation.

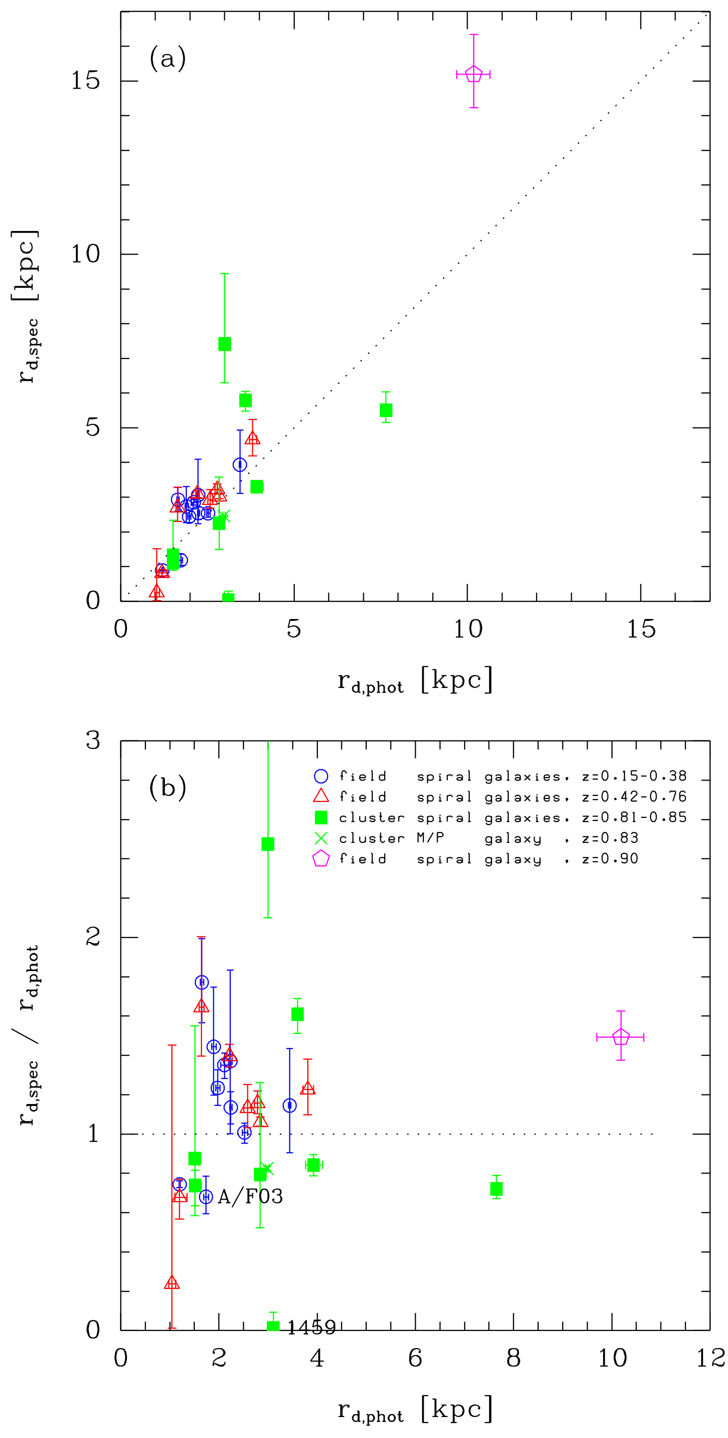

Figure 5.11: (a) Spectroscopic scale length (gas) versus photometric F814W scale length (stars). (b) Same as panel (a), now just plotting the ratio of the two scale lengths. In both panels the dotted line marks the one-to-one relation.
The AGN (1459) clearly stands out.

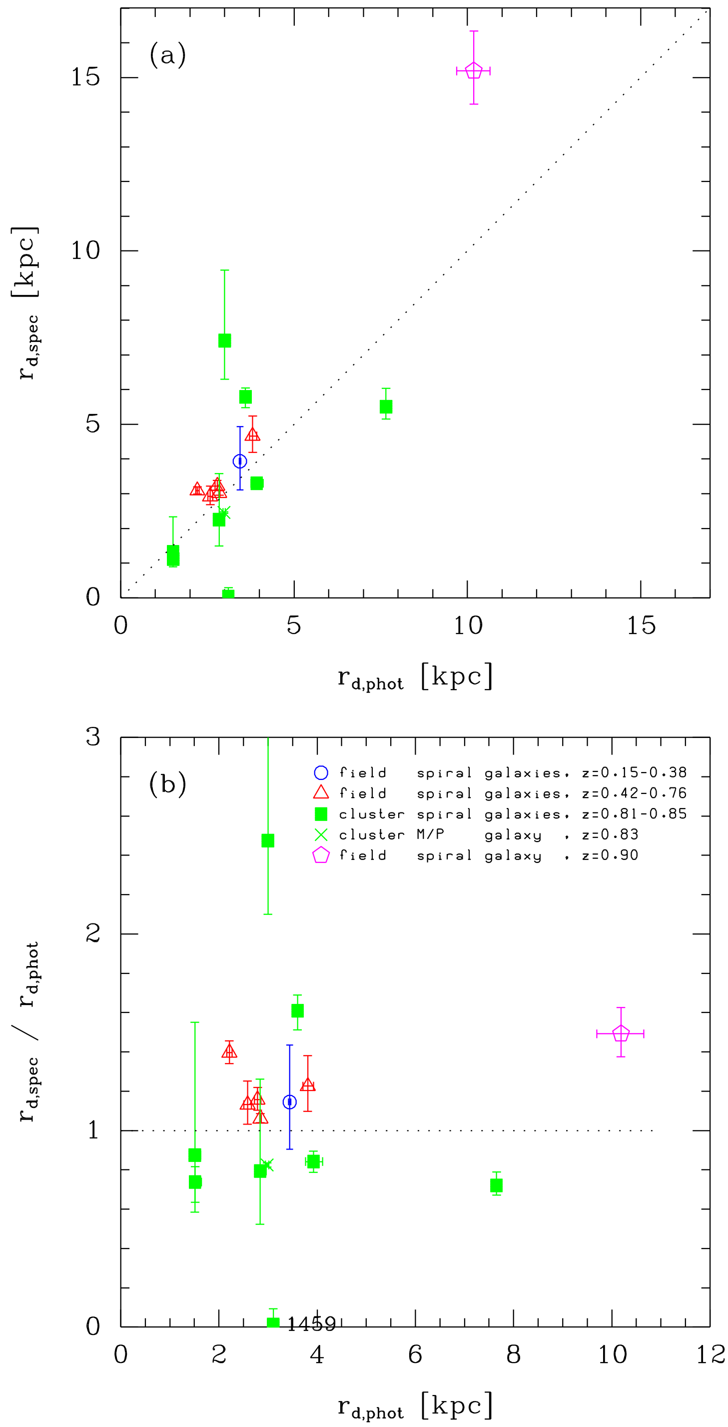

Figure 5.12: As Fig. 5.11, but only showing field galaxies that are in the luminosity range of the cluster galaxies ($M_B^i < -19.8$ mag).

5.5 Star formation rates

The difference we have found between the cluster and the field spirals in the B–band Tully–Fisher diagram could be interpreted as a relative brightening of the cluster galaxies due to higher levels of recent star formation. A direct test of this scenario is whether estimates of the star formation rate are anti–correlated with the B–band Tully–Fisher residuals. For the galaxies at $z \gtrsim 0.5$ we can do this test since we can estimate the SFR from the luminosity of the observed [OII] emission line.

In Sect. 2.4 the [OII] equivalent widths (EWs) and luminosities were derived. This was done for the 16 galaxies with [OII] observed. To illustrate the range of the values, the [OII] EWs and luminosities are plotted against redshift in Fig. 5.13. Ideally, we want the cluster and the field samples to have similar properties, and the distributions of [OII] EW and luminosity are indeed seen to overlap. A Kolmogorov–Smirnov test finds a hint of a difference between the [OII] EW distributions ($P^{\rm K-S}_{\rm diff.\ distr.} = 87\%$) while no difference is found between the $L_{\rm [OII]}$ distributions ($P^{\rm K-S}_{\rm diff.\ distr.} = 12\%$).

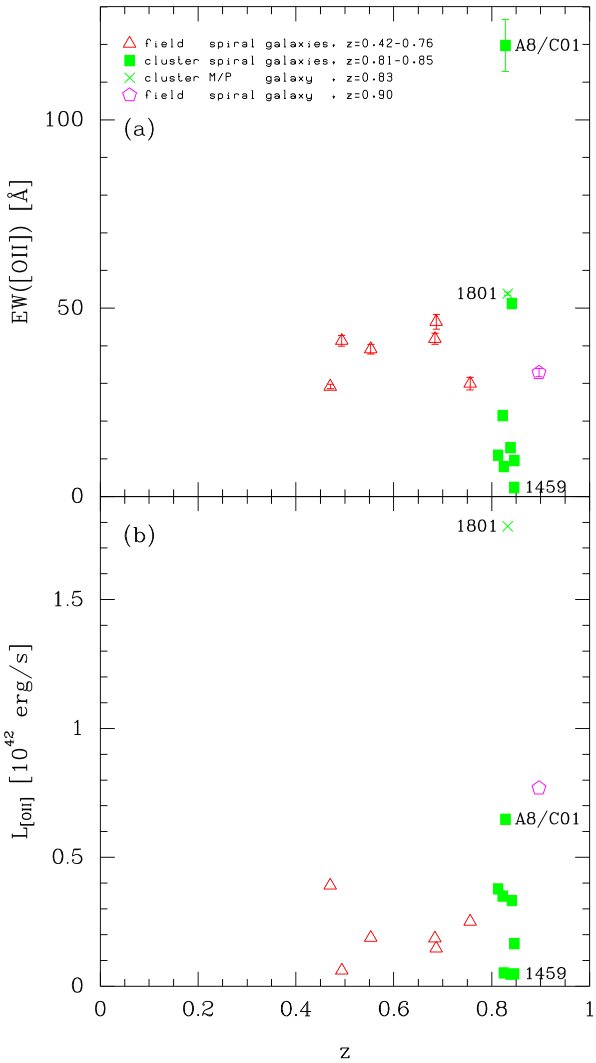

Figure 5.13: [OII] EWs and luminosities versus redshift. Galaxies 1459 and 1801 are excluded from the analysis. Galaxy A8/C01 is the new cluster galaxy found by us.

The sample of galaxies with [OII] observed includes all the MS1054−03 cluster galaxies as well as the single background field galaxy. In terms of foreground field galaxies, 7 galaxies (at $z = 0.47$–0.76) have [OII] observed. With one exception (galaxy C6/F17 at $z = 0.49$) these galaxies are all in the subsample of high luminosity galaxies that has been used in previous sections. Likewise, one high luminosity galaxy (galaxy XX4/F12 at $z = 0.33$) does not have [OII] observed. Thus, for the analysis involving [OII] the cluster sample contains the same 7 spiral galaxies as before, and the field sample contains 7 spiral galaxies as well.

We are interested in estimating the star formation rates (SFRs) of the galaxies. A good tracer of the SFR is the Hα luminosity (see e.g. Kennicutt 1998). Assuming an IMF for the newly formed stars, it is possible to calculate the number of ionizing photons (from massive stars) that give rise to emission lines from the interstellar gas. Unfortunately, Hα is not available for the high redshift galaxies in this study. It is possible to estimate the SFR from the [OII] luminosity, but this is made complicated by its dependence on the excitation state and metallicity of the gas (see e.g. McCall et al. 1985; García-Vargas et al. 1995a,b).

An empirical transformation from [OII] luminosity to the (extinction corrected) SFR has been determined by several authors, but the transformation factor SFR/$L_{\rm [OII]}$ in $M_\odot\,{\rm yr}^{-1}/({\rm erg\,s}^{-1})$ varies considerably from study to study, e.g. 1×10^{-41} (Gallagher et al. 1989), 5×10^{-41} (Kennicutt 1992) and 6.3×10^{-41} (Barbaro & Poggianti 1997) (see also Guzmán et al. 1997). Moreover, Jansen et al. (2001) recently showed that the $L_{\rm [OII]}/L_{\rm H\alpha}$ ratio is a function of the luminosity of the galaxy. That analysis was based on the data from the Nearby Field Galaxy Survey (NFGS, Jansen et al. 2000b,a). A complimentary analysis was done by Aragón-Salamanca et al. (2003b,a) using data for the Universidad Complutense de Madrid (UCM) sample as well as the NFGS data. In agreement with Jansen et al. (2001), $L_{\rm [OII]}/L_{\rm H\alpha}$ was found to decrease with increasing B–band luminosity. This could be interpreted as the more massive galaxies having higher extinction due to a higher metallicity. The $L_{\rm [OII]}/L_{\rm H\alpha}$ ratio was also found to be correlated with the [OII] EW, in the sense that galaxies with large EWs had large $L_{\rm [OII]}/L_{\rm H\alpha}$ ratios. The UCM and NFGS galaxies were found *not* to follow identical relations. This was attributed to a difference in sample selection: the NFGS sample is selected in the B–band, whereas the UCM sample is selected in Hα, which leads to galaxies with high extinction being more underrepresented in the NFGS sample than in the UCM sample.

Aragón-Salamanca et al. (2003a) fitted linear relations between various combinations of the parameters under study: [OII] luminosity ($L_{\rm [OII]}$), Hα luminosity ($L_{\rm H\alpha}$), *extinction corrected Hα luminosity ($L_{H\alpha^0}$)*, [OII] equivalent width ($W_{\rm [OII]}$) and B–band absolute magnitude (M_B). Separate relations were derived for the UCM and the NFGS samples. Here we will use relations from Aragón-Salamanca et al. (2003a) to estimate $L_{\rm H\alpha}$ and more boldly $L_{\rm H\alpha^0}$ from $L_{\rm [OII]}$ and 1 or 2 extra pieces of information: $W_{\rm [OII]}$, M_B, or both. It is clear that $L_{\rm H\alpha^0}$ is the most interesting quantity to estimate, since it is directly related to the extinction corrected SFR. It is stressed by Aragón-Salamanca et al. (2003a) that the derived relations are only strictly valid for samples selected in the same way as the sample in question (UCM or NFGS), and that the relations may not apply in identical form to high redshift galaxies. We will use the relations fitted to the NFGS sample, since the sample selection of our study is closest to that of the NFGS.

For $L_{\mathrm{H}\alpha}$ Aragón-Salamanca et al. (2003a) found

$$\log\left(\frac{L_{[\mathrm{OII}]}}{L_{\mathrm{H}\alpha}}\right) = -1.02 + 0.65\log W_{[\mathrm{OII}]} \qquad \mathrm{MAD} = 0.14 \quad (5.11)$$

$$\log\left(\frac{L_{[\mathrm{OII}]}}{L_{\mathrm{H}\alpha}}\right) = 1.61 + 0.09(M_B + 5\log h_{50}) \qquad \mathrm{MAD} = 0.14 \quad (5.12)$$

$$\log\left(\frac{L_{[\mathrm{OII}]}}{L_{\mathrm{H}\alpha}}\right) = 0.33 + 0.46\log W_{[\mathrm{OII}]} + 0.06(M_B + 5\log h_{50}) \qquad \mathrm{MAD} = 0.12 \quad (5.13)$$

where MAD a measure of the scatter in the relation[5], h_{50} is the Hubble constant in units of $50\,\mathrm{km\,s^{-1}\,Mpc^{-1}}$, and $W_{[\mathrm{OII}]}$ is defined to be positive. As can be seen from the MAD numbers and perhaps more easily from the plots in Aragón-Salamanca et al. (2003b,a), there is considerable (intrinsic) scatter in these relations. The above equations lead to 3 estimates of $L_{\mathrm{H}\alpha}$, namely

$$L_{\mathrm{H}\alpha(1)} = L_{[\mathrm{OII}]}\,10^{1.02}\,(W_{[\mathrm{OII}]})^{-0.65} \quad (5.14)$$

$$L_{\mathrm{H}\alpha(2)} = L_{[\mathrm{OII}]}\,10^{-1.61}\,10^{-0.09(M_B+5\log h_{50})} \quad (5.15)$$

$$L_{\mathrm{H}\alpha(3)} = L_{[\mathrm{OII}]}\,10^{-0.33}\,(W_{[\mathrm{OII}]})^{-0.46}\,10^{-0.06(M_B+5\log h_{50})} \quad (5.16)$$

These 3 estimates are plotted against each other in Fig. 5.14. A reasonable agreement is seen. Some scatter is expected, since the [OII] EW is not perfectly correlated with the B–band luminosity.

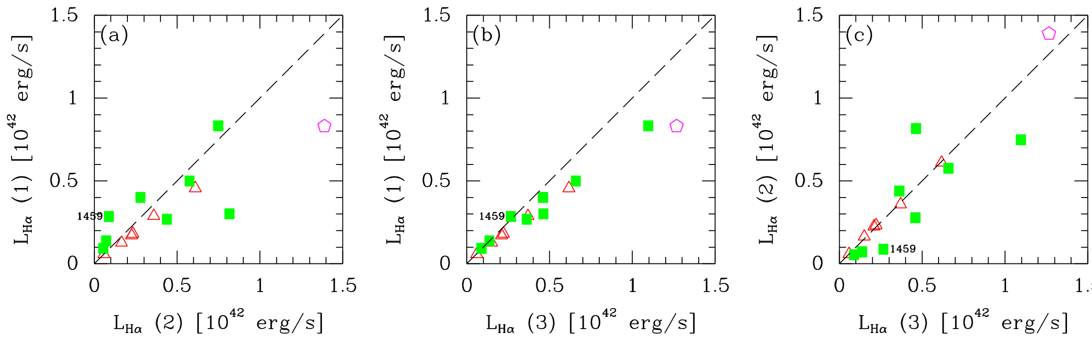

Figure 5.14: The 3 estimates of the non-extinction corrected Hα luminosity. Galaxy 1801 is off the scale of the plots. (Legend: see Fig. 5.13, p. 112.)

For $L_{\mathrm{H}\alpha^0}$ (i.e. extinction corrected), Aragón-Salamanca et al. (2003a) found

$$\log\left(\frac{L_{[\mathrm{OII}]}}{L_{\mathrm{H}\alpha^0}}\right) = -1.93 + 1.10\log W_{[\mathrm{OII}]} \qquad \mathrm{MAD} = 0.26 \quad (5.17)$$

$$\log\left(\frac{L_{[\mathrm{OII}]}}{L_{\mathrm{H}\alpha^0}}\right) = 3.05 + 0.18(M_B + 5\log h_{50}) \qquad \mathrm{MAD} = 0.22 \quad (5.18)$$

$$\log\left(\frac{L_{[\mathrm{OII}]}}{L_{\mathrm{H}\alpha^0}}\right) = 1.40 + 0.50\log W_{[\mathrm{OII}]} + 0.13(M_B + 5\log h_{50}) \qquad \mathrm{MAD} = 0.21 \quad (5.19)$$

[5]Here, MAD is defined as the mean absolute deviation from the sample median. The MAD is a 'robust' estimator of the scatter, meaning that it is less sensitive to outliers (i.e. to the tails of the parent distribution) than the rms.

This leads to 3 estimates of the extinction corrected Hα luminosity, i.e.

$$L_{\mathrm{H}\alpha^0(1)} = L_{[\mathrm{OII}]}\, 10^{1.93}\, (W_{[\mathrm{OII}]})^{-1.10} \tag{5.20}$$

$$L_{\mathrm{H}\alpha^0(2)} = L_{[\mathrm{OII}]}\, 10^{-3.05}\, 10^{-0.18(M_B+5\log h_{50})} \tag{5.21}$$

$$L_{\mathrm{H}\alpha^0(3)} = L_{[\mathrm{OII}]}\, 10^{-1.40}\, (W_{[\mathrm{OII}]})^{-0.50}\, 10^{-0.13(M_B+5\log h_{50})} \tag{5.22}$$

These 3 estimates are plotted against each other in Fig. 5.15. Substantial scatter is seen, particularly in panel (a), where estimate 1 (i.e. using $W_{[\mathrm{OII}]}$) is compared with estimate 2 (i.e. using M_B).

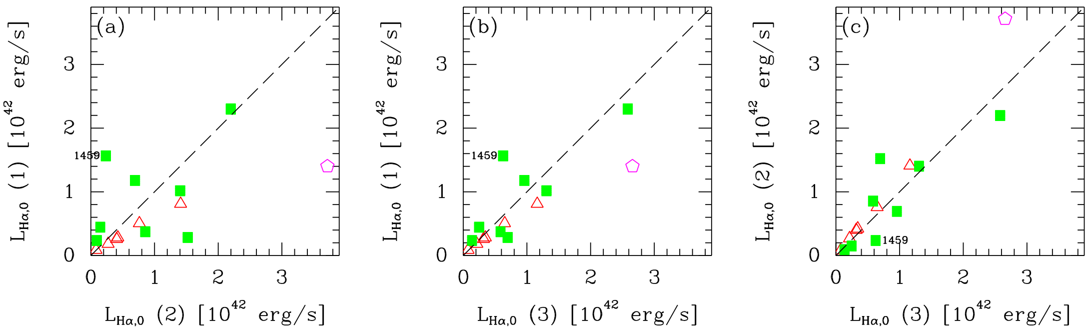

Figure 5.15: The 3 estimates of the extinction corrected Hα luminosity. Galaxy 1801 is off the scale of the plots. (Legend: see Fig. 5.13, p. 112.)

The 3 estimates of $L_{\mathrm{H}\alpha}$ and the 3 estimates of $L_{\mathrm{H}\alpha^0}$ are plotted against $L_{[\mathrm{OII}]}$ in Fig. 5.16 (p. 116). At least some of the estimates of $L_{\mathrm{H}\alpha^0}$ (and hence the SFR) show substantial scatter versus $L_{[\mathrm{OII}]}$. It will therefore not be redundant to plot the Tully–Fisher residuals versus both $L_{[\mathrm{OII}]}$ and the $L_{\mathrm{H}\alpha^0}$ estimates. No plots will be made using $L_{\mathrm{H}\alpha}$.

It should be noted that if using estimate 1, which only uses $W_{[\mathrm{OII}]}$, the residuals are correlated with M_B, and vice versa for estimate 2 (Aragón-Salamanca et al. 2003a). Estimate 3 is therefore likely to be the best estimate, since it uses both $W_{[\mathrm{OII}]}$ and M_B. The above-mentioned caveats about these relations only strictly applying to samples similar to the NFGS sample still apply.

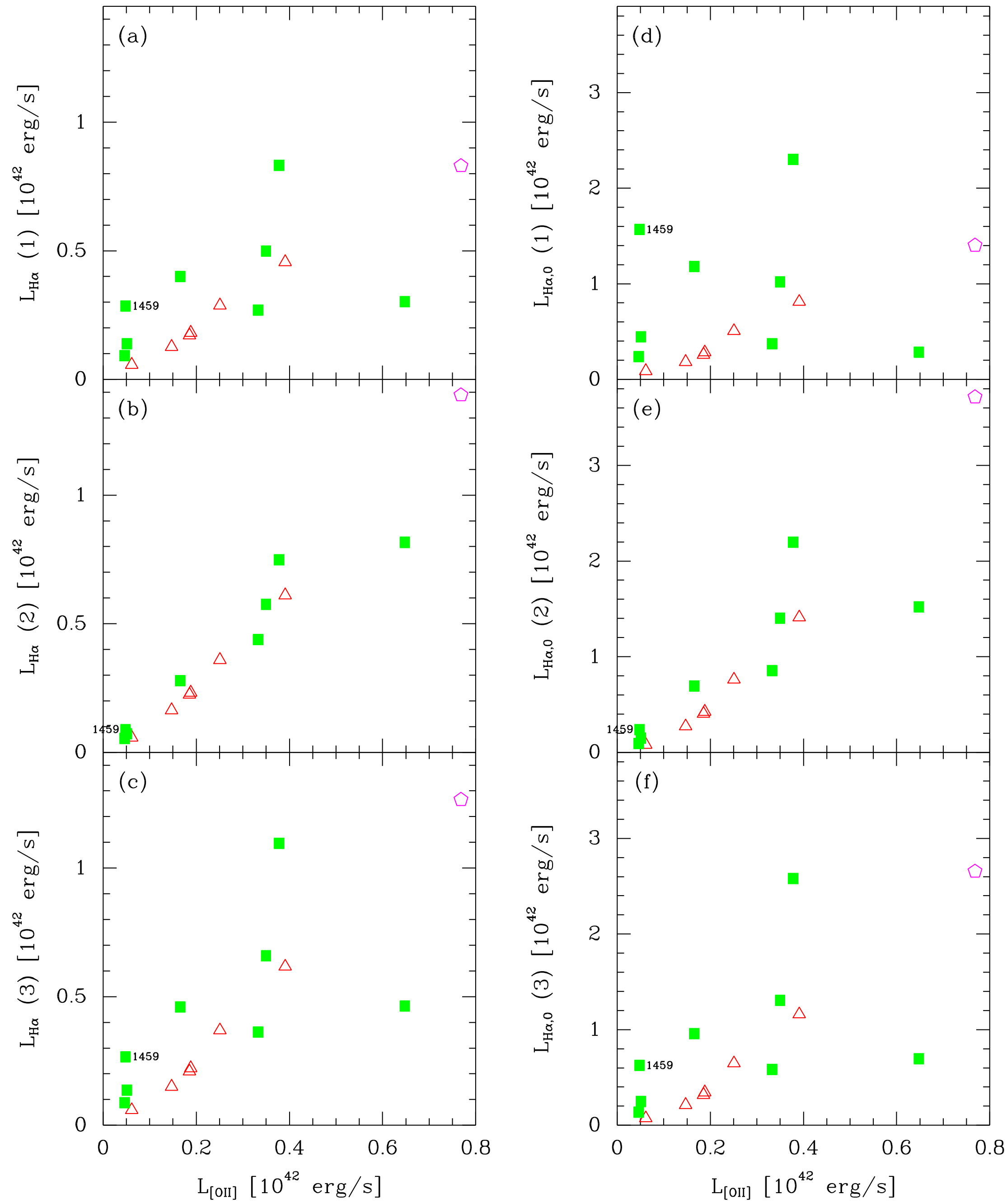

Figure 5.16: (a)–(c): The 3 estimates of $L_{\mathrm{H}\alpha}$; (d)–(f): the 3 estimates of $L_{\mathrm{H}\alpha^0}$. Galaxy 1801 is off the scale of the plots. (Legend: see Fig. 5.13, p. 112.)

In the following we plot the residuals from the B–band Tully–Fisher relation versus various quantities discussed above. In each figure, panel (a) will use the residuals themselves ($\Delta\mathrm{TF}_B$), while panel (b) will use the residuals corrected for the observed evolution of the zero point with redshift ($\Delta\mathrm{TF}_{B,\mathrm{corr}}$). The quantities used on the x–axis are

- $L_{[\mathrm{OII}]}$ (Fig. 5.17, p. 118)
- $L_{\mathrm{H}\alpha^0(1)}$ (Fig. 5.18, p. 119)
- $L_{\mathrm{H}\alpha^0(2)}$ (Fig. 5.19, p. 120)
- $L_{\mathrm{H}\alpha^0(3)}$ (Fig. 5.20, p. 121)
- $W_{[\mathrm{OII}]}$ (Fig. 5.21, p. 122)

Note that since the $L_{\mathrm{H}\alpha^0(2)}$ and $L_{\mathrm{H}\alpha^0(3)}$ estimates of the extinction corrected Hα luminosity depend weakly on the absolute magnitude (cf. Eq. 5.15 and 5.16, p. 114), the quantities plotted in the corresponding figures are not completely independent. Note also, that in the three $L_{\mathrm{H}\alpha^0}$ plots, an extra x–axis shows the SFR, obtained using the conversion

$$\mathrm{SFR} = 7.9 \times 10^{-42}\, M_\odot\,\mathrm{yr}^{-1}/(\mathrm{erg\,s}^{-1})\ L_{\mathrm{H}\alpha^0} \tag{5.23}$$

from Kennicutt (1998).[6]

On each panel of Fig. 5.17–5.21 results from Kendall's tau rank order correlation tests are given. The significance of a possible correlation is given as $P_{\mathrm{corr.}}$. The Kendall's tau coefficient is also given, and in the case of a significant correlation, the sign of tau indicates the direction. Tests have been done for the full cluster+field sample ($N = 14$) as well as for the cluster sample ($N = 7$) [galaxies 1459 and 1801 are still excluded from the analysis] and for the field sample ($N = 7$). What is seen from the correlation tests is that the B–band Tully–Fisher residuals are (anti–)correlated with $L_{[\mathrm{OII}]}$ at $\sim$90% confidence. Since $L_{[\mathrm{OII}]}$ is related to star formation, this already hints that a brightening due to enhanced star formation could be what is driving the B–band Tully–Fisher residuals. When the 3 estimates of $L_{\mathrm{H}\alpha^0}$ are used, the same (anti–)correlation in seen. When using estimate number 3, i.e. the estimate that uses both the [OII] equivalent width and the B–band luminosity, the correlation is detected at $> 95\%$ confidence (Fig. 5.20, p. 121). Since the $L_{\mathrm{H}\alpha^0}$ estimates might be a better proxy for the SFR than $L_{[\mathrm{OII}]}$, the fact that the significance using $L_{\mathrm{H}\alpha^0}$ is somewhat larger than when using $L_{[\mathrm{OII}]}$ could be taken as supporting the conclusion that the B–band Tully–Fisher residuals are driven by star formation.

Could the found anti–correlation between the B–band Tully–Fisher residuals and the [OII] luminosities be due to systematic errors in the rotation velocities? For the cluster galaxies, which are at a single redshift, galaxies with larger [OII] luminosities will have larger line intensities in ADU, and hence higher S/N (although the S/N will also depend on the spatial extend of the emission line and the photon noise from the sky and the continuum). Therefore, to explain the observed anti–correlation in this way, the derived rotation velocities for galaxies with *lower* S/N should be systematically *higher* (and vice versa), which seems counter intuitive. A stronger argument is that the

[6]The merger/peculiar galaxy 1801 is off the scale of the plots, since otherwise the spiral galaxies would get squeezed. The derived SFR for 1801 using the 3 different $L_{\mathrm{H}\alpha^0}$ estimates is 15, 72 and 40 $M_\odot\,\mathrm{yr}^{-1}$, respectively.

analysis of the internal consistency of the rotation velocities (see Fig. 3.15, p. 73), found no trend of the derived rotation velocity with the line intensity in ADU. Therefore, the found anti–correlation probably reflects a physical connection between the Tully–Fisher residuals in terms of a brightening and the star formation rate. No significant correlation is found between the *B*–band Tully–Fisher residuals and the [OII] equivalent width (Fig. 5.21, p. 122). These issues will be discussed in terms of stellar population models in the next section.

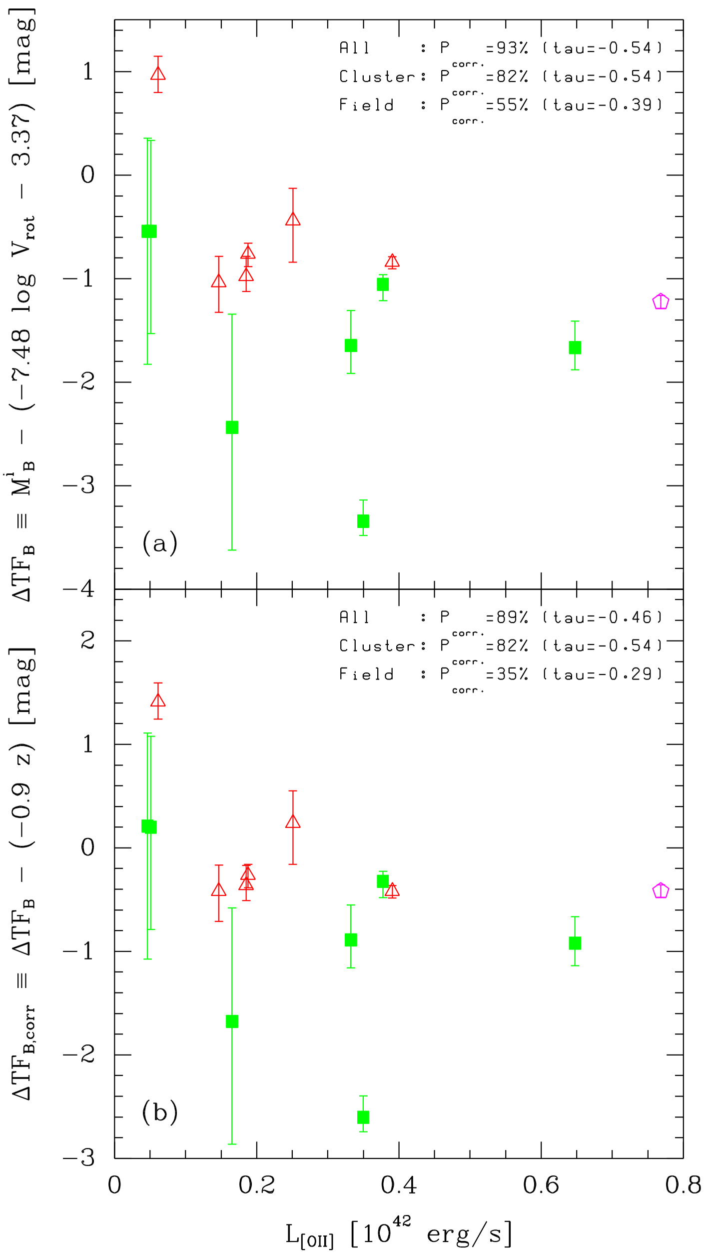

Figure 5.17: *B*–band Tully–Fisher residuals (panel a) and *B*–band Tully–Fisher residuals corrected for redshift evolution (panel b) versus [OII] luminosity. Correlation probabilities based on Kendall's tau tests are given on the panels. (Legend: see Fig. 5.13, p. 112.) Galaxies 1459 and 1801 are off the scale of the plots.

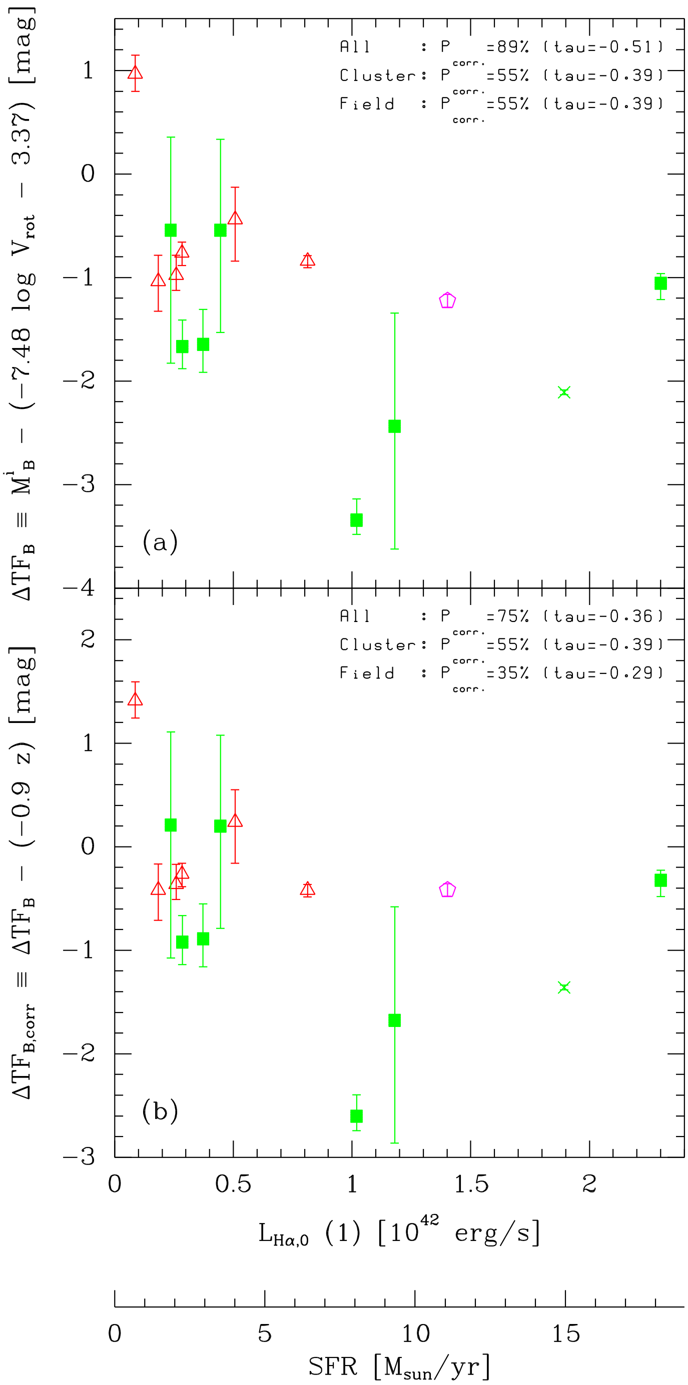

Figure 5.18: B–band Tully–Fisher residuals (panel a) and B–band Tully–Fisher residuals corrected for redshift evolution (panel b) versus an estimate of the extinction corrected Hα luminosity ($\rightarrow$SFR). This $L_{\mathrm{H}\alpha^0}$ estimate is based on $L_{[\mathrm{OII}]}$ and $W_{[\mathrm{OII}]}$. Correlation probabilities based on Kendall's tau tests are given on the panels. (Legend: see Fig. 5.13, p. 112.) Galaxy 1459 (but not 1801) is off the scale of the plots.

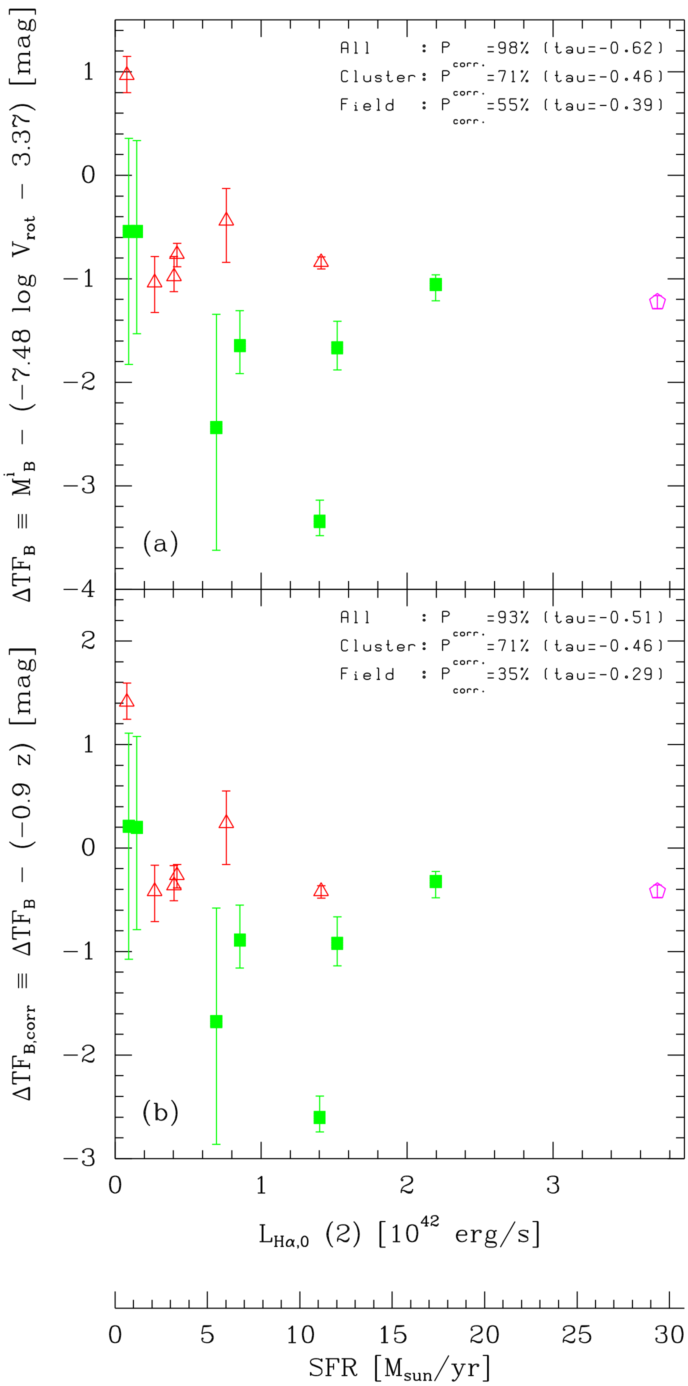

Figure 5.19: B–band Tully–Fisher residuals (panel a) and B–band Tully–Fisher residuals corrected for redshift evolution (panel b) versus an estimate of the extinction corrected Hα luminosity (→SFR). This $L_{\mathrm{H}\alpha^0}$ estimate is based on $L_{[\mathrm{OII}]}$ and M_B. Correlation probabilities based on Kendall's tau tests are given on the panels. (Legend: see Fig. 5.13, p. 112.) Galaxies 1459 and 1801 are off the scale of the plots.

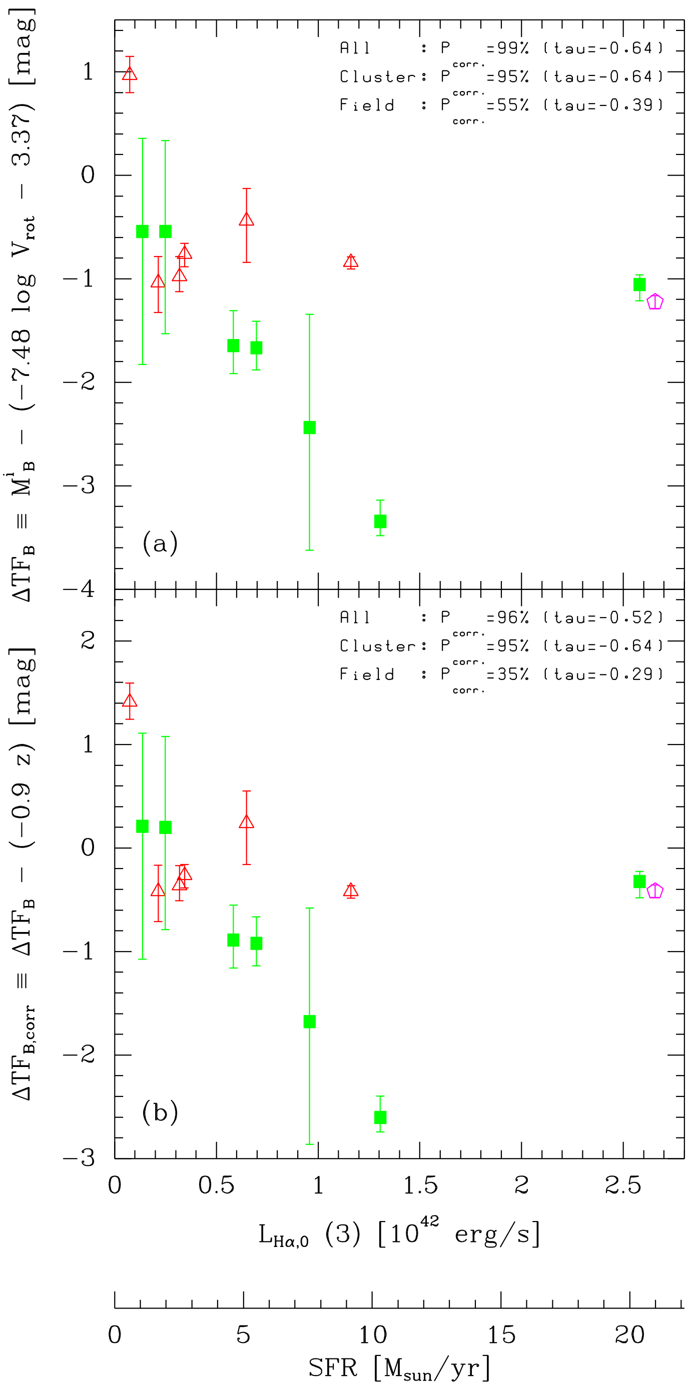

Figure 5.20: B–band Tully–Fisher residuals (panel a) and B–band Tully–Fisher residuals corrected for redshift evolution (panel b) versus an estimate of the extinction corrected Hα luminosity (→SFR). This $L_{\mathrm{H}\alpha^0}$ estimate is based on $L_{[\mathrm{OII}]}$, $W_{[\mathrm{OII}]}$ and M_B. Correlation probabilities based on Kendall's tau tests are given on the panels. (Legend: see Fig. 5.13, p. 112.) Galaxies 1459 and 1801 are off the scale of the plots.

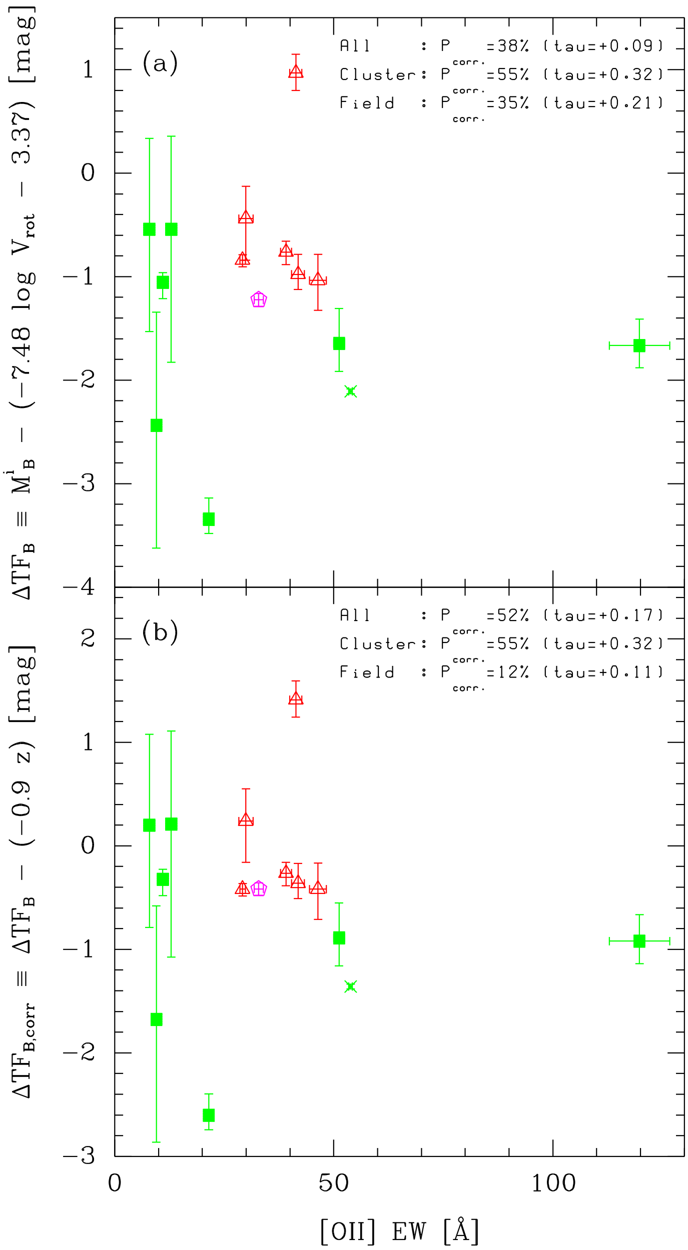

Figure 5.21: *B*–band Tully–Fisher residuals (panel a) and *B*–band Tully–Fisher residuals corrected for redshift evolution (panel b) versus [OII] equivalent width. Correlation probabilities based on Kendall's tau tests are given on the panels. (Legend: see Fig. 5.13, p. 112.) Galaxy 1459 (but not 1801) is off the scale of the plots.

5.6 Stellar population models

We will analyse the findings from the previous section using the stellar population models from Pérez-González et al. (2003). These model galaxies consist of 3 components: an underlying (static) population, a young (or burst) population that goes off at $t = 0$, and the gas which gives rise to emission lines after being photoionised by the young stars. The total mass of the galaxy has been normalised to $1\,M_\odot$, of which a fraction b is in the burst population (the mass of the gas is neglected). The properties of the underlying population (e.g., mass-to-light ratios, colours, Hα equivalent width) are fixed to typical values for a given galaxy type. Seven types are available: E, S0, Sa, Sb, Sc, Irr and BCD. The properties of the young population is calculated using evolutionary synthesis models, and the contributions from the strongest emission lines are calculated based on the predicted number of Lyman photons.

The models have a number of parameters, some of which are choices between different "recipes" (e.g. for the evolutionary synthesis), and some of which are more physical parameters (e.g. metallicity of the stars formed in the burst). We will fix the following parameters: Bruzual & Chalot (1999) [private comm. with Pérez-González et al.] evolutionary synthesis; instantaneous burst; Salpeter (1955) IMF; zero extinction; and solar metallicity for the newly formed stars. This leaves the burst strength b as the only free parameter. The various quantities predicted by the models (e.g. B–band luminosity or Hα equivalent width) can then be plotted versus time or versus each other.

The model tables were kindly provided by Pablo G. Pérez González. Model predictions are available for 4 photometric bands: B, r, J and K. No predictions are made for H, but since the rest-frame $(H - K)$ colour has a narrow range (0.28–0.36 for the 5 SEDs used in this work, cf. Sect. 4.2, p. 79) we approximate H as $K + 0.3$. No predictions are made for the [OII] emission line. Hα equivalent widths were tabulated, but not Hα luminosities. However, since the effective wavelength of the r–band practically coincides with Hα, the continuum luminosity at Hα can be calculated from the tabulated absolute magnitudes of the underlying and the young population. The r–band zero point was taken from Fukugita et al. (1995). The Hα luminosity can then be calculated from the equivalent width.

We want to use the models to analyse the observations. The main observables are the Tully–Fisher residuals. We will assume they reflect a change in absolute magnitude at a fixed rotation velocity ($\sim$dynamical mass), rather than a change in rotation velocity at fixed absolute magnitude. In using the models the hypothesis will be that negative Tully–Fisher residuals (indicating a brightening) are caused by a burst of some strength b occurring some time t prior to the observations. Consequently, the model parameter corresponding to the Tully–Fisher residuals is $\Delta M_B \equiv M_{B,\mathrm{total}} - M_{B,\mathrm{underl}}$, and similarly for the H–band. Since ΔM_B is a difference of magnitudes (which is related to a ratio of luminosities), it does not depend on the mass of the model galaxy. The predicted Hα equivalent width also does not depend of the mass of the model. However, the predicted Hα luminosity *does* depend on the mass; specifically, $L_{\mathrm{H}\alpha}$ scales linearly with the assumed stellar mass.

Model predictions as function of time are shown in Fig. 5.22. An underlying population of type Sc has been used. The plots for Sb and Irr look very similar. Five values of b are plotted, from 0.1% to 10%. Panel (a) shows the the change in B–band absolute magnitude, ΔM_B, while panel (b) shows ΔM_H. It is seen that the burst has a large impact on the broad band luminosities, and substantially more at B than at H.

As expected, the stronger the burst or the shorter the time since the burst, the larger the brightening. The range of B–band Tully–Fisher residuals seen for the high redshift cluster galaxies with respect to the high redshift field galaxies, ∼0–3 mag is spanned by the models. Panel (c) and (d) show the Hα equivalent width and luminosity. The effect of the burst on these two quantities is very dramatic indeed. The time scale is substantially smaller than for the broad band luminosities. It is seen that for a given mass the burst strength b is roughly proportional to the Hα luminosity and hence to the star formation rate an observer would infer. It is also seen that the Hα equivalent width does not depend strongly on the burst strength (∼SFR at a given mass) — the EW mainly measures the time since the burst. These properties could explain why a correlation is seen between the B–band Tully–Fisher residuals and the inferred Hα luminosities while no significant correlation is found between the B–band Tully–Fisher residuals and the [OII] EWs. In other words, the strong age dependence of the EWs could mask the underlying trend between B–band brightening and SFR. It should be noted that our [OII] EWs might not behave completely like the Hα EWs and that our estimated Hα luminosities might not be perfect. It should also be noted that the instantaneous burst model may be incorrect; however, our current observations do not allow us to constrain the star formation history in any detail.

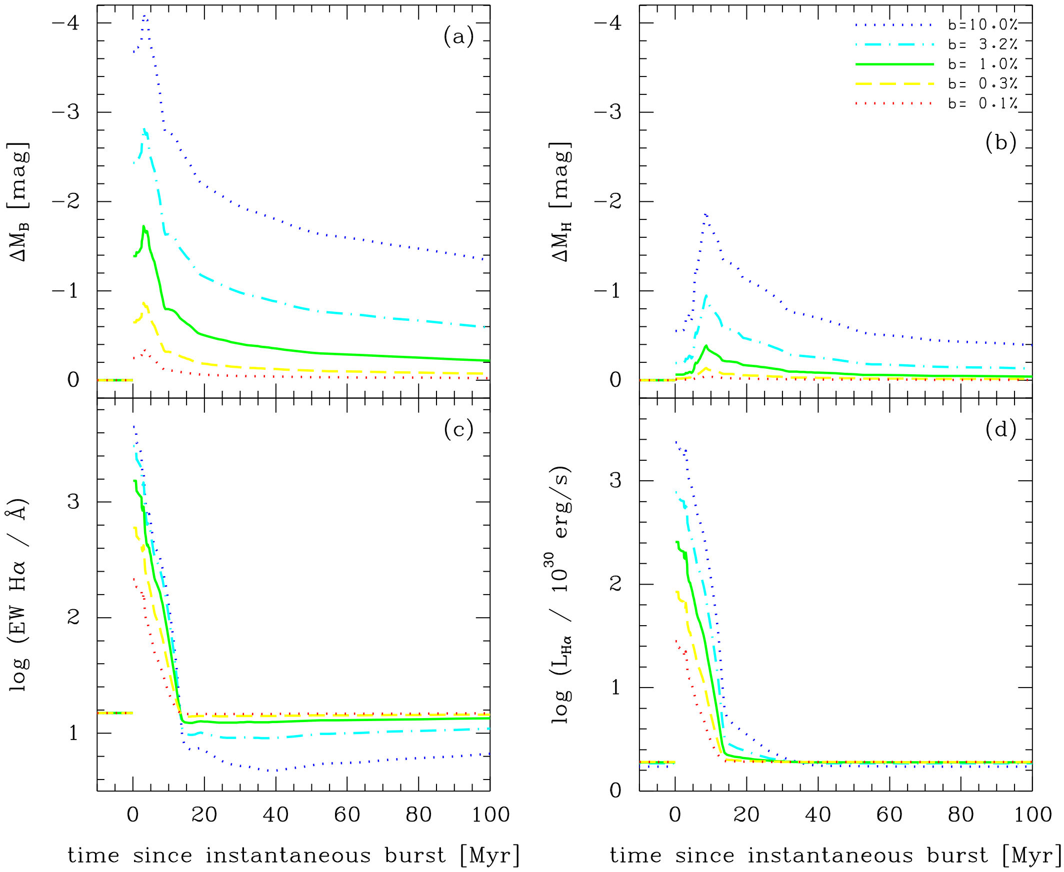

Figure 5.22: Predictions from the Pérez-González et al. (2003) models consisting of an underlying "Sc" population with an instantaneous burst superimposed. The mass of the model galaxy is 1 $M_{\odot}$, of which a fraction b is in the burst. Five models of varying burst strength b are shown. (a) Change in B–band magnitude with respect to the underlying population; (b) Same for the H–band; (c) log(EW Hα); (d) log($L_{\mathrm{H}\alpha}$).

Finally we investigate what brightening is predicted in the H–band relative to that in the B–band. This is shown in Fig. 5.23. The predicted H–band brightening is always smaller than the predicted B–band brightening. This is at variance with the observations which found the H–band brightening to be comparable to or slightly larger than the B–band brightening. This is obviously a very important cause for concern, but we stress that the H–band magnitudes are based on preliminary data and that they are not as reliable as the B–band magnitudes.

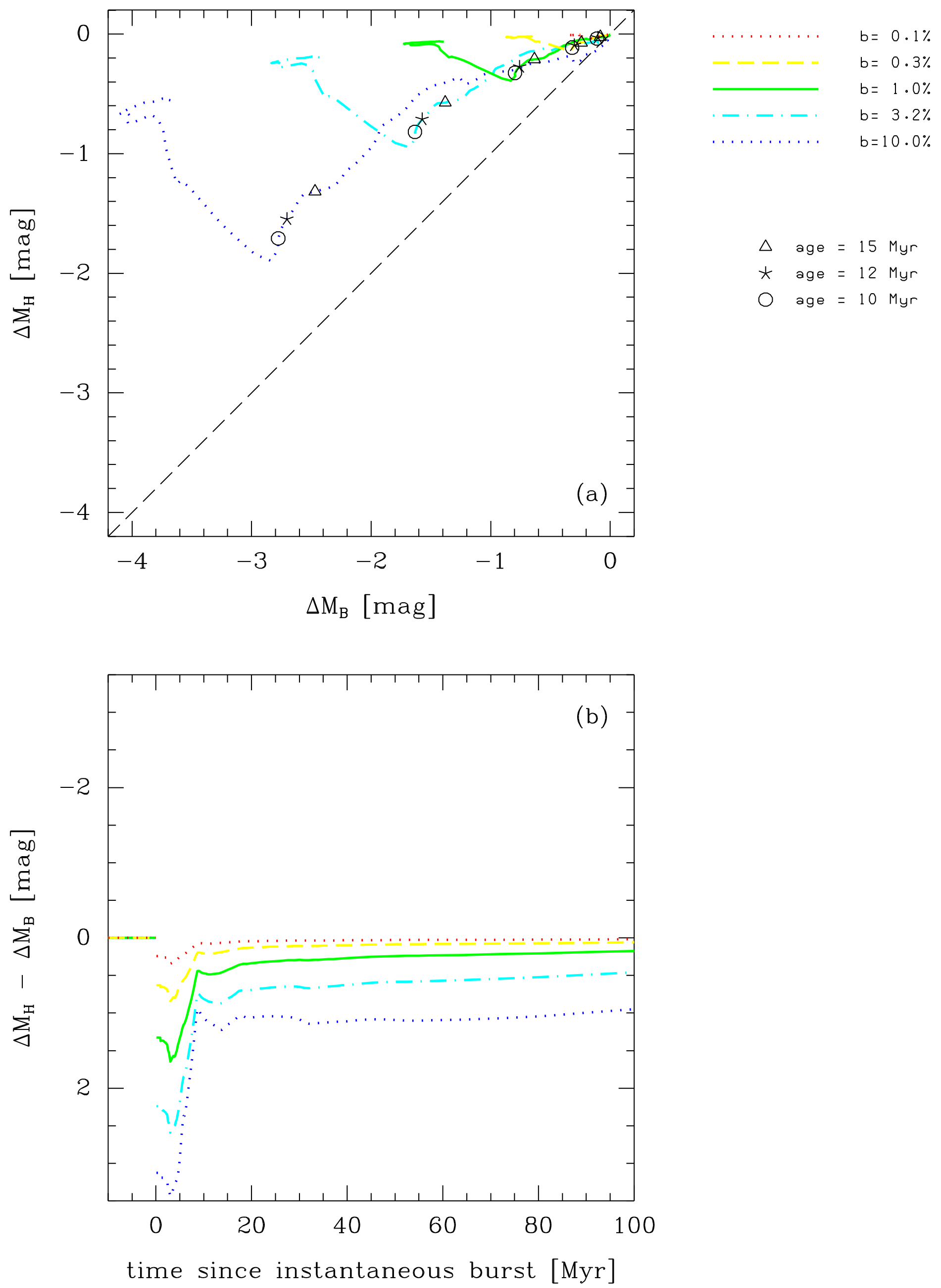

Figure 5.23: H–band brightening compared with B–band brightening for the Sc+burst model shown in Fig. 5.22. In panel (a) the black dashed diagonal line marks the one-to-one relation (i.e., the brightening being the same in B as in H).

The main observational results have been presented in this chapter. The next chapter summarises these results and the conclusions. Following this a number of future projects are outlined.

Chapter 6

Conclusions and future work

6.1 Summary and conclusions

We have observed high redshift cluster and field spirals galaxies using the FORS2 spectrograph at the VLT. The rich cluster MS1054−03 at $z = 0.83$ was targeted. Spiral galaxies were selected partly from the catalogue of known cluster members from van Dokkum (1999), and partly from the available HST images. From the obtained optical spectra of spatially resolved emission lines (e.g. [OII], Hβ and [OIII]), the projected rotation velocities $V_{\rm rot} \sin i$ were derived by fitting 2D model spectra to the data using the method of Simard & Pritchet (1998, 1999). The fits also give the exponential scale length for the line emitting gas, $r_{\rm d,spec}$. For galaxies with several emission lines observed, the derived values of $V_{\rm rot} \sin i$ and $r_{\rm d,spec}$ generally agreeded within the computed errors. Fits were done for 30 spiral galaxies with the slit along the major axis. Two galaxies were rejected due to the intensity profiles in the spectra being more extended than the exponential profile assumed in the model, and one galaxy was rejected due to peculiar kinematics. The remaining 27 spirals galaxies consisted of 8 MS1054−03 cluster members ($z \approx 0.83$) and 19 field galaxies at $z = 0.15$–0.90. For 15 of these spiral galaxies (at $z \gtrsim 0.5$), the [OII] equivalent width and line luminosity were measured. From the HST WFPC2 images total magnitudes in the F606W and F814W filters were determined, and rest-frame B–band magnitudes were calculated using SEDs for local galaxies. The HST images were also used to perform bulge/disk decomposition of the galaxies using the methods of Simard et al. (2002), yielding the line-of-sight inclination of the galaxies and the exponential scale length for the broad band stellar light, $r_{\rm d,phot}$. For the [OII] subsample rest-frame H–band magnitudes were estimated using preliminary NIR ground based magnitudes.

From the analysis of the data, the following was found.

- In the B–band Tully–Fisher plot of log rotation velocity versus absolute B–band magnitude, most of the galaxies in the sample were on the high luminosity / low velocity side of the local Tully–Fisher relation (TFR) from Pierce & Tully (1992). Only a single galaxy (A/F03 at $z = 0.22$) had to be excluded from the analysis solely because it deviated from the rest of the galaxies. A galaxy that hosted an AGN was excluded on that account.

- The residuals in absolute magnitude from the local B–band TFR, ΔTF, were plotted versus redshift. At 93% significance ΔTF decreased with redshift for the field galaxies. A linear chi-square fit constrained to have zero intercept gave

$\Delta \mathrm{TF}_B = (-0.9 \pm 0.3)z$. If the Tully–Fisher residuals are interpreted as a change in luminosity at a fixed velocity rather than vice versa, this fit indicate that the high z field spirals are brighter than the low z ones. There are a number of caveats to this simple interpretation, including the dependence on cosmology and the possibility of a changing TF slope with redshift (for which Ziegler et al. 2002 found some evidence).

- Statistical tests were carried out to investigate a possible difference in the Tully–Fisher residuals between the cluster spirals and the field spirals. The mean value of the TF residuals was found to be $\sim$1 mag more negative for the cluster galaxies compared to the field galaxies at 1.5–2σ significance. If the TF residuals are interpreted as a luminosity change, this means that the cluster spirals in the sample on average are $\sim$1 mag brighter in B than the field spirals. The exact brightening and significance depend on what field sample is used for reference, and whether the apparent redshift evolution of the TF zero-point for the field sample is taken out. It should be noted that this comparison is done *within* our data set, making possible systematic errors in e.g. the rotation velocities cancel out to some extent.

  In this interpretation of the cluster–field difference, the increment in luminosity could be the result of enhanced star formation in spiral galaxies falling onto the cluster.

  It should be noted that the statements in this work about a cluster–field difference applies to those spirals that have emission lines with a certain minimum flux allowing the rotation velocities to be measured. This in turn implies that star formation at some level has to be on-going and that dust is not attenuating the emission lines completely.

  No other studies of the Tully–Fisher relation for cluster galaxies at this redshift have been reported in the literature. Two studies at somewhat lower redshift, $z = 0.3$–0.5, based on a comparable small number of cluster galaxies, have not found the cluster–field difference that we find some evidence of. The larger look-back-time of our study could be the reason that we find some evidence for a cluster–field difference.

- No correlation was found between the B–band Tully–Fisher residuals and the ratio of the gas scale length ($r_{\mathrm{d,spec}}$) to star scale length ($r_{\mathrm{d,phot}}$). This was taken as sign that the derived rotation velocities were not biased downwards by a possible truncation of the gas disk. As another safety check, the TF residuals were found not to correlate significantly with inclination.

- The field galaxies were compared to the samples of high redshift field galaxies from Ziegler et al. (2002) and Barden et al. (2003). The Ziegler et al. sample was found to be brighter than our sample at a fixed rotation velocity. However, the difference was not significant when only considering galaxies in the luminosity range of our cluster galaxies. The Barden et al. sample was also found to be brighter than our sample at a fixed rotation velocity. This difference was significant at the 2σ level (this would decrease somewhat when taking into account a possible error in the Galactic extinction correction applied by Barden et al.). The (small) differences seen between the various studies could be due to systematic differences in the determined rotation velocities. It would be highly valuable to apply the various methods to the same data to quantify such systematic differences.

For the one galaxy in common between us and Barden et al. their rotation velocity is lower than ours, but the difference is within the quoted errors, with their error being substantially larger than ours.

- The B–band Tully–Fisher residuals were plotted versus clustercentric distance. No correlation was found for the cluster galaxies. No correlation was found for the field galaxies, as expected. Due to measurement errors and the dilution of a possible signal by projection effects, larger samples will be needed to test if the Tully–Fisher residuals for the cluster galaxies are correlated with clustercentric distance or projected density. Such studies could potentially give clues to the physical mechanism responsible for the brightening of some of the cluster spirals that we may be seeing.

- Using the preliminary H–band magnitudes for the subset of galaxies with these magnitudes available, the H–band Tully–Fisher relation was studied. A cluster–field difference slightly larger than what was seen in the B–band was found. This is not what is expected from the instantaneous burst models of Pérez-González et al. (2003). Taken alone and at face value, the B versus H–band results point to the Tully–Fisher residuals being driven by differences in velocities at a fixed luminosity rather than the opposite. The results from the H–band data need to be taken with perhaps more caution than the ones for the B–band because the H–band magnitudes are preliminary (and we do not have access to the final ones yet, nor the images) and the transformation from the near–IR magnitudes to H is somewhat more uncertain than from F814W to B. It will be extremely important to repeat the test when the NIR data is finally published. If the result holds, we may need to re-think the interpretation.

- The velocity–size diagram was studied, where 'size' refers to the stellar disk. Only one out of four statistical tests showed a hint of a cluster–field difference. The tentative conclusion is that there are no major differences between cluster and field galaxies in terms of the structure of the galaxies, i.e. the size of the stellar disk at a given rotation velocity ($\sim$mass). If the cluster–field difference found in the B–band Tully–Fisher plot is interpreted as a luminosity effect, the conclusion is that cluster and field spirals in our sample are structurally similar, but that the cluster galaxies on average have lower mass-to-light ratios, possibly indicative of a higher recent star formation. Furthermore, the physical mechanism responsible for the brightening must mainly affect the gas disk and not the stellar disk. Interactions with the intra-cluster medium is one such mechanism that is expected only to affect the gas disk, while gravitational interaction (galaxy–galaxy or galaxy–cluster) could affect both the gas disk and the stellar disk.

- The gas scale lengths derived from the spectra independently from the stellar scale length derived from the broad band images put us in the rather unique position to discuss the spatial extend of the gas that gives rise to the observed emission lines. The two scale lengths, $r_{\mathrm{d,spec}}$ and $r_{\mathrm{d,phot}}$, are found to be highly correlated (at >99.99% significance), strongly suggesting that the derived gas scale lengths are meaningful. The ratio of the two scale lengths, $r_{\mathrm{d,spec}}/r_{\mathrm{d,phot}}$, is found to take on value compatible with what is seen locally (Ryder & Dopita 1994). The median value in our sample is 1.1. The mean value for the cluster galaxies is found to be lower than the mean value for the field galaxies, particularly so when only considering field galaxies in the luminosity range of the cluster galaxies. This could be interpreted as indicating that the star formation is more centrally concentrated in the cluster galaxies than in the field galaxies in the sample, a phenomenon found locally by Moss & Whittle (2000). The implication is that the cluster environment probably is affecting the star-formation regime in cluster galaxies over a large cosmic epoch (i.e. over a large redshift range). Within individual galaxies, more star-formation occurs near the centre of the galaxies in cluster galaxies. This phenomenon could be explained by the interaction of the galaxy gas with the intra-cluster medium or with other galaxies or with the cluster potential, all of which could drive the gas towards the centre through dynamical instabilities and thus produce more concentrated star formation.

- The hypothesis of a brightening of the cluster spirals being due to enhanced levels of star formation was tested directly by using the observed [OII] luminosities. The [OII] luminosity is correlated with the star formation rate (SFR), although there is also a dependence on the excitation state and metallicity of the gas. The B–band Tully–Fisher residuals were found to be anti–correlated with the [OII] luminosities, as expected from the above-mentioned hypothesis. Furthermore, estimates of the extinction corrected Hα luminosity, which is a better indicator of the SFR, were derived using empirical relations from Aragón-Salamanca et al. (2003a). The B–band Tully–Fisher residuals were found to be anti–correlated with these estimated extinction corrected Hα luminosities at >95% confidence, strengthening the case for explaining the B–band Tully–Fisher residuals as due to the enhanced star formation in the cluster spirals. We find no indications that this results could be due to the varying signal-to-noise of the observations.

- No significant correlation was found between the B–band Tully–Fisher residuals and the [OII] equivalent widths (EWs). In the light of the instantaneous burst models of Pérez-González et al. (2003), the explanation could be that the EW mainly measures the time since the burst and only to a lesser extend the strength of the burst ($\sim$the SFR at a given mass).

Overall, we see tantalizing evidence of a cluster–field difference in the sample of high redshift spirals for which rotation velocities can be measured from optical emission lines. Most indicators favour an explanation in terms of a brightening due to enhanced star formation. However, the H–band Tully–Fisher results (based on preliminary data) is the 'odd one out' favouring an explanation in terms of differences in velocities (real or due to errors).

A brightening of the cluster spirals is consistent with the idea that spiral galaxies falling into clusters undergo a burst of star formation before star formation is truncated and the morphology subsequently changed to S0. The later stages of this transformation is the subject of future work, which is described in the following section.

6.2 Future work

The current study has yielded interesting but somewhat tentative results due to the small sample of just 7 high redshift cluster spirals. We are currently in the process of increasing the number of high z cluster spirals with measured rotation velocities by more than an order of magnitude. The sample will also cover a range of redshifts and cluster properties. We are furthermore pursuing complementary avenues to investigate the possible transformation of high z spirals to low z S0s in clusters. These studies include both the putative end product, i.e. the low z S0s, and the possible intermediate stage of the process, i.e. the k+a galaxies at intermediate z with spiral morphologies. These different projects will be described below.

6.2.1 Cluster spirals at $z = 0.2$–0.6 with the VLT and Subaru

We have been successful in getting time on the VLT[1] and on Subaru[2] to study a further set of 8 clusters at $z = 0.2$–0.6. All clusters have extensive HST imaging available and other data from the literature (e.g. redshifts and NIR imaging). The clusters are moderately to very rich, as judged e.g. by the velocity dispersions, see the data in Table 6.1. The clusters were X–ray selected or optically selected as galaxy overdensities. The chosen redshift range was selected to get an evolutionary sequence, which is important.

The VLT observations (Sep 2002) were similar to those described in this work, except a more efficient grism (600RI) was used along with a new CCD system giving a wider wavelength coverage ($\sim$5000–8400 Å). As in this study, the slits were $1''$ wide and aligned with the major axes of the galaxies. The seeing was in the range 0.7–$1.1''$. Thus, the spatial resolution in physical units is better than for the data used in this work. At Subaru similar observations were secured in Aug 2002 using the FOCAS spectrograph. The main difference was that the slits were only $0.6''$ wide. This was done to get a reasonable spectral resolution with the 300B grism, namely $R \sim 700$ (covering $\sim$4700–9400 Å), but it was a wonderful match to the very good seeing of typically $0.5''$. Seeing values down to $0.3''$ were observed for several hours. The excellent spatial resolution of the Subaru data will allow the validity of the various intrinsic rotation curves used in the analysis (currently flat or 'universal') to be tested.

The clusters observed and the number of masks used are listed in Table 6.1. For the cluster MS2053$-$04 ($z = 0.56$) some galaxies were observed both with the VLT and with Subaru, which will enable important consistency checks. It should also be noted Böhm, Ziegler, Jäger, et al., who have published a conference paper on the Tully–Fisher relation for cluster spirals in two clusters at $z = 0.3$–0.5 (Ziegler et al. 2003), are working on a paper that will include 5 more cluster at $z = 0.3$–0.6 (Böhm, private communication). One of these clusters is CL0016+16 ($z = 0.54$) which we have also observed. This will enable further consistency checks.

The reduction of the VLT data is well underway, carried out by Steven Bamford in Nottingham, who will lead the analysis of that data set. Our VLT and Subaru data will increase the number of cluster spirals with rotation velocities by an order of magnitude compared to the sample in this thesis. A similarly large field sample will

[1]Investigators: B Milvang-Jensen, A Aragón-Salamanca, G Hau, I Jørgensen, J Hjorth

[2]Investigators: N Arimoto, A Aragón-Salamanca, B Milvang-Jensen, C Ikuta, Y Yamada, M Onodera

Table 6.1: Clusters observed with the VLT and Subaru

Name	z	$N_{\rm masks}$ VLT	$N_{\rm masks}$ Subaru	σ [km s^{-1}]	kT [keV]	L_x [10^{44} erg s^{-1}]
MS0440+02	0.19	3	–	606	5.3	7.4
A2390	0.23	–	2	1093	11.1	63.5
AC114	0.31	2	–	1649	9.8	38.1
A370	0.37	2	–	1340	7.1	20.8
MS1621+26	0.43	–	2	793	–	8.2
CL0016+16	0.54	–	2	1234	8.0	28.1
CL0054−27	0.56	2	–	<742	–	–
MS2053−04	0.58	2	1	817	8.1	7.9
MS1054−03	0.83	2	–	1170	12.3	19.9

Note: Velocity dispersions and X–ray temperatures and luminosities have been taken from the compilations of Hoekstra et al. (2002), Girardi & Mezzetti (2001) and Wu et al. (1999) for MS2053−04, CL0054−27 and the rest of the clusters, respectively. Please see the these references for the original references.
All clusters observed 2002, except MS1054−03 (this work) which was observed 2001.

also be available. This will allow the study of cluster-to-cluster variations and trends with cluster redshift. More subtle effects can be studied by stacking several clusters.

6.2.2 The EDisCS project: cluster galaxies at $z = 0.5$–0.8

A different approach to the above in selecting distant clusters was used in the Las Campanas Distant Cluster Survey (Gonzalez et al. 2001; see also Gonzalez et al. 2002). In this survey, a large region of the sky was imaged in a single very wide optical passband. Resolved objects (low redshift galaxies and foreground stars) were removed, and high redshift clusters were identified as overdensities of the remaining diffuse light due to unresolved high redshift objects. Twenty clusters from this survey is currently being studied by the ESO Distant Cluster Survey (EDisCS), a large international collaboration headed by Simon White[3]. EDisCS is a so-called ESO large programme, which means it has been awarded a large amount of telescope time (22 nights on the NTT and 36 nights on the VLT) over a two year period of time. This project is in many ways a superset of our own spiral–focused high z cluster project. The EDisCS aims to study high redshift cluster galaxies of all types, and that both in terms of kinematics (rotation velocities or velocity dispersions), stellar population properties (e.g. colours and emission and absorption line strengths) to infer star formation and chemical enrichment histories, and morphologies (e.g. via bulge/disk decomposition). Photometric redshifts were used to target the cluster population in the spectroscopic observations, but a large sample of field galaxies was nevertheless observed simultaneously with the cluster sample and thus forming an ideal reference sample. Finally, the observations will be compared directly to the high resolution N–body simulations / semi-analytical

[3]The full collaboration consists of: A Aragón-Salamanca, R Bender, P Best, M Bremer, S Charlot, D Clowe, J Dalcanton, M Dantel, G De Lucia, V Desai, B Fort, C Halliday, P Jablonka, G Kauffmann, Y Mellier, B Milvang-Jensen, R Pelló, B Poggianti, S Poirier, H Röttgering, G Rudnick, R Saglia, P Schneider, L Simard, S White, D Zaritsky

models that are being run by members of the collaboration.

Ten clusters at $z \sim 0.5$ and ten clusters at $z \sim 0.8$ were selected from the Las Campanas Distant Cluster Survey. The first phase of EDisCS was multi-band optical and NIR imaging of the clusters using 14 VLT nights and 22 NTT nights. The seeing was good, typically $0.6''$ in the optical and $0.7''$ in the NIR. Photometric redshifts were calculated and used for the target selection for the second spectroscopic phase. The target selection was conservative, i.e. it aimed at rejecting very few cluster members, at the expense of a substantial field contamination, which turned out to be just under 50%. No morphological information was used in the target selection. The spectroscopic observations were done in the spring of 2002 and 2003. In 2002 the project had 8 usable nights with good seeing, $\sim 0.8''$. The setup was as for the data in this thesis. In 2003 the project had 11 nights, all usable, with excellent seeing, ~ 0.6–$0.7''$ (and down to $0.4''$). The setup was as for our own recent VLT spectroscopy.

Recently, the EDisCS team was successful in being awarded HST time to image the ten high redshift clusters with the ACS camera. An area of $5' \times 5'$ will be covered by a tile of 4 pointings. These clusters are mostly at $z = 0.7$–0.8, although the redshifts extend down to 0.54. The observations are on-going at the moment and the first reduced image has just been produced. The HST data will be a fantastic asset for an already impressive data set.

The 2002 spectroscopic data has been reduced to the point of having wavelength calibrated sky-subtracted 2D spectra available for each slit. The data are thus ready to be subjected to the 2D emission line fitting (cf. Ch. 3). The fitting can in principle be started right away, although it might be preferable to wait briefly for the HST–based inclinations to be available for the high redshift clusters. The inclinations are needed to construct the synthetic spectra and have a non-negligible effect when the size of the slit is comparable to the size of the galaxy. The 2002 data set includes 5 clusters for which 3 spectroscopic masks were observed. Typically each mask gave 22 usable galaxy spectra of which 13 were cluster members. These 5 clusters are at $z = 0.54$, 0.70, 0.70, 0.75 and 0.80 and will all have HST imaging. This subset of the EDisCS data alone will provide a major improvement at $z \sim 0.7$ for Tully–Fisher studies in clusters and in the field for that matter.

A range in cluster richness is found in the EDisCS sample. The 4 $z = 0.7$–0.8 clusters with spectroscopy from 2002 have velocity dispersions in the range 450–1050 $\mathrm{km\,s^{-1}}$, i.e. generally smaller than for the clusters discussed in the previous section. Coupled with the different cluster selection method, the EDisCS sample will contribute important knowledge about galaxy evolution in clusters that are not necessarily relaxed systems with a very luminous and hot X–ray intra-cluster gas.

6.2.3 The Tully–Fisher relation of low redshift S0 galaxies

If the picture of the morphological transformation of spirals into S0s is correct, then signs of their spiral origin should be present in S0s a low redshift. One way of studying this is to examine the Tully–Fisher plot for S0s. This is challenging since the rotation velocities have to be determined from the absorption lines, which require long integration times to get an adequate S/N. The analysis of the spectra is complicated by the contribution from random motions to the line-of-sight velocity distribution (the so-called asymmetric drift, Binney & Tremaine 1987).

Previous attempts at studying the Tully–Fisher plot for S0s have reached rather different conclusions, see Fig. 6.1. Neistein et al. (1999) found very little indication of any sort of TFR in their data, while Mathieu et al. (2002), using a sophisticated analysis technique, did find evidence of a much tighter TFR. The difference could be due to the less sophisticated analysis of the poorer archival data of Neistein et al., or it could be due to sample differences. Both samples were a heterogeneous collection of field, group and cluster S0s.

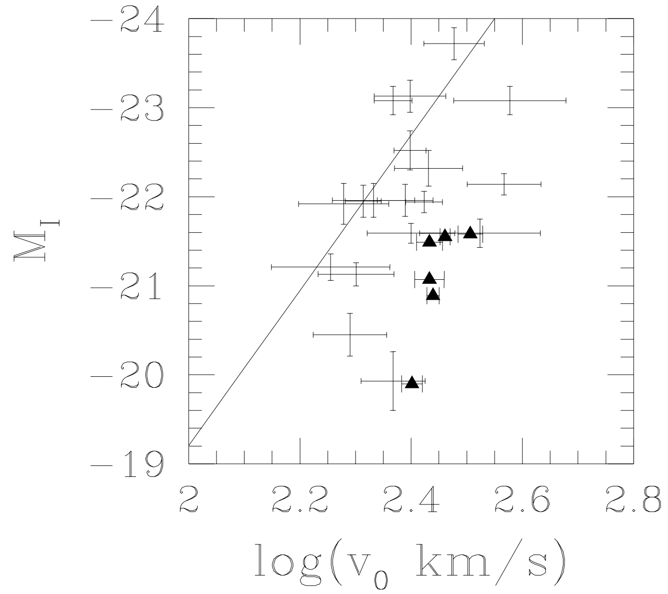

Figure 6.1: The existing attempts at defining a Tully–Fisher relation for S0 galaxies. The error bars show the data from Neistein et al. (1999) while the triangles are from Mathieu et al. (2002). The line shows the spiral galaxy Tully–Fisher relation.
This figure is from our proposal.

For some of the S0 galaxies shown in the Tully–Fisher plot luminosity weighted mean ages have been determined by Terlevich & Forbes (2002) using line indices from a variety of literature sources. In Fig. 6.2 the Tully–Fisher residuals are plotted versus age, and a trend is seen in which the largest fading from the TFR is found for the oldest ages. This makes sense in a picture of spiral to S0 transformation in which a burst occurs at the time of the transformation — the luminosity weighted mean age will roughly measure the time since this burst, and galaxies for which the burst took place a long time ago will have had a longer time to fade. This trend with age could also imply that some of the scatter seen in the Neistein et al. data could be due to age variations.

The heterogeneous nature of the currently available samples, data and analyses prevents any solid conclusions from being reached. On this background we proposed to obtain high S/N VLT spectra of a well defined magnitude limited sample of 11 S0s in the Fornax cluster[4], a sample for which already derived ages (Kuntschner & Davies 1998; Kuntschner 2000) showed a large range. The proposal was accepted, and the observations were carried out in service mode in the period Oct 2002 – Mar 2003. The data has just arrived. ESO was able to observe 9 of the 11 galaxies in the sample. A new postdoc in Nottingham will lead the work on these data.

[4]Investigators: B Milvang-Jensen, A Aragón-Salamanca, M Merrifield, R Peletier, K Kuijken

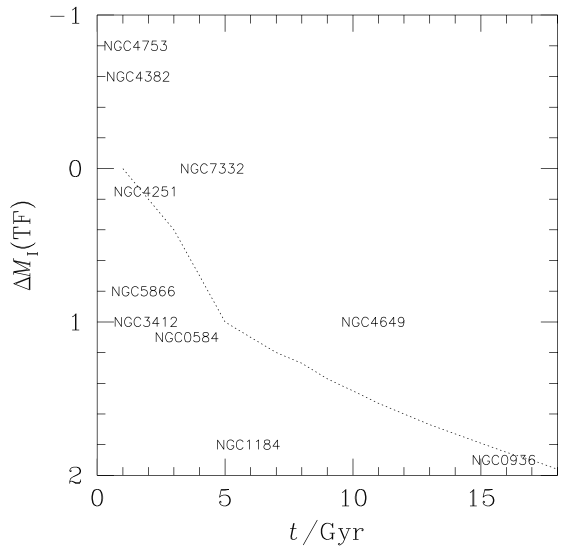

Figure 6.2: The departure in luminosity from the spiral galaxy Tully–Fisher relation as a function of galaxy age (as estimated from line strength indices) for the few galaxies in Fig. 6.1 for which the data exists. The line shows the fading of a single burst of stars as a function of time, as calculated from Worthey's (1994) population synthesis models. This figure is also from our proposal.

6.2.4 The intermediate phase: k+a galaxies

Our group is also planning to study the *transition phase* of the possible spiral to S0 transformation. In an ESO proposal just submitted[5] we propose to obtain integral field spectroscopy of 6 k+a galaxies in clusters at $z = 0.31$, the likely epoch to 'catch the galaxies in the act' of transforming, so to speak. The VIMOS spectrograph will be used, with $0.33''$ pixels and with a required service mode seeing of $\leq 0.6''$. Since the 'k' and 'a' populations have different spectral signatures it will be possible to study the dynamics and stellar populations of these two populations separately. This will shed light on the responsible transformation mechanisms. For instance, if ram-pressure removes the halo gas while compressing/disturbing the disk gas and inducing star-formation, we expect the young stars to be distributed over the galaxy disk, but with increased central concentration since disk instabilities would drive the gas towards the centre. On the other hand, a merger would lead to a more chaotic spatial distribution of the young stars. The dynamics will also help to identify the transformation mechanisms. A strong rotational component in the dynamics of the galaxy would suggest an environmental cause (such as ram-pressure), which does not particularly disturb the stellar disk. Alternatively, a merger is naturally expected to produce a galaxy supported mainly by random motions. Moreover, comparing the dynamics for the young and the old populations will provide an additional test. For a mechanism such as ram-pressure one would expect the dynamics for both young and old populations to be reasonably similar, although a slightly higher rotation would be expected for the young stars, since random motions would have had less time to develop than for the old stars. On the contrary, the young population will have a greater random component (i.e. lower rotation) in the post-merger case.

[5]Investigators: S Bamford, A Aragón-Salamanca, B Milvang-Jensen, M Merrifield

6.2.5 Hα observations of the MS1054−03 galaxies with Subaru

We have just submitted a proposal[6] to observe Hα for the 7 MS1054−03 cluster spirals and the 7 high redshift field spirals studied in this thesis. The purpose is to derive star formation rates directly from Hα, yielding much less uncertain SFR estimates than when using [OII]. These Hα data will allow the suggestive trend seen in this work between the Tully–Fisher residuals and our [OII]–based SFRs to be clarified.

We hope that with this programme of complementary studies we will be able to firmly pin down the evolution of spiral galaxies in clusters and to definitely test the hypothesis that a wholesale spiral to S0 morphological transformation has taken place.

[6] Investigators: A Aragón-Salamanca, N Arimoto, C Ikuta, S Bamford, B Milvang-Jensen

Bibliography

Aaronson, M., Huchra, J., & Mould, J. 1979, ApJ, 229, 1

Aaronson, M., Huchra, J., Mould, J. R., Tully, R. B., Fisher, J. R., van Woerden, H., Goss, W. M., Chamaraux, P., Mebold, U., Siegman, B., Berriman, G., & Persson, S. E. 1982, ApJS, 50, 241

Abadi, M. G., Moore, B., & Bower, R. G. 1999, MNRAS, 308, 947

Andreon, S. 1998, ApJ, 501, 533

Aragón-Salamanca, A. 1991, Ph.D. Thesis, Durham University

Aragón-Salamanca, A., Alonso-Herrero, A., Gallego, J., García-Dabó, C. E., Gil de Paz, A., Pérez-González, P. G., & Zamorano, J. 2003a, AJ, submitted

Aragón-Salamanca, A., Alonso-Herrero, A., Gallego, J., García-Dabó, C. E., Pérez-González, P. G., Zamorano, J., & Gil de Paz, A. 2003b, in Star Formation Through Time, in press (astro–ph/0210123)

Aragón-Salamanca, A., Ellis, R. S., Couch, W. J., & Carter, D. 1993, MNRAS, 262, 764

Avila, G., Rupprecht, G., & Beckers, J. M. 1997, in Proc. SPIE Vol. 2871, p. 1135-1143, Optical Telescopes of Today and Tomorrow, Arne L. Ardeberg; Ed. (available from `http://www.eso.org/instruments/fors/Papers/Spie_96/ladc_paper.ps.gz`), Vol. 2871, 1135–1143

Balogh, M. L. & Bower, R. G. 2002, in Galaxy Evolution: Theory and Observations, in press (astro–ph/0207358)

Balogh, M. L., Morris, S. L., Yee, H. K. C., Carlberg, R. G., & Ellingson, E. 1997, ApJ, 488, L75

Balogh, M. L., Navarro, J. F., & Morris, S. L. 2000, ApJ, 540, 113

Balogh, M. L., Schade, D., Morris, S. L., Yee, H. K. C., Carlberg, R. G., & Ellingson, E. 1998, ApJ, 504, L75

Barbaro, G. & Poggianti, B. M. 1997, A&A, 324, 490

Barden, M., Lehnert, M. D., Tacconi, L., Genzel, R., White, S., & Franceschini, A. 2003, ApJ, submitted (astro-ph/0302392)

Barger, A. J., Aragon-Salamanca, A., Ellis, R. S., Couch, W. J., Smail, I., & Sharples, R. M. 1996, MNRAS, 279, 1

Baugh, C. M., Cole, S., Frenk, C. S., & Lacey, C. G. 1998, ApJ, 498, 504

Baum, W. A. 1959, PASP, 71, 106

Beers, T. C., Flynn, K., & Gebhardt, K. 1990, AJ, 100, 32

Bekki, K. 1998, ApJ, 502, L133

Bekki, K., Couch, W. J., & Shioya, Y. 2001, PASJ, 53, 395

—. 2002, ApJ, 577, 651

Bender, R., Surma, P., Döbereiner, S., Möllenhoff, C., & Madejsky, R. 1989, A&A, 217, 35

Bernstein, G. M., Guhathakurta, P., Raychaudhury, S., Giovanelli, R., Haynes, M. P., Herter, T., & Vogt, N. P. 1994, AJ, 107, 1962

Bertin, E. & Arnouts, S. 1996, A&AS, 117, 393

Best, P. N., van Dokkum, P. G., Franx, M., & Röttgering, H. J. A. 2002, MNRAS, 330, 17

Binney, J. & Merrifield, M. 1998, Galactic astronomy (Princeton: Princeton University Press)

Binney, J. & Tremaine, S. 1987, Galactic dynamics (Princeton: Princeton University Press)

Blain, A. W., Smail, I., Ivison, R. J., & Kneib, J.-P. 1999, MNRAS, 302, 632

Bond, J. R., Cole, S., Efstathiou, G., & Kaiser, N. 1991, ApJ, 379, 440

Bower, R. G. 1991, MNRAS, 248, 332

Bower, R. G., Lucey, J. R., & Ellis, R. S. 1992, MNRAS, 254, 601

Burstein, D., Bender, R., Faber, S., & Nolthenius, R. 1997, AJ, 114, 1365

Burstein, D. & Heiles, C. 1982, AJ, 87, 1165

Butcher, H. & Oemler, A. 1978, ApJ, 219, 18

—. 1984, ApJ, 285, 426

Byrd, G. & Valtonen, M. 1990, ApJ, 350, 89

Clowe, D., Luppino, G. A., Kaiser, N., & Gioia, I. M. 2000, ApJ, 539, 540

Cole, S., Aragon-Salamanca, A., Frenk, C. S., Navarro, J. F., & Zepf, S. E. 1994, MNRAS, 271, 781

Cole, S., Lacey, C. G., Baugh, C. M., & Frenk, C. S. 2000, MNRAS, 319, 168

Coleman, G. D., Wu, C.-C., & Weedman, D. W. 1980, ApJS, 43, 393

Conti, G., Mattaini, E., Chiappetti, L., Maccagni, D., Sant'Ambrogio, E., Bottini, D., Garilli, B., Le Fèvre, O., Saisse, M., Voët, C., Caputi, O., Cascone, E., Mancini, D., Mancini, G., Perrotta, F., Schipani, P., & Vettolani, G. 2001, PASP, 113, 452

Couch, W. J., Barger, A. J., Smail, I., Ellis, R. S., & Sharples, R. M. 1998, ApJ, 497, 188

Couch, W. J., Ellis, R. S., Sharples, R. M., & Smail, I. 1994, ApJ, 430, 121

Couch, W. J. & Sharples, R. M. 1987, MNRAS, 229, 423

Courteau, S. 1997, AJ, 114, 2402

Cowie, L. L., Songaila, A., & Barger, A. J. 1999, AJ, 118, 603

Dalcanton, J. J., Spergel, D. N., & Summers, F. J. 1997, ApJ, 482, 659

de Jong, R. S. & Davies, R. L. 1997, MNRAS, 285, L1

de Vaucouleurs, G. 1948, Annales d'Astrophysique, 11, 247

de Vaucouleurs, G., de Vaucouleurs, A., & Corwin, H. G. 1976, 2nd reference catalogue of bright galaxies containing information on 4364 galaxies with reference to papers published between 1964 and 1975 (University of Texas Monographs in Astronomy, Austin: University of Texas Press, 1976)

de Vaucouleurs, G., de Vaucouleurs, A., Corwin, H. G., Buta, R. J., Paturel, G., & Fouque, P. 1991, Third Reference Catalogue of Bright Galaxies (Volume 1-3, XII, 2069 pp. 7 figs.. Springer-Verlag Berlin Heidelberg New York)

Diaferio, A., Kauffmann, G., Balogh, M. L., White, S. D. M., Schade, D., & Ellingson, E. 2001, MNRAS, 323, 999

Donahue, M., Voit, G. M., Gioia, I., Lupino, G., Hughes, J. P., & Stocke, J. T. 1998, ApJ, 502, 550

Dosaj, A., Jones Forman, C., Forman, W. R., Markevitch, M. L., & Vikhlinin, A. A. 2002, American Astronomical Society Meeting, 200, 0

Dressler, A. 1980, ApJ, 236, 351

Dressler, A. & Gunn, J. E. 1983, ApJ, 270, 7

—. 1992, ApJS, 78, 1

Dressler, A., Oemler, A. J., Butcher, H. R., & Gunn, J. E. 1994, ApJ, 430, 107

Dressler, A., Oemler, A. J., Couch, W. J., Smail, I., Ellis, R. S., Barger, A., Butcher, H., Poggianti, B. M., & Sharples, R. M. 1997, ApJ, 490, 577

Dressler, A., Smail, I., Poggianti, B. M., Butcher, H., Couch, W. J., Ellis, R. S., & Oemler, A. J. 1999, ApJS, 122, 51

Efstathiou, G., Ellis, R. S., & Peterson, B. A. 1988, MNRAS, 232, 431

Ellis, R. S., Smail, I., Dressler, A., Couch, W. J., Oemler, A. J., Butcher, H., & Sharples, R. M. 1997, ApJ, 483, 582

Fabricant, D., Franx, M., & van Dokkum, P. 2000, ApJ, 539, 577

Fabricant, D. G., McClintock, J. E., & Bautz, M. W. 1991, ApJ, 381, 33

Fasano, G., Poggianti, B. M., Couch, W. J., Bettoni, D., Kjærgaard, P., & Moles, M. 2000, ApJ, 542, 673

Franx, M., Moorwood, A., Rix, H.-W., Kuijken, K., Röttgering, H., van der Werf, P., van Dokkum, P., Labbé, I., & Rudnick, G. 2000, The Messenger, 99, 20

Fujita, Y. 1998, ApJ, 509, 587

Fukugita, M., Shimasaku, K., & Ichikawa, T. 1995, PASP, 107, 945

Gómez, P. L., Nichol, R. C., Miller, C. J., Balogh, M. L., Goto, T., Zabludoff, A. I., Romer, A. K., Bernardi, M., Sheth, R., Hopkins, A. M., Castander, F. J., Connolly, A. J., Schneider, D. P., Brinkmann, J., Lamb, D. Q., SubbaRao, M., & York, D. G. 2003, ApJ, 584, 210

Gal-Yam, A., Maoz, D., & Sharon, K. 2002, MNRAS, 332, 37

Gallagher, J. S., Hunter, D. A., & Bushouse, H. 1989, AJ, 97, 700

Gallego, J., García-Dabó, C. E., Zamorano, J., Aragón-Salamanca, A., & Rego, M. 2002, ApJ, 570, L1

García-Vargas, M. L., Bressan, A., & Díaz, A. I. 1995a, A&AS, 112, 13

—. 1995b, A&AS, 112, 35

Gilks, W. R., Richardson, S., & Spiegelhalter, D. J. 1996, Markov chain Monte Carlo in practice (London: Chapman & Hall)

Gioia, I. M., Maccacaro, T., Schild, R. E., Wolter, A., Stocke, J. T., Morris, S. L., & Henry, J. P. 1990, ApJS, 72, 567

Girardi, M. & Mezzetti, M. 2001, ApJ, 548, 79

Gnedin, O. Y. 2003, ApJ, 582, 141

Gonzalez, A. H., Zaritsky, D., Dalcanton, J. J., & Nelson, A. 2001, ApJS, 137, 117

Gonzalez, A. H., Zaritsky, D., Simard, L., Clowe, D., & White, S. D. M. 2002, ApJ, 579, 577

Gunn, J. E. & Gott, J. R. I. 1972, ApJ, 176, 1

Guzmán, R., Gallego, J., Koo, D. C., Phillips, A. C., Lowenthal, J. D., Faber, S. M., Illingworth, G. D., & Vogt, N. P. 1997, ApJ, 489, 559

Hammersley, J. M. & Handscomb, D. C. 1964, Monte Carlo Methods (London: Metheuen)

Hashimoto, Y., Oemler, A. J., Lin, H., & Tucker, D. L. 1998, ApJ, 499, 589

Hoekstra, H., Franx, M., Kuijken, K., & van Dokkum, P. G. 2002, MNRAS, 333, 911

Holmberg, E. 1958, Meddelanden från Lunds Astronomiska Observatorium Serie II, 136, 1

Hubble, E. & Humason, M. L. 1931, ApJ, 74, 43

Hubble, E. P. 1926, ApJ, 64, 321

—. 1936, Yale University Press

Icke, V. 1985, A&A, 144, 115

Jansen, R. A., Fabricant, D., Franx, M., & Caldwell, N. 2000a, ApJS, 126, 331

Jansen, R. A., Franx, M., & Fabricant, D. 2001, ApJ, 551, 825

Jansen, R. A., Franx, M., Fabricant, D., & Caldwell, N. 2000b, ApJS, 126, 271

Jeltema, T. E., Canizares, C. R., Bautz, M. W., Malm, M. R., Donahue, M., & Garmire, G. P. 2001, ApJ, 562, 124

Jones, L., Smail, I., & Couch, W. J. 2000, ApJ, 528, 118

Jørgensen, I. 1997, MNRAS, 288, 161

Jørgensen, I. & Franx, M. 1994, ApJ, 433, 553

Kannappan, S. J., Barton Gillespie, E., Fabricant, D. G., Franx, M., & Vogt, N. P. 2002a, in Galaxy Evolution: Theory and Observations, eds. Avila-Reese, Firmani, Frenk & Allen, in press (astro–ph/0206088)

Kannappan, S. J., Fabricant, D. G., & Franx, M. 2002b, AJ, 123, 2358

Kauffmann, G., White, S. D. M., & Guiderdoni, B. 1993, MNRAS, 264, 201

Kennicutt, R. C. 1992, ApJ, 388, 310

—. 1998, ARA&A, 36, 189

Kobulnicky, H. A. & Gebhardt, K. 2000, AJ, 119, 1608

Kodama, T. & Bower, R. G. 2001, MNRAS, 321, 18

Kodama, T. & Smail, I. 2001, MNRAS, 326, 637

Krist, J. 1993, in ASP Conf. Ser. 52: Astronomical Data Analysis Software and Systems II, Vol. 2, 536

Kuntschner, H. 2000, MNRAS, 315, 184

Kuntschner, H. & Davies, R. L. 1998, MNRAS, 295, L29

Larson, R. B., Tinsley, B. M., & Caldwell, C. N. 1980, ApJ, 237, 692

Lavery, R. J. & Henry, J. P. 1988, ApJ, 330, 596

—. 1994, ApJ, 426, 524

Lewis, I., Balogh, M., De Propris, R., Couch, W., Bower, R., Offer, A., Bland-Hawthorn, J., Baldry, I. K., Baugh, C., Bridges, T., Cannon, R., Cole, S., Colless, M., Collins, C., Cross, N., Dalton, G., Driver, S. P., Efstathiou, G., Ellis, R. S., Frenk, C. S., Glazebrook, K., Hawkins, E., Jackson, C., Lahav, O., Lumsden, S., Maddox, S., Madgwick, D., Norberg, P., Peacock, J. A., Percival, W., Peterson, B. A., Sutherland, W., & Taylor, K. 2002, MNRAS, 334, 673

Lilly, S., Schade, D., Ellis, R., Le Fevre, O., Brinchmann, J., Tresse, L., Abraham, R., Hammer, F., Crampton, D., Colless, M., Glazebrook, K., Mallen-Ornelas, G., & Broadhurst, T. 1998, ApJ, 500, 75

Lilly, S. J., Le Fevre, O., Hammer, F., & Crampton, D. 1996, ApJ, 460, L1

Madau, P., Ferguson, H. C., Dickinson, M. E., Giavalisco, M., Steidel, C. C., & Fruchter, A. 1996, MNRAS, 283, 1388

Mathieu, A., Merrifield, M. R., & Kuijken, K. 2002, MNRAS, 330, 251

McCall, M. L., Rybski, P. M., & Shields, G. A. 1985, ApJS, 57, 1

Metevier, A. J., Koo, D. C., & Simard, L. 2002, in ASP Conf. Ser. 268: Tracing Cosmic Evolution with Galaxy Clusters, 173

Metropolis, N., Rosenbluth, A., Rosenbluth, M., Teller, A., & Teller, E. 1953, J. Chem. Phys., 21, 1087

Milvang-Jensen, B., Aragón-Salamanca, A., Hau, G. K. T., Jørgensen, I., & Hjorth, J. 2003, MNRAS, 339, L1

Milvang-Jensen, B. & Jørgensen, I. 1999, Baltic Astronomy, 8, 535

Mo, H. J., Mao, S., & White, S. D. M. 1998, MNRAS, 295, 319

Moore, B., Katz, N., Lake, G., Dressler, A., & Oemler, A. 1996, Nature, 379, 613

Moore, B., Lake, G., & Katz, N. 1998, ApJ, 495, 139

Moore, B., Lake, G., Quinn, T., & Stadel, J. 1999, MNRAS, 304, 465

Morris, S. L., Hutchings, J. B., Carlberg, R. G., Yee, H. K. C., Ellingson, E., Balogh, M. L., Abraham, R. G., & Smecker-Hane, T. A. 1998, ApJ, 507, 84

Moss, C. & Whittle, M. 2000, MNRAS, 317, 667

Neistein, E., Maoz, D., Rix, H., & Tonry, J. L. 1999, AJ, 117, 2666

Oemler, A. J., Dressler, A., & Butcher, H. R. 1997, ApJ, 474, 561

Osterbrock, D. E. 1989, Astrophysics of gaseous nebulae and active galactic nuclei (Mill Valley: University Science Books)

Osterbrock, D. E., Fulbright, J. P., Martel, A. R., Keane, M. J., Trager, S. C., & Basri, G. 1996, PASP, 108, 277

Pérez-González, P. G., Gil de Paz, A., Zamorano, J., Gallego, J., Alonso-Herrero, A., & Aragón-Salamanca, A. 2003, MNRAS, 338, 508

Peletier, R. F. & Willner, S. P. 1993, ApJ, 418, 626

Persic, M. & Salucci, P. 1991, ApJ, 368, 60

Pierce, M. J. & Tully, R. B. 1992, ApJ, 387, 47

Poggianti, B. M. 2002a, in ASP Conf. Ser.: Matter and energy in clusters of galaxies, in press (astro–ph/0208181)

Poggianti, B. M. 2002b, in Galaxy Evolution in Groups and Clusters, in press (astro–ph/0210233)

Poggianti, B. M. & Barbaro, G. 1996, A&A, 314, 379

—. 1997, A&A, 325, 1025

Poggianti, B. M., Bridges, T. J., Carter, D., Mobasher, B., Doi, M., Iye, M., Kashikawa, N., Komiyama, Y., Okamura, S., Sekiguchi, M., Shimasaku, K., Yagi, M., & Yasuda, N. 2001, ApJ, 563, 118

Poggianti, B. M., Smail, I., Dressler, A., Couch, W. J., Barger, A. J., Butcher, H., Ellis, R. S., & Oemler, A. J. 1999, ApJ, 518, 576

Press, W. H., Teukolsky, S. A., Vetterling, W. T., & Flannery, B. P. 1992, Numerical recipes in FORTRAN. The art of scientific computing (Cambridge: Cambridge University Press, 2nd ed.)

Quilis, V., Moore, B., & Bower, R. 2000, Science, 288, 1617

Raychaudhury, S., von Braun, K., Bernstein, G. M., & Guhathakurta, P. 1997, AJ, 113, 2046

Rix, H. & White, S. D. M. 1990, ApJ, 362, 52

Rubin, V. C., Burstein, D., Ford, W. K., & Thonnard, N. 1985, ApJ, 289, 81

Ryder, S. D. & Dopita, M. A. 1994, ApJ, 430, 142

Saha, P. & Williams, T. B. 1994, AJ, 107, 1295

Salpeter, E. E. 1955, ApJ, 121, 161

Sandage, A. 1972, ApJ, 176, 21

Sarazin, C. L. 1988, X-ray emission from clusters of galaxies (Cambridge Astrophysics Series, Cambridge: Cambridge University Press, 1988)

Schade, D., Lilly, S. J., Crampton, D., Ellis, R. S., Le Fèvre, O., Hammer, F. ., Brinchmann, J., Abraham, R., Colless, M., Glazebrook, K., Tresse, L., & Broadhurst, T. 1999, ApJ, 525, 31

Schade, D., Lilly, S. J., Crampton, D., Hammer, F., Le Fevre, O., & Tresse, L. 1995, ApJ, 451, L1

Schlegel, D. J., Finkbeiner, D. P., & Davis, M. 1998, ApJ, 500, 525

Sérsic, J. L. 1968, Atlas de galaxias australes (Cordoba, Argentina: Observatorio Astronomico)

Shioya, Y., Bekki, K., & Couch, W. J. 2001, ApJ, 558, 42

Shioya, Y., Bekki, K., Couch, W. J., & De Propris, R. 2002, ApJ, 565, 223

Simard, L. & Pritchet, C. J. 1998, ApJ, 505, 96

—. 1999, PASP, 111, 453

Simard, L., Willmer, C. N. A., Vogt, N. P., Sarajedini, V. L., Phillips, A. C., Weiner, B. J., Koo, D. C., Im, M., Illingworth, G. D., & Faber, S. M. 2002, ApJS, 142, 1

Smail, I., Dressler, A., Couch, W. J., Ellis, R. S., Oemler, A. J., Butcher, H., & Sharples, R. M. 1997, ApJS, 110, 213

Smail, I., Kuntschner, H., Kodama, T., Smith, G. P., Packham, C., Fruchter, A. S., & Hook, R. N. 2001, MNRAS, 323, 839

Spergel, D. N., Verde, L., Peiris, H. V., Komatsu, E., Nolta, M. R., Bennett, C. L., Halpern, M., Hinshaw, G., Jarosik, N., Kogut, A., Limon, M., Meyer, S. S., Page, L., Tucker, G. S., Weiland, J. L., Wollack, E., & Wright, E. L. 2003, ApJ, submitted (astro-ph/0302209)

Stuart, A. & Ord, J. K. 1987, Kendall's Advanced Theory of Statistics, 5th ed., vol. 1 (London: Charles Griffin & Company)

Terlevich, A. I. & Forbes, D. A. 2002, MNRAS, 330, 547

Tormen, G. & Burstein, D. 1995, ApJS, 96, 123

Treu, T., Ellis, R. S., Kneib, J. ., Dressler, A., Smail, I., Czoske, O., Oemler, A., & Natarajan, P. 2003, ApJ, in press (astro-ph/0303267)

Tully, R. B. & Fisher, J. R. 1977, A&A, 54, 661

Tully, R. B. & Fouqué, P. 1985, ApJS, 58, 67

Tully, R. B. & Pierce, M. J. 2000, ApJ, 533, 744

Tully, R. B., Pierce, M. J., Huang, J., Saunders, W., Verheijen, M. A. W., & Witchalls, P. L. 1998, AJ, 115, 2264

van Dokkum, P. G. 1999, Ph.D. Thesis, Univ. of Groningen, `http://www.astro.caltech.edu/~pgd/thesis/` or `http://www.ub.rug.nl/eldoc/dis/science/p.g.van.dokkum/`

—. 2001, PASP, 113, 1420

van Dokkum, P. G., Franx, M., Fabricant, D., Illingworth, G. D., & Kelson, D. D. 2000, ApJ, 541, 95

van Dokkum, P. G., Franx, M., Fabricant, D., Kelson, D. D., & Illingworth, G. D. 1999, ApJ, 520, L95

Visvanathan, N. & Sandage, A. 1977, ApJ, 216, 214

Vogt, N. P. 1995, PhD thesis, Cornell University

Vogt, N. P. 1999, in ASP Conf. Ser. 193: The Hy-Redshift Universe: Galaxy Formation and Evolution at High Redshift, 145

Vogt, N. P. 2001, in ASP Conf. Ser. 240: Gas and Galaxy Evolution, 89

Vogt, N. P., Forbes, D. A., Phillips, A. C., Gronwall, C., Faber, S. M., Illingworth, G. D., & Koo, D. C. 1996, ApJ, 465, L15

Vogt, N. P., Phillips, A. C., Faber, S. M., Gallego, J., Gronwall, C., Guzman, R., Illingworth, G. D., Koo, D. C., & Lowenthal, J. D. 1997, ApJ, 479, L121

Watanabe, M., Yasuda, N., Itoh, N., Ichikawa, T., & Yanagisawa, K. 2001, ApJ, 555, 215

Wilson, G., Cowie, L. L., Barger, A. J., & Burke, D. J. 2002, AJ, 124, 1258

Wirth, G. D., Koo, D. C., & Kron, R. G. 1994, ApJ, 435, L105

Worthey, G. 1994, ApJS, 95, 107

Wu, X., Xue, Y., & Fang, L. 1999, ApJ, 524, 22

Zhang, C. Y. 1995, in ASP Conf. Ser. 77: Astronomical Data Analysis Software and Systems IV, Vol. 4, 514

Ziegler, B. L., Böhm, A., Fricke, K. J., Jäger, K., Nicklas, H., Bender, R., Drory, N., Gabasch, A., Saglia, R. P., Seitz, S., Heidt, J., Mehlert, D., Möllenhoff, C., Noll, S., & Sutorius, E. 2002, ApJ, 564, L69

Ziegler, B. L., Boehm, A., Jaeger, K., Fritz, A., & Heidt, J. 2003, in Carnegie Observatories Astrophysics Series, Vol.3: Clusters of Galaxies: Probes of Cosmological Structure and Galaxy Evolution, in press (astro–ph/0303417)

Ziegler, B. L., Bower, R. G., Smail, I., Davies, R. L., & Lee, D. 2001, MNRAS, 325, 1571

(page left blank to get matching page numbers for single and double sided versions)

Appendix A

Cosmic ray event removal

The 14 science frames were trimmed and bias subtracted. The next step was to deal with the pixels affected by cosmic ray events (hereafter cosmics). Cosmics in the data are illustrated in the first column of Fig. A.1. (The other columns of that figure will be referred to later.) First methods that identify cosmics in a *single frame* based on the appearance of the cosmics were tried. These methods (including `figaro.bclean`) did not provide a satisfactory result.

The alternative is to use a method that utilises the fact that *multiple frames* of the same field are available, here 7 frames per spectroscopic mask. The task of such a method is to provide an estimate of the central location (think "mean value") and scale ("dispersion")[1], and then use these estimates to flag values that deviate from the central location by more than a specified factor times the scale. The estimates should of course not be affected by the features that are to be flagged, here the cosmics. The estimate of the central location is easy: the median will provide a good estimate even in the presence of a few outliers. The estimate of the scale is the tricky part. For these data a CCD noise model (photon noise plus read-out noise) will *not* do, first and foremost because the omnipresent sky lines vary in intensity to such an extend that the actual scale is larger than the one predicted by the CCD noise model by factors of up to 20 or more! Other factors that can increase the scale wrt. what the CCD noise model predicts: instrument flexure causing the features to move slightly in the spectral and/or spatial direction from frame to frame, and changing seeing. For the FORS2 data the effect of flexure is small, as will be demonstrated later. The alternative to the CCD noise model is to estimate the scale from the individual data values somehow. A method could be some variation of iterative sigma clipping. This is not implemented in the standard `combine`/`imcombine` IRAF task, so we thought it was not available within IRAF. We later learned that it actually *is* available in the form of the task `gcombine` (Zhang 1995) from the STSDAS package, using the `rsigclip` ("robust sigma clipping") algorithm. How well it would work on these data has not been tested.

Since we did not know of any programme that would satisfactorily identify the cosmics in the data at hand, a new method was developed. identify the cosmics in the data at hand, I decided to develop my own method. The basic idea was to estimate the scale from the *lowest 5* of the 7 data values at each pixel. The number 5 was chosen since it is very unlikely that a given pixel will be affected by a cosmic in more that 2 of the 7 input frames. Since these lowest 5 values should be virtually free from cosmics,

[1] Using the terminology of Beers et al. (1990)

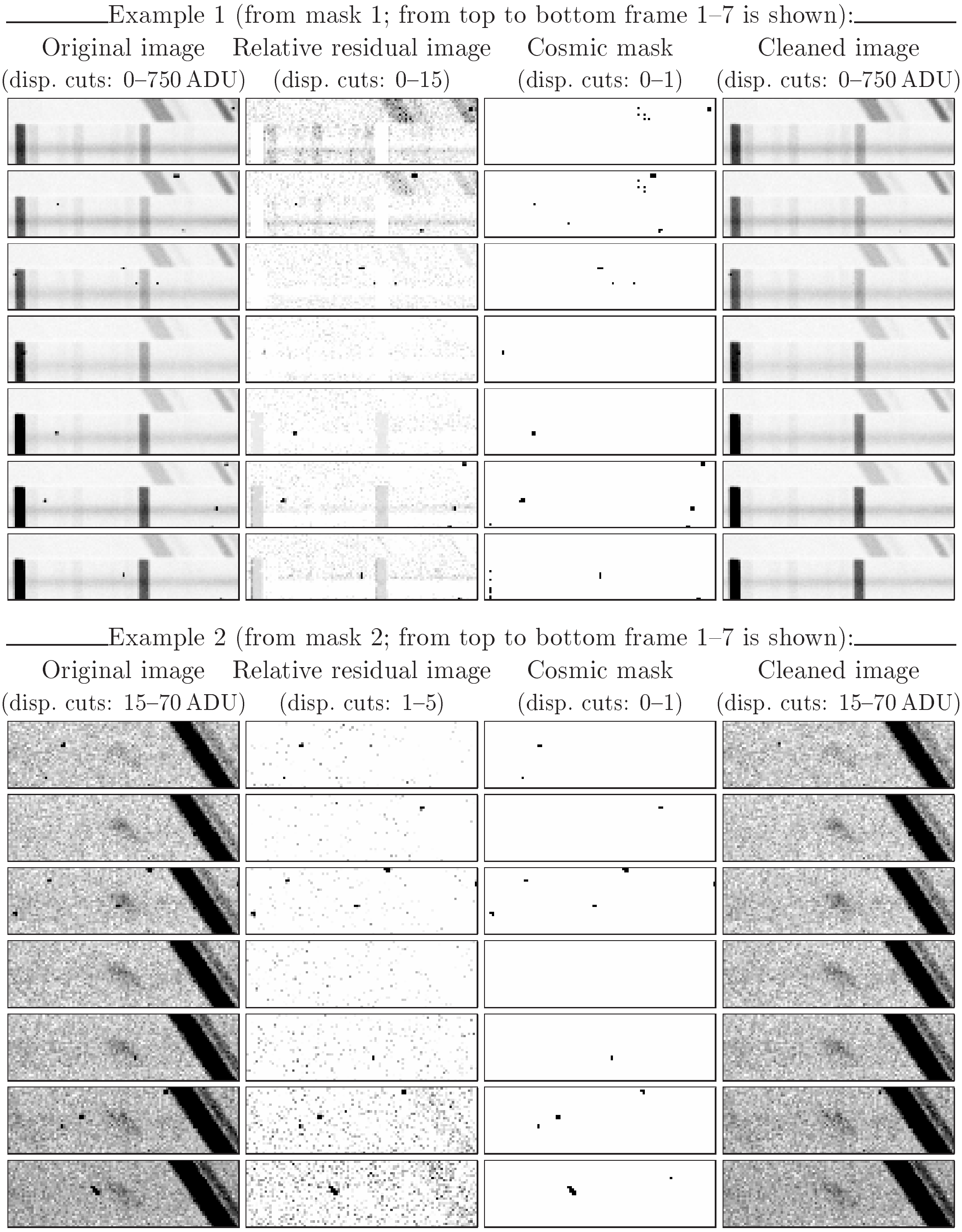

Figure A.1: Illustration of cosmics in the science frames. Wavelength is along the x-axis.
Example 1 (top half of the figure): The image section contains parts of two spectra: In the top spectrum sky lines at 7243,7277 Å are seen, and in the bottom spectrum the very strong 6300,6363 Å sky lines and a reference star spectrum are seen. Note how the intensity of the sky lines vary with time.
Example 2 (bottom half of the figure): The image section contains the [OII] line for galaxy 1896 at $z = 0.82$.

a simple "non-robust" statistic such as the standard deviation (aka. the rms) could be used to estimate the scale. The *sorted* pixel values (lowest, 2nd lowest, ..., highest) is illustrated in Fig. A.2. It turned out that the fraction of pixels in a single image that were affected by cosmics was ~ 0.002 (corresponding to ~ 8000 pixels). From this value the expected fraction of pixels to be hit by cosmics in any 2 of the 7 images is $0.002^2 \cdot \text{Binomial}(7,2) = 8.4 \cdot 10^{-5}$, corresponding to 350 pixels, and the fraction of pixels to be hit by cosmics in any 3 of the 7 images is $0.002^3 \cdot \text{Binomial}(7,3) = 2.8 \cdot 10^{-7}$, corresponding to just 1 pixel.

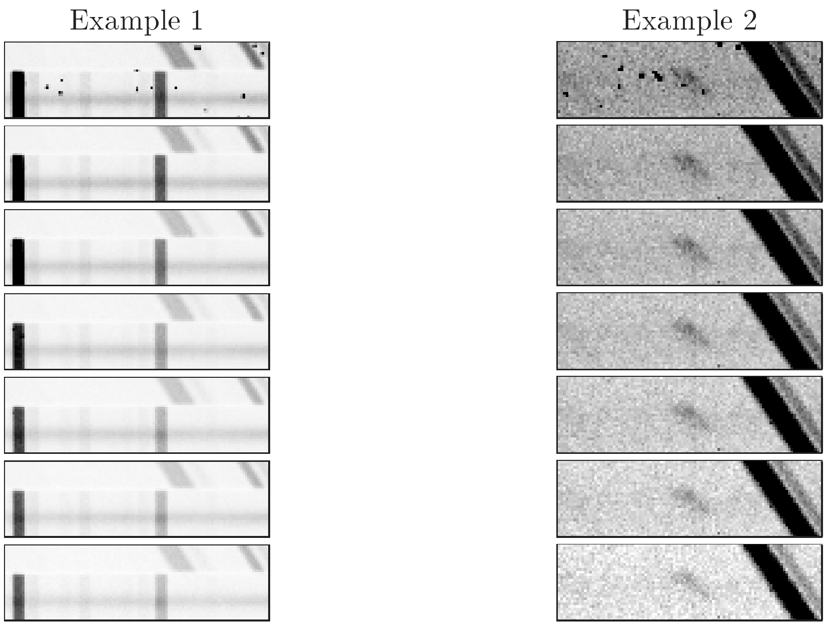

Figure A.2: Illustration of the sorted pixel values for the two examples (cf. Fig. A.1. From top to bottom: the sorted pixel values of the 7 input images, with the highest values on top. Note how the lowest 5 levels are free from cosmics.

The problem was studied using simulations. Realisations of pixel values were created using

$$x_i = x_{\text{true}} + \sigma_{\text{CCD,true}} \cdot X_{\text{gauss}}, \quad i = 1, \ldots, 7, \quad \sigma_{\text{CCD,true}} = \sqrt{\frac{x_{\text{true}}}{\text{gain}} + \text{RON}^2} \;, \quad \text{(A.1)}$$

where X_{gauss} is a random Gaussian variable with zero mean and unity dispersion (created using the routines `ran1` and `gasdev` from Press et al. 1992, translated into IDL). While the parent distribution for the real data will be non-Gaussian (particularly due to the cosmics and to the sky lines, cf. below), it is nevertheless instructive to study the behaviour of the various statistics for a Gaussian distribution. As can be seen a CCD noise model was been used, but the results only depend on the noise being Gaussian. The results are also independent of the assumed level in the absence of noise, x_{true}. For each realisation the following quantities were calculated:

$$\sigma_{\text{low}\,5} = \text{standard deviation of the 5 lowest values} \quad \text{(A.2)}$$

$$\sigma_{\text{all}\,7} = \text{standard deviation of all 7 values} \quad \text{(A.3)}$$

$$\sigma_{\text{pred,CCD,med}} = \sqrt{\frac{\text{median}\{x_i\}_{i=1,\ldots,7}}{\text{gain}} + \text{RON}^2} \quad \text{(A.4)}$$

where $\sigma_{\rm pred,CCD,med}$ is the standard deviation predicted by the CCD noise model when using the median of the 7 values as the estimate of the central location. The reason for calculating this quantity will be explained shortly.

A technical detail: in the case of actual CCD data the data values will be of integer origin (because the voltages from the CCD have be quantised by the A/D converter), and hence the rms will only take on discrete values. This has no practical implications: the rms calculated from the integer numbers is an unbiased estimator of the rms calculated from the real numbers, except for the very low end of the tail, where the integer-based rms distribution has a non-zero density at rms = 0.

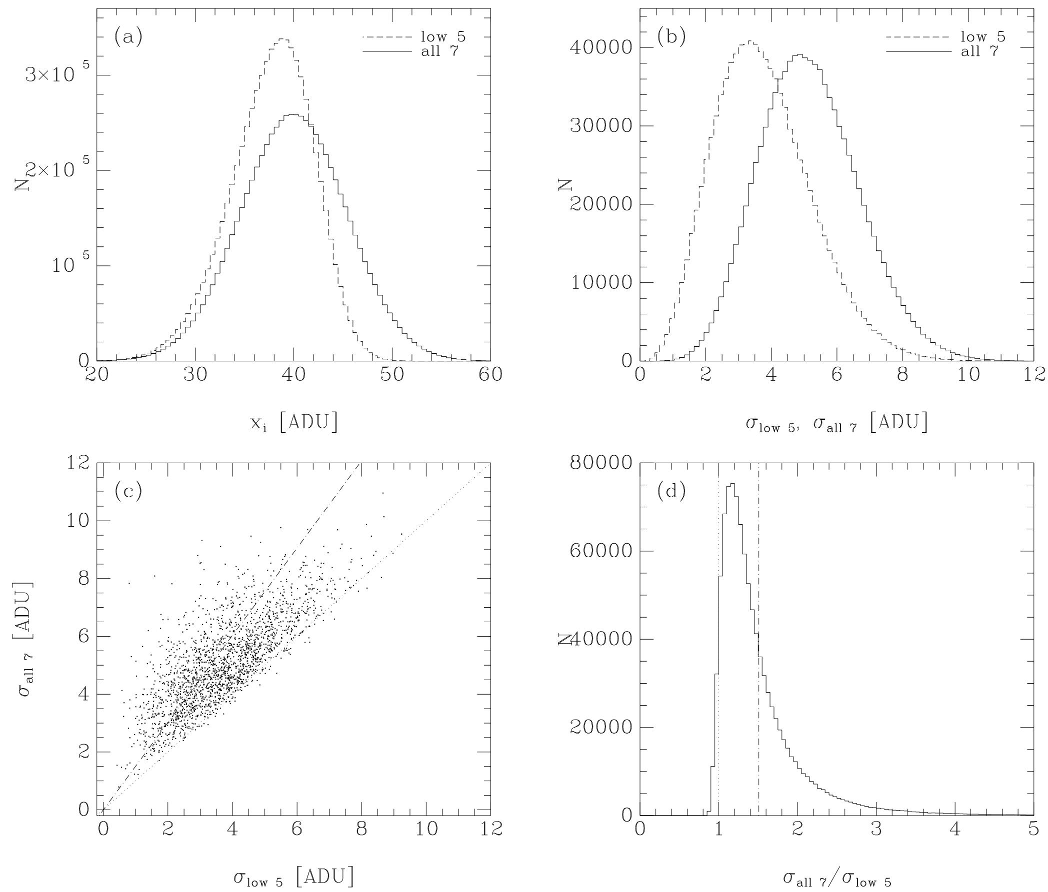

Figure A.3: Results from a simulation. The points were drawn from a Gaussian distribution with mean 40 ADU and dispersion 5.38 ADU. The dot-dashed line in panel (c) and (d) mark the mean relation found in the simulation: $\sigma_{\rm all\,7} = 1.50869\,\sigma_{\rm low\,5}$, and the dotted line mark the one to one relation. The simulation consisted of 10^6 realisations. In panel (c) only 2000 realisations are plotted. In panel (d) the "low 5" distribution has been scaled by a factor 7/5 to match the "all 7" distribution.

Results from a particular simulation with $x_{\rm true} = 40$ ADU are shown in Fig. A.3. Panel (a) shows the distribution of the simulated points. The solid histogram is for all 7 x_i-values – it is nicely Gaussian, per construction. The dashed histogram is for the lowest 5 x_i-values from each realisation – as expected, the mean is lower than for the all 7 distribution, but the shape is also different. Panel (b) shows the distributions

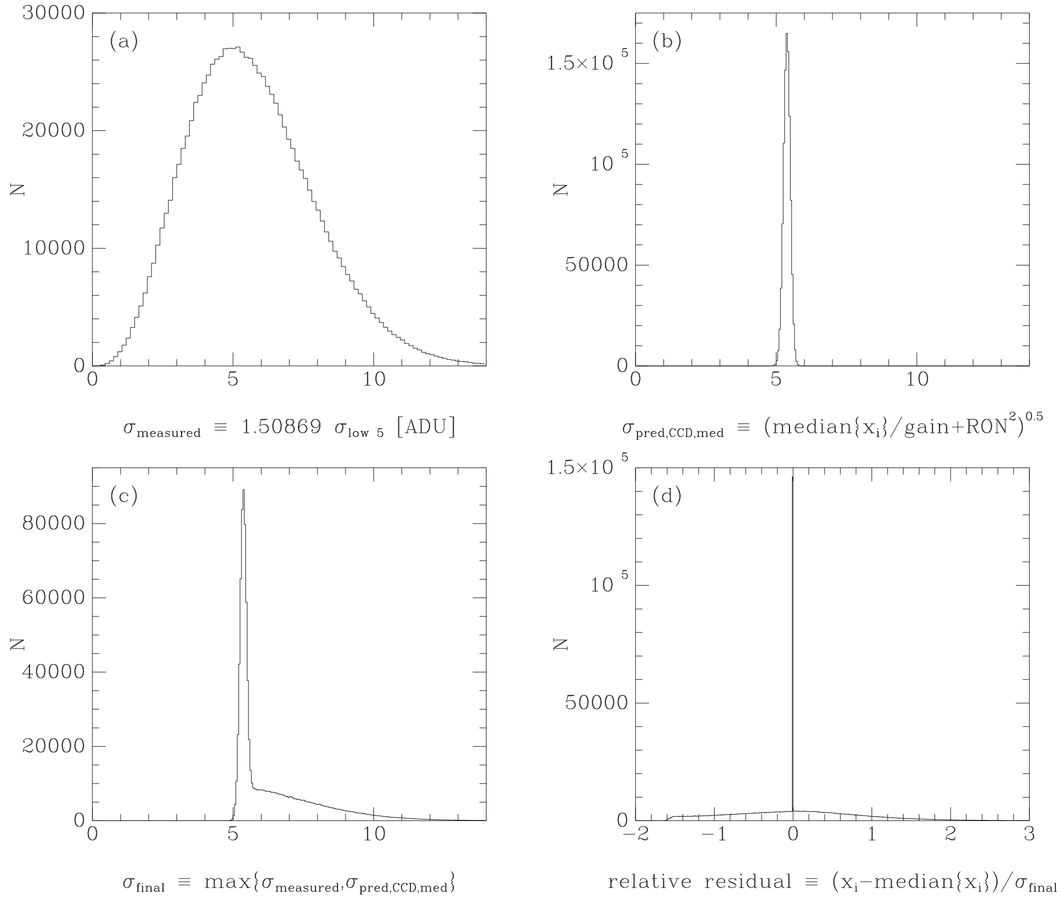

Figure A.4: More plots from the simulation, cf. Fig. A.3 and the text.

of $\sigma_{\rm low\,5}$ and $\sigma_{\rm all\,7}$. In panel (c) $\sigma_{\rm all\,7}$ is plotted against $\sigma_{\rm low\,5}$. In the mean they are related as $\sigma_{\rm all\,7} = 1.50869\,\sigma_{\rm low\,5}$. There is some scatter in this relation, a scatter that is asymmetric, as is also evident from the $\sigma_{\rm all\,7}/\sigma_{\rm low\,5}$ histogram in panel (d). We will use the found mean relation to estimate $\sigma_{\rm all\,7}$ from $\sigma_{\rm low\,5}$, denoting this estimate $\sigma_{\rm measured}$

$$\sigma_{\rm measured} = 1.50869\,\sigma_{\rm low\,5} \quad . \tag{A.5}$$

The name of the quantity ($\sigma_{\rm measured}$) simply reflects that it is derived from the data without being based on a model (such as the CCD noise model). The distribution of $\sigma_{\rm measured}$ is shown in Fig. A.4, panel (a). The estimate of the sigma predicted by the CCD noise model, $\sigma_{\rm pred,CCD,med}$, is shown in panel (b) – note the low scatter. It is seen that for a substantial fraction of the realisations, $\sigma_{\rm measured}$ is lower than $\sigma_{\rm pred,CCD,med}$. Since the CCD noise model is a very good *lower* limit to the sigma expected in real data, we define an improved sigma as

$$\sigma_{\rm final} = \max\left\{\sigma_{\rm measured}, \sigma_{\rm pred,CCD,med}\right\} \quad . \tag{A.6}$$

The distribution of $\sigma_{\rm final}$ for the simulation is shown in panel (c). Finally, using this sigma as our estimate of the scale, and using the median as our estimate of the central location, we can now calculate relative residuals as

$$(\text{relative residual})_i = \frac{x_i - \mathrm{median}\{x_i\}_{i=1,\ldots,7}}{\sigma_{\rm final}} \quad . \tag{A.7}$$

The distribution of the relative residuals for the simulation is shown in panel (d) of Fig. A.4. Since this is a simulation based on a Gaussian distribution, all the data points are "good" (i.e. there are no cosmics in the simulation). It is found that the fraction of points above a relative residual of 3 and 4 is 0.14% and 0.007%, respectively – a normal distribution would have a similar numbers, 0.27% and 0.006%.

The method can now be applied to the data in exactly the same way as for the simulation (also done in IDL). The measured sigma image (i.e. $\sigma_{\mathrm{measured}}$), the predicted sigma image (i.e. $\sigma_{\mathrm{pred,CCD,med}}$) and the final sigma image (i.e. σ_{final}) for the data are illustrated in Fig. A.5. The figure also shows the ratio of the measured to predicted sigma. On top of the sky lines the ratio is substantially greater than one, meaning that the measured variance is substantially larger than what is predicted by the CCD noise model. In the regions only containing continuous background light, the ratio is around 1.1, indicating that the CCD noise model can account for most of the variance seen. Relative residual images are calculated as

$$\text{relative residual image} = \frac{\text{(original image)} - \text{(median image)}}{\text{final sigma image}} \quad . \tag{A.8}$$

The relative residual images for the two examples are found in Fig. A.1, the second column. Note what display cuts have been used in the two examples. The relative residual images have to be displayed and inspected to determine at what level only cosmics are seen. If the lower display cut is too low it will be clear to the eye that e.g. sky lines and perhaps stellar continua are also being "flagged". The lower cut can be then adjusted until only cosmic are seen. (It should be noted that in a test where the CCD noise was *not* used as a lower limit to the estimated scale, it was found that good pixels were being flagged.) Having determined the sigma-level, a cosmic mask-image can be produced by identifying all pixels in the relative residual image that is above the chosen sigma-level, say 4.5. The cosmic masks for the two examples are found in Fig. A.1, the third column.

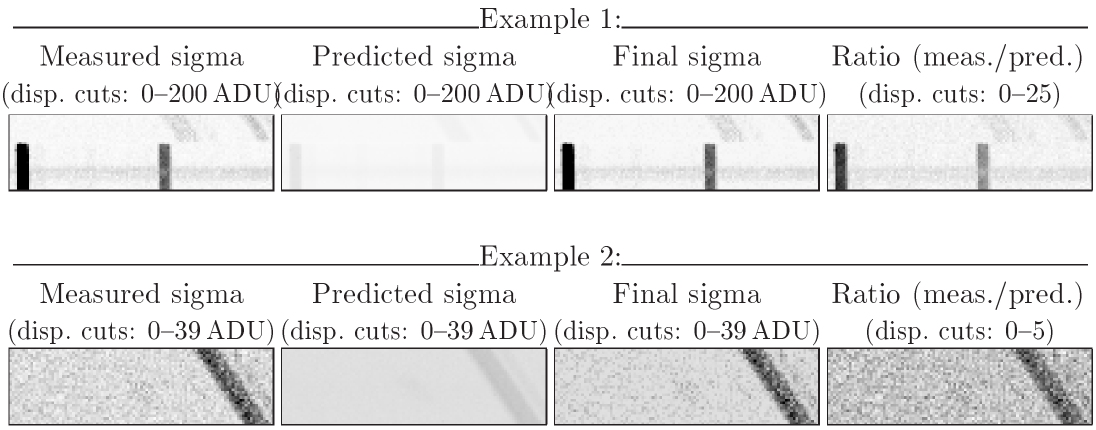

Figure A.5: Illustration of the different sigma images. Note how the measured sigma in the case of certain sky lines exceeds the sigma predicted by the CCD noise model by factors of up to ~ 25. The final sigma (third column of the figure) is the maximum of the measured and the predicted sigma.

The cosmic masks were used as input to the `fixpix` task to create individual cleaned images using linear interpolation. At the same time, bad columns were "removed", cf.

the next section (Sect. 2.3.3). The cleaned images for the two examples are found in the fourth column of Fig. A.1 (page 148). As an experiment, an average image of the 7 cosmic cleaned science images for each mask was made. Since it turned out that the shifts from frame to frame in the wavelength direction and in the spatial direction were sufficiently small (as discussed below in Sect. 2.3.10 and 2.3.12), these two average images could be used for the analysis (rotation curves, etc.). It could be argued that instead of simply averaging the cosmic cleaned images, one should have combined the images using the cosmic masks to mask out the cosmic pixels. The difference between the two approaches should be small, however.

The sigma-levels adopted for the 14 science frames are given in Table A.1. The simulations, which were based on a normal parent distribution, showed that a sigma-level of 4 would have been a reasonable value. As can be seen from the table, in some cases a much higher level was needed in order not to flag "good" pixels, particularly sky line pixels. The reason for this must be that the parent distribution for the sky line pixels is *not* normal, due to the intensity of the sky lines changing rapidly near the start or end of the night. That the sky lines vary in intensity with time (frame number) is seen in Fig. A.1, example 1. Therefore, particularly in the images where the sky lines are at the bright tail of the distribution (e.g. the first image of mask 1) there is a conflict between wanting to flag faint cosmics and not wanting to flag sky line pixels. In this case the sigma-levels were set so that only a few sky line pixels were flagged. The downside is that in frame 1 of mask 1, where a sigma-level of 12 was adapted, faint cosmics are left in the data, which can actually be seen in the cleaned image, see Fig. A.1 for that frame. Despite of this, the cosmic cleaning worked well. It should also be emphasized that each emission line used in the analysis was inspected in the combined images, and in no cases were there any remaining cosmics to be seen. The reason not wanting to flag sky line pixels is the following: If we want to create individual cleaned images, then rejecting all the pixels on a given sky line will also reject all the information about the object spectrum underneath the line. If we only want to create a combined cleaned image, rejecting all the pixels on a given sky line in say 2 of the 7 input frames would "only" decrease the S/N – except if there are small shifts in wavelength between the 7 frames, in which case the rejection of all pixels only in certain regions in some of the input frames could create a slightly inconsistent combined image[2].

While the method produced good results, could it be improved? It would seem an interesting exercise to try other estimator for the scale, and maybe also for the central location. The principle applied in this work (for the scale estimate) of first removing the highest 2 of the 7 data points (say) could be kept or abandoned. A good source of possible estimators is Beers et al. (1990). Using the CCD noise model as a lower limit to the scale seem a good idea in any case.

How few frames will the method work with? This has not yet been tested. One constraint will be what fraction of the pixels in each image are affected by cosmics, since that determines how many data value need to be excluded from the measurement of the rms. The problem is also that the fewer the data values used to calculate the rms, the larger the noise in the estimate of the scale. To estimate the scale one needs at

[2]Of course, if such shifts are large the cosmic identification method stops being useful since the measured sigma would be dominated by the effect of the shifts. However, if the images are well sampled, shifts larger that one pixel could be dealt with by shifting the input images by an integer amount of pixels before applying the cosmic identification method.

Table A.1: Sigma-levels adopted for the different science frames

Image	Sigma-level	Any minor problems with flagging of non cosmic pixels?
`mask1_1_rr`	12.0	Only a few-ish sky line pixels flagged
`mask1_2_rr`	7.0	Only a few sky line pixels flagged
`mask1_3_rr`	4.5	no
`mask1_4_rr`	4.0	no
`mask1_5_rr`	4.0	no
`mask1_6_rr`	4.5	Only a very few refstar pixels flagged
`mask1_7_rr`	5.0	Only a few sky line pixels flagged (6300,6363?)
`mask2_1_rr`	4.0	no
`mask2_2_rr`	4.0	no
`mask2_3_rr`	4.0	no
`mask2_4_rr`	4.5	no
`mask2_5_rr`	4.5	no
`mask2_6_rr`	6.0	no / very few sky line pixels flagged
`mask2_7_rr`	6.0	Only a few sky line pixels flagged

least 2 data points, so the lower limit for the method is 3 images, of which the scale is estimated from the 2 lowest values at each pixel. It should be noted that Zhang (1995) states that `gcombine` has a mode for removing outliers using only two images.

As an alternative to the elaborate method described in this section, one might consider producing a cosmic cleaned combined image by simply taking the median of the input frames. This procedure is very good at removing cosmics. The price is lower signal-to-noise: Compared to an image that is the mean of the input frames, the median will have $\sqrt{\pi/2} \approx 25\%$ larger noise (known as standard error in the statistical terminology), assuming a normal parent distribution (e.g. Stuart & Ord 1987). Another problem with this procedure is that only a combined image is produced, not individual cleaned images.

A final comment – after the cosmic identification method described here had been developed, van Dokkum (2001) published a new method to identify cosmics in single frame, using Laplacian edge detection plus a consideration of the symmetry of the identified features. We have not tried the method, but from the examples shown in the paper it seems very good (the examples are imaging and longslit spectra [with a non-tilted slit]). However, the notes[3] accompanying the corresponding IRAF task strongly recommends that the sky lines in spectroscopic frames be subtracted before the method is applied, and here lies the problem: for spectra with tilted slits (and hence tilted sky lines), the sky lines cannot be subtracted before the data (still 2D) have been wavelength calibrated. On the other hand, the wavelength calibration interpolates the pixel values, causing the sharp edges of the cosmics to be lost. A workaround could be to apply the wavelength calibration, extract the 2D sky spectrum (using some robust method that was unaffected by the cosmics), and apply the *inverse* 2D wavelength calibration to get a cosmic free 2D sky spectrum with tilted lines that could be subtracted from the original data. However, within IRAF there is no task that will compute the necessary inverse of a given transformation.

[3] `http://www.astro.caltech.edu/~pgd/lacosmic/notes.html`

Appendix B

Atlas of images and spectra

This atlas shows for each galaxy the HST images in the 2 available filters (F606W and F814W) and the continuum subtracted 2D spectra for the available emission lines. Each row of the figures shows 3 images: observed, model (GIM2D or ELFIT2D) and residual. The direct images are modelled using the GIM2D bulge/disk decomposition procedure, see Sect. 4.3. The 2D spectra are modelled using ELFIT2D, see Ch. 3.

The HST images have been rotated so that the direction of the slit is vertical. This makes it easy to compare the direct images with the 2D spectra, which have the y–axis as the spatial axis. The slit is not shown on the HST images and needs to be imagined: it runs through the centre of the galaxy and has a width of $1'' \cdot \cos(\theta_{\rm slit})$ [cf. Fig. 2.2, p. 19]. The size of the image sections shown is given on the figures. The size has been chosen to match the spatial size of the spectral postage stamp images. The stated size always refers to the area outlined by the dashed line. In some cases (e.g. galaxy C2/F14, p. 169) the underlying HST postage stamp image is smaller than this area. This is because the underlying postage stamp images are those generated by GIM2D based on the isophotal size of the galaxy. A detail: the HST images are centered at the SExtractor controid of the given galaxy, but the centre of the bulge/disk model is a free parameter, so the model might not be centered exactly in the postage stamp image (an example of a 'large' displacement is galaxy B1/F22, p. 186).

The model spectra and the listed values of $V_{\rm rot} \sin i$ and $r_{\rm d}$ are based on the Universal Rotation Curve and 4–times spectral oversampling, cf. Sect. 3.1. As discussed in Sect. 3.3.2, some emission lines were rejected, based on a visual inspection, for one of two reasons. For some galaxies the morphology of the emission lines did not match the model used by ELFIT2D. These galaxies were excluded from the analysis and are labelled "*not used: mismatch*" in the atlas (p. 157; p. 159; p. 161). Some emission lines were damaged by an imperfect subtraction of a sky line. These individual lines were excluded from the analysis, but other lines were available. The damaged lines are labelled "*not used: data damaged*" in the atlas (e.g. p. 171).

The listed intensity cuts are in ADU. The emission lines are named as follows

3727 = [OII]
4340 = Hγ
4861 = Hβ
4959 = [OIII]λ4959
5007 = [OIII]λ5007
6563 = Hα
6583 = [NII]

Note: The reproduction on paper does not always do the spectra full credit.

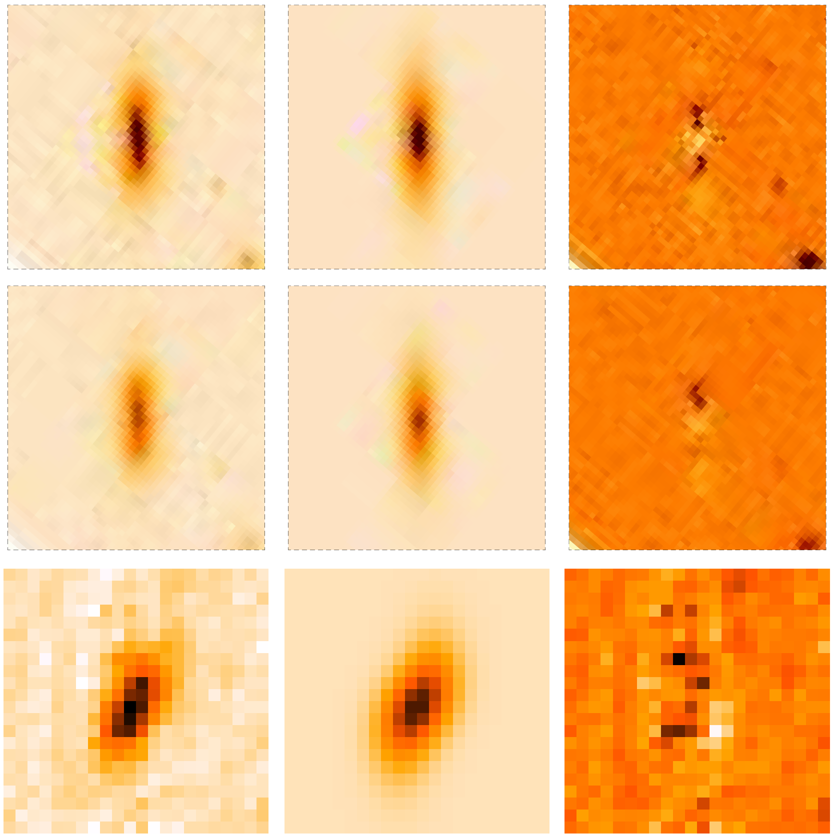

filter: F606W
image sizes: $5.1'' \times 5.1''$
image1+2 cuts: $(-5, 50)$
image3 cuts: $(-10, 10)$

filter: F814W
image sizes: $5.1'' \times 5.1''$
image1+2 cuts: $(-5, 50)$
image3 cuts: $(-10, 10)$

line: 6563
image sizes: $24\,\text{Å} \times 5.1''$
image1+2 cuts: $(-5, 40)$
image3 cuts: $(-10, 10)$
$V_{\rm rot} \sin i = 73.3^{+3.7}_{-2.4}\,{\rm km\,s^{-1}}$
$r_{\rm d} = 0.37^{+0.01}_{-0.01}{}''$

Figure B.1: Galaxy Z/F01 at $z = 0.1538$ ($\theta_{\rm slit} = +30°$).

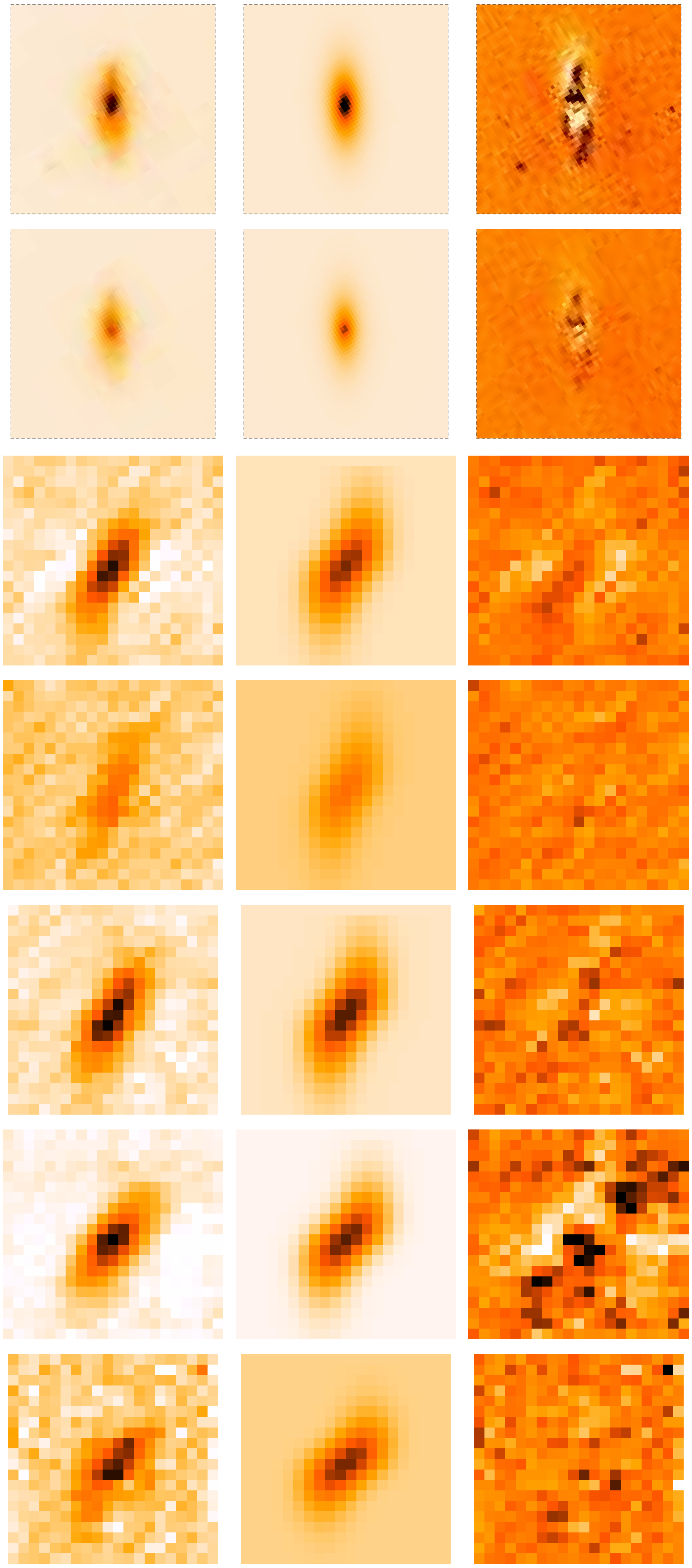

filter: F606W
image sizes: $6.0'' \times 6.0''$
image1+2 cuts: $(-9, 125)$
image3 cuts: $(-10, 10)$

filter: F814W
image sizes: $6.0'' \times 6.0''$
image1+2 cuts: $(-9, 125)$
image3 cuts: $(-10, 10)$

line: 4861
image sizes: $23\,\text{Å} \times 6.0''$
image1+2 cuts: $(-5, 30)$
image3 cuts: $(-10, 10)$
$V_{\rm rot} \sin i = 105.4^{+2.1}_{-2.5}\,\rm km\,s^{-1}$
$r_{\rm d} = 0.73^{+0.02}_{-0.02}{''}$
not used: mismatch

line: 4959
image sizes: $23\,\text{Å} \times 6.0''$
image1+2 cuts: $(-5, 25)$
image3 cuts: $(-10, 10)$
$V_{\rm rot} \sin i = 87.8^{+8.1}_{-6.8}\,\rm km\,s^{-1}$
$r_{\rm d} = 0.81^{+0.05}_{-0.04}{''}$
not used: mismatch

line: 5007
image sizes: $21\,\text{Å} \times 6.0''$
image1+2 cuts: $(-5, 45)$
image3 cuts: $(-10, 10)$
$V_{\rm rot} \sin i = 104.2^{+3.0}_{-2.7}\,\rm km\,s^{-1}$
$r_{\rm d} = 0.74^{+0.02}_{-0.02}{''}$
not used: mismatch

line: 6563
image sizes: $23\,\text{Å} \times 6.0''$
image1+2 cuts: $(-5, 100)$
image3 cuts: $(-10, 10)$
$V_{\rm rot} \sin i = 95.9^{+1.1}_{-1.8}\,\rm km\,s^{-1}$
$r_{\rm d} = 0.59^{+0.01}_{-0.02}{''}$
not used: mismatch

line: 6583
image sizes: $21\,\text{Å} \times 6.0''$
image1+2 cuts: $(-5, 25)$
image3 cuts: $(-10, 10)$
$V_{\rm rot} \sin i = 98.4^{+3.0}_{-3.1}\,\rm km\,s^{-1}$
$r_{\rm d} = 0.45^{+0.02}_{-0.03}{''}$
not used: mismatch

Figure B.2: Galaxy XX6/F02 at $z = 0.1807$ ($\theta_{\rm slit} = +48°$).

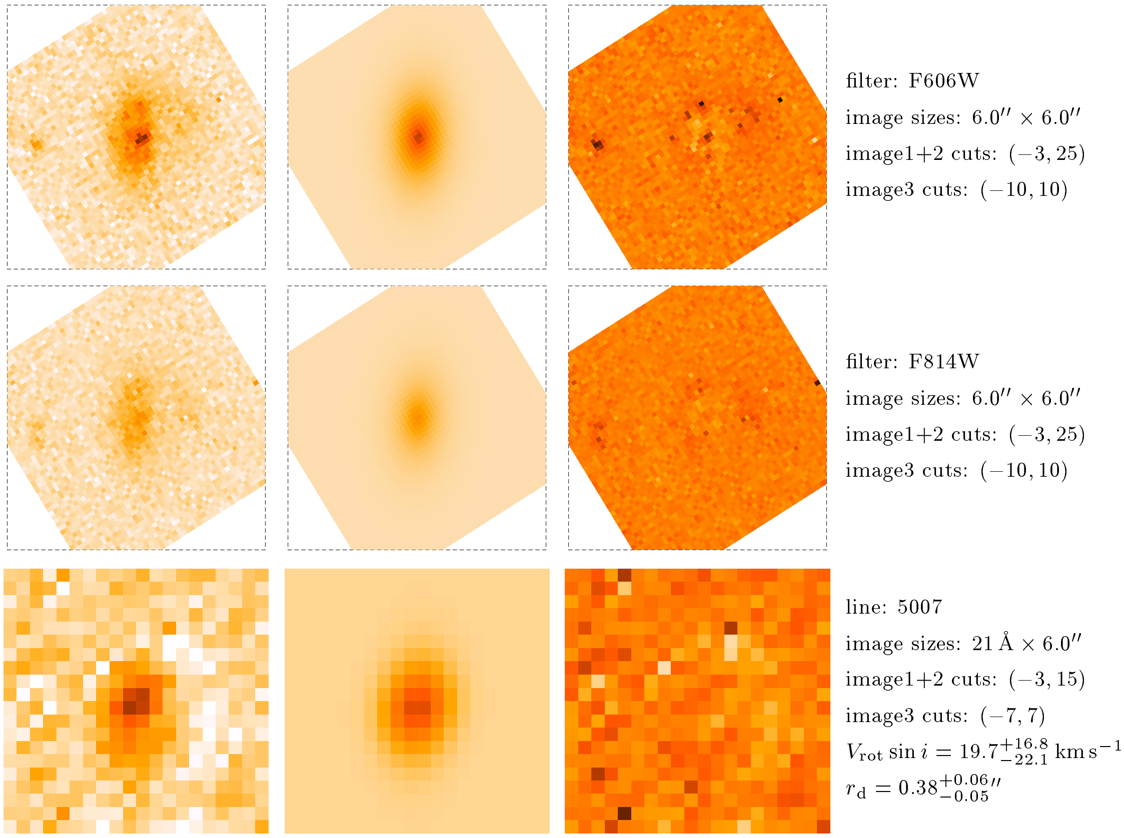

Figure B.3: Galaxy A/F03 at $z = 0.2172$ ($\theta_{\rm slit} = +48°$).

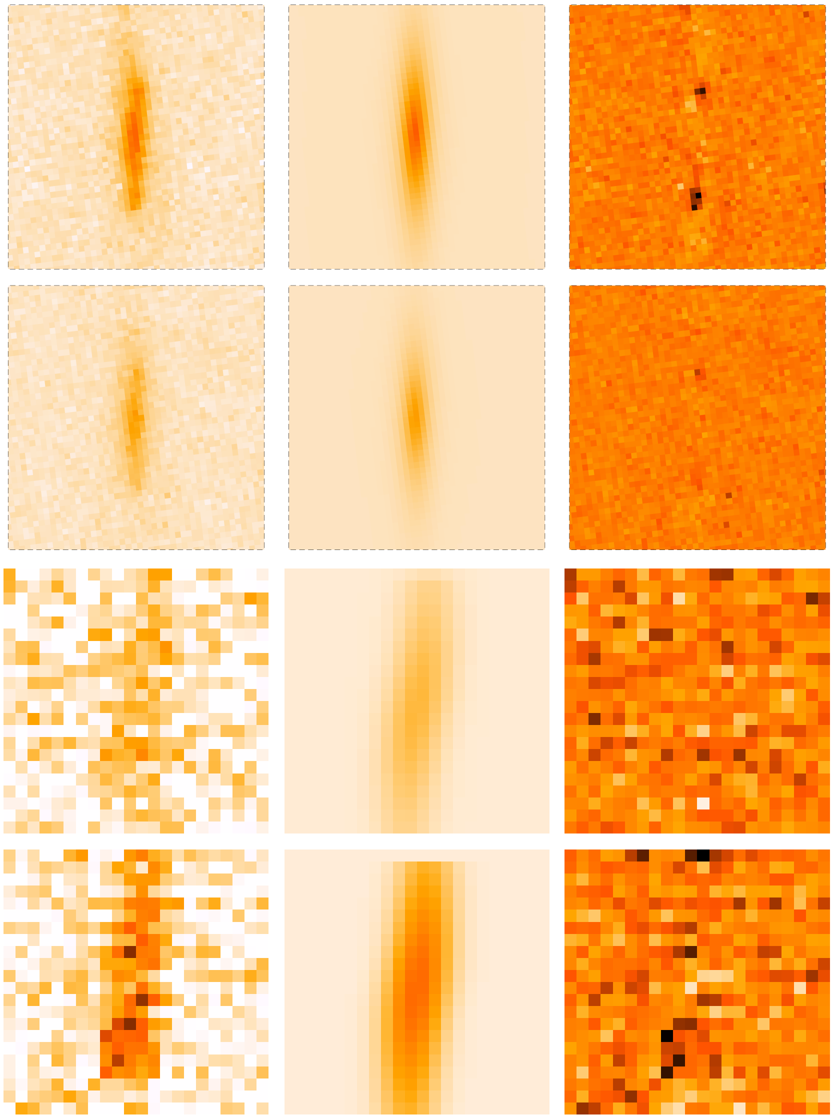

Figure B.4: Galaxy V/F04 at $z = 0.2297$ ($\theta_{\rm slit} = -17°$).

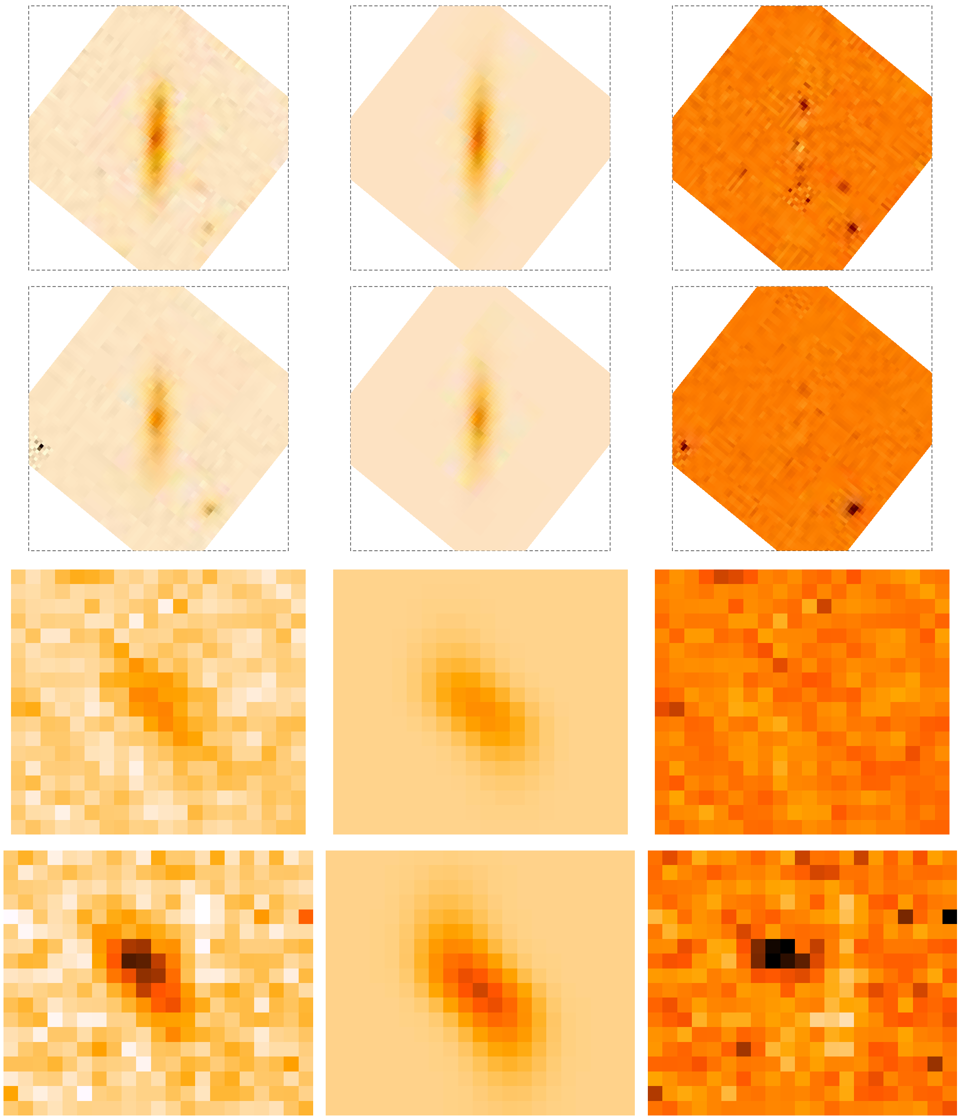

filter: F606W
image sizes: $7.7'' \times 7.7''$
image1+2 cuts: $(-5, 50)$
image3 cuts: $(-10, 10)$

filter: F814W
image sizes: $7.7'' \times 7.7''$
image1+2 cuts: $(-5, 50)$
image3 cuts: $(-10, 10)$

line: 4861
image sizes: $21\,\text{Å} \times 7.7''$
image1+2 cuts: $(-5, 25)$
image3 cuts: $(-10, 10)$
$V_{\rm rot} \sin i = 110.3^{+11.6}_{-12.5}\,{\rm km\,s^{-1}}$
$r_{\rm d} = 0.61^{+0.06}_{-0.06}{''}$

line: 5007
image sizes: $23\,\text{Å} \times 7.7''$
image1+2 cuts: $(-5, 25)$
image3 cuts: $(-10, 10)$
$V_{\rm rot} \sin i = 118.1^{+6.8}_{-7.8}\,{\rm km\,s^{-1}}$
$r_{\rm d} = 0.79^{+0.04}_{-0.04}{''}$

Figure B.5: Galaxy G/F05 at $z = 0.2495$ ($\theta_{\rm slit} = -62°$).

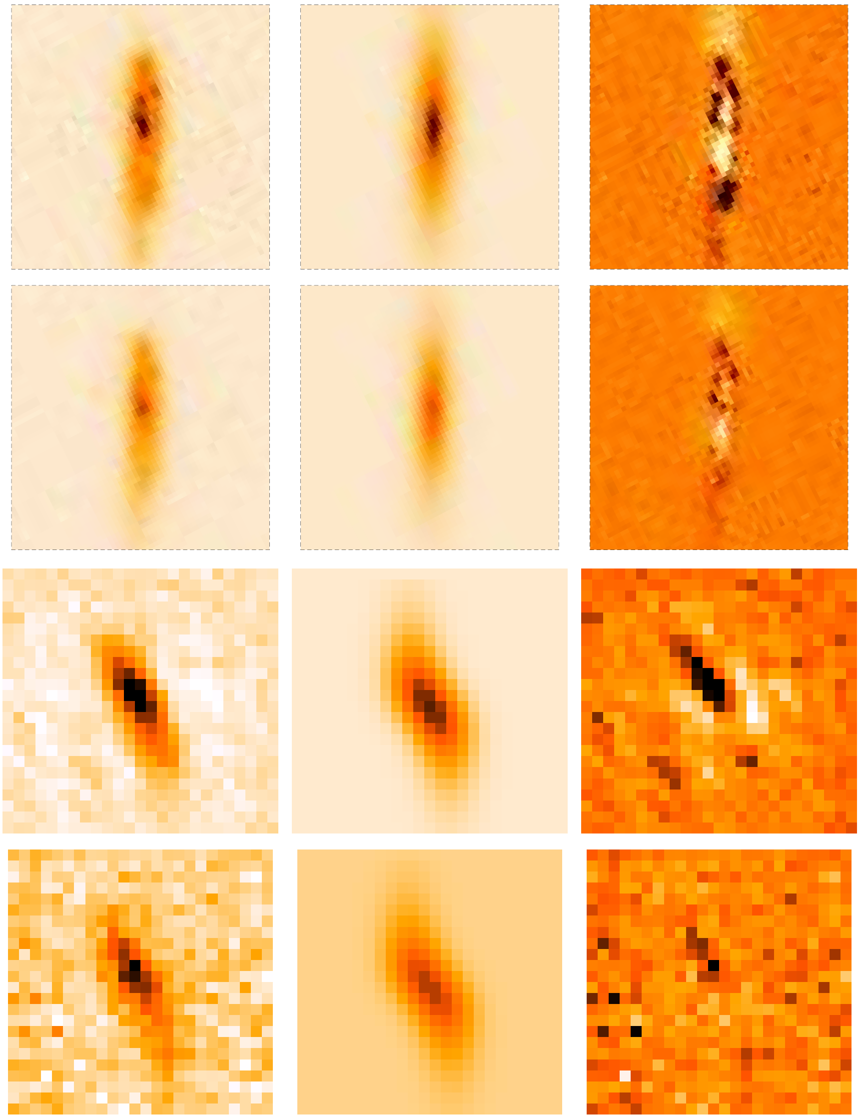

filter: F606W
image sizes: $6.0'' \times 6.0''$
image1+2 cuts: $(-5, 60)$
image3 cuts: $(-10, 10)$

filter: F814W
image sizes: $6.0'' \times 6.0''$
image1+2 cuts: $(-5, 60)$
image3 cuts: $(-10, 10)$

line: 4861
image sizes: $27\,\text{Å} \times 6.0''$
image1+2 cuts: $(-5, 45)$
image3 cuts: $(-10, 10)$
$V_{\rm rot} \sin i = 104.0^{+1.4}_{-1.3}\,{\rm km\,s^{-1}}$
$r_{\rm d} = 0.62^{+0.01}_{-0.01}{}''$
not used: mismatch

line: 4959
image sizes: $26\,\text{Å} \times 6.0''$
image1+2 cuts: $(-5, 25)$
image3 cuts: $(-10, 10)$
$V_{\rm rot} \sin i = 115.6^{+4.6}_{-4.8}\,{\rm km\,s^{-1}}$
$r_{\rm d} = 0.64^{+0.03}_{-0.02}{}''$
not used: mismatch

Figure B.6: Galaxy A4/F06 at $z = 0.2594$ ($\theta_{\rm slit} = -37°$).

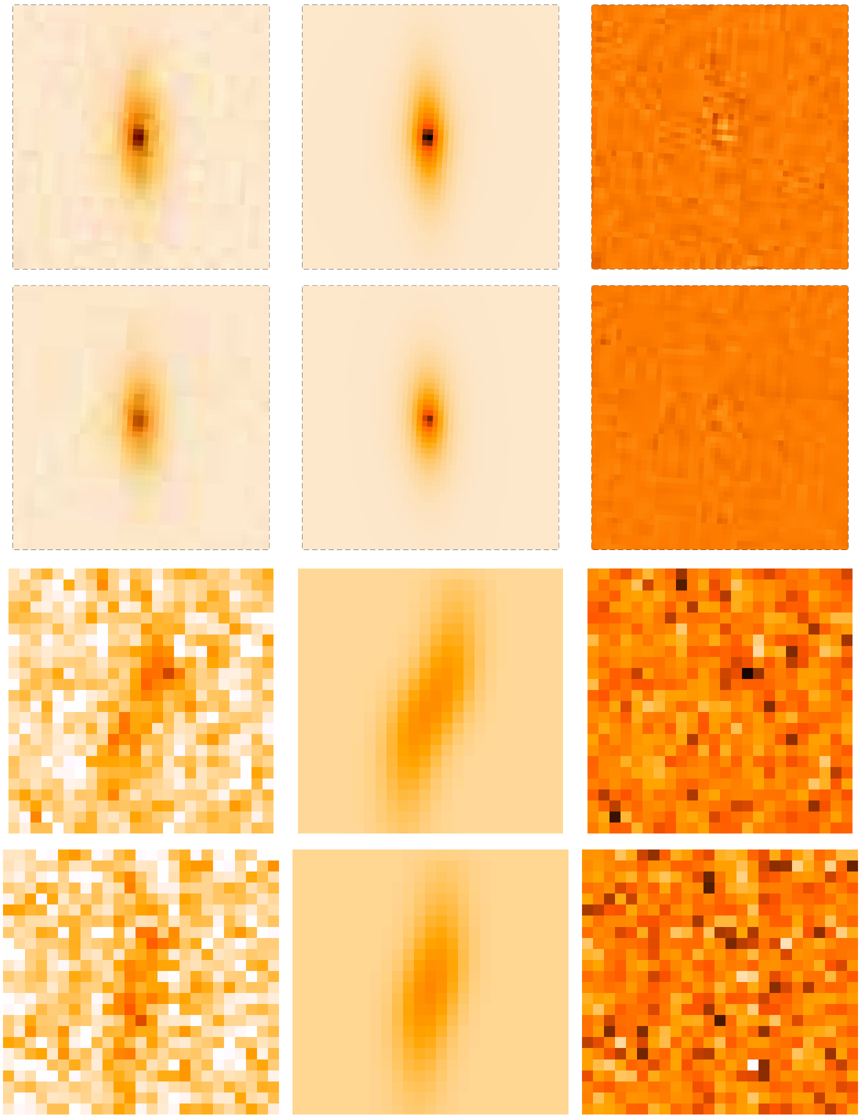

Figure B.7: Galaxy C/F07 at $z = 0.2640$ ($\theta_{\rm slit} = -7^{\circ}$).

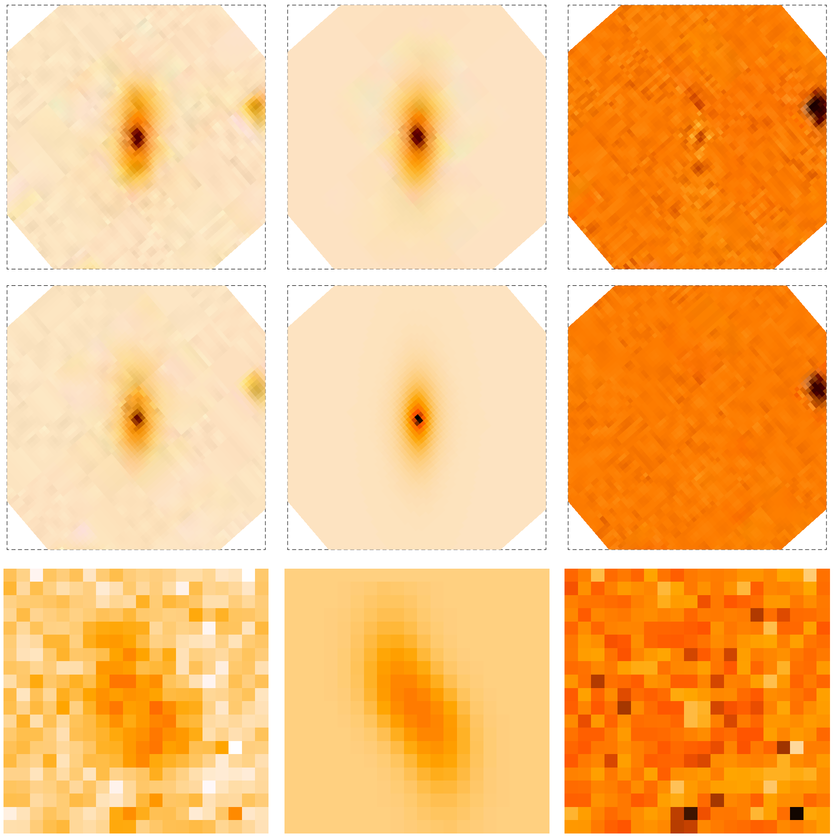

filter: F606W
image sizes: $6.4'' \times 6.4''$
image1+2 cuts: $(-5, 50)$
image3 cuts: $(-10, 10)$

filter: F814W
image sizes: $6.4'' \times 6.4''$
image1+2 cuts: $(-5, 50)$
image3 cuts: $(-10, 10)$

line: 5007
image sizes: $21\,\text{Å} \times 5.2''$
image1+2 cuts: $(-4, 20)$
image3 cuts: $(-7, 7)$
$V_{\rm rot} \sin i = 110.3^{+8.4}_{-9.4}\,{\rm km\,s^{-1}}$
$r_{\rm d} = 0.60^{+0.07}_{-0.06}{}''$

Figure B.8: Galaxy U/F08 (mask 1) at $z = 0.2870$ ($\theta_{\rm slit} = +39°$).

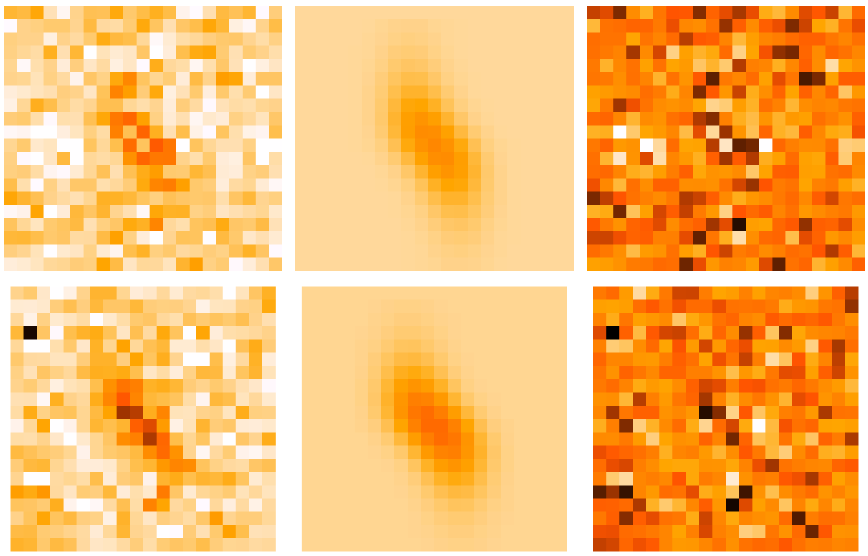

line: 4861
image sizes: $23\,\text{Å} \times 6.4''$
image1+2 cuts: $(-4, 20)$
image3 cuts: $(-7, 7)$
$V_{\rm rot} \sin i = 98.6^{+20.3}_{-11.4}\,{\rm km\,s^{-1}}$
$r_{\rm d} = 0.80^{+0.17}_{-0.12}{}''$

line: 5007
image sizes: $21\,\text{Å} \times 6.4''$
image1+2 cuts: $(-4, 20)$
image3 cuts: $(-7, 7)$
$V_{\rm rot} \sin i = 100.0^{+7.9}_{-7.4}\,{\rm km\,s^{-1}}$
$r_{\rm d} = 0.65^{+0.06}_{-0.07}{}''$

Figure B.9: Galaxy U/F08 (mask 2) at $z = 0.2870$ ($\theta_{\rm slit} = -51°$).

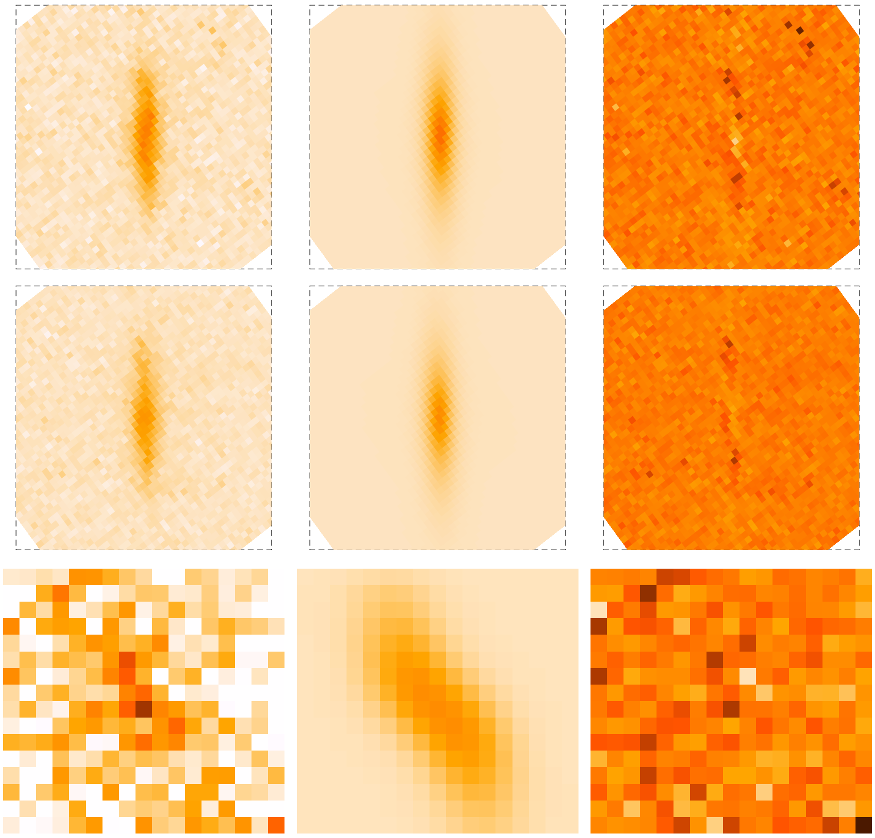

filter: F606W
image sizes: $4.4'' \times 4.4''$
image1+2 cuts: $(-5, 50)$
image3 cuts: $(-10, 10)$

filter: F814W
image sizes: $4.4'' \times 4.4''$
image1+2 cuts: $(-5, 50)$
image3 cuts: $(-10, 10)$

line: 5007
image sizes: $18\,\text{Å} \times 4.4''$
image1+2 cuts: $(-1, 10)$
image3 cuts: $(-7, 7)$
$V_{\rm rot} \sin i = 153.9^{+30.4}_{-31.9}\,\mathrm{km\,s^{-1}}$
$r_{\rm d} = 0.74^{+0.25}_{-0.20}{}''$

Figure B.10: Galaxy P/F09 at $z = 0.3232$ ($\theta_{\rm slit} = +43°$).

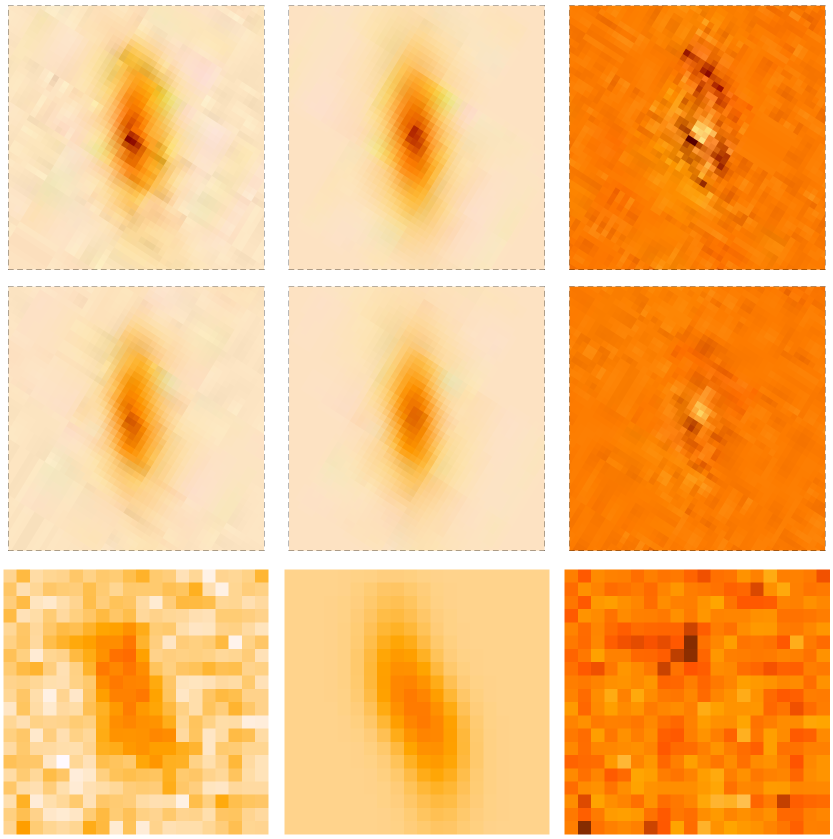

Figure B.11: Galaxy A7/F10 at $z = 0.3237$ ($\theta_{\rm slit} = +23°$).

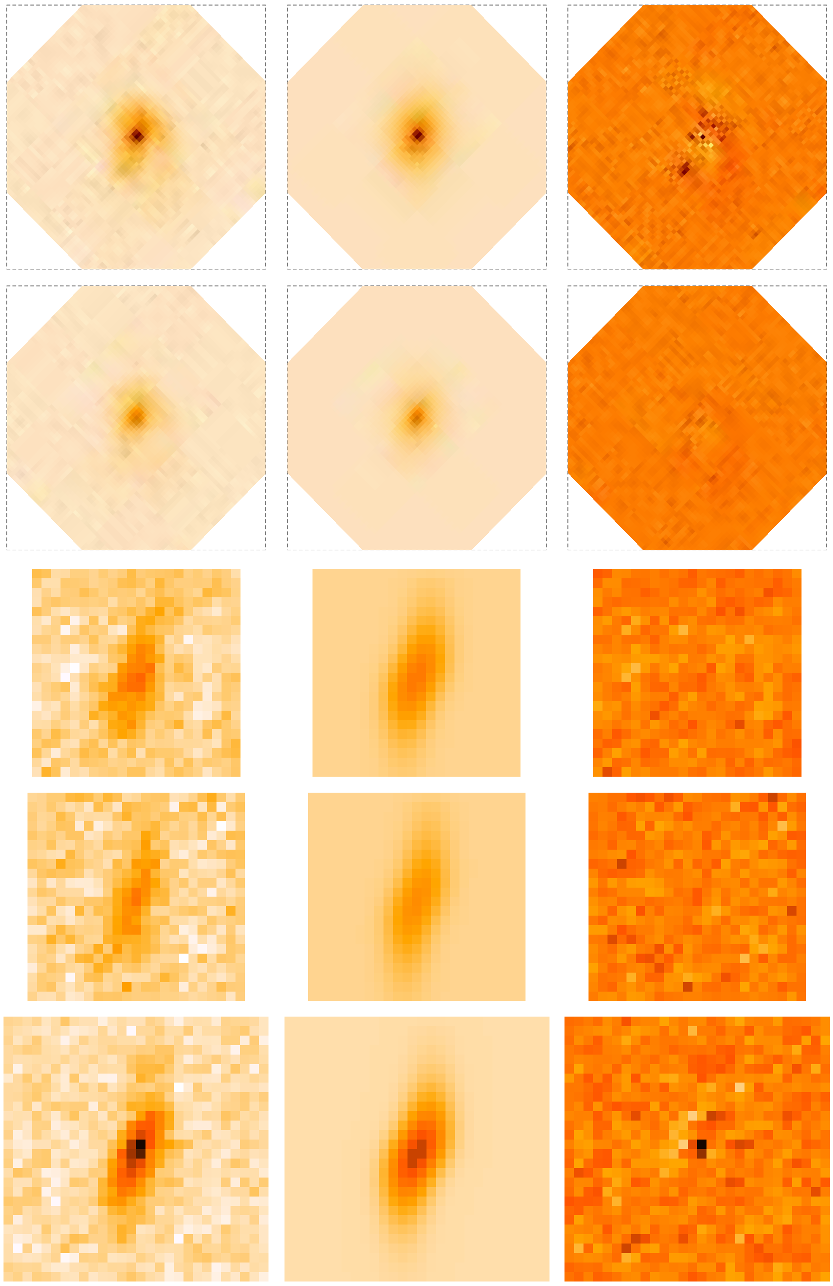

filter: F606W
image sizes: $6.9'' \times 6.9''$
image1+2 cuts: $(-5, 50)$
image3 cuts: $(-10, 10)$

filter: F814W
image sizes: $6.9'' \times 6.9''$
image1+2 cuts: $(-5, 50)$
image3 cuts: $(-10, 10)$

line: 4861
image sizes: $24\,\text{Å} \times 5.4''$
image1+2 cuts: $(-5, 25)$
image3 cuts: $(-10, 10)$
$V_{\rm rot} \sin i = 70.3^{+6.8}_{-8.3}\,{\rm km\,s^{-1}}$
$r_{\rm d} = 0.76^{+0.06}_{-0.05}{}''$

line: 4959
image sizes: $25\,\text{Å} \times 5.4''$
image1+2 cuts: $(-5, 25)$
image3 cuts: $(-10, 10)$
$V_{\rm rot} \sin i = 66.0^{+9.0}_{-8.4}\,{\rm km\,s^{-1}}$
$r_{\rm d} = 0.96^{+0.15}_{-0.10}{}''$

line: 5007
image sizes: $30\,\text{Å} \times 6.9''$
image1+2 cuts: $(-5, 35)$
image3 cuts: $(-10, 10)$
$V_{\rm rot} \sin i = 75.2^{+2.6}_{-2.7}\,{\rm km\,s^{-1}}$
$r_{\rm d} = 0.67^{+0.02}_{-0.02}{}''$

Figure B.12: Galaxy N/F11 at $z = 0.3248$ ($\theta_{\rm slit} = +35°$).

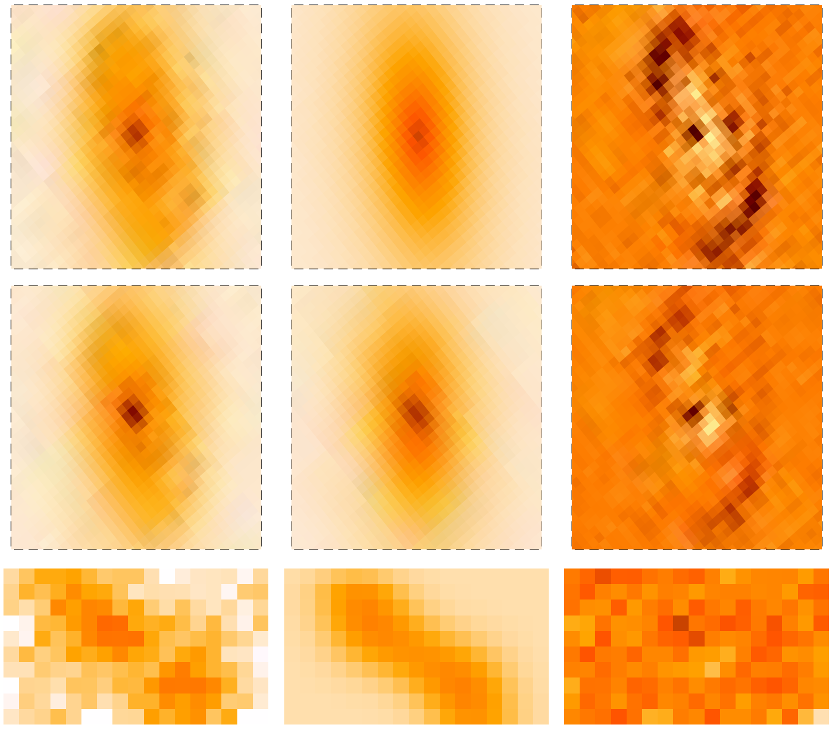

filter: F606W
image sizes: $2.7'' \times 2.7''$
image1+2 cuts: $(-5, 70)$
image3 cuts: $(-10, 10)$

filter: F814W
image sizes: $2.7'' \times 2.7''$
image1+2 cuts: $(-5, 70)$
image3 cuts: $(-10, 10)$

line: 4861
image sizes: $18\,\text{Å} \times 2.7''$
image1+2 cuts: $(-3, 15)$
image3 cuts: $(-7, 7)$
$V_{\rm rot} \sin i = 236.6^{+9.7}_{-7.6}\,{\rm km\,s^{-1}}$
$r_{\rm d} = 0.95^{+0.24}_{-0.20}{''}$

Figure B.13: Galaxy XX4/F12 at $z = 0.3253$ ($\theta_{\rm slit} = +41°$).

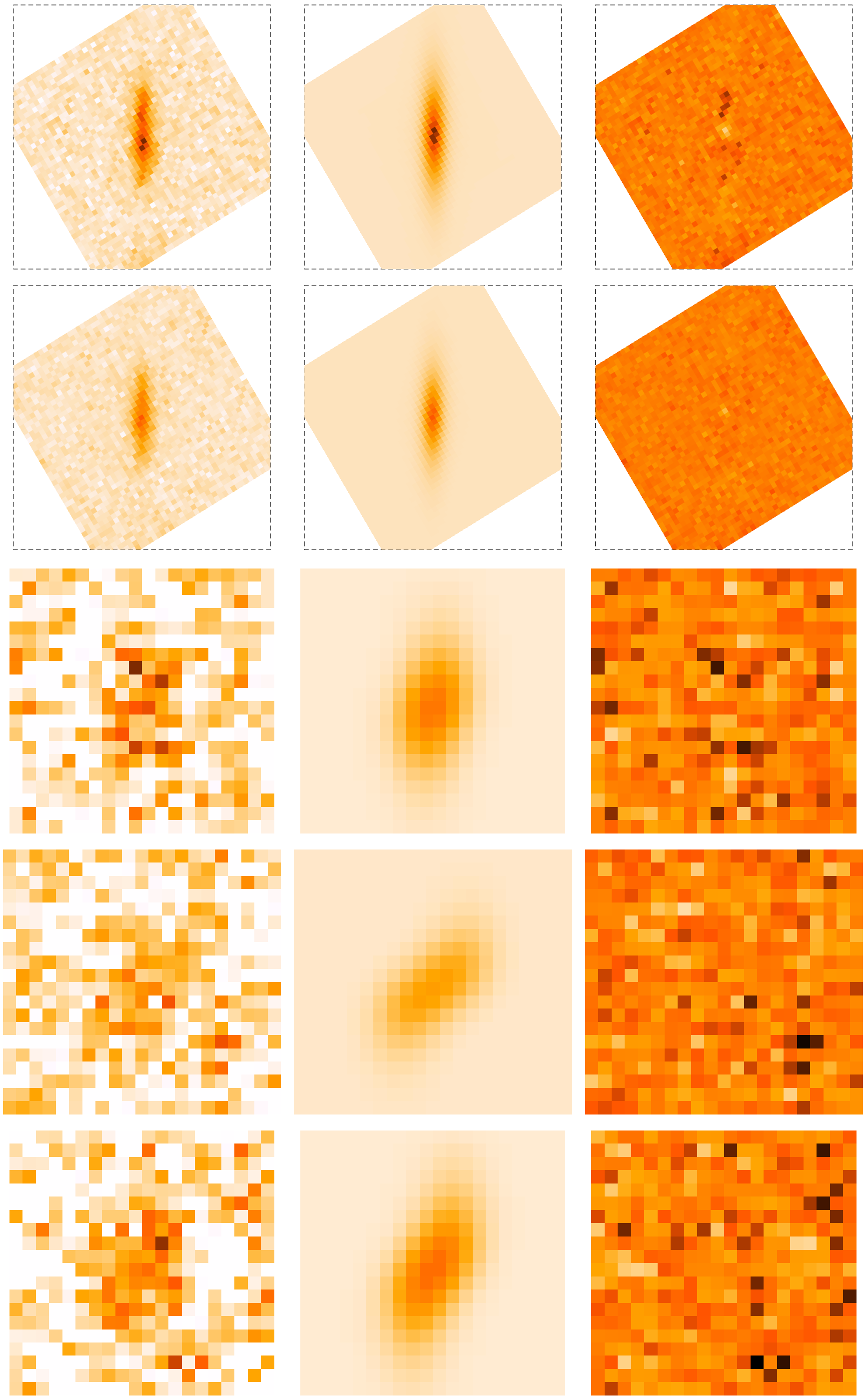

filter: F606W
image sizes: 5.3″ × 5.3″
image1+2 cuts: (−3, 30)
image3 cuts: (−10, 10)

filter: F814W
image sizes: 5.3″ × 5.3″
image1+2 cuts: (−3, 30)
image3 cuts: (−10, 10)

line: 4861
image sizes: 21 Å × 5.3″
image1+2 cuts: (−1, 10)
image3 cuts: (−7, 7)
$V_{\rm rot}\sin i = 33.4^{+19.6}_{-25.2}\,{\rm km\,s^{-1}}$
$r_{\rm d} = 0.52^{+0.08}_{-0.09}{}''$
not used: data damaged

line: 4959
image sizes: 23 Å × 5.3″
image1+2 cuts: (−1, 10)
image3 cuts: (−7, 7)
$V_{\rm rot}\sin i = 134.3^{+35.0}_{-33.8}\,{\rm km\,s^{-1}}$
$r_{\rm d} = 0.41^{+0.15}_{-0.13}{}''$
not used: data damaged

line: 5007
image sizes: 21 Å × 5.3″
image1+2 cuts: (−1, 10)
image3 cuts: (−7, 7)
$V_{\rm rot}\sin i = 82.0^{+21.0}_{-18.0}\,{\rm km\,s^{-1}}$
$r_{\rm d} = 0.61^{+0.13}_{-0.10}{}''$

Figure B.14: Galaxy B5/F13 at $z = 0.3737$ ($\theta_{\rm slit} = -41°$).

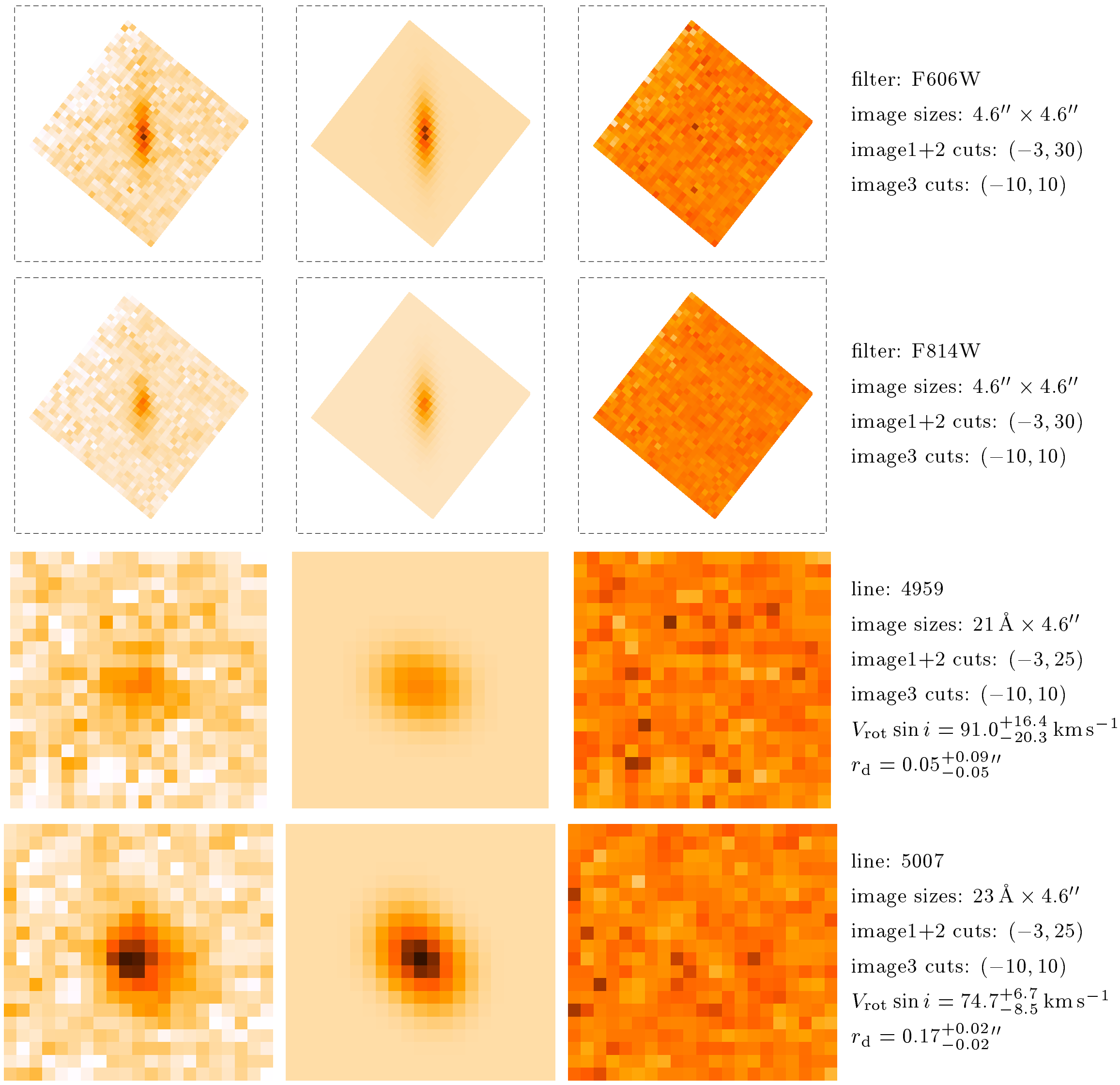

Figure B.15: Galaxy C2/F14 at $z = 0.4290$ ($\theta_{\rm slit} = +29°$).

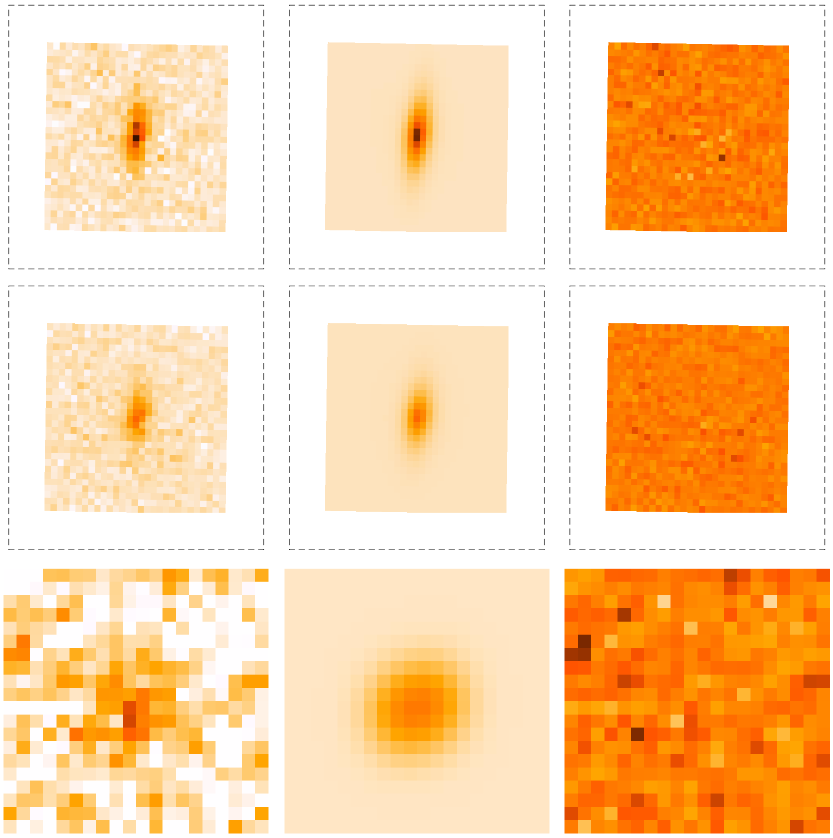

filter: F606W
image sizes: $4.1'' \times 4.1''$
image1+2 cuts: $(-3, 30)$
image3 cuts: $(-10, 10)$

filter: F814W
image sizes: $4.1'' \times 4.1''$
image1+2 cuts: $(-3, 30)$
image3 cuts: $(-10, 10)$

line: 4861
image sizes: $21\,\text{Å} \times 4.1''$
image1+2 cuts: $(-1, 10)$
image3 cuts: $(-7, 7)$
$V_{\rm rot} \sin i = 97.4^{+17.9}_{-42.9}\,\mathrm{km\,s^{-1}}$
$r_{\rm d} = 0.05^{+0.25}_{-0.05}{}''$

Figure B.16: Galaxy D/F15 at $z = 0.4693$ ($\theta_{\rm slit} = -9°$).

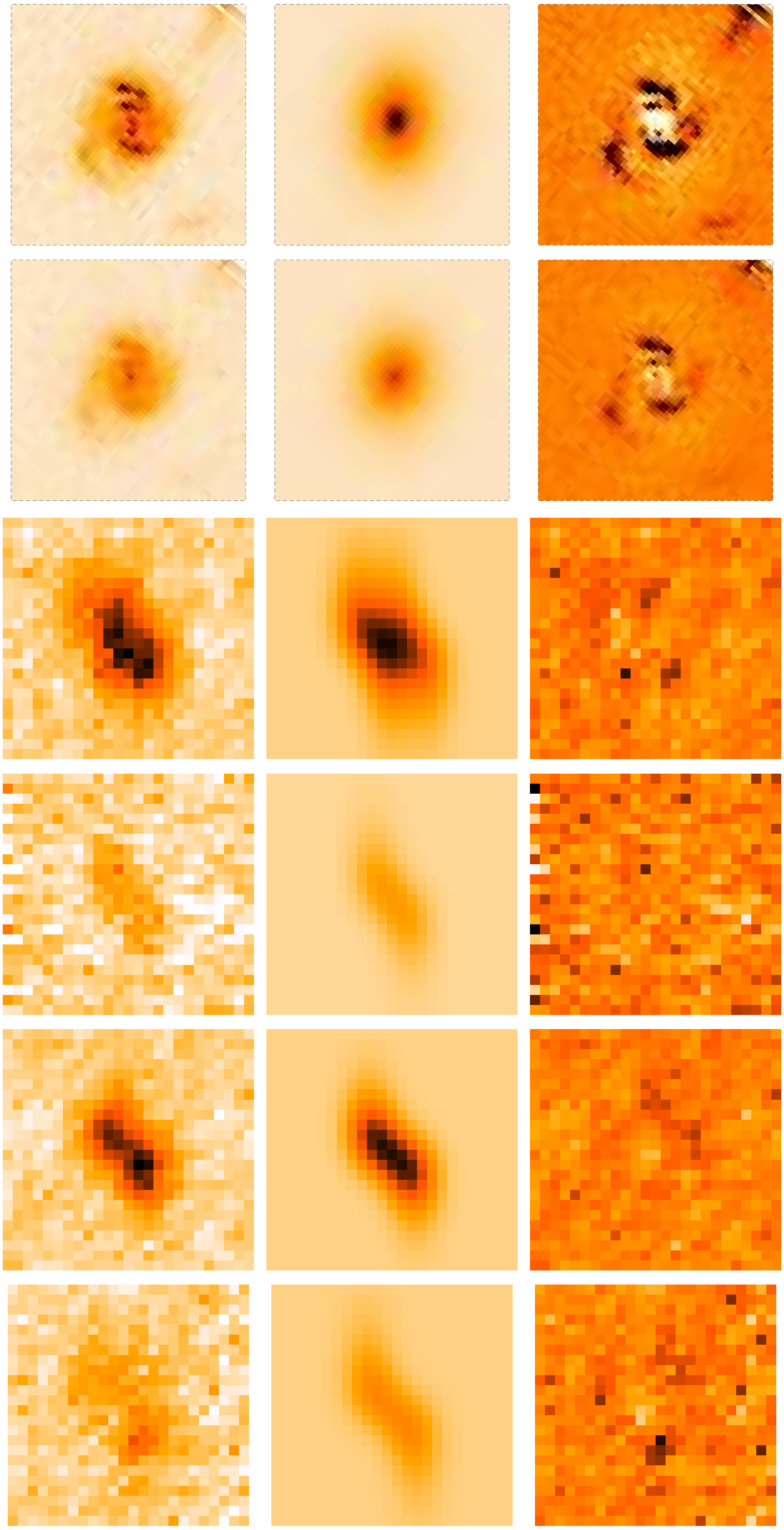

filter: F606W
image sizes: $5.6'' \times 5.6''$
image1+2 cuts: $(-5, 50)$
image3 cuts: $(-10, 10)$

filter: F814W
image sizes: $5.6'' \times 5.6''$
image1+2 cuts: $(-5, 50)$
image3 cuts: $(-10, 10)$

line: 3727
image sizes: $27\,\text{Å} \times 5.6''$
image1+2 cuts: $(-5, 25)$
image3 cuts: $(-10, 10)$
$V_{\rm rot} \sin i = 103.2^{+3.3}_{-2.6}\,{\rm km\,s^{-1}}$
$r_{\rm d} = 0.73^{+0.02}_{-0.02}{}''$

line: 4340
image sizes: $27\,\text{Å} \times 5.6''$
image1+2 cuts: $(-5, 25)$
image3 cuts: $(-10, 10)$
$V_{\rm rot} \sin i = 103.7^{+8.5}_{-7.4}\,{\rm km\,s^{-1}}$
$r_{\rm d} = 0.67^{+0.10}_{-0.08}{}''$

line: 4861
image sizes: $27\,\text{Å} \times 5.6''$
image1+2 cuts: $(-5, 25)$
image3 cuts: $(-10, 10)$
$V_{\rm rot} \sin i = 112.5^{+0.7}_{-1.4}\,{\rm km\,s^{-1}}$
$r_{\rm d} = 0.48^{+0.02}_{-0.01}{}''$

line: 5007
image sizes: $26\,\text{Å} \times 5.6''$
image1+2 cuts: $(-5, 25)$
image3 cuts: $(-10, 10)$
$V_{\rm rot} \sin i = 118.0^{+5.2}_{-12.9}\,{\rm km\,s^{-1}}$
$r_{\rm d} = 0.77^{+0.06}_{-0.06}{}''$
not used: data damaged

Figure B.17: Galaxy XX1/F16 at $z = 0.4701$ ($\theta_{\rm slit} = +30°$).

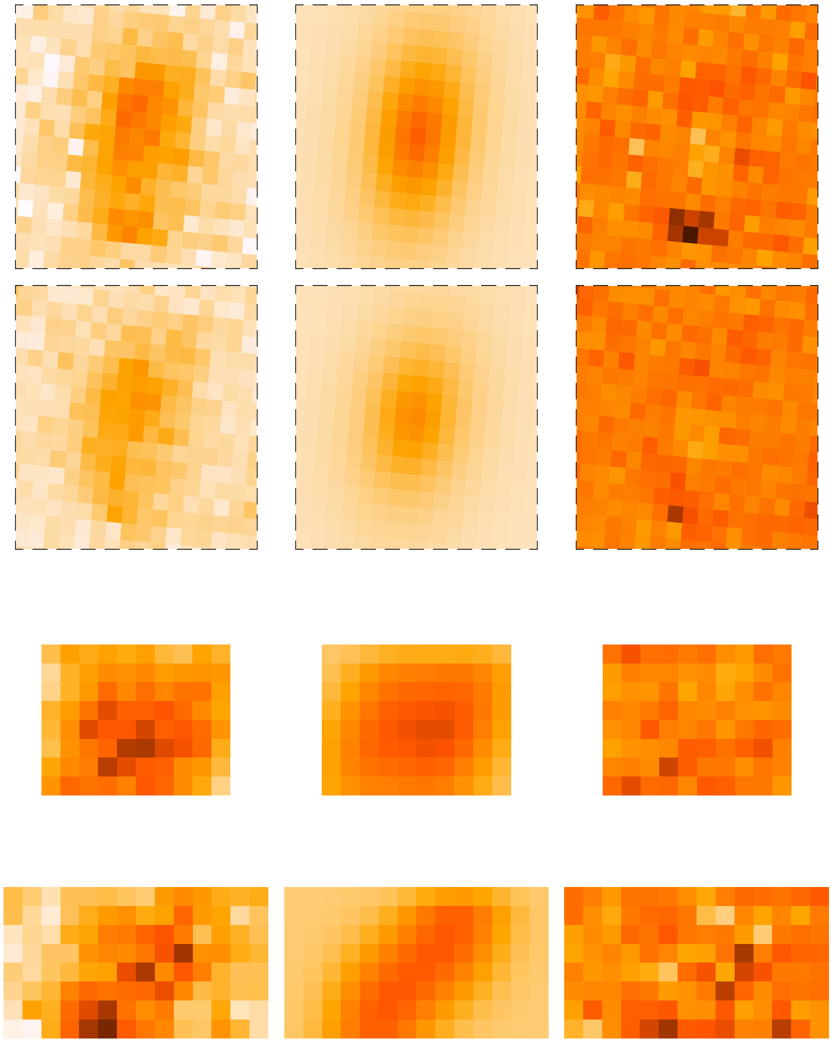

filter: F606W
image sizes: $1.6'' \times 1.6''$
image1+2 cuts: $(-3, 30)$
image3 cuts: $(-10, 10)$

filter: F814W
image sizes: $1.6'' \times 1.6''$
image1+2 cuts: $(-3, 30)$
image3 cuts: $(-10, 10)$

line: 3727
image sizes: $11\,\text{Å} \times 1.6''$
image1+2 cuts: $(-5, 20)$
image3 cuts: $(-10, 10)$
$V_{\rm rot} \sin i = 80.9^{+15.7}_{-8.3}\,\rm km\,s^{-1}$
$r_{\rm d} = 0.41^{+0.14}_{-0.08}{}''$

line: 5007
image sizes: $15\,\text{Å} \times 1.6''$
image1+2 cuts: $(-5, 20)$
image3 cuts: $(-10, 10)$
$V_{\rm rot} \sin i = 146.3^{+7.1}_{-7.4}\,\rm km\,s^{-1}$
$r_{\rm d} = 0.75^{+0.17}_{-0.16}{}''$

Figure B.18: Galaxy C6/F17 at $z = 0.4935$ ($\theta_{\rm slit} = -5°$).

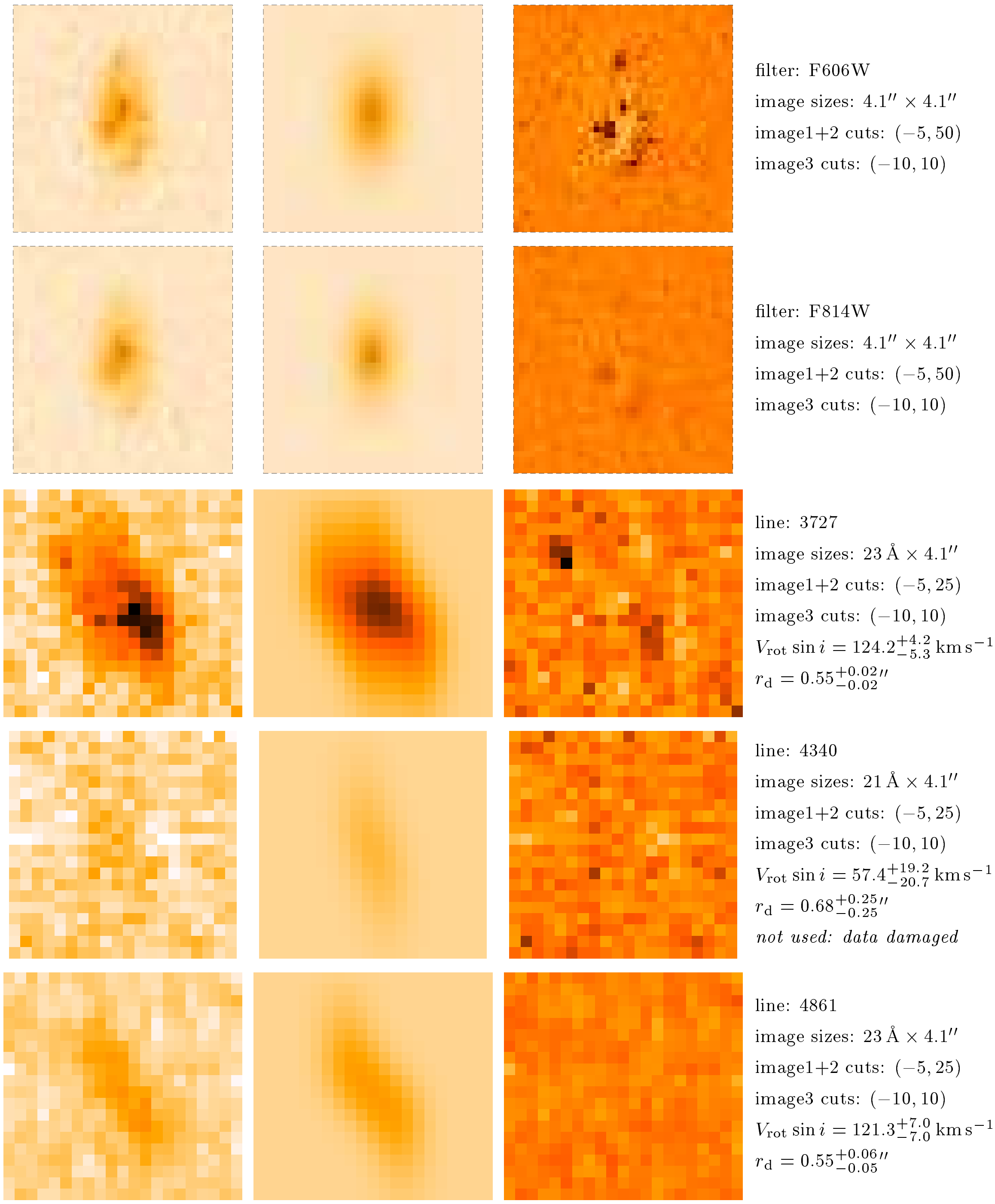

Figure B.19: Galaxy Y/F18 at $z = 0.5529$ ($\theta_{\rm slit} = -10°$).

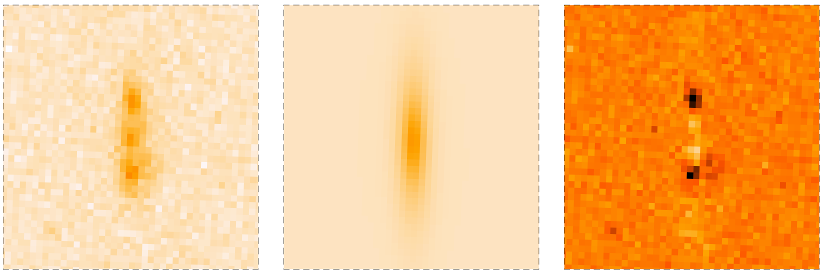

filter: F606W
image sizes: $4.1'' \times 4.1''$
image1+2 cuts: $(-5, 50)$
image3 cuts: $(-10, 10)$

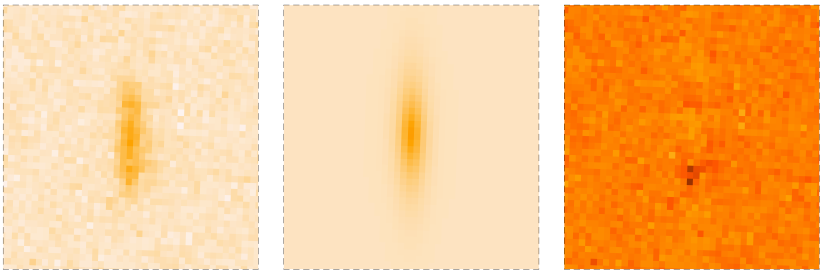

filter: F814W
image sizes: $4.1'' \times 4.1''$
image1+2 cuts: $(-5, 50)$
image3 cuts: $(-10, 10)$

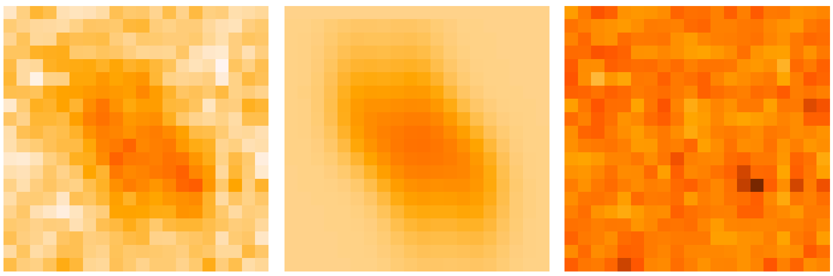

line: 3727
image sizes: $21\,\text{Å} \times 4.1''$
image1+2 cuts: $(-5, 25)$
image3 cuts: $(-10, 10)$
$V_{\rm rot} \sin i = 144.4^{+8.7}_{-6.2}\,{\rm km\,s^{-1}}$
$r_{\rm d} = 0.52^{+0.03}_{-0.02}{}''$

Figure B.20: Galaxy D2/F19 at $z = 0.6841$ ($\theta_{\rm slit} = -7°$).

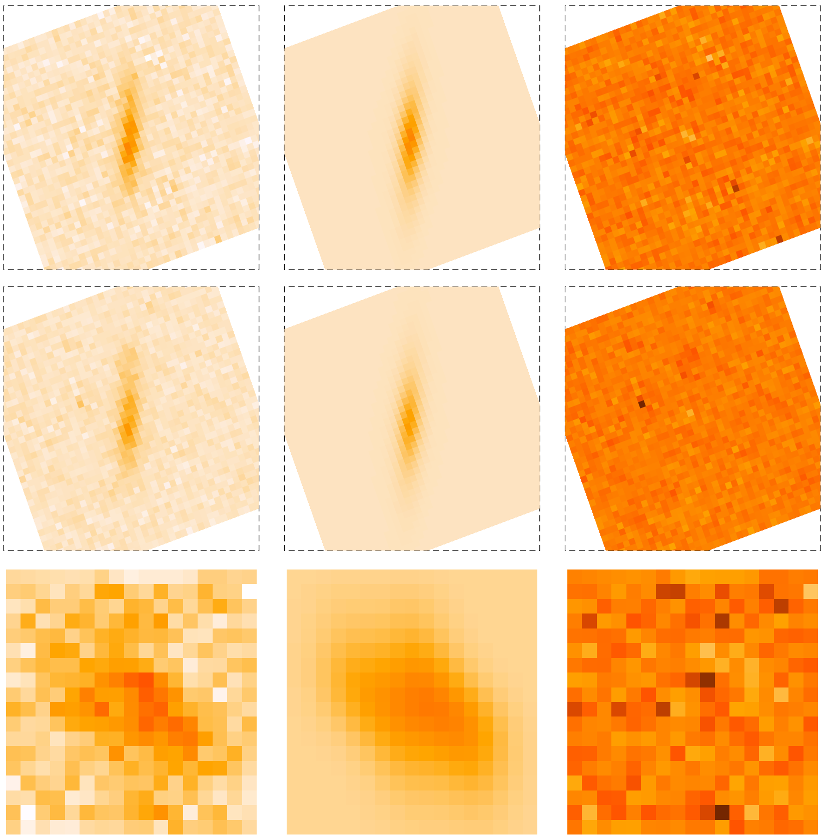

filter: F606W
image sizes: $4.2'' \times 4.2''$
image1+2 cuts: $(-5, 50)$
image3 cuts: $(-10, 10)$

filter: F814W
image sizes: $4.2'' \times 4.2''$
image1+2 cuts: $(-5, 50)$
image3 cuts: $(-10, 10)$

line: 3727
image sizes: $18\,\text{Å} \times 4.2''$
image1+2 cuts: $(-5, 25)$
image3 cuts: $(-10, 10)$
$V_{\rm rot} \sin i = 131.1^{+10.4}_{-11.1}\,{\rm km\,s^{-1}}$
$r_{\rm d} = 0.48^{+0.05}_{-0.04}{}''$

Figure B.21: Galaxy B4/F20 at $z = 0.6865$ ($\theta_{\rm slit} = -30°$).

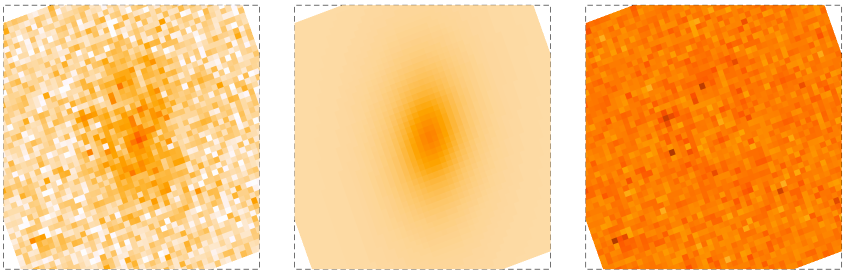

filter: F606W
image sizes: 4.6″ × 4.6″
image1+2 cuts: (−2, 15)
image3 cuts: (−10, 10)

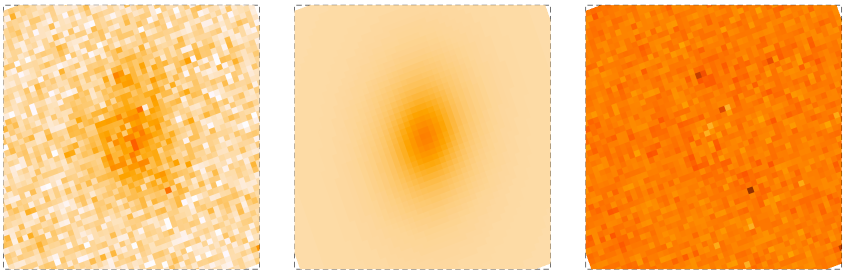

filter: F814W
image sizes: 4.6″ × 4.6″
image1+2 cuts: (−2, 15)
image3 cuts: (−10, 10)

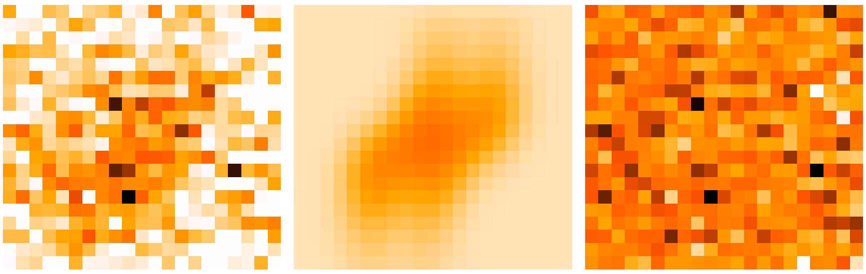

line: 3727
image sizes: 23 Å × 4.2″
image1+2 cuts: (−1, 10)
image3 cuts: (−7, 7)
$V_{\rm rot} \sin i = 140.6^{+13.2}_{-15.3}\,{\rm km\,s^{-1}}$
$r_{\rm d} = 0.73^{+0.09}_{-0.07}{}''$

Figure B.22: Galaxy D6/F21 at $z = 0.7558$ ($\theta_{\rm slit} = -30°$).

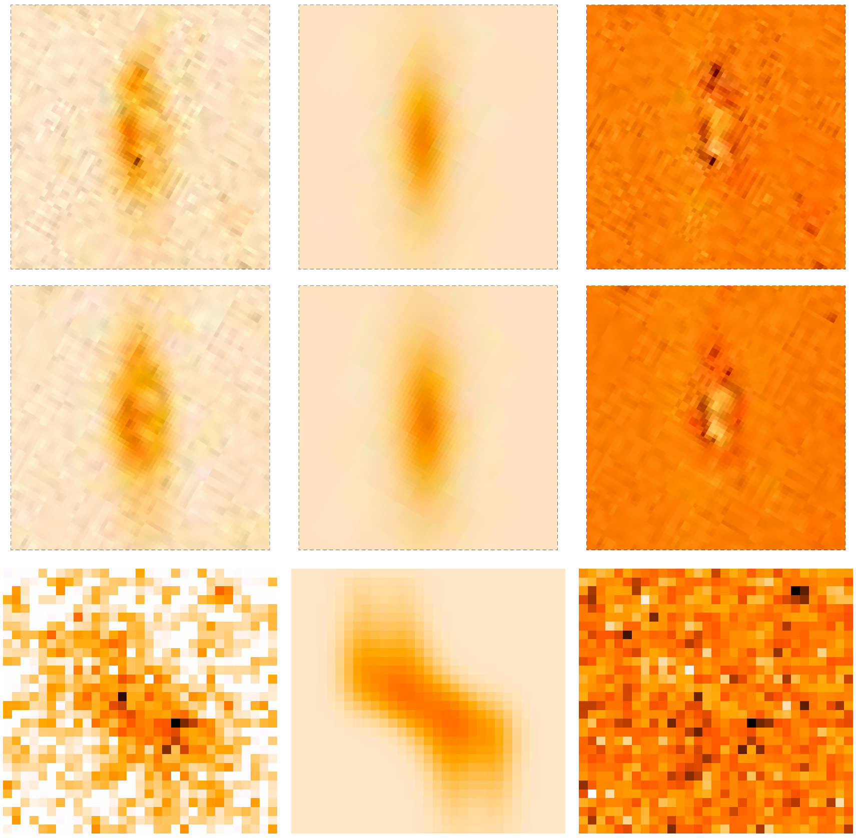

filter: F606W
image sizes: $6.4'' \times 6.4''$
image1+2 cuts: $(-3, 30)$
image3 cuts: $(-10, 10)$

filter: F814W
image sizes: $6.4'' \times 6.4''$
image1+2 cuts: $(-3, 30)$
image3 cuts: $(-10, 10)$

line: 3727
image sizes: $33\,\text{Å} \times 6.4''$
image1+2 cuts: $(-1, 12)$
image3 cuts: $(-7, 7)$
$V_{\rm rot}\sin i = 270.8^{+8.0}_{-12.7}\,{\rm km\,s^{-1}}$
$r_{\rm d} = 0.84^{+0.08}_{-0.06}{}''$

Figure B.23: Galaxy 1403 at $z = 0.8132$ ($\theta_{\rm slit} = +20°$).

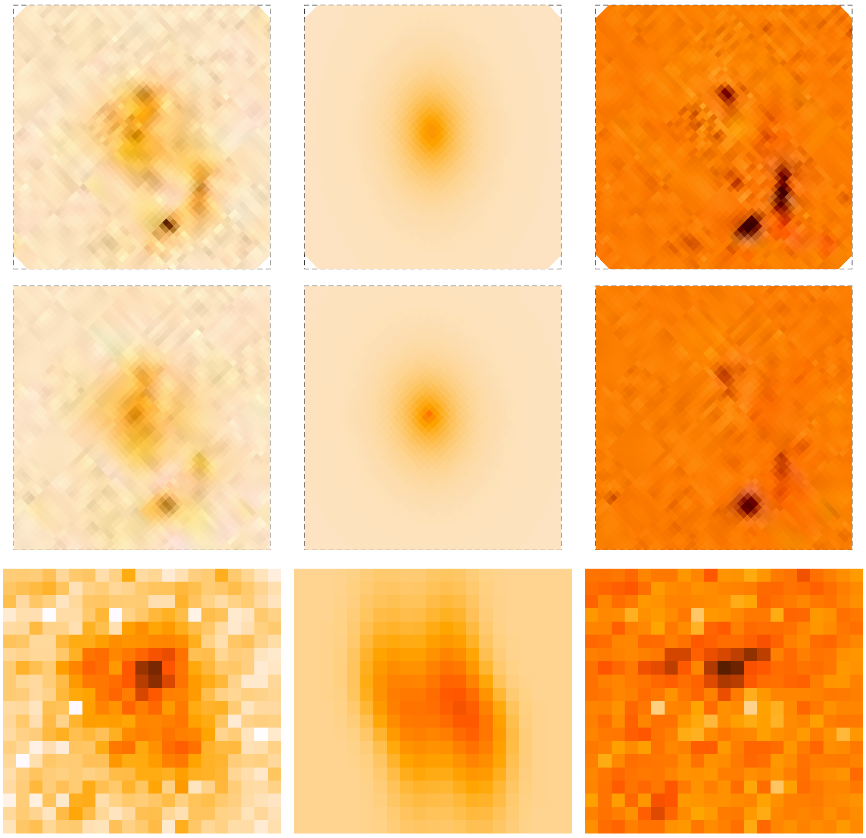

filter: F606W
image sizes: $5.0'' \times 5.0''$
image1+2 cuts: $(-3, 30)$
image3 cuts: $(-10, 10)$

filter: F814W
image sizes: $5.0'' \times 5.0''$
image1+2 cuts: $(-3, 30)$
image3 cuts: $(-10, 10)$

line: 3727
image sizes: $23\,\text{Å} \times 5.0''$
image1+2 cuts: $(-4, 20)$
image3 cuts: $(-10, 10)$
$V_{\rm rot} \sin i = 59.0^{+3.1}_{-1.9}\,{\rm km\,s^{-1}}$
$r_{\rm d} = 0.88^{+0.04}_{-0.05}{}''$

Figure B.24: Galaxy 1896 at $z = 0.8224$ ($\theta_{\rm slit} = +37°$).

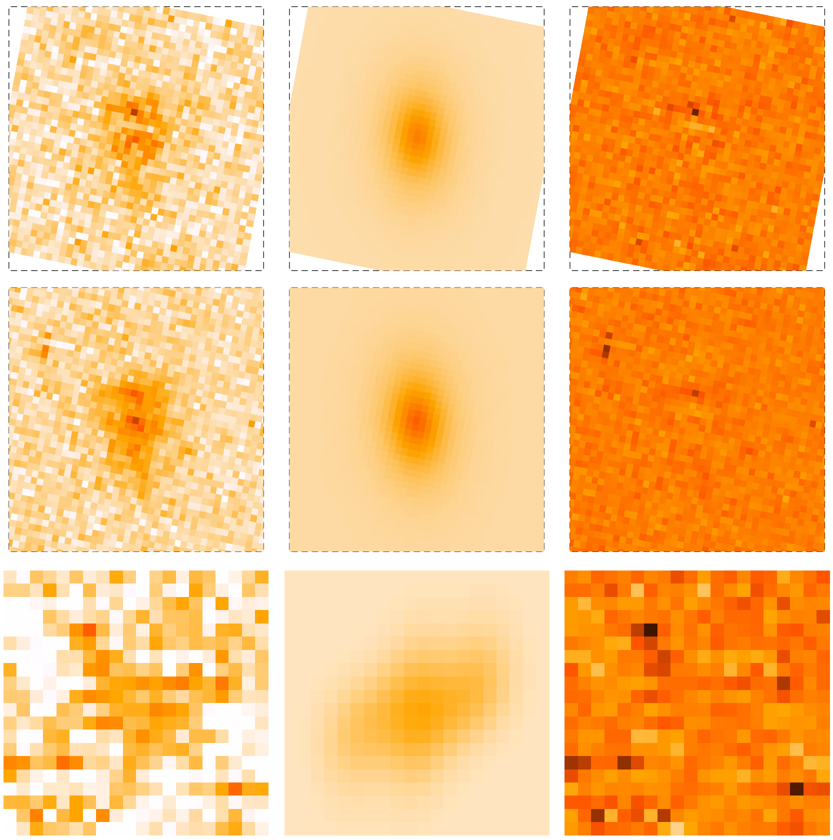

Figure B.25: Galaxy 2130 at $z = 0.8245$ ($\theta_{\rm slit} = +1^{\circ}$).

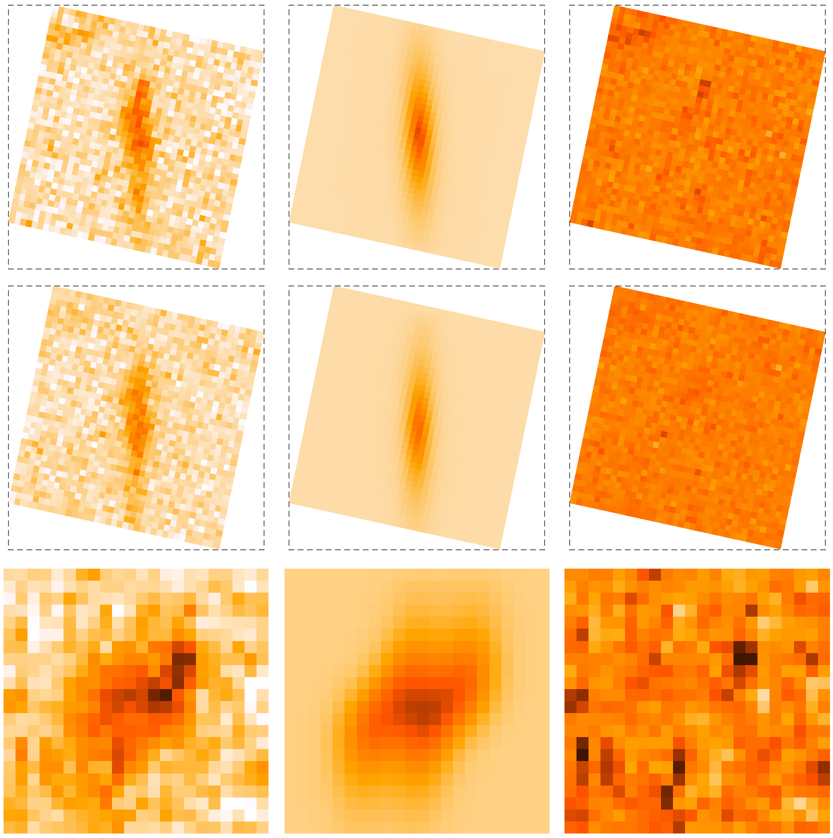

filter: F606W
image sizes: $4.4'' \times 4.4''$
image1+2 cuts: $(-2, 15)$
image3 cuts: $(-10, 10)$

filter: F814W
image sizes: $4.4'' \times 4.4''$
image1+2 cuts: $(-2, 15)$
image3 cuts: $(-10, 10)$

line: 3727
image sizes: $24\,\text{Å} \times 4.4''$
image1+2 cuts: $(-3, 15)$
image3 cuts: $(-7, 7)$
$V_{\rm rot} \sin i = 128.6^{+10.4}_{-8.1}\,{\rm km\,s^{-1}}$
$r_{\rm d} = 0.50^{+0.02}_{-0.02}{}''$

Figure B.26: Galaxy A8/C01 at $z = 0.8280$ ($\theta_{\rm slit} = +3°$).

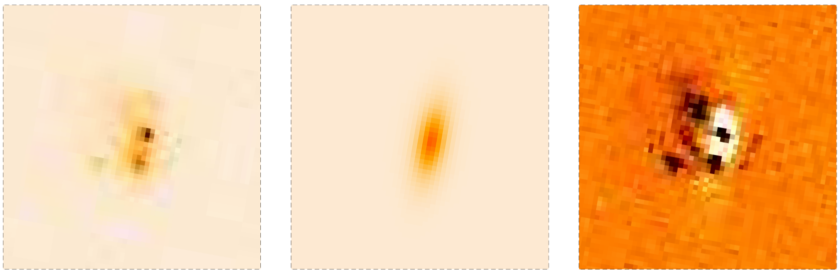

filter: F606W
image sizes: $5.6'' \times 5.6''$
image1+2 cuts: $(-9, 125)$
image3 cuts: $(-10, 10)$

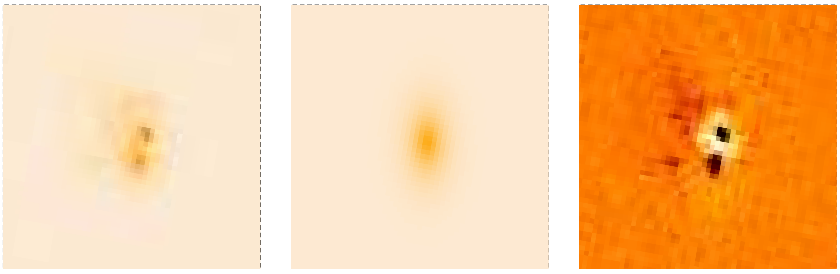

filter: F814W
image sizes: $5.6'' \times 5.6''$
image1+2 cuts: $(-9, 125)$
image3 cuts: $(-10, 10)$

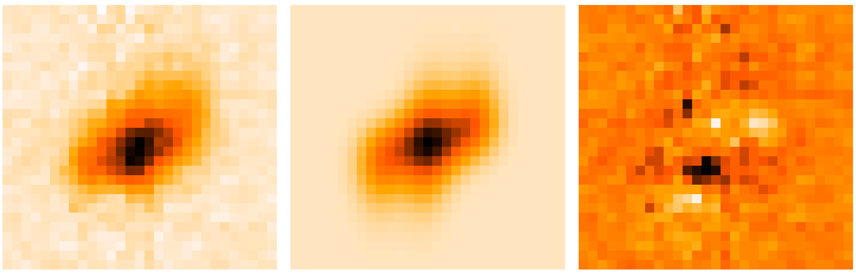

line: 3727
image sizes: $31\,\text{Å} \times 5.6''$
image1+2 cuts: $(-7, 72)$
image3 cuts: $(-13, 13)$
$V_{\rm rot} \sin i = 147.0^{+0.3}_{-0.2}\,\mathrm{km\,s^{-1}}$
$r_{\rm d} = 0.37^{+0.00}_{-0.00}{}''$

Figure B.27: Galaxy 1801 at $z = 0.8328$ ($\theta_{\rm slit} = 0°$).

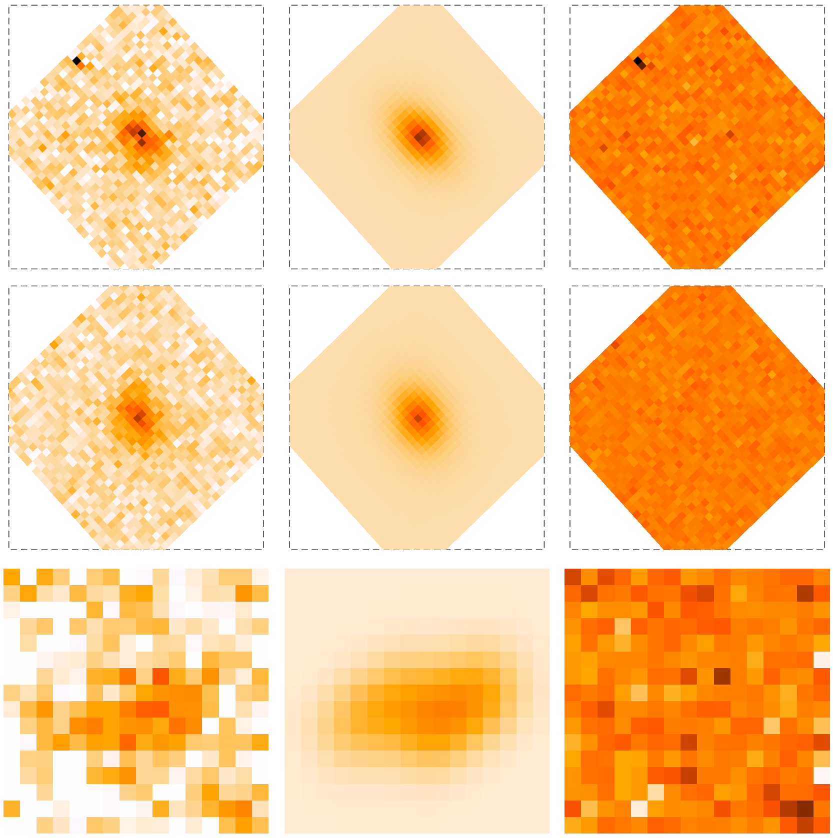

filter: F606W
image sizes: $4.0'' \times 4.0''$
image1+2 cuts: $(-2, 15)$
image3 cuts: $(-10, 10)$

filter: F814W
image sizes: $4.0'' \times 4.0''$
image1+2 cuts: $(-2, 15)$
image3 cuts: $(-10, 10)$

line: 3727
image sizes: $17\,\text{Å} \times 4.0''$
image1+2 cuts: $(-1, 10)$
image3 cuts: $(-7, 7)$
$V_{\rm rot} \sin i = 94.4^{+29.7}_{-30.1}\,{\rm km\,s^{-1}}$
$r_{\rm d} = 0.20^{+0.15}_{-0.06}{}''$

Figure B.28: Galaxy 1763 at $z = 0.8384$ ($\theta_{\rm slit} = +37°$).

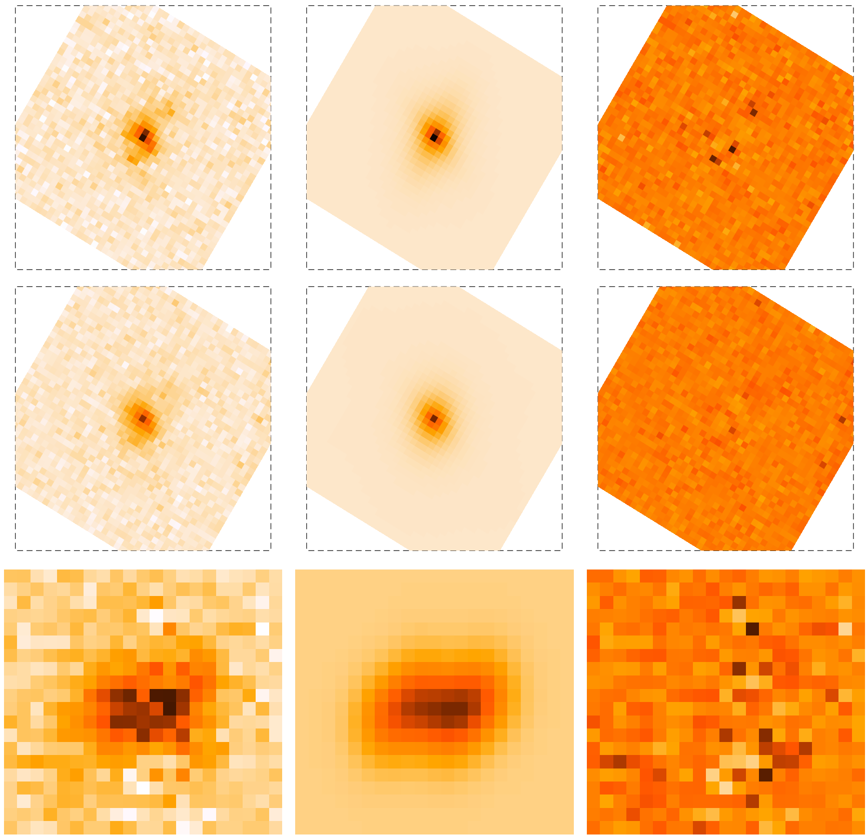

filter: F606W
image sizes: $4.3'' \times 4.3''$
image1+2 cuts: $(-3, 35)$
image3 cuts: $(-10, 10)$

filter: F814W
image sizes: $4.3'' \times 4.3''$
image1+2 cuts: $(-3, 35)$
image3 cuts: $(-10, 10)$

line: 3727
image sizes: $23\,\text{Å} \times 4.3''$
image1+2 cuts: $(-5, 25)$
image3 cuts: $(-10, 10)$
$V_{\rm rot} \sin i = 84.8^{+6.0}_{-5.5}\,{\rm km\,s^{-1}}$
$r_{\rm d} = 0.17^{+0.02}_{-0.02}{''}$

Figure B.29: Galaxy 2011 at $z = 0.8411$ ($\theta_{\rm slit} = +21°$).

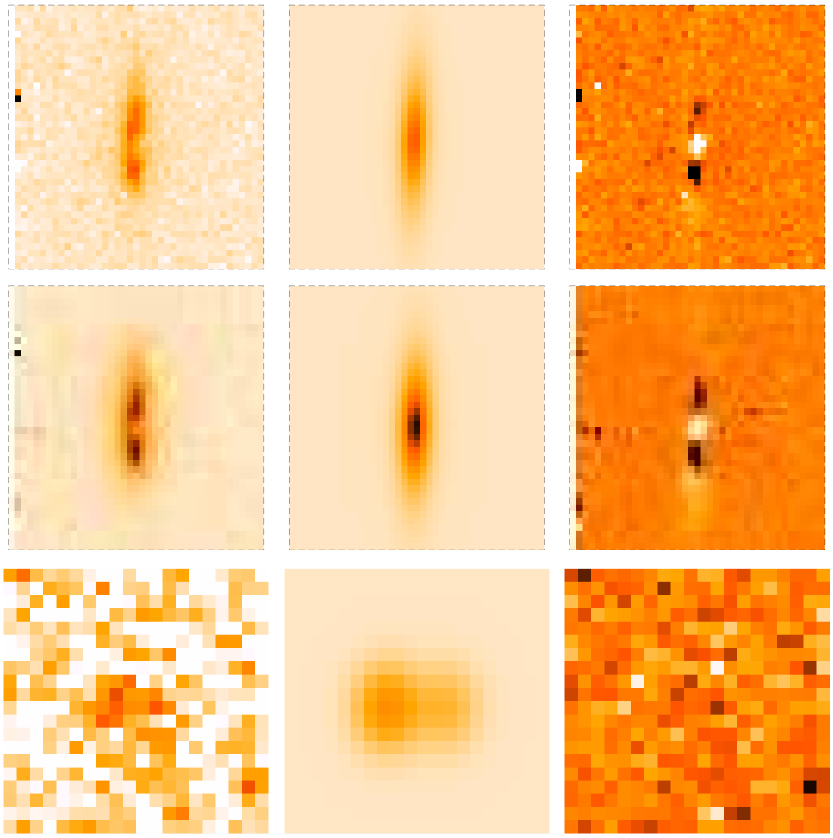

filter: F606W
image sizes: $4.1'' \times 4.1''$
image1+2 cuts: $(-5, 50)$
image3 cuts: $(-10, 10)$

filter: F814W
image sizes: $4.1'' \times 4.1''$
image1+2 cuts: $(-5, 50)$
image3 cuts: $(-10, 10)$

line: 3727
image sizes: $21\,\text{Å} \times 4.1''$
image1+2 cuts: $(-1, 10)$
image3 cuts: $(-7, 7)$
$V_{\rm rot} \sin i = 9.6^{+4.5}_{-5.3}\,{\rm km\,s^{-1}}$
$r_{\rm d} = 0.01^{+0.04}_{-0.01}{}''$

Figure B.30: Galaxy 1459 at $z = 0.8459$ ($\theta_{\rm slit} = -10°$).

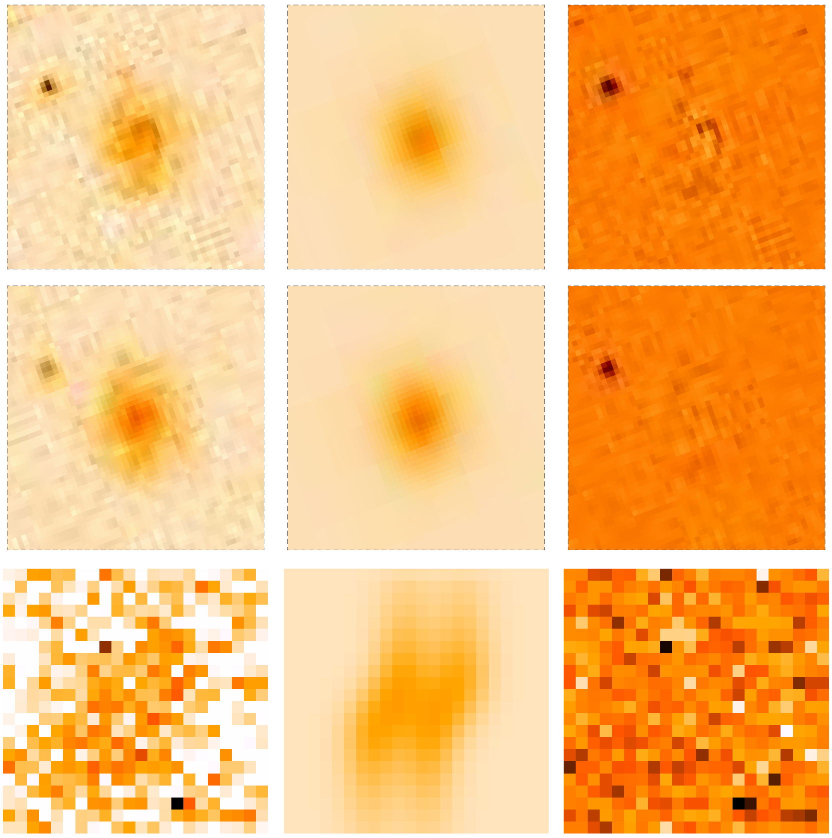

filter: F606W
image sizes: $5.1'' \times 5.1''$
image1+2 cuts: $(-3, 25)$
image3 cuts: $(-10, 10)$

filter: F814W
image sizes: $5.1'' \times 5.1''$
image1+2 cuts: $(-3, 25)$
image3 cuts: $(-10, 10)$

line: 3727
image sizes: $24\,\text{Å} \times 5.1''$
image1+2 cuts: $(-1, 10)$
image3 cuts: $(-7, 7)$
$V_{\rm rot} \sin i = 71.3^{+28.3}_{-21.6}\,\mathrm{km\,s^{-1}}$
$r_{\rm d} = 1.11^{+0.30}_{-0.17}{}''$

Figure B.31: Galaxy 661 at $z = 0.8462$ ($\theta_{\rm slit} = -30°$).

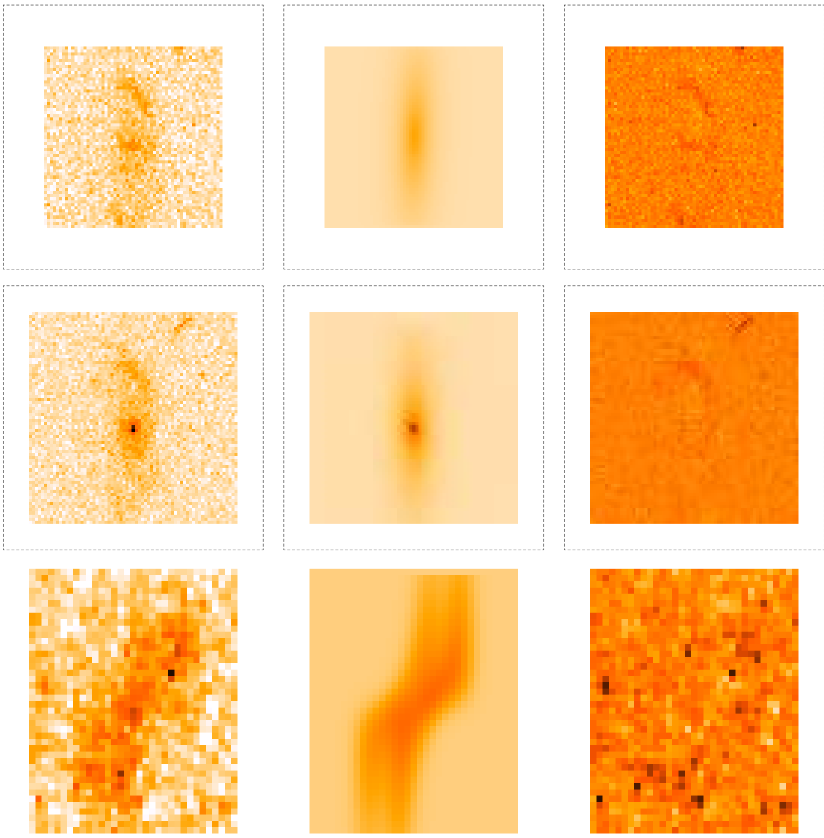

filter: F606W
image sizes: $8.6'' \times 8.6''$
image1+2 cuts: $(-2, 16)$
image3 cuts: $(-10, 10)$

filter: F814W
image sizes: $8.6'' \times 8.6''$
image1+2 cuts: $(-2, 16)$
image3 cuts: $(-10, 10)$

line: 3727
image sizes: $35\,\text{Å} \times 8.6''$
image1+2 cuts: $(-2, 12)$
image3 cuts: $(-7, 7)$
$V_{\rm rot}\sin i = 235.9^{+3.7}_{-4.0}\,{\rm km\,s^{-1}}$
$r_{\rm d} = 2.24^{+0.17}_{-0.14}{}''$

Figure B.32: Galaxy B1/F22 at $z = 0.8965$ ($\theta_{\rm slit} = -10°$).